A detailed study of anodization current in ion irradiated silicon

by

Dang Zhiya (党志亚)

Bachelors in Physics (Electronic Devices & Materials Engineering)

Lanzhou University

Thesis Submitted For the degree of

Doctor of Philosophy

Department of Physics

National University of Singapore

2013

Declaration

I hereby declare that the thesis is my original work and it has been written in its entirety. I have duly acknowledged all the sources of information which have been used in the thesis.

This thesis has also not been submitted for any degree in any university previously.

Zhiya Dang

12th Dec 2013

Acknowledgements

Families always give me the strongest support when I need courage and strength in PhD, thank you, my parents, sister and brother. Centre for Ion Beam Applications (CIBA), has become a home in Singapore for me, with its lovely and brilliant people.

The entire thesis is finished under my supervisor Prof Mark's constant support and numerous discussions. Monthly discussion in silicon micromachining group and exchange of insights on the new results was very useful, thanks to the group members, Isaac, Aky, Sara, Jiao, Haidong. Weekly discussion with Prashant on photonic crystal topic helped me to continue with the relevant work in spite of great challenges. Frequent discussions with Malli on variety of topics give me inspirations.

Besides, several experiments of this thesis were carried out collaboratively. Characterization session of photonic crystals using FTIR was a lot of fun with Aga and Chris' help. The simulation of current flow using COMSOL was carried out by Jacopo and Prof. Ettore through frequent discussions. Without their help in simulation, the first part of thesis on theoretical study would be not possible. The simulation of photonic crystals using MPB package was carried out by Gonzalo, with Prof. Martin's support. Cesium irradiation was carried out by Yiteng with support of Prof Tok. Helium ion irradiation intrigued our interest on diffusion current component, and I would like to thank Fang Chao, Vignesh, Prof. Pickard's efforts in Helium ion microscope training. Current voltage characteristic study of ion irradiated silicon was carried out by Dongqing with Prof. Blackwood's support. Focused ion beam for imaging the cross section was carried out with Linke and Zeiss's help. The proton beam writing was carried out with help of many labmates in CIBA (Yao Yong, Yinghui, Isaac) at different times. I had several useful discussions on photonic crystals with Prof. Andrew. UV lithography was carried out with help of Liu Fan. PL was carried out with help of Prashant. SEM sessions were helped by Mr Ho, and AFM by Mr Ong. Ion beam tuning was helped by Armin.

Thanks for NUS providing scholarship, and the support from Prof Mark for visiting labs, and conferences.

Table of Contents

Summary

Ion beam irradiation of p-type silicon combined with subsequent electrochemical anodization has been used for 3D silicon micromachining. However, the basic understanding of anodization current flow has been lacking, which has hindered effectively controlling the structural parameters and further applications. In this thesis, a detailed study on the change of electrical properties in p-type Si caused by ion irradiation, as well as its effect on current flow, is carried out. Instead of only considering a pure increase of resistivity and resultant reduction in drift current and etching rate in previous studies, this thesis takes the reduction of effective doping concentration, hole mobility, and hole density into account, which leads to a previously ignored but important current component, a diffusion current. In wafers with non-uniform hole densities, funneling of current along the doping gradient is shown to be very important in this mode of machining. This discovery not only lays a foundation for effective controlling and optimization of silicon micromachining, but also opens a new way for patterning porous silicon, and glass by forming highly porous silicon regions based on the funneling effect. Several factors that were previously ignored, including amorphization, sputtering, time evolution, and interface between electrolyte and Si are discussed in this thesis, along with the importance of fluence, ion type, ion energy, etc. Apart from basic exploration on the mechanism, bulk and surface structuring method of Si, structuring of porous silicon, and glass, this thesis also explores their applications in mid-infrared photonic crystals.

List of Tables

List of Figures

List of Symbols

Na	Doping concentration
Na^{eff}	Effective doping concentration
μ_p	Hole mobility
D	Diffusion coefficient
ϕ	Ion fluence
ψ	Electric potential
f	Fraction of donors
J_{diff}	Diffusion current density
J_{drift}	Drift current density
J_{total}	Total current density
ρ	Resistivity
q	Electric charge of electron
p	Hole density
v	Defect density
W	Space charge region width
k_0	Boltzmann's constant
T	Absolute temperature
S	Selectivity coefficient
t	Time
W_{core}	Core width
H_{core}	Core height

k	Wave vector
a	Period
λ	Wavelength
ω	Frequency
c	Speed of light
r	Radius
h	Thickness
R_i	Ion range
b	Beam size
s	Scattering size
n	Refractive index
ε	Dielectric constant
d	Pore size

List of publications

- M. D. Ynsa, **Z.Y. Dang**, M. Manso-Silvan, J. Song, S. Azimi, J. F. Wu, H. D. Liang, V. Torres-Costa, M. B. H. Breese, J. P. Garcia-Ruiz, Reprogramming hMSCs morphology with silicon/porous silicon asymmetric micro-patterns, Biomedical Microdevices (2013 accepted)
- S. Azimi, J. Song, **Z. Y. Dang**, and M. B. H. Breese, A thousand-fold enhancement of photoluminescence in porous silicon using ion irradiation, J. Appl. Phys. 114, 053517 (2013)
- **Zhiya Dang,** Agnieszka Banas, Sara Azimi, Jiao Song, Mark Breese, Yong Yao, Shuvan Prashant Turaga, Gonzalo Recio-Sánchez, Andrew Bettiol, and Jeroen Van Kan, Appl. Phys. A 112 (3), 517 (2013**)**
- J. Song, **Z. Y. Dang**, S. Azimi, & M. B. H. Breese, Fabrication of silicon nanowires by ion beam irradiation. In MRS Proceedings (Vol. 1512, pp. mrsf12-1512). Cambridge University Press. (2013, January)
- S. Azimi, **Z. Y. Dang**, J. Song, M. B. H. Breese, E. Vittone, J. Forneris, Defect enhanced funneling of diffusion current in silicon. Applied Physics Letters, 102(4), (2013) 042102-042102
- **Z.Y. Dang**, J. Song, S. Azimi, M.B.H. Breese, J. Forneris, E. Vittone, On the formation of silicon wires produced by high-energy ion irradiation, Nuclear Instruments & Methods in Physics Research B 296 (2013), 32–40
- S Azimi, J Song, **Z Y Dang**, H D Liang and M B H Breese, Three-dimensional silicon micromachining, J. Micromech. Microeng. 22 (2012) 113001
- M. Motapothula, S. Petrović, N. Nešković, **Z. Y. Dang**, M. B. H. Breese, M. A. Rana and A. Osman, Origin of ring like angular distributions observed in rainbow channeling in ultrathin crystals, Phy. Rev. B (2012) 86, 205426.
- Gonzalo Recio-Sánchez, **Zhiya Dang**, Vicente Torres-Costa, Mark BH Breese and Raul-Jose Martín-Palma, Highly flexible method for the fabrication of photonic crystal slabs based on the selective formation of porous silicon, Nanoscale Research Letters 2012, 7:449

- **Zhiya Dang**, Mark BH Breese, Gonzalo Recio-Sánchez, Sara Azimi, Jiao Song, Haidong Liang, Agnieszka Banas, Vicente Torres-Costa and Raúl José Martín-Palma, Silicon-based photonic crystals fabricated using proton beam writing combined with electrochemical etching method, Nanoscale Research Letters 2012, 7:416
- J. Song, **Z. Y. Dang**, S. Azimi, M. B. H. Breese, J. Forneris and E. Vittone, On the formation of 50nm Diameter free-standing silicon wires produced by ion irradiation, ECS Journal of Solid State Science and Technology 1 (2012) 66-69
- M. Motapothula, **Z.Y. Dang**, T. Venkatesan, M. B. H. Breese, M. A. Rana, and A. Osman, Axial ion channeling patterns from ultra-thin silicon membranes, Nuclear Instruments & Methods in Physics Research B 283 (2012) 29-34
- M. Motapothula, **Z.Y. Dang**, T. Venkatesan, M. B. H. Breese, M. A. Rana, and A. Osman, Influence of the Narrow {111} Planes on Axial and Planar Ion Channeling, Physical Review Letters 108, 195502 (2012)
- S Azimi, M B H Breese, **Z Y Dang**, Y Yan, Y S Ow and A A Bettiol; Fabrication of complex curved three-dimensional silicon microstructures using ion irradiation, Journal of Micromechanics Microengineering 22 015015 (2012)
- **Z. Y. Dang**, M. Motapothula, Y. S. Ow, T. Venkatesan, M. B. H. Breese, M. A. Rana, and A. Osman, Fabrication of large-area ultra-thin single crystal silicon membranes, Applied Physics Letters 99, 223105 (2011)
- M. B. H. Breese, S. Azimi, Y. S. Ow, D. Mangaiyarkarasi, T. K. Chan, S. Jiao, **Z. Y. Dang**, and D. J. Blackwood; Electrochemical Anodization of Silicon-on-Insulator Wafers Using an AC, Electrochemical and Solid-State Letters, 13 8 H271-H273 (2010)

Chapter 1 . Introduction

In this chapter, Section 1.1 introduces silicon, porous silicon and glass obtained by fully oxidizing p-Si. These are the three important materials used in this thesis. Section 1.2 firstly reviews the methods of patterning and structuring silicon. Then the method of electrochemical etching of ion irradiated p-type silicon is introduced which is the major focus of this thesis. Section 1.3 is a thesis overview.

1.1 Silicon, Porous Silicon and Fully Oxidized Porous Silicon

1.1.1 Silicon

Silicon (Si) is widely used in integrated circuits and it is the basis of modern technology. Si has diamond cubic crystal structure, with a lattice spacing of 5.43 Å. Pure silicon is an intrinsic semiconductor. With a low conductivity, it is commonly doped with other elements to increase the conductivity. Doped silicon comprises two types; p-type silicon is doped with group III elements, such as boron, with excess holes, and n-type is doped with group V elements, such as phosphorous, with excess electrons. Group V elements behave as electron donor, while group III elements behave as acceptor. p-type boron doped [1 0 0] Si wafers with several different doping densities are used throughout this thesis. Apart from its electrical properties, Si also exhibits good mechanical properties. [1] One such example as a single-crystal material is that it has a tendency to cleave along major crystallographic planes.

1.1.2 Porous Silicon (p-Si) and fully oxidized p-Si (FOPS)

Porous Silicon (p-Si), the next important material of this thesis, is a structure with pores in silicon. There are two methods to introduce pores in silicon, one is through electrochemical anodization, and the other is through stain etching. In the former method, a platinum cathode and a Si wafer as anode are immersed in hydrogen fluoride (HF) electrolyte solution. By passing an electrical current through the back to the front wafer surface, p-Si is formed at the interface of the electrolyte and silicon. The second method to obtain thin p-Si films is through stain-etching with hydrofluoric acid, nitric acid and water. In this thesis, the method of electrochemical anodization of p-type silicon wafer in hydrogen fluoride electrolyte is used primarily and is discussed further below.

p-Si is categorized into three types according to the pore size (d) namely as microporous($d < 2$ nm), mesoporous($2 \text{ nm} < d < 50$ nm) and macroporous($d > 50$ nm) silicon.[2] Pore width d is defined as the distance between two opposite walls of the pore.

Table 1.1 Comparison of three types of p-Si on p-type silicon

p-Si type	Pore size	Doping density	Anodization mechanism
Microporous Silicon	d < 2 nm	10^{16}-10^{17}cm^{-3}	QC effect
Mesoporous Silicon	2 nm < d < 50 nm	>10^{18}cm^{-3}	Tunnelling
Macroporous Silicon	d >50 nm	<10^{16}cm^{-3}	Diffusion

The comparison between three types of p-Si is summarized in Table 1.1 above. For p-type silicon, a space charge region(SCR) forms at the interface when doping density is below 10^{18}cm^{-3}, the diffusion and thermionic emission of holes occurs across the SCR, and this charge transfer is responsible for formation of macropores for doping density below 10^{16}cm^{-3}. When doping densities exceed 10^{18}cm^{-3}, the charge transfer at p-type electrode is dominated by tunnelling through the SCR, and this is responsible for formation of mesopores. With doping densities 10^{16} ~10^{17}cm^{-3}, microporous silicon is formed due to quantum confinement effect.

There are two parameters that are important for the following chapters. One is porosity, which is defined as fraction of pores to the total volume of sample, the other is effective refractive index. p-Si is a material which can have variable porosity, enabling variable refractive index. A multilayer of porous silicon with alternative porosities has been used previously for distributed Bragg reflectors. [3] p-Si has large surface-to-volume ratio, which can be infiltrated with a medium of choice and has been used for gas or liquid sensing applications. [4, 5] Microporous silicon produces photoluminescence(PL),[6] and has been used for active devices.[7]

Glass is an amorphous (non-crystalline) solid material. Glass is widely used in optoelectronics, for light-transmitting optical fibers. Glass can be obtained by fully oxidizing p-Si, where the volume expansion during oxygen incorporation and SiO_2 formation completely fills the voids in porous silicon matrix, resulting in a continuous glass volume. An oxidized fraction of 100% can be

reached on a scale of hours only if the initial porosity of p-Si is greater than about 56%.[8]

1.2 Silicon structuring

1.2.1 Silicon Micromachining

Si structuring, also called silicon micromachining, represents patterning of Si on or beneath surface. Silicon structuring processes include deposition, patterning and etching. Lithography is used for transfer of a pattern to a radiation-sensitive material by selective exposure to a radiation source. It includes a variety of different types of processes, such as photolithography, electron beam lithography, ion beam lithography, X-ray lithography, etc. Etching is the removal of material by an etchant which is either a solution or reactive gas. Alkaline etchants are used to make microstructures, and to control the vertical dimension, many different etch stop techniques are used. Silicon, which is highly doped with boron, etches slowly in alkaline solutions, allowing fabrication of 3D structures.[9, 10] Buried mask layers, such as silicon dioxide, silicon nitride, and silicon carbide, can be used as an etch stop. Silicon on insulator wafers can be directly used in this case. [11] Electrochemical etching (ECE) is a process for dopant-selective removal of silicon. Either type of dopants are created by implantation, diffusion or epitaxial deposition to act as the etch stop material. It can be used to fabricate sensors, [12] actuators, photonic components,[13] etc.

Surface machining uses deposited thin films or SOI wafers.[14, 15] The top layer is selectively etched using mask patterns; then the sacrificial layer is removed, producing free-standing silicon structures. Focused ion beams (FIB) are also used for silicon surface patterning. [16] A common method for bulk silicon machining is deep reactive ion etching (DRIE). [17] Gallium ion implanted Si behaves as a mask for reactive ion etching to fabricate high aspect ratio nanostructures in Si [18] or by combining with wet etching, free standing structures can be fabricated.[19] Metal assisted etching of silicon has been used by using templates based on nanosphere lithography, anodic aluminum oxide masks, interference lithography, and block-copolymer masks. [15, 17, 20] An 800nm fs laser was also used to write grooves on Si. [17] p-Si and glass structuring methods will be briefly reviewed in section 6.3 and 6.4.

1.2.2 Ion beam irradiation combined with Electrochemical etching of p-type Si (CIBA process)

Several electro- and photo-electrochemical processes are mentioned above which allow silicon microstructures to be formed within ion-implanted silicon wafers.[16]Ion beam irradiation combined with electrochemical etching of p-type Si is a true 3D Si micromachining method, which is referred as CIBA process in this thesis. This process has two patterning methods, one of which is direct nanobeam writing, and the other is projection of a large area uniform ion beam through mask. In direct nanobeam writing, a finely focused beam of MeV ions[21] is scanned over the Si wafer surface and as it penetrates the semiconductor, the ion stopping process damages the Si crystal by producing additional vacancies in the semiconductor.[22] By controlling the dosage of the focused beam at different locations, any pattern of localized damage can be built up. The irradiated wafer is then electrochemically anodized in HF electrolyte in which an electric current is passed through the wafer, and p-Si is formed selectively. After removal of p-Si, Si structures are obtained. [23, 24] These two methods will be discussed further in detail in chapter 6, and be used in various chapters throughout the whole thesis.

CIBA process has been used for producing micropatterned Si surfaces[25], controlled photoluminescence from patterned porous Si, [26] and controlled reflectivity from patterned porous Si Bragg reflectors,[27] waveguides,[28] and holographic imaging.[29] However, the process is controlled more empirically since the basic mechanism of electrochemical anodization of ion irradiated p-type silicon has not been studied thoroughly. The structural shape and size are not controllable, which hinders its further applications. Therefore, to enable better control and new fabrication methods, there is a great need to study the basic mechanism of anodization in such ion irradiated Si, which is the main focus of this thesis. In order to study the basic mechanism, this thesis starts from studying the variation of electrical properties of p-type silicon after ion irradiation. Based on this the anodization current flow is studied by combining a simplified model based simulations and experiment evidences. The physical processes, time dependent evolution and electrochemical aspects that are ignored in the simulations are taken into account and used to explain

various experiment results under different conditions in the later chapters. Apart from the applications in optics and photonics mentioned above, it is tempting to apply this method for fabricating photonic crystals, which is the major application field explored in this thesis.

1.3 Thesis overview

Chapter 1 discusses three materials of central importance, silicon, porous silicon, and glass, as well as methods used for Si micromachining. Chapter 2 introduces experimental facilities and tools that are used in the following chapters, including ion irradiation tools, material analysis tools, morphology study tools, and set up of electrochemical etching. Chapter 3 discusses a current voltage characteristic study of p-type wafers which are entirely irradiated with high energy protons, and possible mechanism is proposed. Chapter 4 mainly discusses the two components of hole current in electrochemical anodization of ion irradiated p-type silicon, and introduces the concept of funnelling effect, which can be influenced by variety of factors. This is the first highlight of this thesis, which is to provide a full picture of current transport in ion irradiated p-type Si. Chapter 5 discusses the core formation mechanism in wafers of two different resistivity used in relevant work, and different factors that influence the core formation are discussed in detail. Chapter 6 discusses the silicon micromachining results, which include fabrication of high aspect ratio silicon walls, silicon pillars, fabrication of free-standing tip-arrays, wires, and grids. Chapter 6 also discusses p-Si structuring and oxidized p-Si (glass) patterning. Chapter 7 introduces silicon surface patterning, and the effects of amorphization, sputtering, reduction of work function are incorporated into the anodization current flow study in this context. It is a complementary study of chapter 4. Chapter 8 discusses the application of silicon and p-Si structuring processes in fabrication of photonic crystals in the Mid-infrared range, and initial trials in characterization process. Chapter 9 concludes the whole thesis and discusses several examples of the further work that will be carried out.

The main contribution of this thesis is in understanding of fundamental physical mechanism of current flow in a charged particle irradiated semiconductor, which in this specific context, is the mechanism of hole current flow in ion irradiated p-type silicon. The use of this mechanism in Si and p-Si, glass structuring and its applications in photonic crystal and further in photonic devices, as well as integrated photonic circuits is also explored.

A comparison of this thesis and previous work in terms of basic concepts, ions used, resultant structures, and application areas are listed in Table 1.2.

Table 1.2 Comparison of this thesis and previous work

Comparison	Previous work	This thesis
Change in ion irradiated silicon	Increase of resistivity	Reduction of effective doping concentration, and hole mobility
Current component considered	Drift current	Drift and diffusion current
Effect on etching rate	Slowed down	Either enhanced, or reduced, depending on experimental conditions
Etching mode used	Direct current	Direct, and alternating current
Ions used	High energy protons, helium ions (100keV~2MeV), focused down to 200nm	Apart from listed on the left, 30keV He^+ focused down to 1nm, 15keV Cs^+
Resultant structures	Silicon walls, pillars, free-standing silicon wires	Apart from listed on the left, buried channels in porous silicon, fully oxidized porous silicon
Application areas	Waveguides	Photonic crystals, microfluidics, etc.

Chapter 2 . Experimental facilities & Background

This chapter will introduce the experimental facilities, setups used, as well as background knowledge on defect distribution in Si due to ion irradiation. Section 2.1 discusses the ion irradiation facilities used in this thesis. Section 2.2introduces the electrochemical setup for HF etching and tools for morphology study. Section 2.3 introduces the background knowledge on defect distribution in silicon due to ion irradiation. Apart from tools and facilities, this chapter leads to the curious question of how the ion irradiation generated defects modify the current flow during the etching process, and how these mechanisms lead to resultant structures, and selective formation of p-Si, which is one of the main motivations of this thesis.

2.1 Ion irradiation facilities

(1) 100 keV~2 MeV Protons and Helium ions

A particle accelerator uses electrostatic fields to propel charged particles to high speeds and to contain them in well-defined beams. Electrostatic accelerators use static electric fields to accelerate particles, such as Van de Graaff generator.

High energy particle beams are very useful for both fundamental and applied research in the sciences, and also in many technical and industrial fields. Low energy particle accelerators are used in the manufacture of integrated circuits.

Single-ended accelerators operate with the ion source inside the terminal, where the terminal potential is positive and the ion source produces positive ions that are then accelerated away from the terminal. Tandem, or double-ended, accelerators operate with a negative ion source at close to ground potential. The negative ions are drawn in toward the positive terminal where they are stripped to positive ions and accelerated.

Once the beam has been accelerated, it is transported to a variety of beamlines by a bending magnet, where the momentum dispersion of the bending magnet can reduce the momentum spread of the beam entering the beamline.

Figure 2.1 shows the schematics of 3.5MeV Singletron accelerator in Centre for Ion beam applications in National University of Singapore. Currently there are five beamlines, as shown in Figure 2.1. The proton beam writing (PBW)[21] beamline is used for photoresist patterning, [30] silicon micromachining, [24] metal mold fabrication, [31] etc. The structures have been used in photonics, [32] microfluidics, [33] etc. The 2nd generation PBW beamline aims at focusing the beam down to sub-ten nanometers. [34]The bioimaging beamline is used as a tool for the whole cell imaging.[35] The nuclear probe in the material analysis beamline is used for Rutherford backscattering spectroscopy (RBS), [36] Proton induced X-ray emission (PIXE), [37] Scanning transmission ion microscopy (STIM), [38] etc. The high resolution RBS (HRBS) beamline [39] enables analysis with resolution of single digit nanometers in depth.

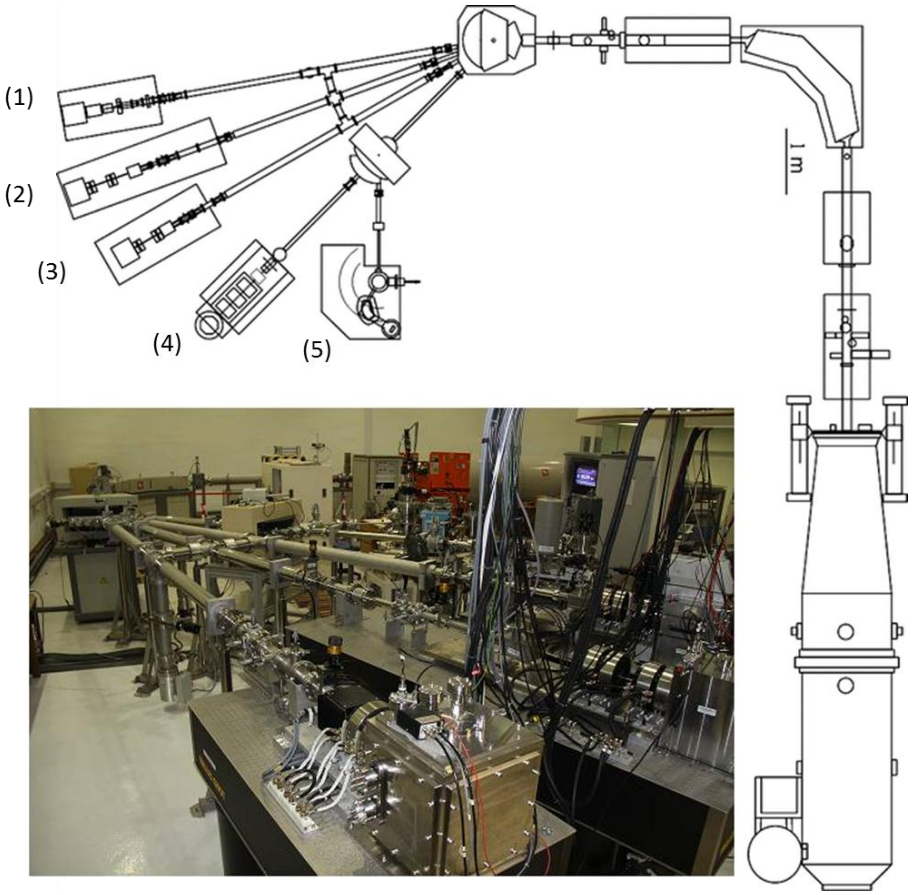

Figure 2.1 Acelerator in Centre for Ion Beam applications(CIBA) and the beamlines: (1) Proton beam writing(PBW); (2) 2nd generation PBW; (3) Bioimaging; (4) Nuclear microprobe and broad beam exposure; (5) High resolution RBS.

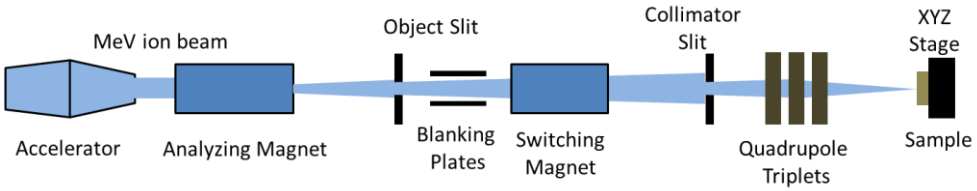

Figure 2.2 Schematic diagram of Proton beam writing line in CIBA(Reproduced from Ref. [40])

The accelerator in CIBA has several beamlines, where the proton beam writing beamline is the most frequently used as shown in the schematics of Figure 2.2. A beam of high energy-ions coming from the terminal after the bending magnet passes through an object aperture and is demagnified by a strong focusing lens system to form a probe at the sample (Focusing procedures shown in Appendix). Proton beam writing is a new direct-writing

process that uses a focused beam of MeV protons to pattern resist materials at nano-scale dimensions. [21] The advantage of this method is that high energy protons have deeper penetration in materials while maintaining a straight path and it has been used to fabricate three-dimensional, high aspect ratio structures with vertical, smooth sidewalls and low line-edge roughness in different photoresists. [41] This method has also been used for silicon micromachining by inducing designed damage into silicon crystal, as discussed in section 1.2.2.

A scanning program has been developed in-house which includes the ability to perform combined stage and magnetic (or electrostatic) scanning. The scanning modes for proton beam writing include point scan mode, and line scan mode.[42] The maximum scan size for point scan mode is 500 μm x 500 μm, while for line scan, it can be about a cm long.

As discussed above, the maximum scan size in point scan is limited, while the line scan is limited to only lines. Meanwhile, the ion fluence needed for silicon micromachining is very high and low ion current is needed to achieve a focused beam spot, therefore, to irradiate Si with PBW is time-consuming. Therefore, a large area irradiation method has been developed, where designed patterns are fabricated on photoresist or metal which is pre-coated on a silicon wafer surface, and then the pattern is transferred to silicon by irradiating the whole wafer surface with a uniform large-area ion beam. The first projection work was reported in Ref. [43].

For the large-area beamline, the beam current is much higher than the proton beam writing line, thus, it enables fabrication of large area structures in a relatively short time. As shown in Figure 2.3, with an extension pipe, the focused beam diverges into a beam with large area. By cutting the outer edge of beam with collimator slits, the shape of ion beam can be adjusted into a well-defined square with uniform intensity. This enables accurate control of the fluence and uniform irradiation of the whole surface.

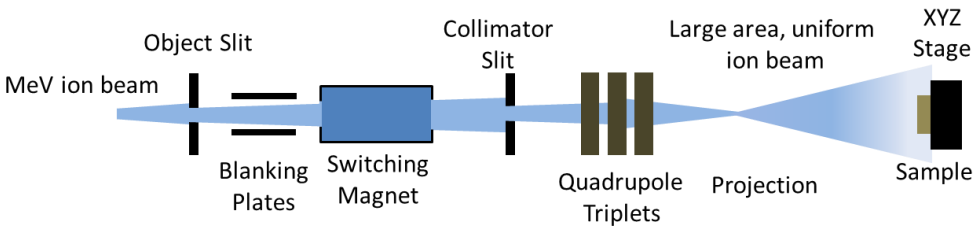

Figure 2.3 Schematic diagram of large area irradiation facility in CIBA.

A photoresist mask is fabricated by UV or e-beam lithography. UV lithography can produce large area patterns with relatively coarse structures with feature sizes of >2 μm depending on the thickness of photoresists. With a pre-coated metal seed layer, nickel can be filled into the gaps between the photoresist patterns by electroplating and serves as the mask for ion irradiation. Electron beam (e-beam) writing is conducted by a standard SEM located at SSLS in NUS, for which the resolution can reach tens of nanometers. However, e-beam writing produces small area patterns, and only works for thin photoresists (less than 1 μm). The energy of electrons is very low (tens of keV energies) and produces structures with small height or depth.

(2)30 keV He ions

The helium ion microscope(HIM)[44] in NUS was used to generate a 30 keV helium beam with beam size of around 0.5nm containing a current around 0.5 pA. Compared with high energy protons, the defects generated during collision of 30 keV helium ions with material atoms are located much closer to the surface.

(3) 15 keV Cs ions

Secondary ion mass spectrometry (SIMS)[45] is a technique used in material science and surface science to analyze the composition of solid surfaces and thin films by sputtering the surface of the specimen with a focused primary ion beam and collecting and analyzing ejected secondary ions. One type of ion gun in SIMS generates Cs^+ primary ions, in which cesium atoms vaporize through a porous tungsten plug and are ionized during evaporation. In NUS, there is an UHV system for spectroscopic (SIMS) study which can produce a

Cs^+ microbeam source. A 15 keV Cs^+ ion beam with a size of 25 μm, containing a beam current ranging from 0.01 nA~1 nA, which is able to scan over 500 μm x 500 μm area, is available. The Bragg peak of 15 keV Cs^+ is in Si is located at the surface of Si.

2.2 Other experimental tools & facilities

2.2.1 Electrochemical etching set-up

After ion irradiation, the silicon wafers are electrochemically anodized in HF electrolyte. The design of an electrochemical setup depends on a variety of requirements, such as sample size, uniformity of porous silicon layer, sample fragility, single-side or double-side porous silicon formation, ease of observation of morphology of sample surface, illumination conditions, etc. p-type silicon is mainly used in this thesis for which two different electrochemical setups are adopted.

1) Back-side protection by epoxy

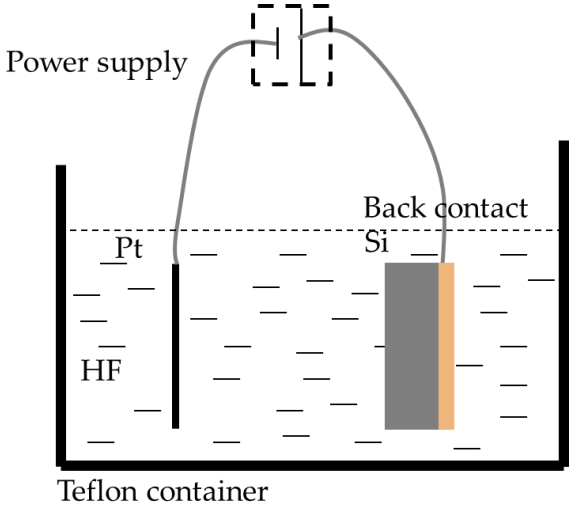

Figure 2.4 Setup of first method of electrochemical etching of p-type silicon

In its simplest form, the etching process is conducted by protecting the back-face of wafer from HF by using epoxy glue. Copper wires are electrically connected using GaIn eutectic paste to the back surface and held in place under the epoxy. The overall setup of this first method is shown in Figure 2.4. Most samples comprise a bulk single-side polished p-type silicon wafer, with a thickness of 525 μm or 275 μm, for which the top 1~50 μm layers in the following chapters are partially damaged on the front surface by the ion beam. A silicon wafer exposed in ambient air has a native oxide layer, which is removed by dipping the wafer in 2% HF for 5 mins, to enhance the low resistance contact on the back side.

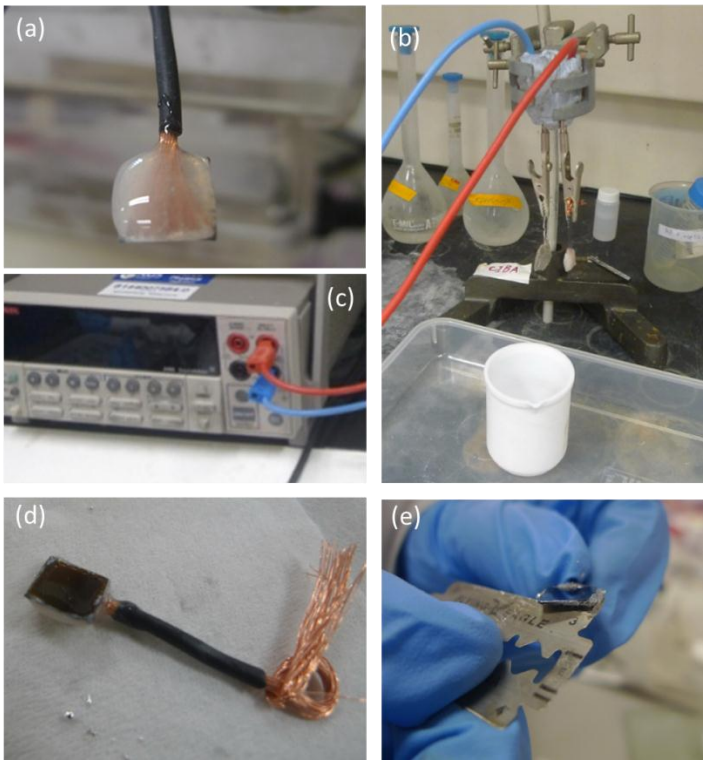

Figure 2.5 Procedures of electrochemical etching by back-contact method: (a) Ohmic contact and protection from electrolyte: Spreading copper wires, applying EGaIn paste, applying mixed epoxy; (b) Overall etching setup; (c) Zoom-in of the power supply; (d) Etched silicon surface; (e) Removal of epoxy.

To form a uniform layer of p-Si, copper wires are spread, and connected to the back surface of samples using EGaIn paste to ensure a low contact resistance between the wires and back surface of silicon. In addition to a good electrical contact, a good protection for the copper wires and back surface of silicon from HF electrolyte is necessary for which an epoxy resin (Araldite) is used. The resin does not react with HF electrolyte, and can be easily removed later by a sharp blade. The epoxy resin is formed by mixing the hardener and an adhesive, which is applied onto the back surface when it is soft and wet. It becomes dry and hard within 1-2 hours. A good insulation is important for avoiding any current leakage. It is important to protect the back surface of wafer, as well as the edges as shown in figure 2.5(a). The appropriate mix of the epoxy resin enables us to etch the sample in 24% HF for more than 30 mins. The conducting back-side protected by epoxy is connected to a positive bias and a platinum cathode is placed face-to-face with the silicon wafer at a

certain distance shown in figure 2.5(b). Both the anode and cathode are placed into HF electrolyte and connected to a power supply. A close-up picture of the power supply connected to the anode and cathode is shown in Figure 2.5(c). The power supply is 2400 Keithley Source Meter. It provides precise voltage and current sourcing as well as measurement capabilities.

This method enables a uniform etching of large silicon wafers (refer to figure 2.5(d)). However, due to the usage of EGaIn paste, epoxy and copper wire, the presence of impurities is unavoidable in the porous silicon layers as well as the HF electrolyte. This does not affect most of the photonic applications, since either the porous silicon layer is removed in the final structures, or the effective refractive index remains constant in spite of minor impurities. Finally, the epoxy is removed carefully by a blade depicted in figure 2.5(e). With this process, it is impossible to form porous silicon on both sides of a silicon wafer. It is also difficult to etch free-standing thin silicon membranes because of the presence of the back contact, the membranes get broken easily. Most of the etching in this thesis is performed following the above mentioned procedure.

2) Teflon cell design and etching

To have a porous silicon layer containing less impurities, or to etch both wafer surfaces, or to etch free-standing thin silicon films, an etch cell is a good choice.

Polytetrafluoroethylene (PTFE) can be used for the cell body, and polyvinyl chloride (PVC) can be used for transparent windows. Standard black O-rings made of acrylonitrile-butadiene copolymer can be used, which are stable in 50% concentrated HF. The O-ring should be held under medium pressure while tightening the cells to avoid breaking the sample, but a good seal is important to avoid the leakage of HF electrolyte.

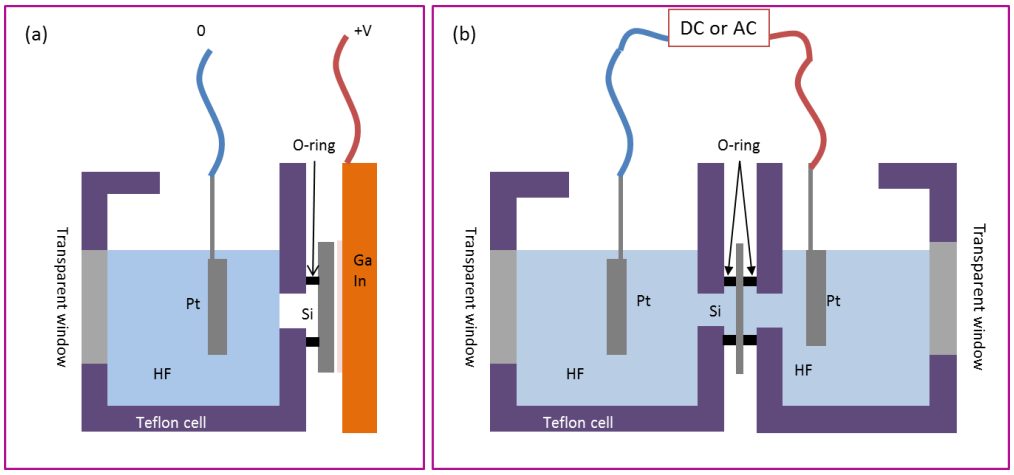

Figure 2.6 Setup for cell electrochemical etching of silicon: (a) single-cell; (b) double-cell.

There are two types of cell geometries for different purposes, as shown above. To etch a single side of a silicon wafer, the cell configuration depicted in Figure 2.6(a) can be adopted, where EGaIn paste can be applied on the back surface of silicon wafer pressed against a copper electrode to achieve a good Ohmic contact. Figure 2.6(b) has double-cell design where HF electrolyte fills both sides. When a DC bias is applied, only the surface with a positive voltage is etched; whereas, when an AC bias is applied, porous silicon layer forms on both sides of a silicon wafer. Especially, the double-cell design was used for etching Silicon-on-insulator (SOI) wafers, as discussed in [46]. Here, the SOI wafer works as a capacitor where the device layer and substrate work as two conducting plate and the oxide layer as a dielectric material and etching takes place on either surface alternatively because of the applied alternative bias. Cell etching can also be used to remove the oxide layer of the electrolyte exposed area on top of the silicon wafers. This cut in the oxide, in turn, can be used as a window for KOH etching, as shown in Figure 2.7.

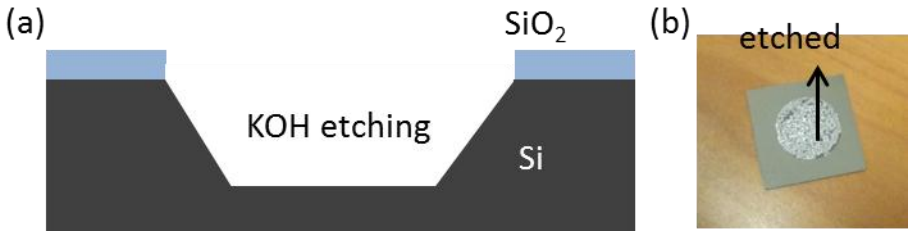

Figure 2.7 Example using cell for etching: Cell etching was used to remove SiO_2 to work as a window for KOH etching to produce Silicon membranes: (a) Cross-section Schematic (b) Image of 525 µm silicon wafer with 12mm area diameter 200 µm thick silicon etched away.

Cell etching is suitable for producing p-Si on both sides of a single wafer at the same time, and also enables etching of a free-standing silicon thin film supported by a thick frame. Cell etching results in less contamination of the porous silicon film and HF electrolyte. However, the limitation of this technique is that the etching is faster at the edge of the O-rings compared to the central region. This causes non-uniform etching across the exposed area. In addition to this, the clamping increases the risk of breaking fragile wafers, and any inappropriate clamping may cause leakage of the electrolyte.

2.2.2 Material analysis and morphology studies

After ion irradiation and electrochemical etching, the following facilities are used for the analysis and morphology studies.

(1) Material analysis: RBS

Rutherford backscattering spectrometry (RBS) is a common analytical technique used in materials science. In CIBA, we have high resolution RBS facility which is used to determine the structure and composition of materials by measuring the backscattering of a beam of high energy ions impinging on a sample. [47]

(2) Morphology: OM, SEM, AFM, FIB

The optical microscope (OM) uses visible light and a system of lenses to magnify images of small samples. The image from an optical microscope can be captured by normal light-sensitive cameras to generate a micrograph. In this thesis, OM is used for instant observation of structures. A scanning

electron microscope (SEM) produces high resolution images of up to 50000x magnification of a sample by scanning a focused beam of electrons, producing and detecting various signals that contain information about the sample's surface topography and composition. [48]Atomic force microscopy (AFM) is a very high-resolution type of scanning probe microscopy.[49] AFM is used in this thesis for producing the topographical map of the etched surface of ion irradiated Si samples. AFM is one of the foremost tools used for imaging, measuring, and manipulating matter at the nanoscale level. Piezoelectric elements that facilitate tiny, but accurate and precise movements enable very precise scanning and positioning. Focused Ion Beam (FIB) has applications in imaging, machining, deposition, material analysis, etc. FIB can be used for cross-sectional cutting of structures with small size; however, FIB is destructive to the samples. [50]

2.3 Defect distribution and fluence definitions

The previous sections introduced all the necessary tools and facilities used in this work. To produce required structures using these facilities, a basic understanding of the influence of ion irradiation on electrical properties and its subsequent effect on the porous silicon formation, is needed. Ion irradiation induces damage to the crystal lattice. The generation of these defects is the reason why electrical properties are changed and selective p-Si formation during subsequent etching occurs. Theoretical models could approximately tell the number of displaced atoms by a projectile. Here Stopping and Range of Ions in Matter (SRIM)[22] calculations are used to discuss ion range, ion straggling, and the defect distributions. SRIM is computer program based on a Monte Carlo simulation method that calculates the interaction of ion with matter.

The resultant energy transfer during ion collisions with the electron cloud or atomic nuclei, while passing through matter, causes the ions to slow down until they come to rest at some depth in the material.[51] The average range R_i which ions with MeV range and low mass travel through matter before coming to rest can be evaluated as

$$R_i = \int_0^{E_0} \frac{dE}{dz}^{-1} dE \qquad 2\text{-}1$$

This is also known as the ion range. Low energy heavier ions have low penetration through materials while high energy light ions have large range. [51] Figure 2.8 shows the range of protons, helium, Cesium ions in Si with respect to ion energy from SRIM calculations.[22] It shows that for the same energy, lighter ions have larger ion range than heavier ions. For example, for energy of 2 MeV/ion, a proton has range of 48 μm in Si; a helium ion has range of 7 μm in Si, while a Cesium ion only has range of 0.8 μm in Si.

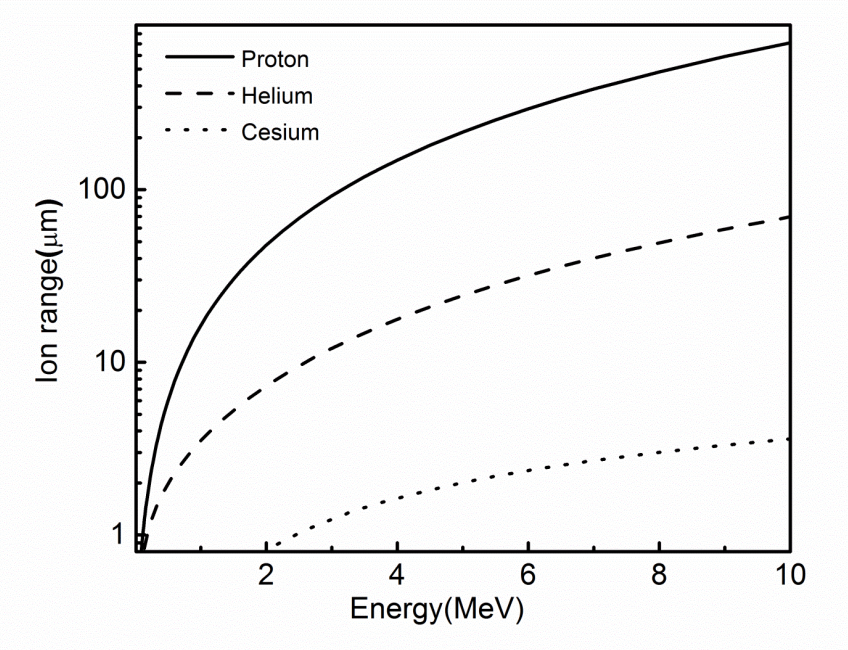

Figure 2.8 SRIM calculation of ion range. Ion range of proton, helium, cesium ions in silicon with respect to ion energy (vertical scale is in logarithm).

Fluctuations in the number and geometry of collisions give rise to a distribution in the energies of initially monoenergetic ions after traversing a depth of material. This results in a variation in the distance to which individual ions penetrate the material, which is called longitudinal straggling. Variations in the number and geometry of the ion-electron collisions also results in a distribution of the transverse momentum acquired by the ions. This alters the trajectory angle of the ions through the material, so that they stop at different lateral distances away from the beam axis; that is, there is a lateral straggle or spread.[51] For line or point irradiation, where the lateral straggling is larger than the feature size on surface, lateral straggling, rather than the beam spot size on the material surface, ultimately defines the minimum spatial resolution for micromachining process.[24] Figure 2.9(a) shows the longitudinal and lateral straggling of protons, helium, Cesium ions in silicon with respect to ion energy, from SRIM calculation.[22] It shows that for the same ion energy, lighter ions have larger straggling. For example, for ion energy of 2MeV, protons have a straggling of ~ 2 μm in Si, helium ions have a straggling of ~ 0.3 μm in Si, while Cesium ions only have a straggling of ~ 0.16 μm in Si. Except when the ion energy is as low as less than 200 keV, helium ions have

larger straggling than protons, shown in the inset figure. Figure 2.9 (b) shows the straggling with respect to energy/nucleon, which has no significant variation for different ions, and an opposite trend compared to Figure 2.9(a).

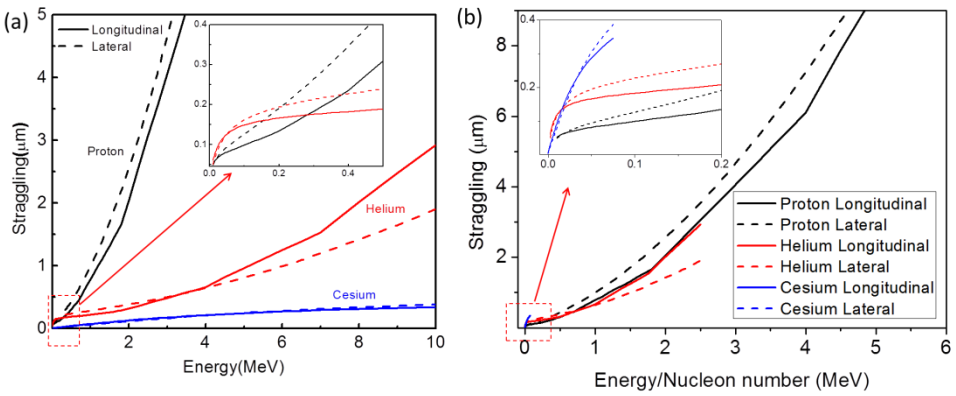

Figure 2.9 SRIM calculation of straggling. Straggling (longitudinal, lateral) of proton, helium, cesium ions in Silicon with respect to ion energy (vertical scale is in logarithm).

In silicon micromachining, the ion range determines the depth of end-of-range regions, and straggling partially determines the structure size. These two factors will be discussed in more detail on how they determine the formation of cores at end of range regions in section 5.3.1, where one of them is dominant for different conditions. By combining the above two figures, Figure 2.10 shows the ratio of longitudinal and lateral straggling over ion range of protons, helium ions, Cesium ions in silicon with respect to ion energy per nucleon. It shows that for protons and helium ions, with increasing nucleon energy, this ratio decreases. This slope becomes smaller, and tends to a constant at high energy when the energy is higher than ~ 600 keV. This graph can explain the difference of core shapes for lower and higher energy of cores. Since the slope becomes smaller, the ion range plays a more important role for higher energy ions, which results in a higher height over width ratio of the core in 0.02 Ω.cm wafer, which will be discussed in chapter 5 in detail. The same trend is observed for helium ions.

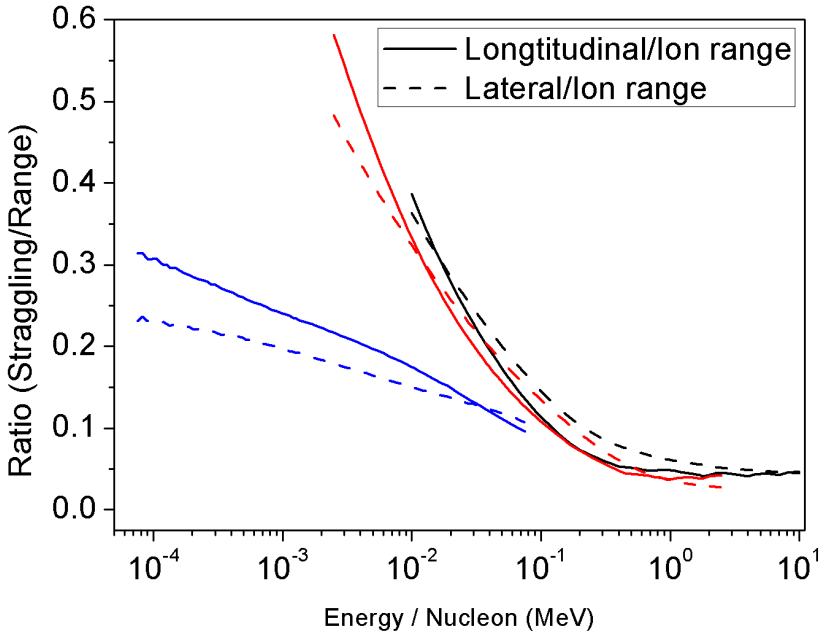

Figure 2.10 Ratio of straggling and ion range. Ratio of straggling (longitudinal, lateral) and ion range of proton(black), helium(red), cesium(blue) ions in Silicon with respect to ion energy per nucleon (lateral scale is in logarithm).

Transfer of energy to atomic nuclei during a collision causes ion induced defects owing to the displacement of the atomic nuclei from their original sites. Simple lattice defects can occur when an atomic nucleus does not acquire sufficient energy to displace other nuclei after escaping from its own lattice site. The resultant vacancy/interstitial pair, consisting of the displaced lattice atom and the resultant empty lattice site, is called a Frenkel defect.[52] However, if the struck lattice atom is displaced with enough kinetic energy, then it can travel away from its original lattice site and may collide with other lattice atoms, causing displacements of more lattice nuclei which in turn may displace others. The high kinetic energy of the originally displaced lattice atom is thus dissipated in producing a cascade of vacant lattice sites and interstitial displaced nuclei.[51] Protons tend to produce a mixture of simple defects and complex defect clusters, mostly simple defects, whereas heavier ions tend to produce a higher proportion of defect clusters as they can impart higher kinetic energy to the displaced lattice nuclei. [51]

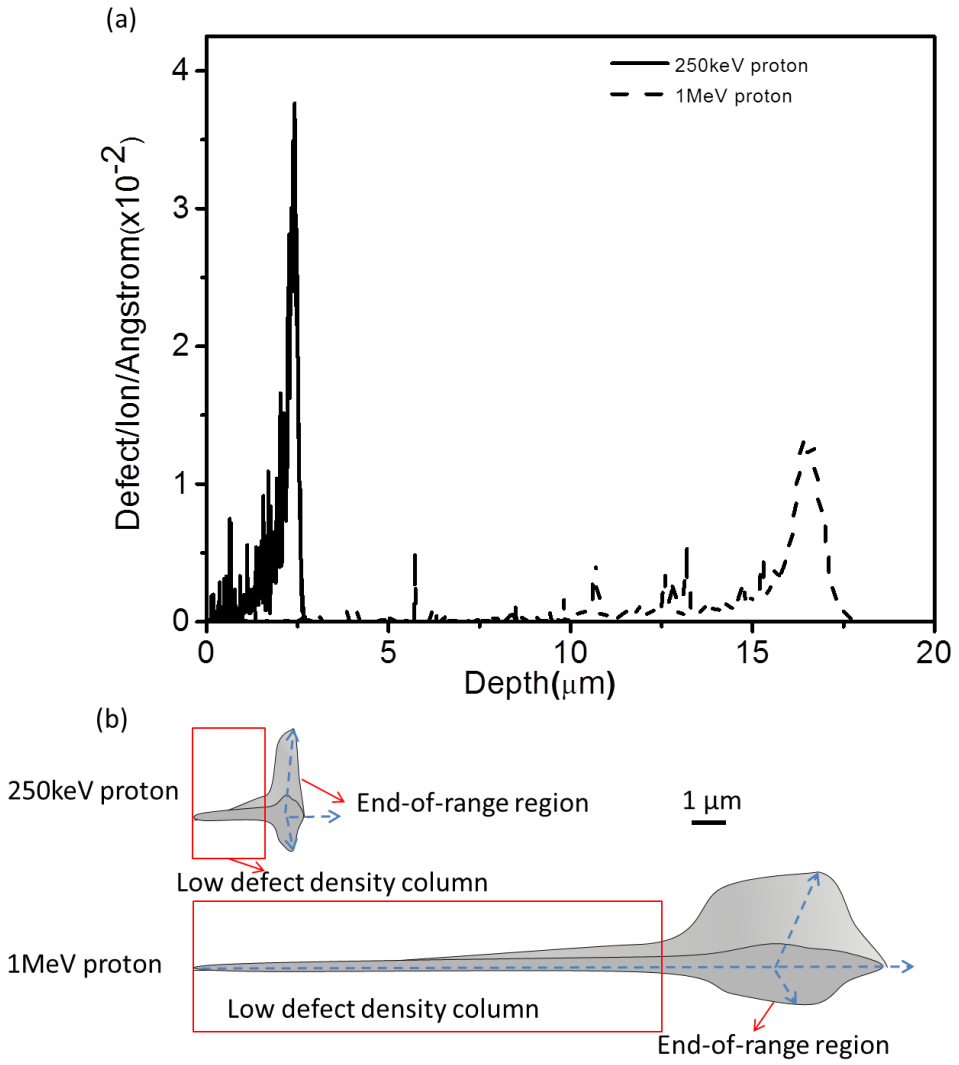

Figure 2.11 Depth defect distribution. (a) Defect distribution with respect to depth for 250 keV and 1 MeV proton in silicon; (b) Low defect density column and end-of-range region.

The number of defects produced along the initial portion of the trajectories is fairly constant and then increases sharply towards the end-of-range, due to the lower velocity of ions and larger interactions with atoms after collisions. Therefore, the defect regions include the end-of-range region with higher defect density and a low defect density column with low defect density. Most of the defects concentrate at the end-of-range regions. Figure 2.11(a) shows the 2D defect distribution with respect to depth for 250 keV protons and 1 MeV protons in silicon, where horizontal scale is the depth and the defects at certain depth are integrated and shown in the vertical scale. Figure 2.11(b) shows the 3D defect distribution, which defines two regions, the low defect

density column and end-of-range region, in which three axes are depth, one parallel to the wafer surface, and the defect density integrated over certain area. It clearly shows most of the defects concentrate at the end-of-range regions. 250 keV protons have a narrower, sharper peak at the end of range. The narrower peak is due to the smaller scattering for low energy ions, as shown in Figure 2.10. Figure 2.12 shows the defect distribution across the end of range regions for protons with three different energy, 50keV, 250keV, and 1MeV. It indicates a narrower, higher defect density distribution for lower energy ions at the end of range regions.

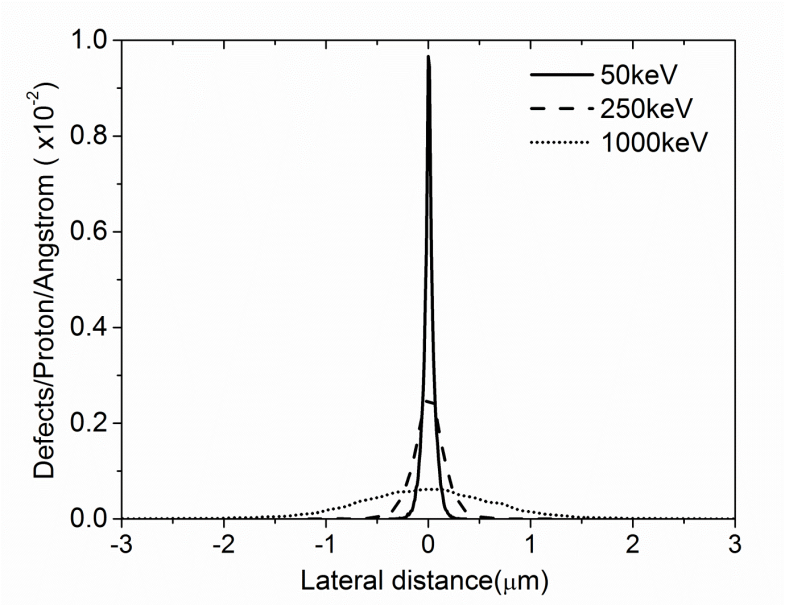

Figure 2.12 Lateral defect distributions. Lateral defect distribution for protons with different energy in silicon at the end of range regions.

Low energy ions have less scattering and a more concentrated defect density at the end of range regions. Therefore, low energy ions are more appropriate to produce silicon wires with smaller diameters, e.g. in Ref. [53] 50keV protons were used to produce silicon wires with diameter down to 50nm. Though the defect density is lower for higher energy ions, the total number of defects is still higher for higher energy ions. Figure 2.13 shows the total number of defects per ion for proton, helium ions, and cesium ions, respectively, which is important when it comes to explaining the current voltage characteristics with respect to ion energy in Chapter 3. It shows the increase of the total number of

defects produced per ion with ion energy. This increase becomes more rapidly for heavier ions.

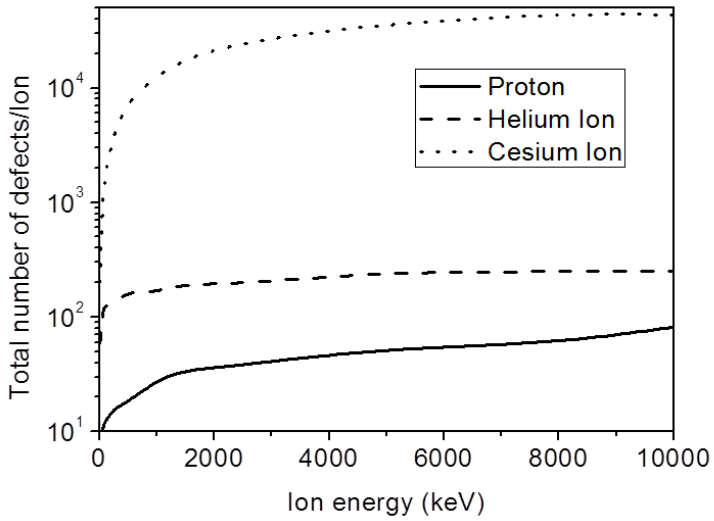

Figure 2.13 Total number of defect per ion for proton, helium, and cesium ions in silicon (both the vertical and lateral scale are in logarithm).

Figure 2.14 shows how the average defect density within the end-of-range region changes with irradiated surface line width for a fixed fluence for different proton energies. Even though the area fluence remains the same, as the irradiated line width reduces the average defect density in the high defect region decreases. Larger straggling at higher proton energies (Figure 2.14 right column) results in defects distributed over a larger distance away from the beam axis, so in Figure 2.14, the reduction in defect density is more pronounced at higher energies.

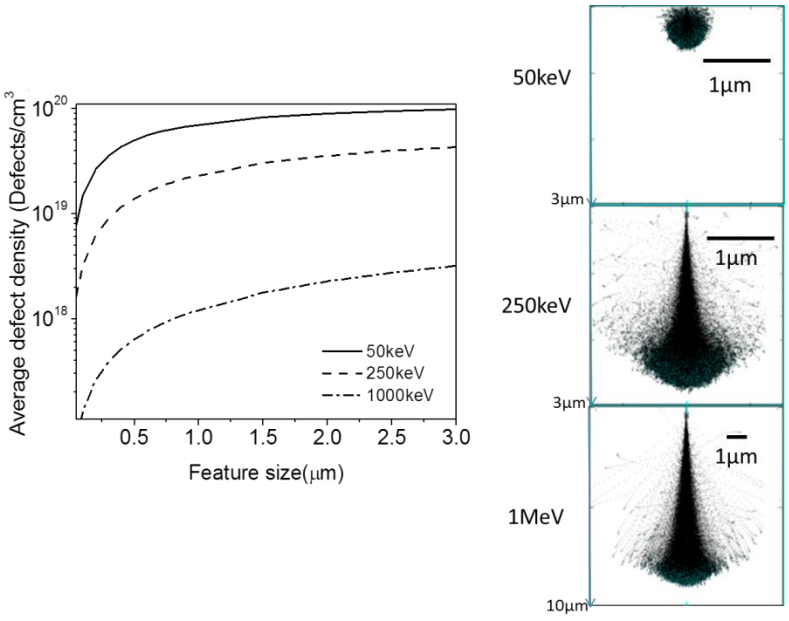

Figure 2.14 Necessity of line fluence. Variation of average defect density of core regions with feature size of proton beam for different energies (Assume fluence: 1x10^{15} proton/cm^2).

Here a definition of line fluence is suitable for such line irradiation where it is defined as illustrated in Figure 2.15(b),[54] the number of ions used for irradiating a line of zero width per centimeter of line length and its unit is ions/cm. Therefore, there are three definitions of fluence, depending on the type of irradiation. The effective beam size on the surface of a sample is b_x and b_y, and the straggling size at the end of range is s_x and s_y. When $s_x << b_x$ and $s_y \ll b_y$, the definition of area fluence, is suitable to use, which is defined as number of ions per unit of area of irradiation, as shown in Figure 2.15(a), and the unit is ions/cm^2. This is standard definition used for all broad beam work where irradiated beam area is much larger than end of range scattering. However, in the regime where $(s_x > b_x,\ s_y \sim b_y)$, or $(s_x \sim b_x, s_y > b_y)$, which occurs when a highly focused high energy ion beam is used for producing micro- and nano-scale line or point structures, the defect density across the line or point irradiation is much lower than for the large area irradiation case when the same area fluence is used. The calculation between line fluence and area fluence is line fluence=Number of ions/area $\cdot\ b_x$ *or* b_y. E. g. a proton beam focused in *x* direction with 100 nm beam size is used to

write lines in y direction with area fluence of $1x10^{16}$ proton/cm^2, then the line fluence is $1x10^{11}$ protons/cm. Line fluence is widely used in the following chapters where focused proton beam with energy of 250 keV~2 MeV is used to produce silicon wires or buried channels in porous silicon. This definition is independent of the irradiated line width on the surface and it simplifies the experimental aspects of fabricating small wires since the only parameters are the total number of ions used, their energy and type. [24, 53, 54]For point irradiations, where beam size in both directions on the surface is smaller than the straggling size, the definition of point fluence is more suitable, where the unit is Ions/point. It is defined as the number of ions per point, equal to areal fluence x $b_x b_y$, as in Figure 2.15(c). For example, a helium beam focused in x and y direction with 1nm beam size is used to write dots with an area fluence of $1x10^{16}$ helium ions/cm^2, in this case the point fluence is 25 helium ion/point.

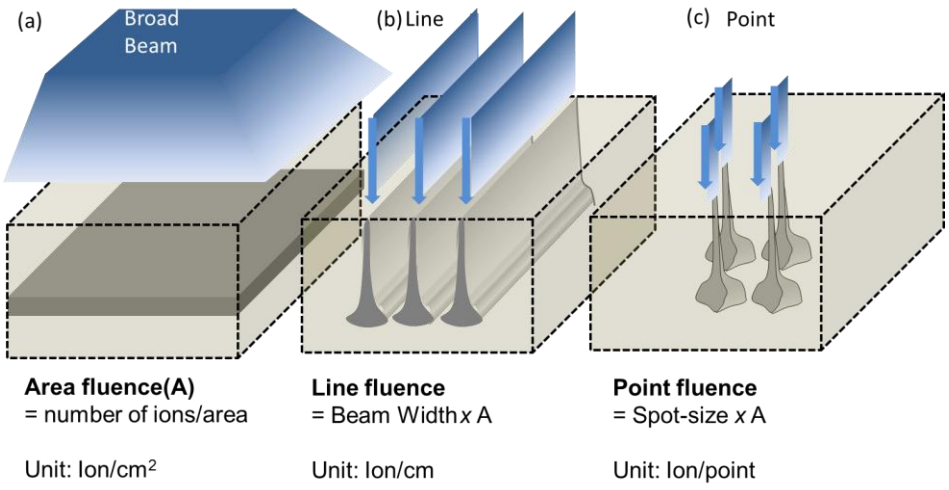

Figure 2.15 Definition of three fluences: (a) areal fluence; (b) line fluence; (c) point fluence.

Conclusion

Ions with different masses, energies and spatial resolutions can be generated from different systems. The ions are used to irradiate p-type Si, and generate defects through collision with the crystal atoms. The irradiated p-type Si is then electrochemically etched in a HF electrolyte with either a back contact method or a cell. The effect of irradiation on etching can be characterized by morphology studies which can also help to further optimize the experimental conditions. Apart from the experimental tools that are used in this work, the defect distribution in ion irradiated Si is studied in detail and three types of fluence are defined according to irradiation type.

Chapter 3 . Current voltage characteristics of large area ion irradiated Si

Before discussing about the study of current flow in locally irradiated wafers, this chapter entails the study of large area irradiated wafers in order to understand the basic electrochemical etching behavior of ion irradiated silicon. Section 3.1 introduces concept of Helmholtz layer, and space charge region and typical current voltage (IV) characteristics of pristine p-type silicon wafers upon electrochemical anodization in HF electrolyte. Section 3.2 presents and discusses the experimental results on the variation of IV characteristics of large area ion irradiated 0.4 Ω.cm p-type silicon with respect to ion fluence for three different proton energies. Section 3.3 discusses the possible mechanisms of IV curve changes with irradiation.

3.1 Basic concepts in electrochemical anodization of Si

Double layers or Helmholtz layers form at the interface of a solid and electrolyte. In the first layer, the on-surface charge (either positive or negative), comprises of ions adsorbed directly onto the object due to a host of chemical interactions and the second layer is composed of ions attracted to the surface charge via the coulomb force, electrically screening the first layer. Helmholtz's view of this region is shown in Figure 3.1.

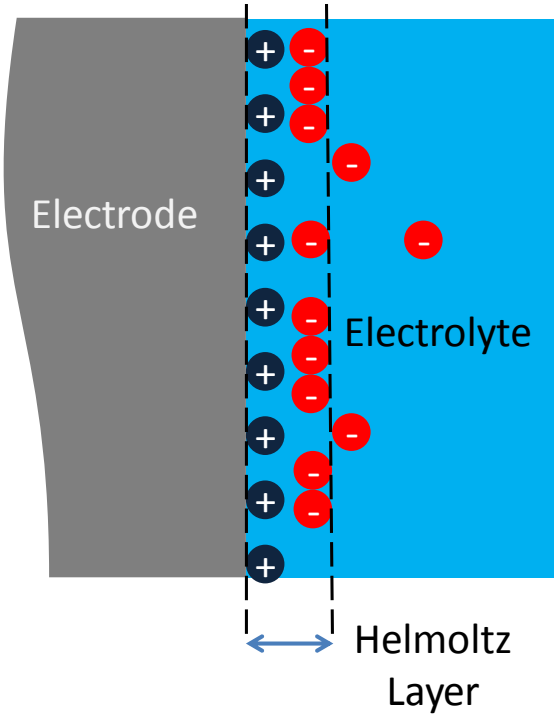

Figure 3.1 Schematics of Helmholtz layer

More specifically in our case, the interface of silicon and electrolyte leads to formation of the space charge layer and Helmholtz layer as described by Figure 3.2. The space charge region is dependent on the doping level of semiconductor and the surface states. Ions present in the solution therefore affect the space charge region and the surface states. Also, it depends on the voltage applied at the semiconductor electrolyte interface or the back metal contact.

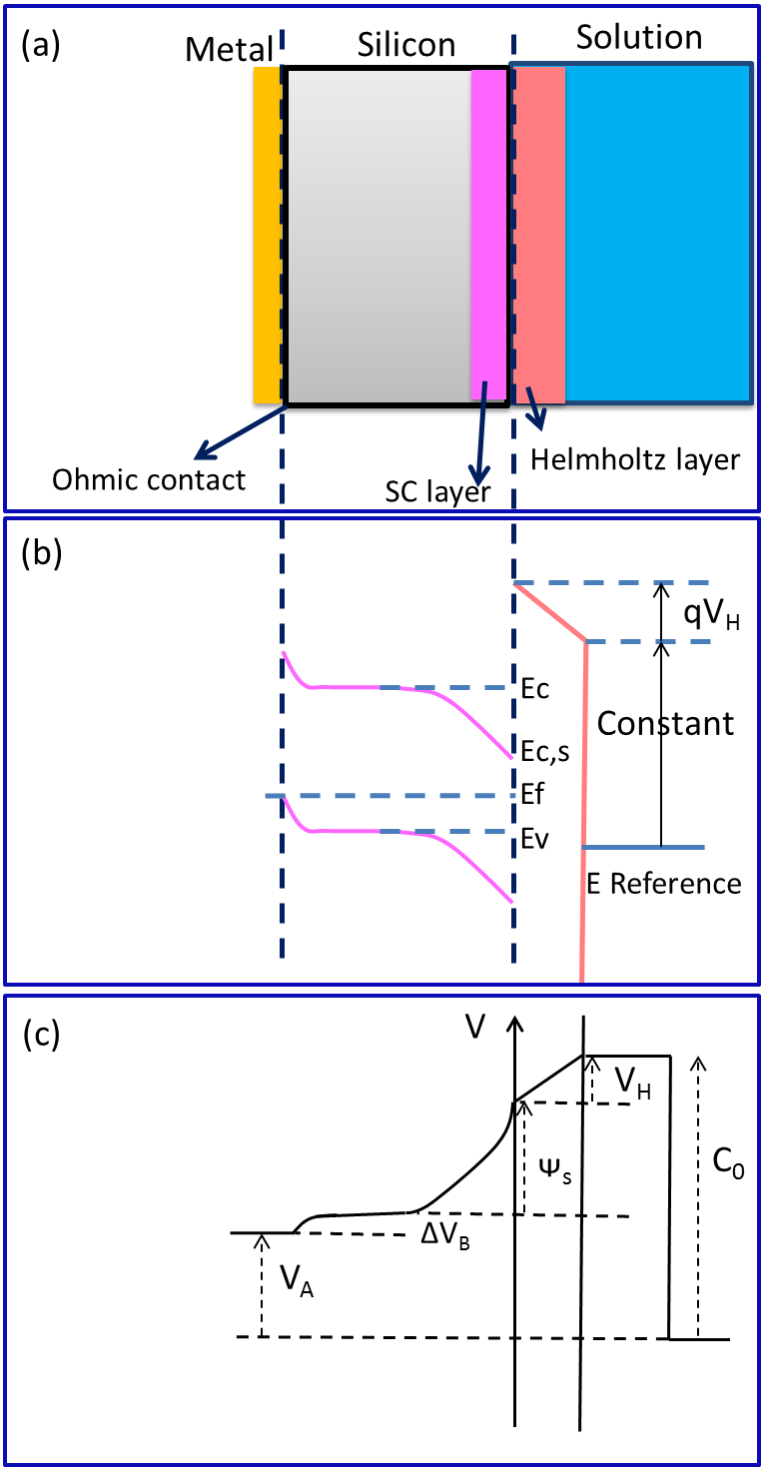

Figure 3.2 Interface of silicon and electrolyte. (a) Schematics of space charge layer and Helmholtz layer at the interface; (b)Energy band diagram and (c) related potential distribution through the thickness of the system metal-semiconductor-electrolyte upon anodic polarization V_A applied to the electrode against the reference electrode (reproduced from Ref. [55])

In Ref [55],Gaspard et al have drawn a linear relation between applied potential and doping concentration. Consider the potential drop across the electrolyte, silicon, and metal and their interfaces, which are schematically shown in Figure 3.2. Energy band bending causes a potential difference ψ_s between the surface and bulk of the semiconductor, and the ohmic contact gives rise to a voltage difference ΔV_B, which can be assumed as constant, and the Helmholtz layer introduces a voltage difference V_H. The reference potential with respect to liquid phase, C_0 is a constant, and equal to the sum of all the voltages, Figure 3.2(c).

Anodic behavior can be characterized by an I-V curve. Figure 3.3 is a typical anodic I-V curve for a p-Si sample in HF solution in the dark.

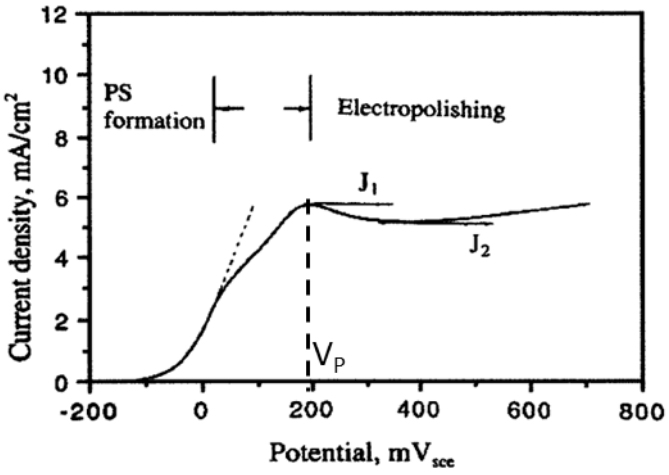

Figure 3.3 Anodic I-V curve of p-type silicon in electrolyte. Typical anodic I-V curve measured for a moderately doped p-type Si in 1% HF solution.

It includes three regions, in the first region, the current increases exponentially with increasing potential. In the second region, it breaks off from the exponential behavior at larger potentials, exhibits a peak, J_1, and then attains a relatively constant value at J_2. At potentials between the maximum slope and the current peak, a porous layer may still form but its surface coverage would not be uniform. Electropolishing occurs at potentials larger than that of the current peak. The relationship between anode current and potential as revealed

by an I-V curve varies with HF concentration, doping-type, and doping concentration.

The current is determined by the majority carriers which can flow over the potential barrier, as in Equation 3-1 below.

$$i = Kp_0 e^{\frac{-q\psi_S}{k_0 T}} = K_0 e^{\frac{q(V_H + V_A)}{k_0 T}} \quad 3\text{-}1$$

where $K_0 = Kp_0 e^{\frac{-q(C_0 - \Delta V_B)}{k_0 T}}$, K is a constant, p_0 is the hole density, ψ_s is the potential difference between the surface and bulk of the semiconductor, k_0 is Boltzmann's constant, T is absolute temperature, V_H is the voltage different introduced by the Helmholtz layer, V_A is the potential applied to the electrode against the reference electrode.

For lightly doped wafer, V_H is very small, and can be neglected, such that $i = K_0 e^{\frac{qV_A}{k_0 T}}$; while in heavily doped wafers, it cannot be neglected, and $i = K' e^{\frac{qV_A}{k_0 T}}$, and K' is dependent on V_H.Therefore, the same linear regime in the semi-logarithmic plot of the current-voltage characteristic is expected, and is obtained, for lightly and heavily doped silicon, at the porous silicon formation regime in Figure 3.3.

Table 3.1 Applied potential drops. Distribution of the applied potential in the electric layers at the silicon/electrolyte interface in HF solutions (Reproduced from Ref. [56])

Material	OCP(Open circuit potential) to V(i~0)	Exponential region	V>V_p(potential at current peak J_1)
Heavily doped p-type Si	Helmholtz layer	Helmholtz layer	Oxide film
Non-heavily doped p-type Si	Space-charge layer	Helmholtz layer and space-charge layer	Oxide film

The applied potential is dropped principally in the oxide film at a potential higher than V_p (potential at current peak J_1) for all materials. For heavily doped materials, the surface degenerates and the material behaves like a metal electrode, meaning that the charge-transfer reaction in the Helmholtz double layer is the rate-determining step and the potential drops mostly in the Helmholtz layer. For non-heavily doped p-Si, the potential is mostly dropped within the space-charge layer before the onset of current. At potentials higher than that at which the current becomes measurable, the change in potential may be dropped also in the Helmholtz layer in addition to the space-charge layer, which is listed in Table 3.1.[56]

3.2 IV curve of large area irradiated silicon wafers

In this section, IV curves of ion irradiated p-type Si wafers are shown and discussed. A uniformly distributed, large area proton beam with energy of 200 keV, 500 keV and 2 MeV over an area of 1.5 cm x 1.5 cm was used to irradiate the whole surface of 0.4 Ω.cm p-type silicon wafers with different fluences by varying the irradiation time for a constant beam current. The fluences range from 1×10^{10} to 1×10^{16} proton/cm^2 covering the range of ion irradiation which significantly influences the anodization behavior of 0.4Ω.cm p-type silicon.

The surface area exposed to the electrolyte was confined to 0.017 cm^2 by an O-ring attached to the polytetrafluoroethylene (PTFE) cell. Samples were cleaned in diluted HF, to remove the native oxide, just before mounting in the cell. Ohmic contacts were made by applying EGaIn on the back sides of the samples. I-V curves were recorded using a standard three-electrode PTFE cell with a Si working electrode, a platinum mesh counter electrode, and a saturated calomel reference electrode (SCE). All potentials quoted in this section are with respect to SCE. The reference electrode was furnished with a polyethylene luggin capillary with the tip positioned at ~5 mm away from the working electrode. The anodizing solution was 2% wt. HF + 0.5 M NH_4Cl dissolved in a 1:1 mixture of H_2O and ethanol. The samples were potentiodynamically polarized at a sweep rate of approximately 5 mV/s from -300 mV, using the potentiostat and sweep generator components of an ACM Instruments field machine.

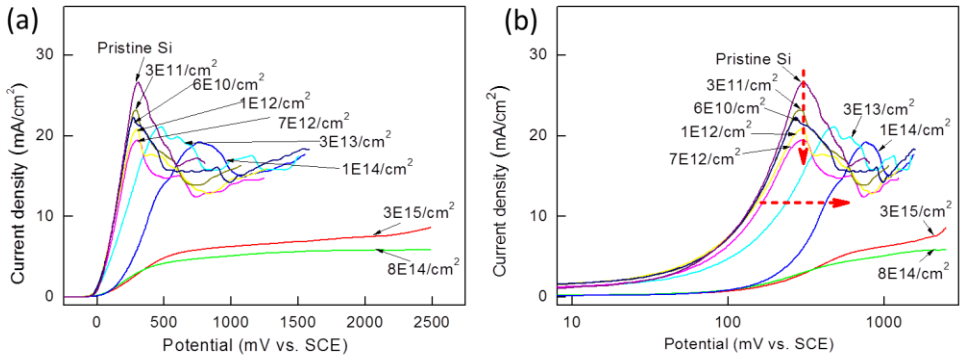

Figure 3.4 I-V curves for 200 keV proton irradiated samples. I-V curves for p-type silicon (0.4 Ω.cm) of different ion fluence in 2 wt. % HF + 0.5 M NH_4Cl. (a) Both scales in linear scale; (b) Potential in logarithm scale.

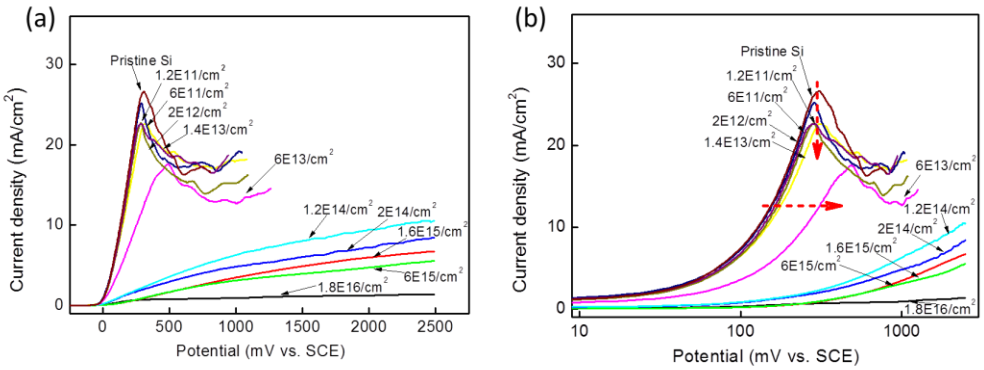

Figure 3.5 I-V curves for 500keV proton irradiated samples. I-V curves for p-type silicon (0.4 Ω.cm) of different ion fluence in 2 wt. % HF + 0.5 M NH_4Cl. (a) Both scales in linear scale; (b) Potential in logarithm scale.

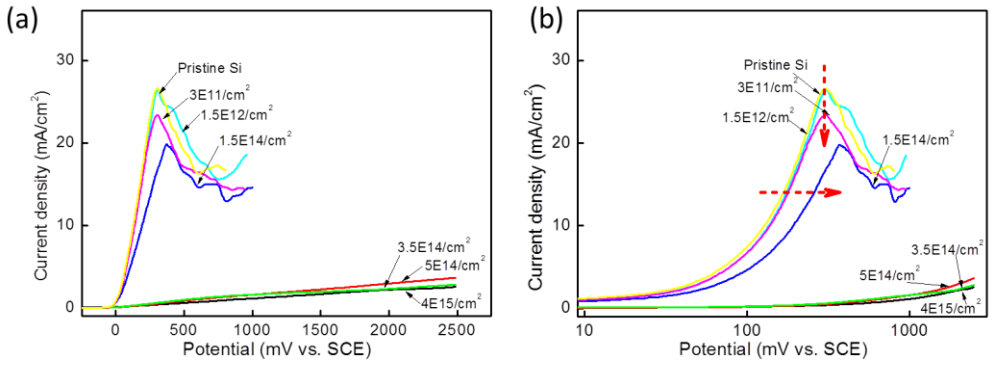

Figure 3.6 I-V curves for 2MeV proton irradiated samples. I-V curves for p-type silicon (0.4 Ω.cm) of different ion fluence in 2 wt. % HF + 0.5 M NH_4Cl. (a) Both scales in linear scale; (b) Potential in logarithm scale.

Figure 3.4, 3.5, 3.6 show I-V curves for proton irradiated samples for different fluence of protons of energy 200 keV, 500 keV, 2 MeV, respectively. From Figure 3.4, which shows I-V curves for different fluence for 200 keV protons, the current density generally decreases with fluence. However when the fluence is in different regimes, the trend of the curves is quite diverse. When the fluence is $\leq 7\times10^{12}$ /cm^2, the shape of the I-V curve and the position of the peak current density is nearly the same as that of pristine silicon, except that the value of peak current density drops 2~3 mA/cm^2 with increasing fluence within the range of $6x10^{10}$ to 7×10^{12}/cm^2. For 3×10^{13} /cm^2 $\leq$ fluence $\leq 1\times10^{14}$ /cm^2, not only the peak current density drops with increasing fluence, but also, the I-V curve shifts to the right, and the slope of porous silicon formation region decreases. For fluence $\geq 8\times10^{14}$ /cm^2, the I-V curves no longer show the typical trend of one for silicon dissolution, at least in the potential range concerned. In figure 3.5 and 3.6, the same trends of I-V curves with increasing fluence are observed and only the threshold values of fluence are different for different energy. Some curves have multiple peaks after the peak current density, and this is due to oxide formation.

3.3 Mechanism

In this section, the above results are discussed and a possible mechanism is given. Defects are generated during the collision between incident ions and crystal atoms. As discussed in chapter 2, the defect distribution for high energy light ions in silicon is composed of two parts, a long defect region with lower defect density along the ion track, and a short high defect region with about ten times higher defect density than the region above. This is located at the end-of range-region where the ions lose most of their energy. The defect density at the low defect region close to the surface reduces with increasing ion energy. The defect density at the low defect region is defined as the "surface defect density" in the following context; the interface plays an important role in the electrochemical test above. The surface defect densities generated by a single proton with energies of 200keV, 500keV and 2MeV are 2×10^{-4}, 1×10^{-4} and 2×10^{-5} Defects/Ion/Angstrom respectively. The first regime is where the only variation is a decrease of the peak current density of I-V curve with fluence, when the surface defect density is less than 10^{17} /cm^3. The third regime is where the I-V curve no longer shows a typical I-V curve shape and the current density is extremely low in the potential range concerned when the surface defect density is greater than ~10^{18} /cm^3. Between these two regimes is the transition regime, where the I-V curve has a slight reduction in peak current density and also right-shifts.

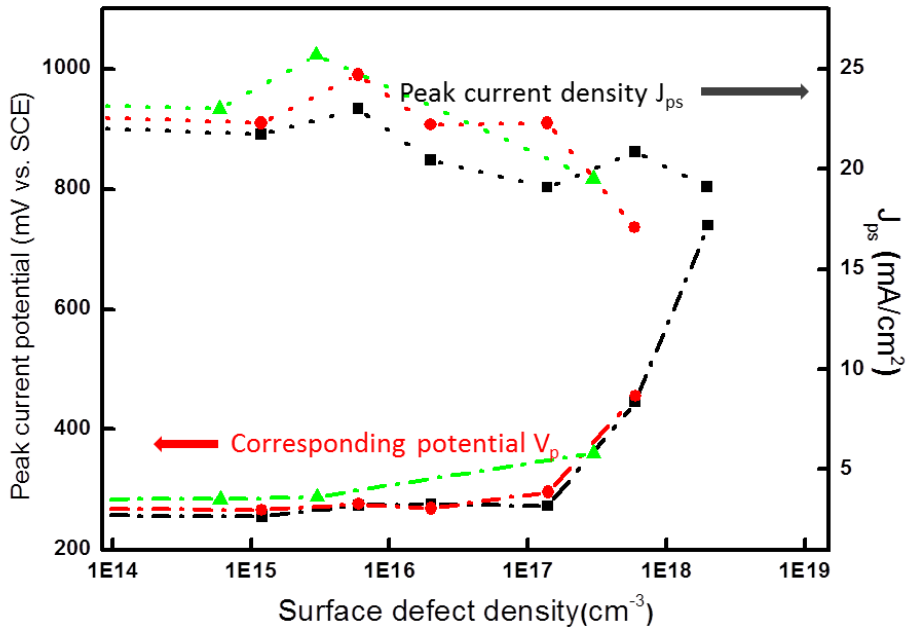

Figure 3.7 Variation trends of peak current density and corresponding voltage. The dependence of the values of V_{ps} and J_{ps} with surface defect density: ■ 200KeV, ● 500KeV, and ▲2MeV.

Firstly, to explain the variation of peak current density and the voltage for peak current density for three energies, we refer to a study in Ref. [57] on the curve changes for different resistivity wafers. To explain the reduction of peak current density with respect to resistivity, they adopted p-Si formation mechanism originally proposed by Allongue et al. [58]which is schematically shown in the figure 3.8 below.

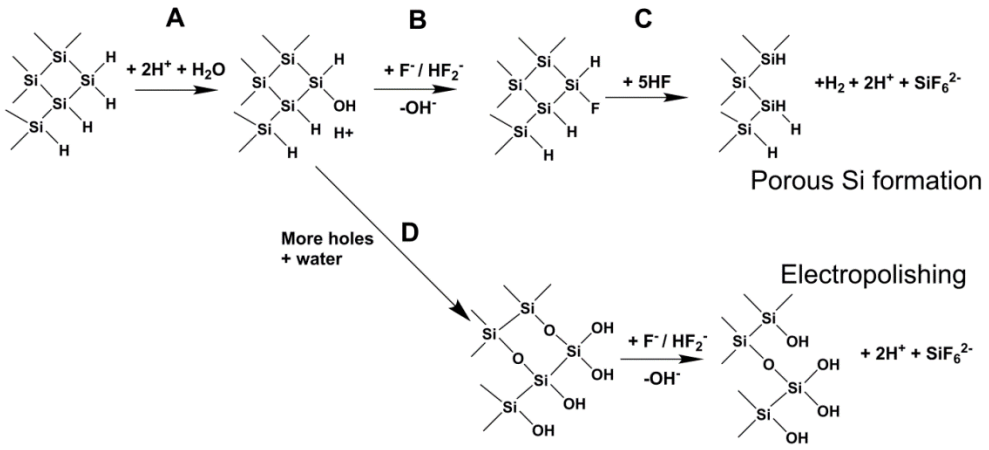

Figure 3.8 p-Si formation mechanism. Schematic representation of the p-Si formation mechanism(From Ref. [57], [58])

The porous silicon formation is initiated by hole injection from silicon into the electrolyte interface (Step A). Then, the hydroxyl group can be replaced by a fluoride ion (step B), allowing sufficient polarization of the Si-Si back-bonds to break them and release the silicon atom (step C) before a third charge reaches that Si atom (step D). The value of the critical current density depends on the rate of step B and C. Step B is determined by the available surface states ready to interact with electrolyte species; Step C is determined by electrolyte species concentration and applied potential which is the rate-limiting step with a low or opposite polarity field. Electropolishing occurs when the current density reaching the silicon/electrolyte interface exceeds the capability of steps B and C to absorb it, thereby increasing the likelihood of additional charge reaching the surface silicon atoms to allow oxide formation prior to their dissolution. In the same electrolyte the reaction rate of step B and step C are the same for both pristine and irradiated samples. [57]

Here is one possible explanation for such variation. For ion irradiated samples, there are two factors to consider. The first one is whether the irradiated silicon surface still have the same ability to attract the electrolyte species to form the Helmholtz layer at the surface. Assume the surface silicon atoms have the same ability to attract the reactive species in electrolyte as pristine silicon. Then the second factor matters, that is, whether some

silicon atoms at the interface of electrolyte and silicon wafer become not as active as the pristine silicon, in which case the number of silicon atoms that can be consumed reduce, and not all the electrolyte species are used. With less effective electrolyte species, less current density is required to exceed the capacity of p-Si pathway to absorb it, this explains the reduction of the peak current density with respect to ion fluence. However, the previous results did not consider the edge effect, and Ref[59] shows that for a p-type wafer with doping concentration distribution of less doped layer on top of highly doped layer eliminate the edge effect, such that for ion irradiated silicon peak current density decreases as well. Therefore, more quantitative study on the edge effect is necessary for verification of the mechanism mentioned above. This work is still under progress.

The right shift of I-V curves with increasing fluence in the second regime is due to its influence on charge transfer in step A. p-Si formation occurs while the silicon is in a depletion region, with the current increasing exponentially with applied potential. In this region, it is found that the charge exchanges from the bulk silicon to the semiconductor surface and the process occurs through a thermionic emission mechanism over the Schottky barrier.[55] Previously, the interface of ion implanted n-type Si and electrolyte was described with a p^+-i-n model. [60] In this model, it was discussed that introduced damage in n-type Si shows acceptor character, and results in a charge compensation, which results in an increase of the resistivity with implantation dose and conversion into i-type at high doses. Because of ion irradiation, a lot of traps are introduced into the band gap of silicon, and the carriers will recombine with these traps. Due to the presence of a high defect concentration in the insulating region the mobility of carriers is low and the recombination rate is high, resulting in a lowering of the carrier flux across the interface. This induces an increase of the Schottky barrier height.

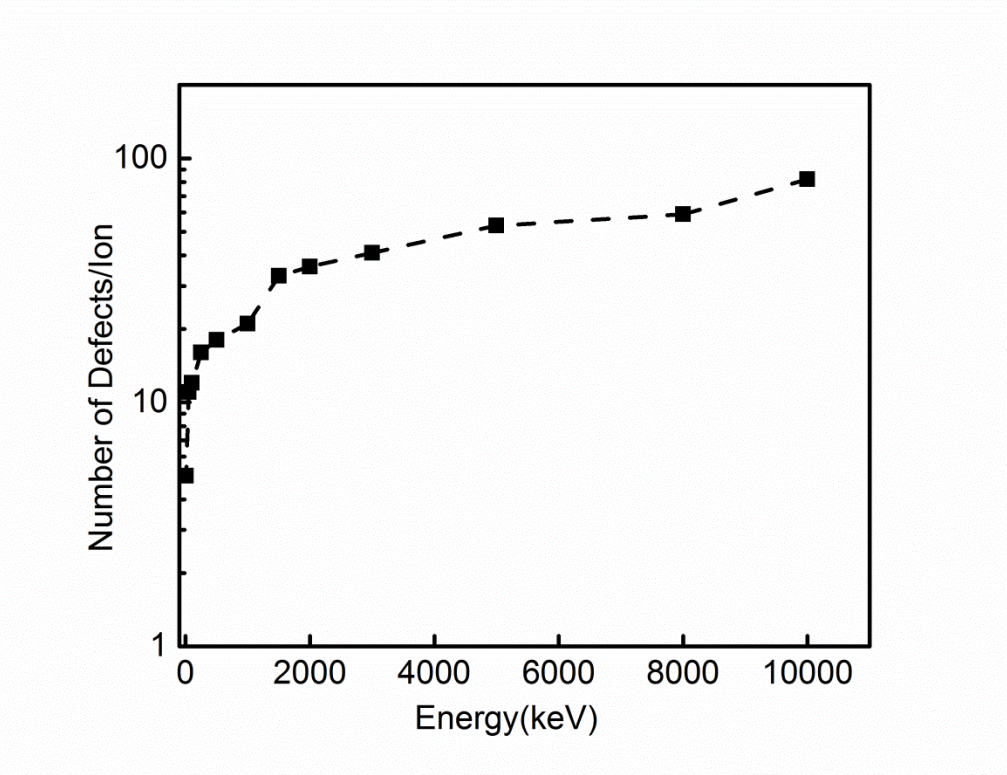

Figure 3.9 Total numbers of defects in silicon per ion for protons with respect to energy

The I-V curves in Figure 3.4, 3.5, 3.6 show a similar trend with increasing fluence for different proton energy, but not exactly the same. Different ion energies cause a different defect depth distribution for a given fluence. Figure 3.7 (a) shows that in the fluence regime ranging from 10^{13} /cm^2 to 10^{14} /cm^2 lower ion energy causes a larger right shift of the I-V curves. To remove the influence arising from different surface defect densities for different energy ions, Figure 3.7(b) plots the variation with respect to surface defect density instead. This shows at the same surface defect density, higher ion energy gives a larger right shift and decrease of J_{ps} for the I-V curve which is due to a larger overall number of defects as shown in Figure 3.9.

Conclusion

The influence of ion fluence and energy on electrochemical anodization behavior of ion irradiated silicon in HF electrolyte was investigated by studying the I-V curves. The decrease in the magnitude of J_{ps} with increasing fluence was explained by a slower charge transfer in certain defect site, in which case some attractive reactive electrolyte species cannot dissolve silicon. The I-V curves also show a positive potential shift with increasing fluence, explained in terms of an increase of the Schottky barrier for ion irradiated samples. The influence of energy mainly arises from the surface defect density and overall number of defects. It is found that a larger total number of defects and a larger surface defect density induce a larger deviation of the I-V curves when compared to pristine silicon.

In above discussions the whole surface of Si is completely irradiated with ions, different from the case of local irradiation used for Si micromachining in all the following chapters. However, it gives us several indications on the effect of interface between electrolyte and Si surface.

A. Ion irradiation causes an increase of the Schottky barrier height and charge exchanges from the bulk silicon to the semiconductor surface through thermionic emission over the Schottky barrier are more difficult.

B. For heavily doped materials such as 0.02 Ω.cm wafers the potential drops mostly in the Helmholtz layer. However, ion irradiated wafers have reduced doping concentration, and the potential drops on both the Helmholtz layer and space charge layer. For non-heavily doped p-type Si such as 0.4 Ω.cm wafers, at potentials higher than that at which the current becomes measurable, the potential drops on both the Helmholtz layer and space charge layer. In ion irradiated wafers, more potential drops on the space charge region due to a reduced doping concentration.

C. Besides, both the Helmholtz and space charge layer behave like a capacitor and plays important role when an alternating current is used in

the electrochemical anodization processes, which will cause different structural features as discussed in chapter 5.

D. The surface of ion irradiated silicon has the same ability to attract reactive electrolyte species as pristine silicon; however during the dissolution process the charge transfer of holes may be slower in certain defect distributed sites for ion irradiated samples, which means some attractive reactive electrolyte species cannot dissolve silicon.

Chapter 4 . Diffusion current, drift current & funnelling effect in ion irradiated silicon wafers

---

At the end of chapter 2, it was shown that ion irradiation on silicon results in the generation of defects. This chapter considers a variety of changes in the electrical properties caused by these defects, one of which is the reduction of effective doping concentration and a simple model is developed for COMSOL simulations to calculate a 2D hole concentration map around an irradiated region. Two current components in the electrochemical etching process of ion irradiated p-type Si were simulated and compared with the experimental results. A new concept of funnelling effect and its experimental proofs, along with interesting applications, as well as factors that influence this effect are discussed. This work helps to understand the significance of different regimes of fluence and deliberates on its application for new fabrication approaches. Section 4.1 introduces the background knowledge on modification

of p-type silicon properties due to ion irradiation, and especially introduces the concept of effective doping concentration. Section 4.2 introduces the simulation model used in COMSOL for following sections. Section 4.3 describes the built-in potential at the defect regions as previously understood [23] and its influence on the drift component of the anodization current during electrochemical etching of ion irradiated silicon wafers. This was previously considered as the only component of the electrical hole current flowing. [23] Section 4.4 discusses the effective doping gradient and resultant diffusion current component flowing in ion irradiated silicon wafers. This component is equally important, and in some cases even dominates the current flow, but its significance was not previously realized. Section 4.5 discusses a universal funnelling effect which is predicted to exist in all the charged particle locally irradiated semiconductors due to the diffusion current component flowing towards small regions, and the resultant formation of highly porous silicon regions. Section 4.6 discusses different interesting regimes for two cases where the highest defect density is located either at the surface or beneath the surface, leading to new fabrication methods and applications. Section 4.7 discusses factors that influence the funneling effect. In the concluding part, a reasonably complete picture of the basic mechanism is elaborated.

4.1 Effective doping density

The electronic properties of semiconductor, which are most seriously affected by ion induced damage, are the diffusion length of minority charge carriers because the ion induced defects act as trapping and recombination centers, as well as the majority carrier concentration because the defects exhibit donor/acceptor characteristics. [51] [61] In Ref. [62], the change in minority-carrier diffusion length L is expressed as the variation of inverse of diffusion length square is proportional to the ion fluence. More importantly, the change in the majority carrier concentration

$$\Delta p = p_0 - p_\Phi = \sum I_{tj} f(E_{tj}) \Phi \approx R_c \Phi \qquad 4\text{-}1$$

p_0 is the initial majority carrier concentration, p_Φ is the final majority carrier concentration, Φ is the fluence, I_{tj} is the introduction rate of *j*th majority-carrier trap center by proton irradiation, $f(E_{tj})$ is the capture rate of majority carriers by *j*th majority-carrier trap center, and R_C is the carrier removal rate. $p_\Phi = p_0 e^{-R_C \Phi / p_0}$. [63] Apart from the removal of majority carriers, some of the defects also act as doping centers with opposite characteristics. For example, in Ref [64], proton implantation generated a donor state in p-type Si and hence, forming a n-type layer selectively in p-type Si; in Ref. [65], in a n-type silicon, the creation rate of acceptor-like states is β, and the experimental data were fitted according to:

$$N_{eff}(\Phi) = N_{d0} e^{-c\Phi} - \beta\Phi - N_{A0} \qquad \mathbf{4\text{-}2}$$

N_{d0}, N_{A0} are the initial phosphorus and boron concentrations, respectively, c is the removal rate of donors and Φ is the fluence. [65]

In p-type silicon, defects either removes the initial acceptor concentration by hole trapping, or create donor-like impurities, then the effective acceptor concentration is:

$$N_{eff}(\Phi) = N_{a0}e^{-c\Phi} - \beta\Phi \quad \textbf{4-3}$$

N_{a0} is initial boron concentration, c is the removal rate of acceptors, β is the creation rate of the donor-like states, and Φ is the fluence.

By looking at the role of these two terms in more detail, the main contribution of defects is the creation of donor-like states. For example, in Ref. [66], the defect concentration that behaves as electron trap has higher level than hole trap, which indicates the main contribution of defect generation is creation of electron traps. In Table 1 of [23], the electron traps are dominant, which indicates that the removal rate of acceptors is relatively small. Therefore, here estimation is made by only considering donor creation in ion irradiated p-type silicon, that is, the removal rate of acceptor c is zero. The effective doping concentration is:

$$N_{eff}(\Phi) = N_{a0} - \beta\Phi = N_{a0} - fv\Phi \quad 4\text{-}4$$

β=*fv*, *v* is the defect density per ion, and *f* is a factor included for account for the fraction of defects that act as donors, and Φ is the fluence. It shows there is a linear relationship between effective doping concentration and the fluence. However, such approximation gives a higher level of effective doping concentration than actual values, since it ignores the removal of original acceptors. Therefore, a more proper estimation requires a larger β, the generation rate of donor-like states, which leads to a larger *f*, than the true value.

A simple rough estimation of *f* is made as follows. In 0.4 Ω.cm wafers, the initial doping concentration is 4.8 x 10^{16}/cm^3, and Φ~5 x 10^{10}/cm is used to form buried wires for an etch current density of 30~300mA/cm^2 for 250 keV

proton with 200 nm beam size. The defect density at end of range area is ~1.2 x 10^5 defects/ion/cm from SRIM calculation, such that

$$N_{eff}(5 \text{ x } 10^{10}/\text{cm}) \sim 4.8 \text{ x} \frac{10^{16}}{cm^3} - \frac{f \text{ x } 1\text{x}10^5 \frac{\text{defects}}{\text{ion}}}{\text{cm}} \text{x } 5 \text{ x} \frac{10^{10}}{\text{cm}} \text{ x } \frac{1}{200\text{nm}}$$

The effective doping concentration is zero to form a complete depletion region, which will be discussed in chapter 5, therefore,

$$4.8 \text{ x} \frac{10^{16}}{cm^3} \sim \frac{f \text{ x } 1\text{x}10^5 \frac{\text{defects}}{\text{ion}}}{\text{cm}} \text{x } 2.5 \text{ x} \frac{10^{15}}{cm^2}$$

Thus, $f \sim 1.9 \text{ x } 10^{-4}$.

f depends on the ion energy, wafer resistivity, and ion fluence. However, the order of magnitude is the same, and a single estimation $f = 1 \text{ x } 10^{-4}$ is used in the following simulations to simplify the problems.

When the fluence is very high, the number of donor-like defects is larger than the initial boron concentration, and the inversion of doping occurs.

For fabricating buried wires which is mainly discussed in chapter 5, type-inversion occurs only in 0.4 Ω.cm wafers, as discussed below. Because in 0.4 Ω.cm wafer, when line fluence is higher than $\Phi \approx 8$ x 10^{10}/cm the defect density at the center of end-of-range region of 250keV protons with 200 nm beam size is higher than 4.8 x 10^{20}/cm^3, and it already starts to convert to n-type Si. In 0.02 Ω.cm wafer, only when line fluence is higher than $\Phi \approx 8$ x 10^{12}/cm defect density at the center of end of range region of 250keV protons with 200nm beam size is higher than 4.8 x 10^{22}/cm^3, and it starts to convert to n-type Si, but the fluences used for fabricating buried wires is only in the order of 10^{11}/cm. (end-of-range defined in section 2.3)

For fabricating silicon walls which is discussed in section 6.2.1, in the end-of-range regions of both resistivity wafers type inversion already occurs, and it occurs in the low defect density column of 0.4 Ω.cm wafer as well but it still remains as p-type in low defect density column of 0.02 Ω.cm. Because in 0.4

Ω.cm wafer line fluence of 2 x 10^{12}/cm, and in 0.02 Ω.cm wafer a line fluence of 2 x 10^{13}/cm is used to completely stop p-Si formation. (Low defect density column defined in section 2.3)

For a lower energy, it needs lower fluence to have type inversion. For a heavier ion, it needs lower fluence to have type inversion. Type inversion occurs for most of the fluences used in following studies using 30 keV He and 15 keV Cs. Because for 30keV He ion, the line fluence for a 0.5 nm beam size to have type inversion in 0.4 Ω.cm wafer is 1 x 10^{7}/cm. For 15 keV Cs ion, the areal fluence to have type inversion in 0.4 Ω.cm wafer is only 2 x 10^{12}/cm^{2}.

This estimated value of f is used in the following simulations and the simulated results matches with experimental results.

4.2 Model for current flow simulation using COMSOL and hole concentration

The anodization current flow of locally ion irradiated p-type silicon is studied based on simulations carried out with the FEM code COMSOL MULTIPHYSICS 3.5a. [54] For the case of 30 keV He^+ line irradiation in 0.4 Ohm.cm p-type silicon, where the direct nanobeam patterning is used, the hole concentration p and the electric potential ψ were evaluated by solving the Poisson's and the hole continuity equation using COMSOL:

$$\begin{cases} \nabla^2\psi = \dfrac{q}{\varepsilon}\left[p - doping\right] \\ \nabla\left[D_p \cdot \nabla p - \mu_p \cdot E \cdot p\right] = 0 \end{cases} \quad 4\text{-}5$$

The domain of integration is $x \in [-1.5, 1.5]$ and $y \in [-2, 0]$. The dimensional unit is μm.

The boundary conditions for electric potentials are:

$$\begin{cases} \psi(y = 0) = 0 \\ \psi(y = -2) = V_{bias} \\ \dfrac{\partial \psi}{\partial x}\Big|_{x=\pm 1.5} = 0 \end{cases} \quad 4\text{-}6$$

The first two conditions represent Dirichlet Boundary conditions at the electrodes; at x=±1.5 μm, Neumann boundary conditions are considered to model zero charge/symmetry.

The boundary conditions for hole concentrations are:

$$\begin{cases} p(y = 0) = doping \\ p(y = -2) = doping \\ \dfrac{\partial p}{\partial x}\Big|_{x=\pm 1.5} = 0 \end{cases} \quad 4\text{-}7$$

The first two conditions indicate that the two electrodes are ohmic, Neumann boundary conditions are considered to model zero flux in the horizontal direction.

Figure 4.1(a) shows the schematics of simulation, where a current density of 40 mA/cm^2 is applied on the back surface, and front surface grounded. The potential applied on the front at depth of 2 μm is 3.2 x 10^{-6} V and the color scale represents the potential. The lateral region is 3 μm and ion irradiation is at the center. Figure 4.1(b) shows the simulation results for the hole concentration map, where the color represents the hole concentration, of 30 keV He^+ line irradiation in 0.4 Ω.cm p-type silicon, where N_{a0}= 4.8x10^{16}/cm^3, [67] for which the hole density dramatically decreases at the topmost tens of nanometers, and then increases gradually back to the pristine value. As discussed at the end of last section, the effective doping concentration is negative, which means type-inversion at high fluences. However, the effect of n-type Si formed at high fluence is ignored in the following simulations, which only consider the holes as free carriers. The lifetime is assumed to be infinite, that is, the hole diffusion length is considered longer than the extension of the damaged region. Therefore, the recombination occurring in the damaged region is assumed to be negligible. Figure 4.1(c) plots hole concentration with respect to depth for different fluences. It shows that along the depth, the hole density decreases sharply from initial value to minimum first and then gradually increases to the initial value. Figure 4.1 (d) shows the magnified part of (b), marked by a solid circle, respectively. The slope of the curves in the first 10 nm in (c) marked by dashed circle is much larger than at the end of range part in (e). However, since native oxidation, amorphization and slight sputtering occurs in the topmost surface, the topmost part can be ignored, and the hole density distribution can be simplified as having a minimum at the surface and decreases gradually with depth. Extracting the absolute value of slope of curves in (d), Figure 4.1 (e) plots the variation of gradient of the hole density with respect to the line fluence. The hole density gradient first increases slowly, and then sharply and again slowly with ion fluence. As shown, at a low line fluence 10^7/cm, hole density is slightly reduced, and the gradient is quite small, ~4 x 10^{15} /cm^3/μm. However, when the fluence increases from 10^7/cm to 10^8/cm, 5x10^8/cm, 10^9/cm, 2x10^9/cm, the minimum hole density decreases, and the gradient is increased. When the fluence further increases to 5x10^9/cm, the region is completely depleted, the

minimum hole density is zero, and the gradient increases to ~7 x 10^{17} /cm^3/μm. One point worth noting is that the region with zero hole density no longer follows the defect region shape when the fluence is very high, 10^{10}/cm, and it covers the region surrounding the defect region as well.

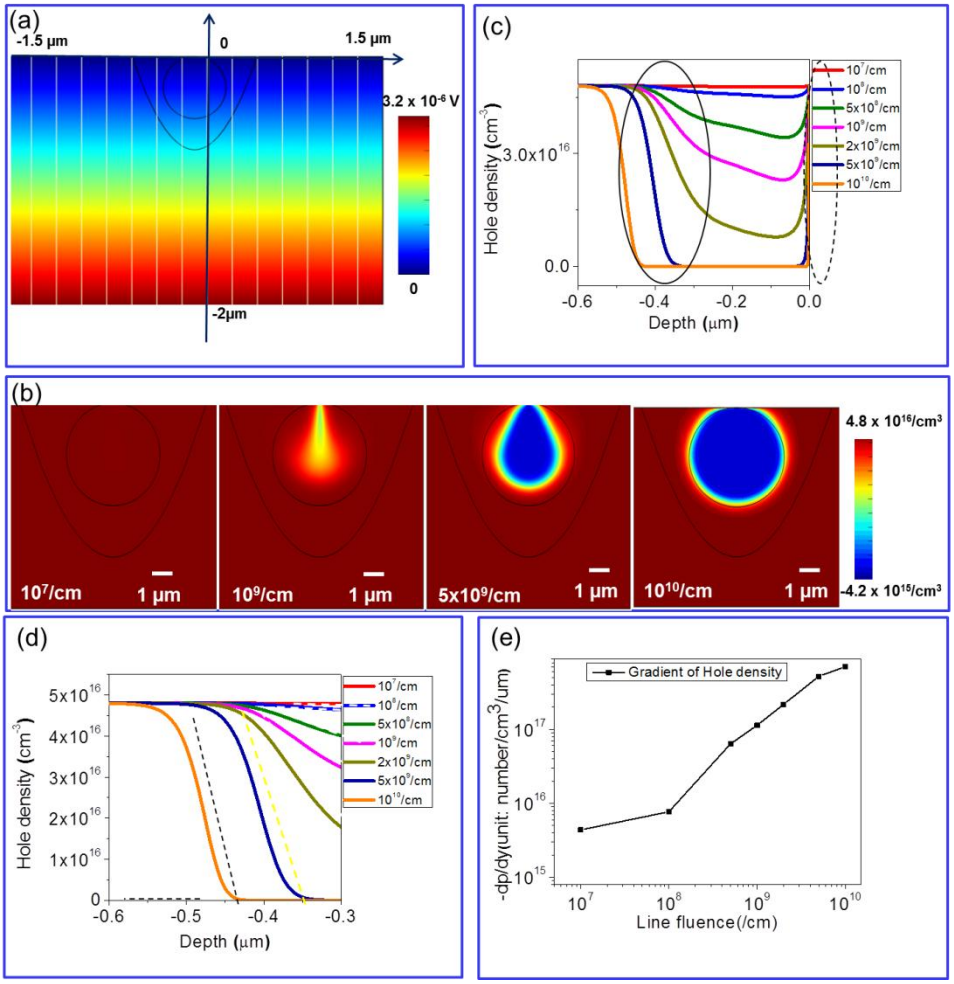

Figure 4.1 Hole concentration in ion irradiated Si. (a) Schematics of simulation and potential map; (b) Hole concentration map; (c) Hole concentration distribution with respect to depth for different line fluence of 30 keV He^+ line irradiation in 0.4 Ω.cm p-type silicon; (d) Magnified figure of marked part in (c) by solid circle; (e) Plot of gradient of hole density with respect to line fluence.

The above simulation is for the case of low energy ions with a line irradiation where the beam size is close to zero, one can use the same calculations by incorporating the beam profile. The vacancy density per single ion generated by a 250 keV proton beam with a nominal size of 200 nm, was calculated by

the convolution of the vacancy density from a delta-like point source, as results from the SRIM2010 simulation, with a Gaussian lateral profile of 200 nm FWHM, assuming a displacement energy of 15 eV. Simulation results will be shown and discussed in Figure 4.6 of later section.

Such simulations are shown to be useful in predicting the general behaviour and formation of the ion-irradiated structure after anodization, but should not be interpreted in an absolute manner, since they don't take account of the time evolution of the anodization process or interface between electrolyte and ion irradiated Si, as well as the amorphization of surface layer, sputtering effect, inversion of the semiconductor type at very high fluences and the effect of implanted ions on the work function of the material. Therefore, these simulations provide good indication in predicting and explaining certain results, especially for shallow etching, where time evolution is not very important; and for low and moderate fluences of light ions, where sputtering and amorphization are not prominent. However, for other studies such as formation of end of range silicon core, the time evolution of the etching front plays a significant role, and this is specifically discussed in chapter 5; the interface plays an equally important role, which was discussed in the electrochemical study in chapter 3. For low energy heavy ions, sputtering and amorphization may be important and for Cs^+ ion irradiation, the effect of the implanted ions on the work function cannot be ignored, all of which is discussed chapter 7.

4.3 Built-in potential and drift current

Drift current is the electric current, or the movement of charge carriers, due to the electric field. Drift current obeys the following equation:

$$J_{Drift} = qp\mu_p E \quad 4\text{-}8$$

J_{Drift} is the drift current density, q is the charge of electrical holes, p is the density of holes, E is the total electric field and μ_p is the mobility. In ion irradiated silicon, the total electric field is a superposition of applied electric field and built-in electric field, as discussed in [23, 54, 67]. The mobility μ_p is reduced due to increased impurity density in ion irradiated silicon, which is derived as:

$$\mu_p = \frac{\mu_{p0}}{\sqrt{1+\frac{N_{Imp}}{N_{Ref}+\frac{N_{Imp}}{81}}}} \quad 4\text{-}9$$

where $N_{Ref} = 4 \times 10^4 \mu m^{-3}$, [68] μ_{p0} is the original mobility in pristine silicon. N_{Imp} is the total concentration of charged impurities in the semiconductor, thus,

$$N_{Imp} = N_{a0} + fv\Phi \quad 4\text{-}10$$

N_{a0} is the doping concentration in pristine silicon, f is the fraction of defects that act as donors, v is the defect density, Φ is the fluence. Figure 4.2 shows the simulated hole mobility map of 30 keV He^+ irradiated 0.4 Ω.cm p-type silicon for different line fluences. The hole mobility decreases in general, and the higher the fluence, the lower the mobility.

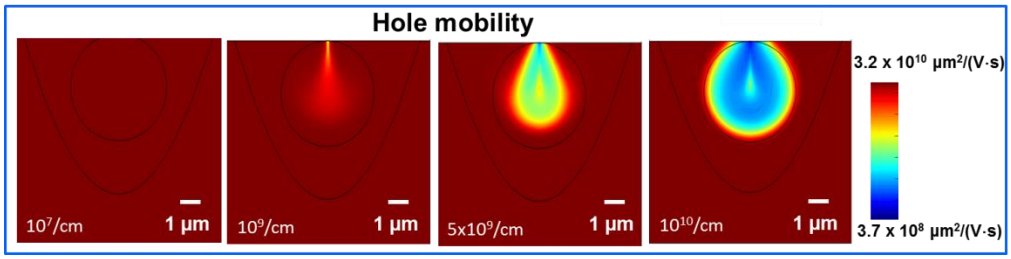

Figure 4.2. Hole mobility map of 30 keV He^+ irradiated 0.4 Ω.cm p-type Silicon for different line fluences, with the beam focused to a 0.5 nm spot size.

According to Ref. [65], the irradiation of n-type silicon results in a build-up of negative space-charge in depletion region due to the introduction of deep acceptor trap levels (acceptor-like states) in the band gap. Here in p-type silicon, one would expect similar effect of build-up of positive space-charge in depletion region due to introduction of donor trap levels in the band gap. According to Ref. [23], the hole capture coefficients are greater than the electron capture coefficients for four of the five defect trap levels present, and gives a net positive charge to the irradiated regions, proportional to the defect density, producing an electric field (E-field) directed outwards, as in Figure 4.3. The short lines show the direction of electric field. The built-up space charge produces electric field pointing outwards even outside the edge of the defect regions, and with higher ion fluence, this electric field extends to regions further away. MEDICI is a device simulation program that can be used to simulate the behaviour of MOS and bipolar transistors and other semiconductor devices.[69] MEDICI models the two-dimensional (2D) distributions of potential and carrier concentrations in a device. Ref. [23] models two-dimensional distributions of potential and carrier distributions in semiconductors by solving Poisson's equation and the electron and hole current continuity equations across the simulated region. It can predict the electrical characteristics within the material for any applied bias conditions for a given distribution of specified defects. Defects are incorporated by defining their energy level in the band gap, their electron and hole trap lifetimes, and their relative concentrations. While the defects are incorporated in the Model used in COMSOL simulations by defining an effective doping concentration.

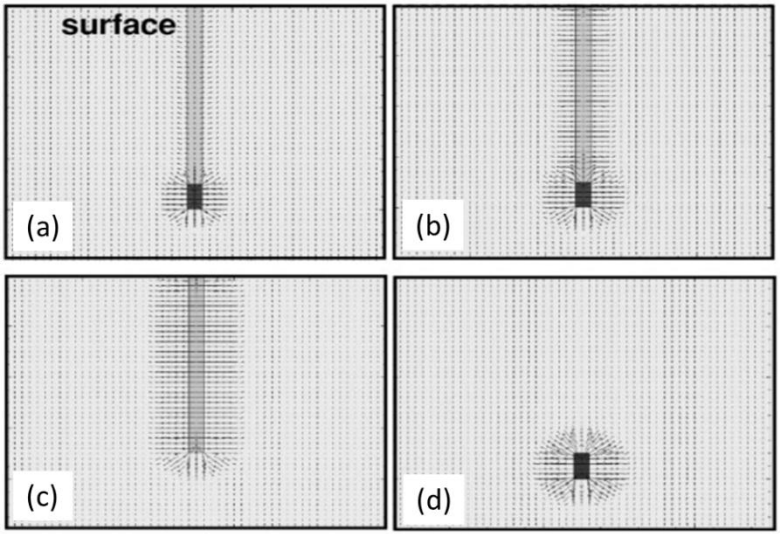

Figure 4.3 Electric field in anodization of ion irradiated Si. Fig. 4 of [23]. MEDICI plots of E-field during anodization in a region of 3 Ω.cm wafer containing a line irradiated with a 2MeV proton of line fluence of (a) $2x10^6$/cm; (b) $2x10^8$/cm; (c) and (d) shows the low defect density column and end-of-range region respectively for line fluence of $2x10^9$/cm.

The electric field and electrical potential arising from the built-up space-charge are called built-in electric field and built-in potential.

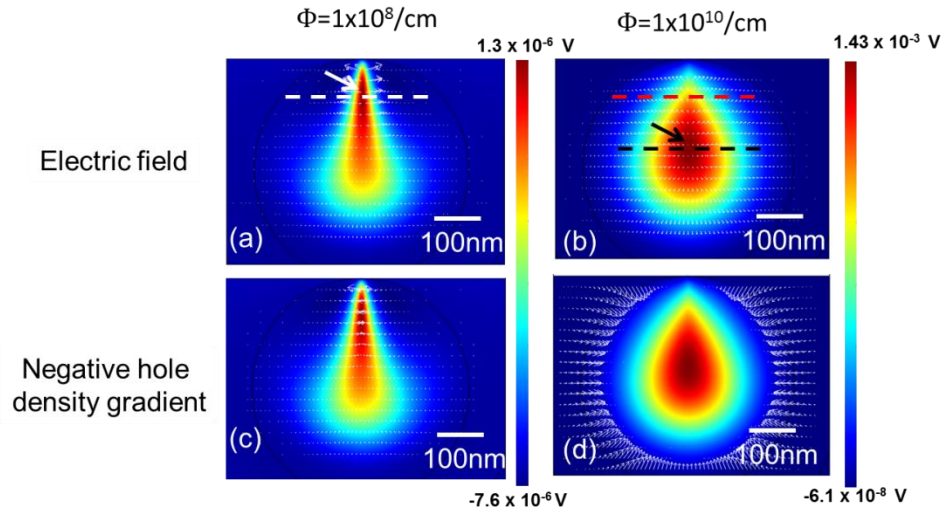

Figure 4.4 Built-in potential and negative hole density gradient in ion irradiated Si. The potential for line fluence of $1x10^{8}$/cm (a, c) and $1x10^{10}$/cm (b, d). White arrows indicate direction and strength of the electric field for (a) and (b); White arrows indicate direction and intensity of the negative gradient hole concentration ($-\nabla p$) for (c) and (d).

The white arrows in Figure 4.4 (a) and (b) indicate the electric field for two different fluences, and color map shows the electrical potential, the sum of built-in potential and applied potential where the potential consists of several contours, and innermost contour is the highest. At $1x10^{8}$/cm the highest defect region has highest potential, marked by the arrow in (a). In regions beneath the surface, the electrical potential is positive and a residual electric field points towards the surface. With an increase in ion fluence from to $1x10^{8}$/cm to $1x10^{10}$/cm, more net positive charges are built in and the potential increases dramatically, noting that the scale of color bar increased from to $1.3x10^{-6}$ to $1.43x10^{-3}$ V. Besides, the net positive charge tends to saturate in the highest defect density region, and the potential at larger depth (marked by black dash line in (b)) becomes higher than the depth marked by red dash line in (b). The other reason for an increase in the depth of the highest electric potential position is a higher electric potential arising from the applied electric field at a larger depth. At the regions very close to the surface, the electric potential changes from positive to negative from (a) to (b).

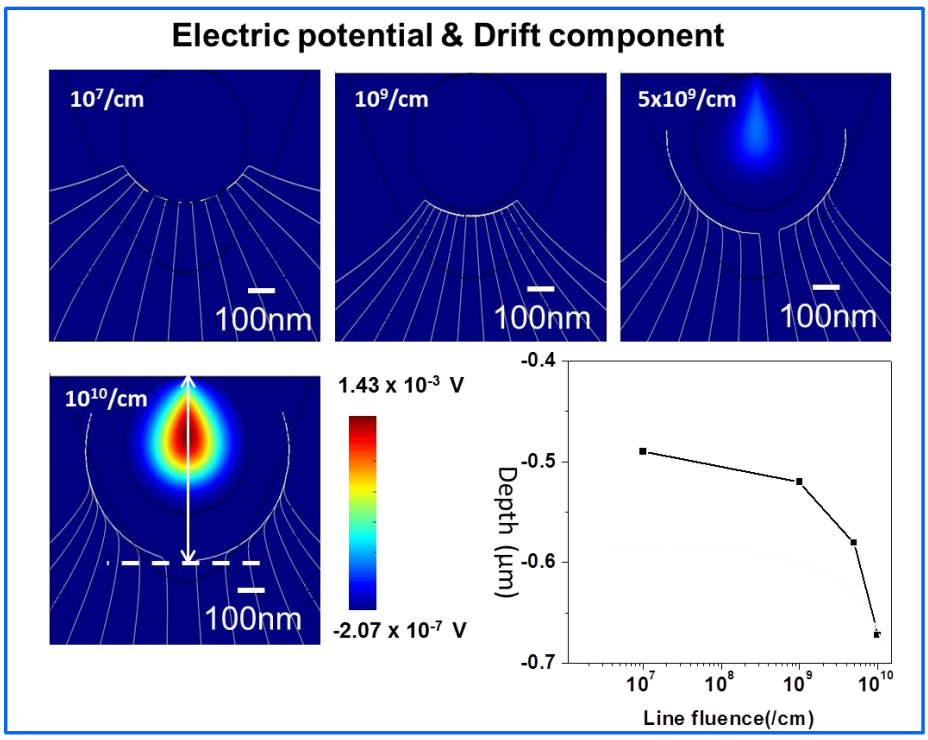

Figure 4.5 Electric potential and drift current in 30 keV 0.5 nm He^+ irradiated 0.4 Ω.cm p-type silicon for different line fluence, and plot of depth that the drift current is stopped.

The color maps in Figure 4.5 show the electrical potential and streamlines of the drift component of the current density. Streamlines visualize a vector quantity on sub-domains. A streamline is a curve which is everywhere a tangent to the instantaneous vector field. The drift current is stopped at the high potential region at low fluence, such as 10^7/cm. At higher fluences of 10^9/cm & $5x10^9$/cm, the drift current is stopped at a distance far away from the high potential regions due to hole repulsion. Moreover, the higher the fluence, the larger the depth that the drift component is stopped, and the vertical distance with respect to line fluence is plotted in the last figure, where the black dash line shows the depth that the defects extend to (~0.5 μm). It shows that the drift current is stopped before reaching the defect region when the fluence is high. For 10^8/cm, this depth reaches 0.67 μm. The same is observed for the horizontal distance at which the drift component is stopped.

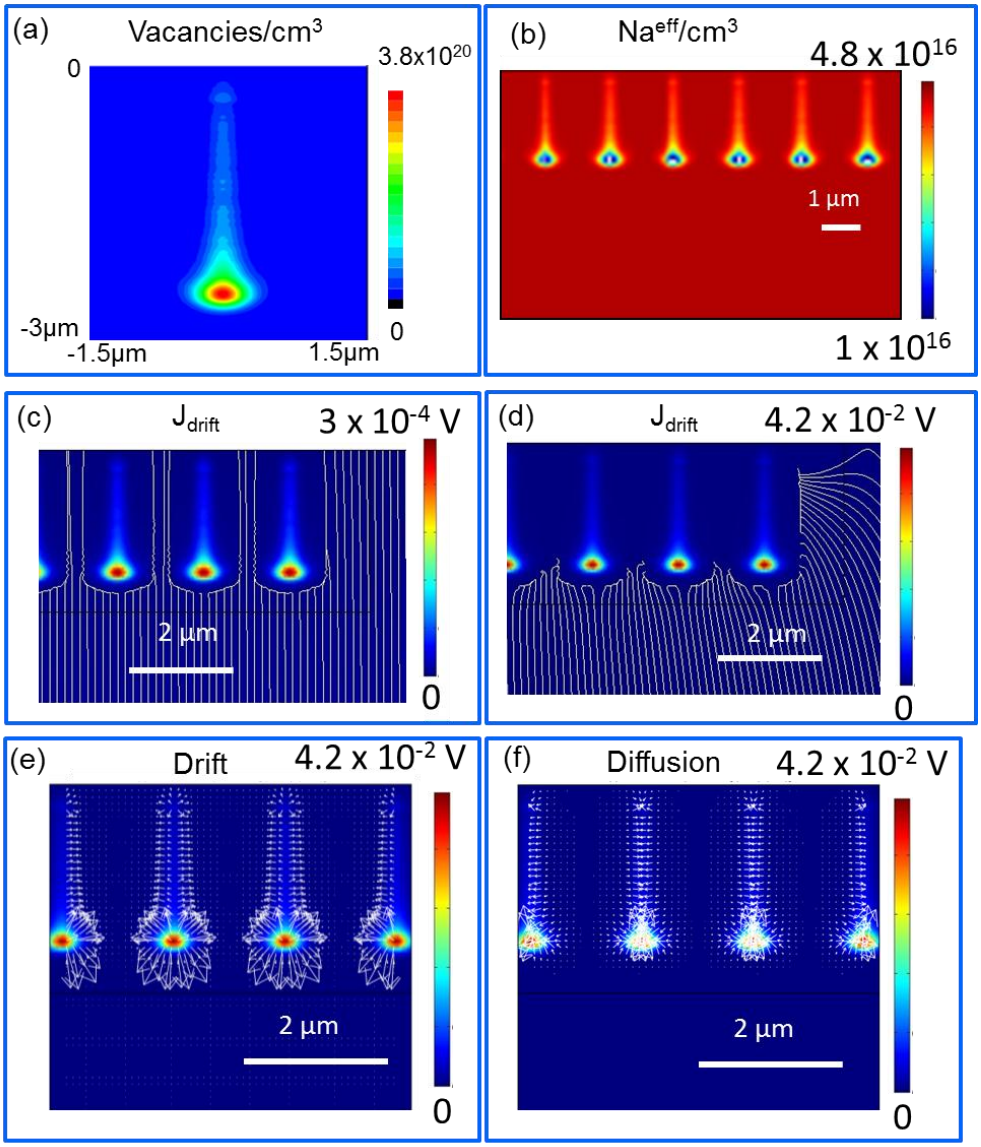

Figure 4.6 250 keV proton in 0.4 Ω.cm wafer: (a) Defect density distribution for single line irradiation with line fluence of $6x10^{10}$/cm; (b) Effective acceptor concentration distribution for eight identical line irradiation with line fluence of 4.2 x 10^{10}/cm; (c, d) Magnified image of drift component for eight identical line irradiation with line fluences of (c) 6 x 10^{8}/cm and (d) 4.2 x 10^{10}/cm; (e, f) Arrow plot of the (e) drift and (f) diffusion components of the current with line fluence of 4.2 x 10^{10}/cm. The lengths of the arrows are proportional to the module of the current components.

Figure 4.6 shows simulations for line irradiation using direct nanobeam patterning with 250 keV protons of 100nm beam size in 0.4 Ω.cm wafer. With a line fluence of $6x10^{10}$/cm, the defect density distribution in (a) has the

highest value of 3.8 x 10^{20}/cm^3, in the center of end of range region, which corresponds to an effective acceptor concentration of 1 x 10^{16}/cm^3, shown in (b). The charges are mainly built at the end of range region, and the drift component is shut down between 1.7 μm spaced line irradiations at a high fluence of 4.2 x 10^{10}/cm, as in (d). With a lower fluence 6 x 10^8/cm, few drift component streamlines pass between the adjacent lines, as in (c). Figure 4.6 (e) shows the colour map of the potential and arrow plot of electric field of 250 keV protons in 0.4Ω.cm wafer. It shows a strong deflection of the holes from the high defect region in all directions, and the strongest in the downwards direction. Along the low defect column region, the electric field points outwards horizontally with a significantly reduced strength due to a much lower built-in potential as well as a relatively lower applied potential compared to the high defect regions. Figure 4.6 (f) shows the diffusion component which will be discussed further in next section. Built-in potential is strongly dependent on the native doping concentration. For the same fluence, a much stronger potential is built in to 0.4 Ω.cm wafers than 0.02 Ω.cm wafers, which causes stronger repulsion of holes and will be discussed further in later sections.

4.4 Hole density gradient and diffusion current

A diffusion current in a semiconductor is caused by the diffusion of charge carriers (holes and/or electrons). It can be in the same or opposite direction of a drift current. It occurs even though an electric field is not applied to the semiconductor. The direction of the diffusion current depends on the change in the carrier concentrations, that is, the carrier concentration gradient, not the concentrations themselves.

In p-type silicon, the diffusion current density is defined as:

$$\overrightarrow{J_{diff}} = qD\nabla p \qquad \textbf{4-11}$$

$\overrightarrow{J_{diff}}$ is the diffusion current density, D is the diffusion coefficient for carriers, q is charge, while ∇p is the gradient of hole concentration. Figure 4.4 (c, d) showed negative ∇p for two fluences, where at low fluence the defect region is partially depleted, while at high fluence $\nabla p = 0$ inside the depletion region and a large value of the amplitude of ∇p is expected at the interface of complete depletion region and surrounding region. This explains the highly porous silicon formation around the silicon cores and will be explained in the next section. Figure 4.6(f) shows J_{diff} towards the highest defect density region from all the directions. Along the low defect column region, a horizontal J_{diff} points towards the centre of the column region from both sides. One can view the current flow of the diffusion component by streamlines, as shown in Figure 4.7. The streamlines of diffusion current density around a 30 keV focused He^+ irradiated line in 0.4 Ω.cm p-type wafer with different line fluences. $\overrightarrow{J_{diff}}$ points towards the surface at low fluence. Differing from the drift component which is deflected away from the high potential regions, the diffusion current is focused into a small narrow point as in figure below. Therefore for the same amount of holes, the current density for diffusion would be much higher than drift component due to its small crossing area. It is this focusing effect of diffusion component towards small narrow area that leads to its dominant role in the total current flow, which will be discussed in later sections.

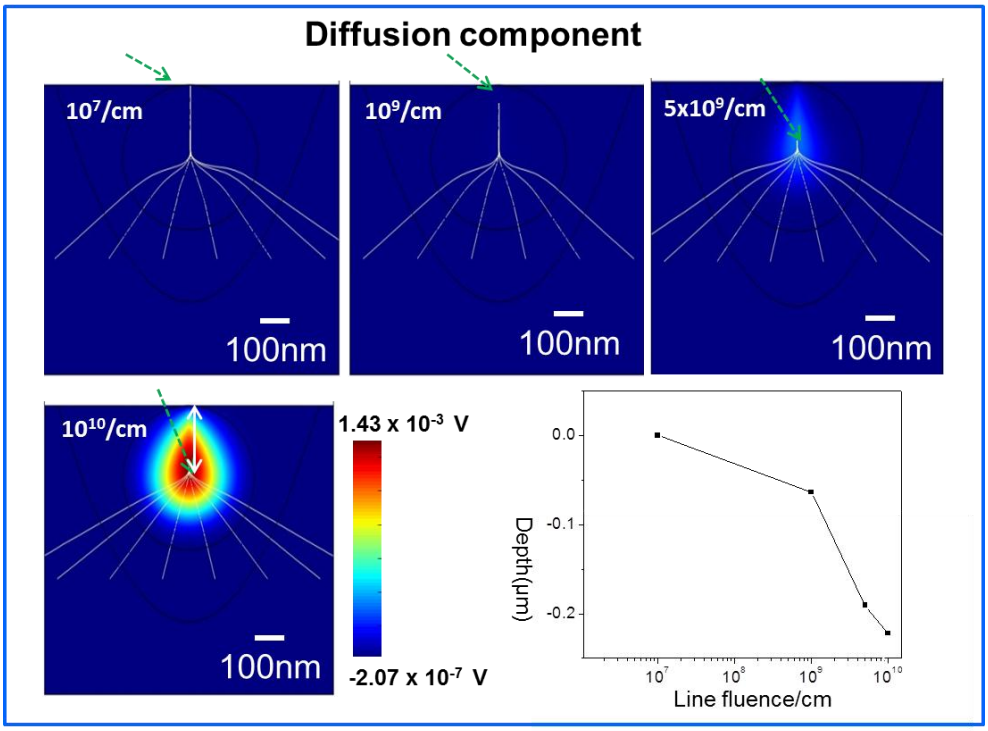

Figure 4.7 Streamlines of diffusion current for different line fluences. The color scale represents the potential map, and plot of depth that the diffusion current is stopped and focused to.

The focusing point (marked by green dashed arrows) goes deeper as the fluence increases. The depth that the diffusion current is stopped and focused to is plotted with respect to line fluence in the last figure. At low fluence, it is focused to the surface, with increasing fluence, this point moves beneath of surface, and reaches ~ 220 nm when the fluence is 10^{10}/cm. This matches with the observation from Figure 4.1(c) that the region with lowest hole density goes deeper with increasing fluence.

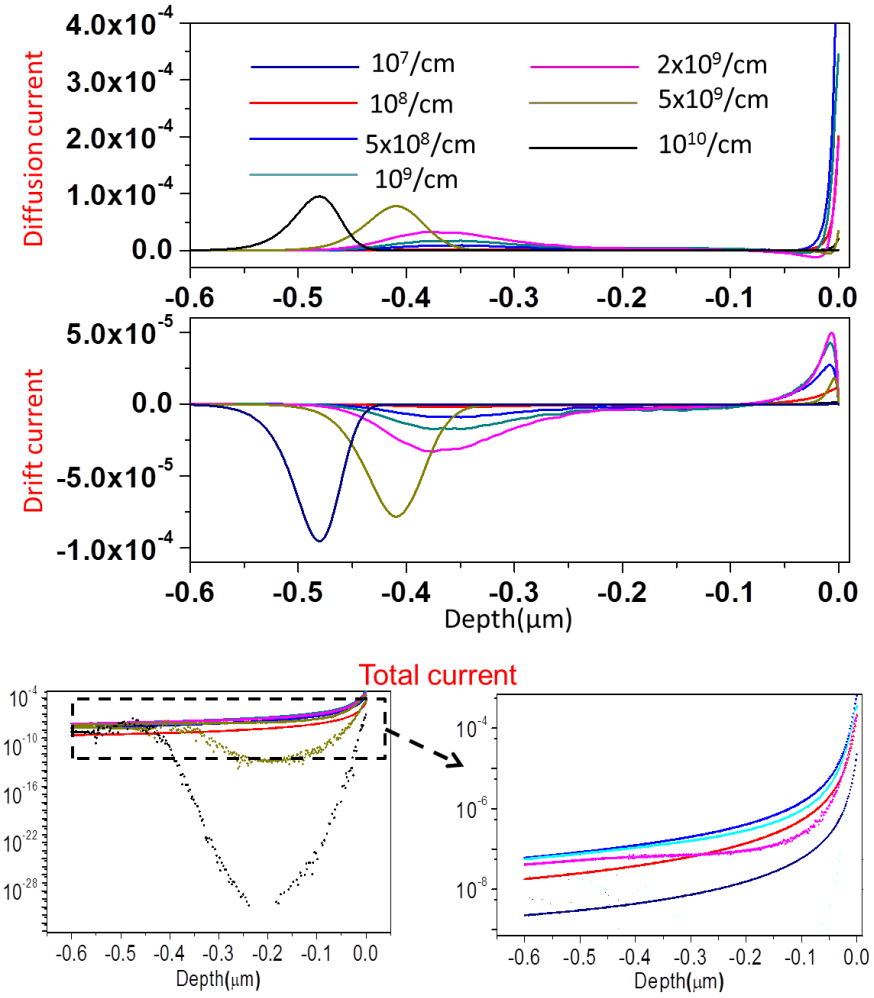

Figure 4.8 Vertical component of the diffusion, drift, and total current density profile at x=0 for 30 keV He^+ line irradiation in 0.4 Ω.cm wafer (see the common key in the highest plot, the unit for vertical scale is $A/\mu m^2$).

Figure 4.8 represents the variation of vertical component of drift, diffusion and total current density with respect to depth for different line fluences at irradiated position. Near the end-of-range region, holes diffuse into this region and the diffusion current is positive, meanwhile they are repelled away by built-in potential and the drift current is negative. Therefore, the total current is very small at this depth, but still positive due a slightly higher diffusion current, as shown in the bottom plot. For high fluences, the damaged region is practically fully depleted. This fact reduces the effect of diffusion for a very few holes which overcome the first potential barrier, but which do not find any

further concentration gradient to diffuse towards the surface. This is clearly shown in the last two maps of Figure 4.4. Therefore, the total current is very small for high fluences. At low fluence, the holes diffuse through the potential barrier, and the gradient of the hole concentration enables the injected carriers to move upwards. Finally, in regions very close to the surface, a residual electric field drifts the holes towards the surface (see Figure 4.4). Therefore, closer to surface, the total current is quite high. The total current streamlines are perpendicular to the etch front, and the interface between Si and p-Si, which is evident in the cross section SEM images, and will be discussed in corresponding context. Cross section SEM images show the current flow and match with the simulation predicted behaviour.

The direct experimental proof of the role of diffusion current in ion irradiated p-type silicon can be obtained by etching an ion irradiated Si with zero applied bias. Figure 4.9 illustrates the experimental procedure in cross sectional view wherein focused ion beam is used to irradiate silicon (represented by the grey color regions) in designed pattern, and generate defect regions(represented by the dark grey color regions), shown in (a).

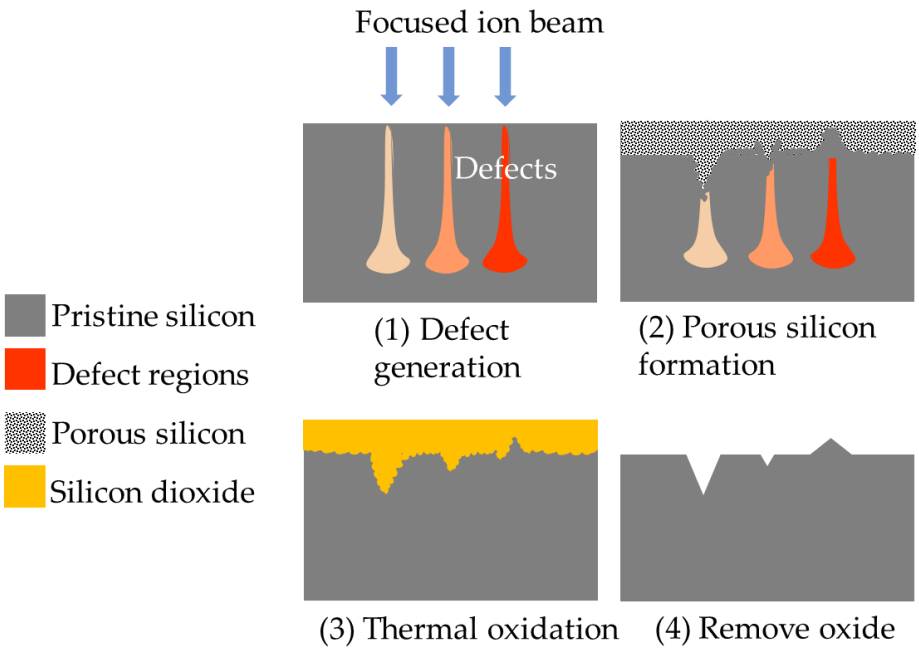

Figure 4.9 Experiment process to observe the surface profile of etched surface

Then a shallow electrochemical etching is performed to form a p-Si layer (represented by the texture color regions), for which the etch depth is usually only tens of nm, and the etching front around the defect regions is modified, shown in (b). p-Si is removed by dilute KOH solution, and surface patterns on silicon are achieved, shown in (c). However, the surface is very rough, and a smoothening step is needed. A thermal annealing is carried out (in (c)) to form a thin oxide layer (represented by the yellow color). After removing the oxide layer by a dilute HF solution, relatively smooth patterns on silicon are obtained, as in (d). The surface morphology is studied on sample surface with the help of AFM and SEM techniques. This procedure of surface patterning will be referred as "surface patterning process" in the later chapters. With different irradiation conditions, the feature is either a groove, or a bump, which will be explained in more detail in the following texts. To observe the effect due to diffusion current, zero bias is applied to etch a line irradiated wafer. For a zero bias, the current density due to depletion and Helmholtz layer is very small for 0.4 Ω.cm wafer, and negligible compared to the diffusion current density. The etching, therefore, is caused by diffusion current primarily.

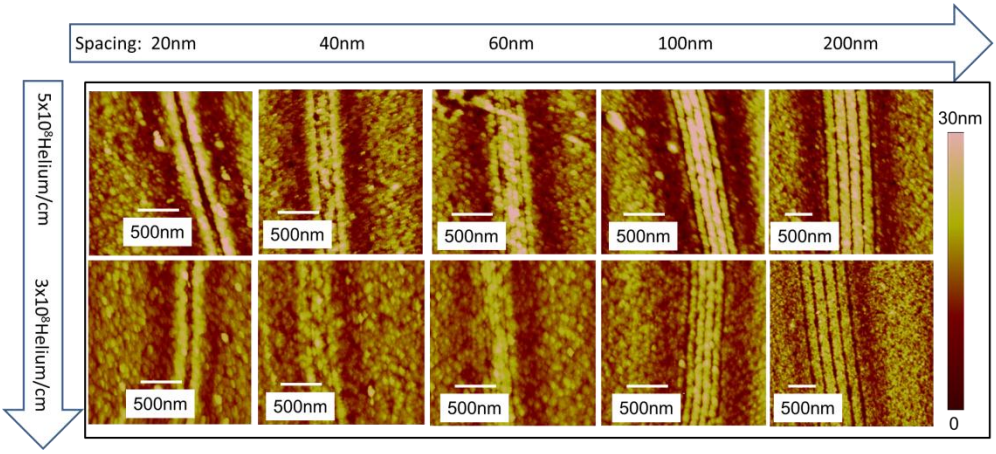

Figure 4.10 Effect of diffusion current (etched with zero bias). AFM image of surface profile: 30 keV He^+ beam focused to 0.5 nm used to write lines on 0.4 Ω.cm p-type Si and etched with zero bias

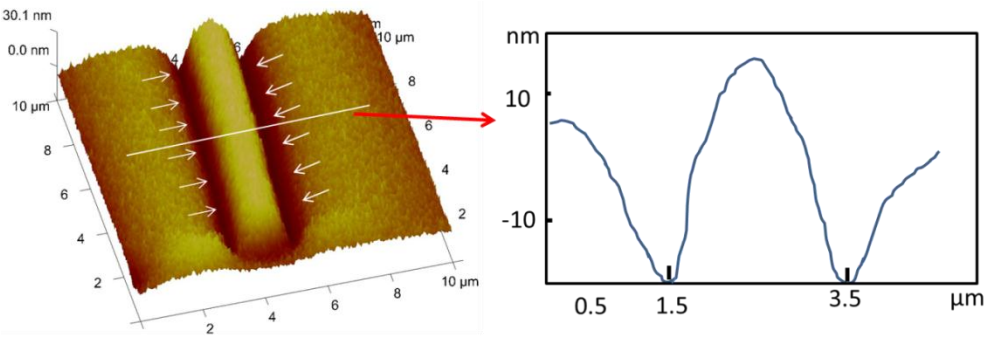

Figure 4.11 Diffusion current towards low defect density column for line irradiation. 2 MeV H_2^+ ions focused to 100 nm, used to write lines with 10 µm spacing, with a high line fluence of $1x10^{13}$ protons/cm with line width of 2 µm on 0.4 Ω.cm p-type Si. Left: AFM 3D profile, Right: AFM linescan along the white line in left figure.

Figure 4.10 shows the results of lines written on 0.4 Ω.cm p-type Si using direct nanobeam patterning with spacing of 20nm, 40 nm, 60 nm, 100 nm, 200 nm, and line fluence of $5x10^8$ Helium/cm, and $3x10^8$Helium/cm, using 30 keV He^+ beam focused to 0.5 nm. The irradiated wafer was etched in 24% HF with a closed circuit but no extra bias for 2 mins. Porous silicon was removed afterwards in KOH. A weaker diffusion current when the line fluence decreases from $5x10^8$/cm to $3x10^8$/cm, which is indicated by the shallower grooves at the lower row (both rows have the same color bar).

This is not only for the case where the defect density is located at the surface. By applying the same procedure of Figure 4.9, using direct nanobeam patterning with2 MeV H_2^+ to irradiate lines and etching the sample with zero applied bias, the same phenomenon is observed, as in Figure 4.11. 2 MeV H_2^+ focused to 100 nm was used to write lines with 10 μm spacing, with line fluence of $1x10^{13}$proton/cm with line width of 2 μm on 0.4 Ohm.cm p-type Si, and then etched in 24%HF for 2mins with closed circuit without extra bias. p-Si is removed by KOH solution. The right figure is the height profile along a horizontal line across the irradiated region, in which the dip at the edge of the line is due to the diffusion from sideways towards the irradiated column.

The etch profile of the silicon surface in Figure 4.11 is attributed to the diffusion current due to the hole density gradient from non-irradiated region towards the low defect density column region, indicated by the groove besides the irradiated line. This is a direct proof of the transverse nature of diffusion current shown by horizontal white arrows in Figure 4.6(f). The same effect is observed for point ion irradiations, Figure 4.12, where the same procedure as in Figure 4.9 is applied for a dot pattern, points with 2 μm spacing, with point fluence of $1.25x10^8$proton/point with line width of 2 μm are written using 2MeV H_2^+ focused to 500 nm on 0.4 Ω.cm p-type Si, and then etched in 24%HF for 2 mins with closed circuit without extra bias. p-Si is removed by KOH solution. The right figure is a height profile along a horizontal line across the irradiated region, which shows the ring surrounding the irradiated points (marked by the white dash circle), due to diffusion current from unirradiated regions to irradiated regions (marked by white arrows).

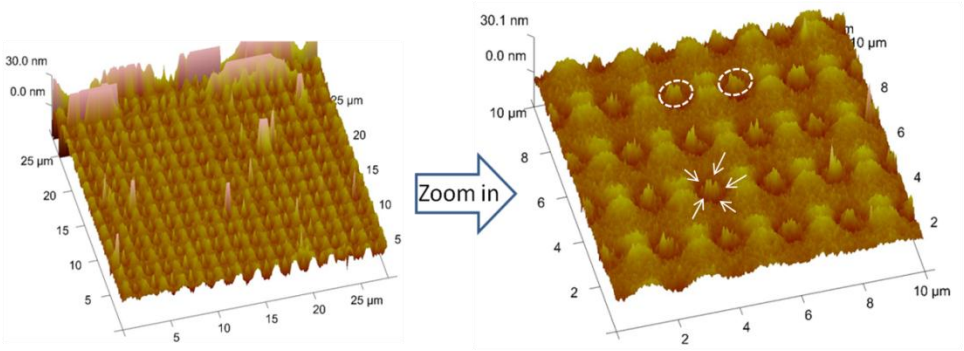

Figure 4.12 Formation of rings due to diffusion current for point irradiation. 2 MeV H_2^+ ions focused to 500 nm used to write points with 2 µm spacing, with point fluence of 1.25x10^8 proton/point on 0.4 Ω.cm p-type Si

So far, two current components have been discussed separately, namely the drift current, which is modified by the built-in potential from net charges, and the diffusion current, arising from hole density gradient ∇p. In the practical etching process, total anodization current is the sum of these two components, and due to the small area that diffusion current points towards, the diffusion current density can be very high, such that a funnelling of total current density occurs, which will be discussed in next section.

4.5 Funnelling effect and formation of highly porous silicon regions

The total current density is the sum of drift and diffusion current densities, in equation 4-12.

$$\overrightarrow{J_{total}} = \overrightarrow{J_{drift}} + \overrightarrow{J_{diff}} \qquad 4\text{-}12$$

Due to the small area that diffusion current points towards, the total current density can be dominated by the diffusion component at the region with large amplitude of ∇p. Meanwhile the resistivity ρ at these regions increases due to a decreased hole concentration p and reduced hole mobility μ_p.

$$\rho = \frac{1}{q \cdot \mu_p \cdot p} \qquad 4\text{-}13$$

A higher current density and a higher resistivity result in the formation of high porosity p-Si, shown by the arrow in Figure 4.13[2], which shows porosity with respect to the doping density for different current densities. Assuming the doping concentration decreases by about 5 times, being etched with an applied current density of 30mA/cm^2, the local current density increases to 300 mA/cm^2 for defect region, and the porosity increases from 0.6 to about 0.82 for 0.02 Ω.cm wafers while for 0.4 Ω.cm wafers the porosity increase from 0.74 to 0.96. This increase in porosity is much higher than the previous understanding which only considered increase of resistivity due to ion irradiation[70] for explanation of variation in photoluminescence(PL) arising from ion irradiated regions. In the case of a pure resistivity increase, the porosity only increases from 0.6 to 0.67 for 0.02 Ω.cm wafers and 0.74 to 0.79 for 0.4 Ω.cm wafers, for the same induced variation of resistivity. Therefore, a much higher PL intensity is produced when both resistivity and current density increase are considered than only considering a resistivity increase.[71] This particular aspect has been studied by capturing the PL image from cross section view, shown in Figure 4.14(b). (PL was excited using a wavelength of 330 to 380 nm) In Figure 4.14, direct nanobeam patterning was used where a

focused 2 MeV proton beam was used to irradiate 1 µm lines with varying ion fluences on 0.02 Ω.cm wafers. The higher the porosity, the easier the p-Si gets oxidized, such that the highly p-Si regions gets oxidized after leaving the etched wafers in air for several days while the rest of p-Si still remains almost unaffected. By including a further step of dipping in HF, the oxidized p-Si is removed, and hollow regions form, Figure 4.14(c), which enables structuring of p-Si, which will be discussed in more detail in section 6.3.

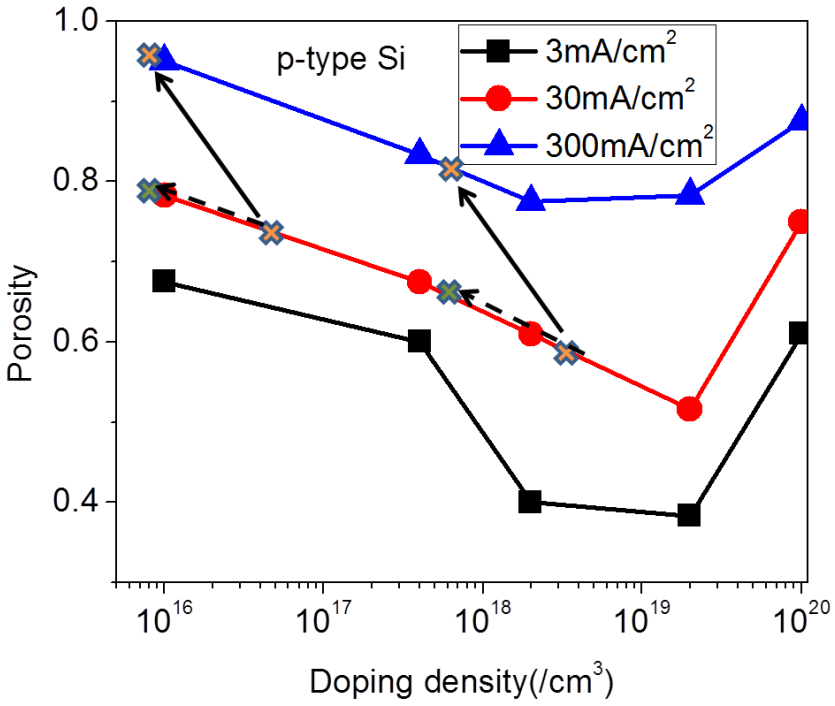

Figure 4.13 Porosity increase in ion irradiated Si. (Reproduced from Fig. 6.9(a) of Ref. [2]): Porosity as a function of doping density for p-type (1 0 0) Si electrodes

Figure 4.13 shows that the optimum initial doping concentration of $2x10^{18}$~$1x10^{19}/cm^3$ is ideal for such an increase of porosity. This matches with the discussions on a higher selectivity of etching between non-irradiated and irradiated regions only for highly doped wafers in section 5.1, which is important in the context of end of range core formation.

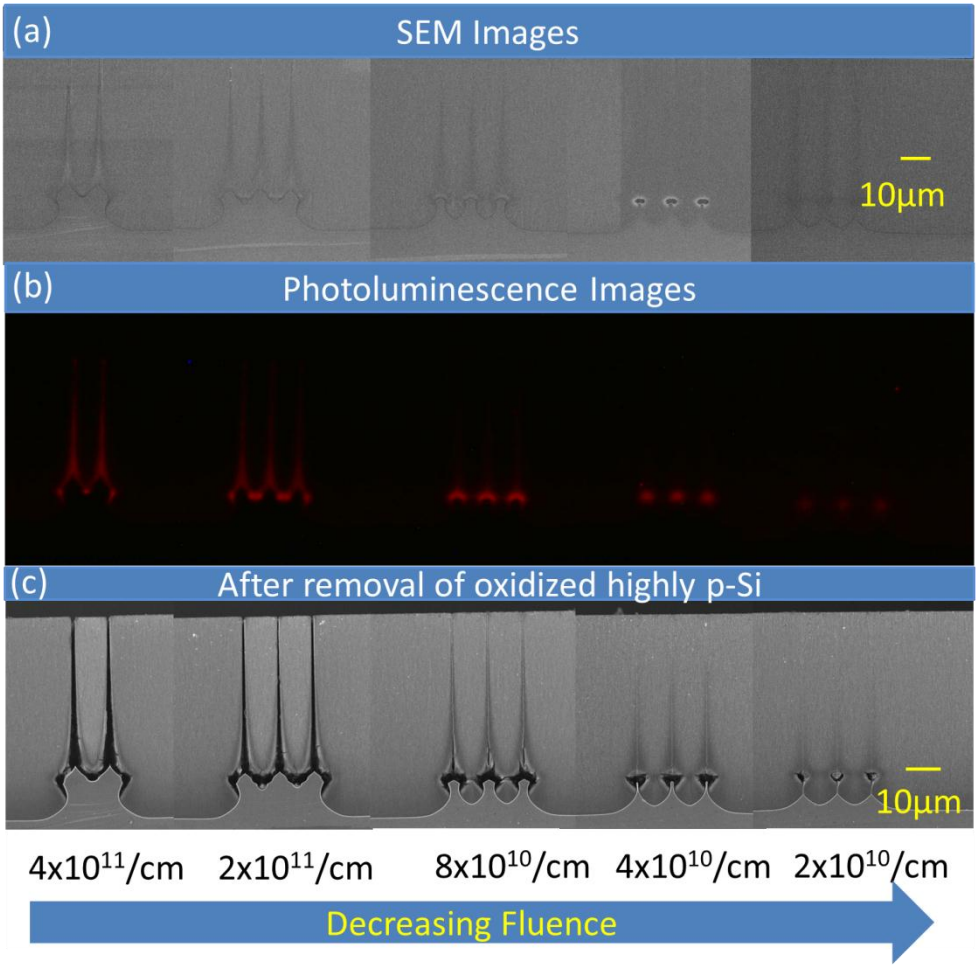

Figure 4.14 Cross section images of lines irradiated with 2 MeV proton of increasing fluence on 0.02 Ω.cm wafer, etched with 100 mA/cm^2 for 15 mins, with 1μm line width, 10 μm line spacing on wafer surface: (a) SEM after etching; (b) PL OM after etching; (c) SEM after oxidation for 1week in air, and removal of oxidized p-Si with 2%HF.

The funnelling effect is defined as the focusing of the hole streamlines towards the region with lowest carrier density along the gradient,[67] in which the holes from across an extended region are focused towards a small region, as a result, a locally enhanced total current density ion irradiated Si. The funnelling effect is a universal effect in all wafers with non-uniform carrier distribution. However, its role in different cases depends on the irradiation geometry, energy and fluence. For example, for high energy proton irradiated Si, where the ion fluence is low so that the defect density within end of range region is not high enough to deflect away the diffused holes, highly

p-Si forms within the end of range regions, shown by the simulation results in Figure 4.15(a, b). However, when the ion fluence increases even though holes tend to diffuse towards the highest defect density region, they are repelled by the built-in electric field from this region, Figure 4.15(c). Therefore, the total current is bent around this highest defect density region towards the region above. The higher the fluence, the stronger the repulsion and the total current bent towards the more above region, Figure 4.15(d). These simulations are only for the current flow at initial stage of etching, however, it predicts the core formation at higher fluences, as well as the current funneling effect, which is evident in the experimental results on the right, where the yellow dashed circle region is highly p-Si and produces high intensity PL in the 0.02 Ω.cm.

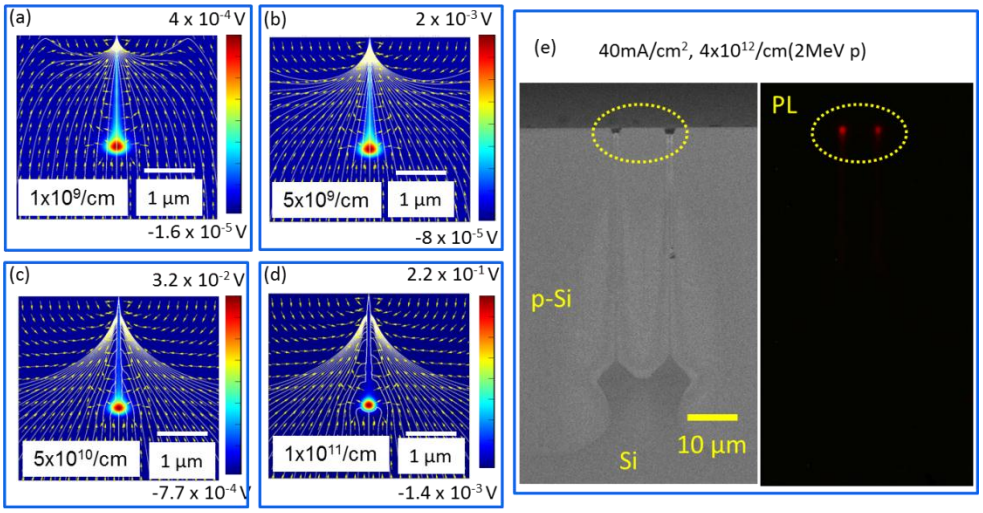

Figure 4.15 (a~d)Simulation results of etching current distribution in 0.4 Ω.cm silicon irradiated by 250 keV protons with increasing ion fluence; (e)SEM and PL image of enhanced funneling at the surface.

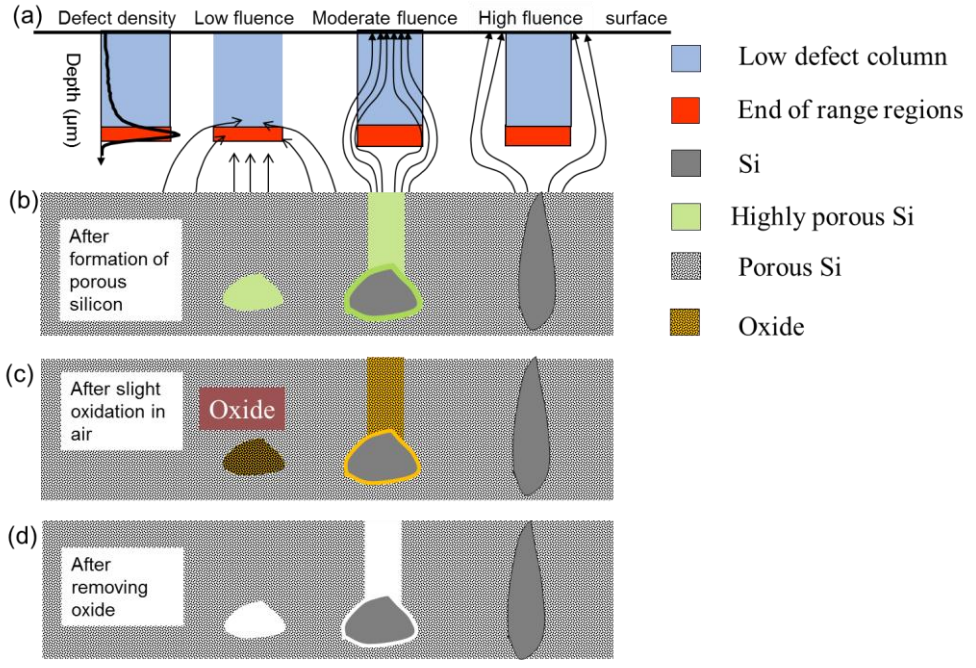

Figure 4.16 Three regimes of high energy proton irradiation

In this case, highly p-Si forms at the interface of p-Si and the silicon core and the low defect region column above the end-of-range region where the amplitude of ∇p is large. The formation of this highly p-Si region enables an additional interesting method of structuring p-Si and glass. Such an etched Si

sample was dipped into HF electrolyte and sub-surface hollow channels in p-Si were seen in the cross sectional image. The mechanism is that after etching, the highly porous silicon regions were easily oxidized when left in air for several days. The oxide can be removed by HF solution, and hence, leads to formation of either hollow regions surrounded by the p-Si, or free-rotating silicon wires surrounded by the p-Si at a slightly high fluence, or a hollow column between p-Si walls at an even higher fluence, as in Figure 4.16 and SEM images in Figure 4.14.

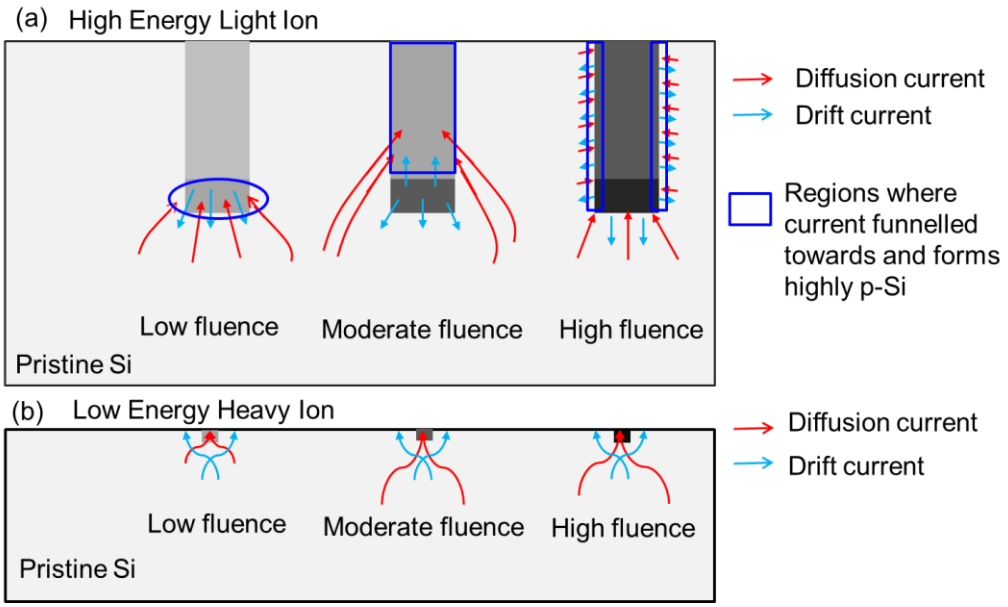

Figure 4.17 Schematically showing role of diffusion current and counter electric field on funnelling effect in (a)high energy light ion case, (b)low energy heavy ion case

Therefore, diffusion and drift current play roles together in the universal funnelling effect. A comparison of the role of two current components in funnelling effect and the region where highly p-Si forms is listed in Table 4.1 and 4.2 for different ion irradiation conditions, which is shown schematically in Figure 4.17(a) and 4.17(b) respectively.

Table 4.1 Role of diffusion current and counter electric field in funnelling effect and region of highly p-Si formed for high energy light ion case

Component	low fluence	moderate fluence	high fluence
Diffusion	Dominant, Enhancing the funnelling effect	Dominant, Enhancing the funnelling effect	Dominant, enhancing the funnelling effect
Built-in potential	Hindering the funnelling effect	Enhancing the funnelling effect of low defect column	Hindering the funnelling effect
Region where highly p-Si forms	End-of-range	Surrounding the end of range core and low defect column	At interface of end of range core, silicon wall and the surrounding
Structures formed after removal of oxide	Buried channels	Free-rotating silicon wires and hollow columns	Si walls separated from p-Si by narrow air gap

Table 4.2 Role of diffusion and drift current components in funnelling effect and region of highly p-Si formed for low energy heavy ion case, such as 30 keV He^+.

Component	low fluence	moderate fluence	high fluence
Role of diffusion component in funnelling	Dominant, enhancing, but very trivial	Dominant, enhancing, strong	Dominant, enhancing, very strong
Role of drift component in funnelling	Hindering, can be ignored	Hindering, weak	Hindering, very strong

In this section, a funnelling effect due to high diffusion current density and formation of high porosity p-Si is discussed, which leads to a method of producing buried p-Si regions with very strong PL, as well as buried hollow channels, and free-rotating silicon wires, hollow columns surrounded by p-Si, which will be discussed further in chapter 6. The next interesting question is what determines this funnelling effect.

4.6 Factors that influence the funnelling effect

Funnelling will occur in any semiconductor with a non-uniform hole density. In the case of ion irradiated Si wafers, it is usually dominant and enhanced by diffusion current, and either enhanced or hindered by drift current, as discussed in Figure 4.17. There are many factors that influence the funnelling effect.

4.6.1 Ion fluence

Ion fluence is the main factor that influences the funnelling effect. Figure 4.18 shows for 30 keV He^+ line irradiation, the same as in the modeling section of current flow, direct nanobeam patterning is used to pattern on a 0.4 Ω.cm wafer. At lowest fluence $1x10^6$/cm funneling occurs but is relatively weak, while on increasing the fluence to $1x10^8$/cm very strong funneling occurs due to the dominance of diffusion current where holes from an extended region are funnelled to a single point. By further increasing the line fluence to $2.5x10^9$/cm the repulsion from the built-in potential is strong and current is deflected first and then focused at the surface; on further increasing the line fluence to $7.5x10^9$/cm, the repulsion is very strong and becomes dominant. This was schematically discussed in Figure 4.17(b) and summarized in Table 4.2. To experimentally demonstrate the effect of ion fluence on diffusion current and drift current, as well as on the combined funneling effect, Figure 4.19(a) shows AFM results on dips formed by point irradiation of 30 keV He^+ ions and dip depth and width defined by the AFM line plot along the white dash line. The experiment procedure has been described in section 4.4. Figure 4.19(b) shows the variation of dip depth and width with respect to point fluence. Dip depth indicates the intensity of diffusion current, since a diffusion current enhances the etching rate in the centre of the line while dip width indicates the intensity of repulsion of holes away by the built-in potential. Therefore, both components increase with fluence. However, it is not possible to make quantitative comparison between the simulations and experiment results, since the simulation ignores time evolution, and amorphization of the damaged regions. These aspects will be discussed further in the later chapters.

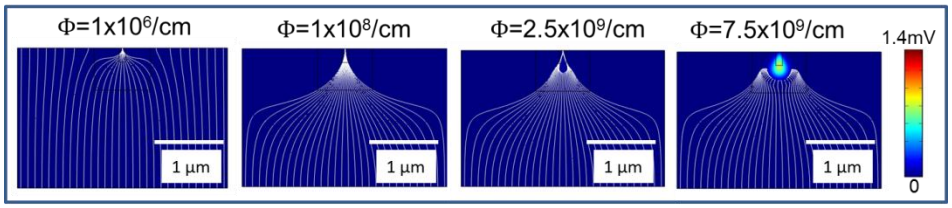

Figure 4.18 Simulation results on total current density for increasing line fluence of 30 keV He^+

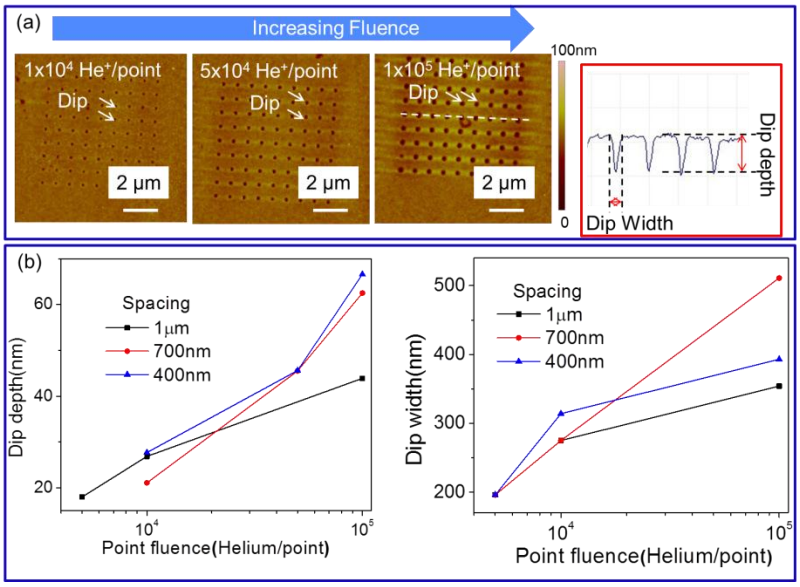

Figure 4.19 Influence of fluence. (a) Experimental results on dips (marked by white arrows) formed by point irradiation with 700 nm spacing, while increasing the ion fluence(unit: Helium/point), (b) plots showing increased dip depth and width, defined from the most right AFM lineplot along the white dash line.

4.6.2 Geometry

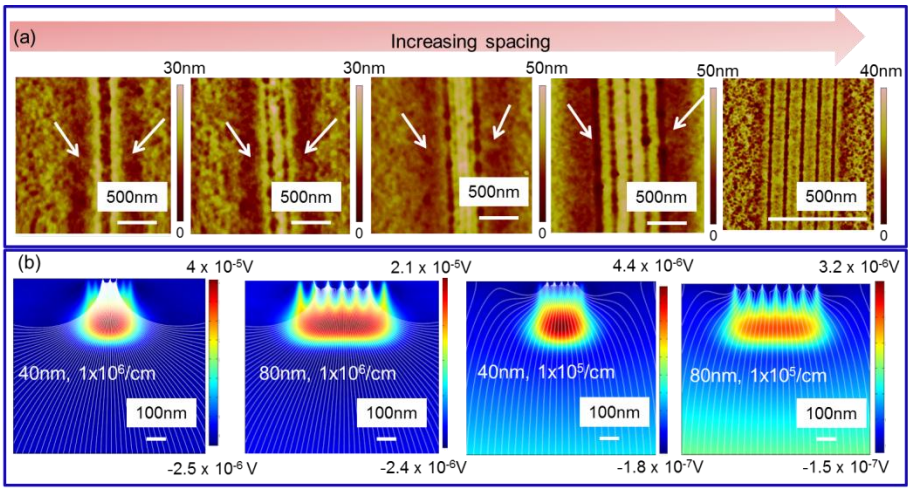

Figure 4.20 Influence of spacing. (a) Experimental ($5.9x10^8$/cm) and (b) simulation results showing the effect of variation of spacing on the current distribution and resultant structures

The spacing between irradiated features such as lines or dots is another important parameter. The effect of different spacing on funneling is shown in Figure 4.20. Five lines with a spacing of 20 nm~500 nm were irradiated, and the experiment procedure was taken as described in section 4.4. With decreasing spacing, the effect from defect regions of adjacent features starts to influence each other and they can no longer be considered as isolated irradiations. The experiment results is consistent qualitatively with the simulated results, where for spacing and fluence of 40 nm, $1x10^6$/cm; 80 nm, $1x10^6$/cm), current converges together. This is matching with the experimental observation that lines merge together for spacing of 20 nm, 40 nm, and 60 nm. For the same fluence, with increasing spacing the current streamlines can be better resolved, as in the simulation results ($1x10^5$/cm: 40nm and 80nm). The definition of a separate feature is when the spacing between adjacent features is large enough such that the current streamlines do not intersect. Experimentally, this is indicated by the lack of a dark shadow around the whole irradiation area, while the dark shadow is marked by white arrows for the non-separate features. Therefore, the lines in Figure 4.20(a) cannot be considered as resolved for spacing of $\leq$ 200 nm for this particular fluence and etch condition. When the spacing between adjacent features is so small that

they behave as a single feature, effective ion fluence can be adopted. For example, the 5 lines with 20 nm spacing with a line fluence of 5.9×10^8/cm in Figure 4.20(a) can be considered as a single line with fluence 5 times as large, i.e. about 3×10^9/cm.

4.6.3 Applied bias on the wafer

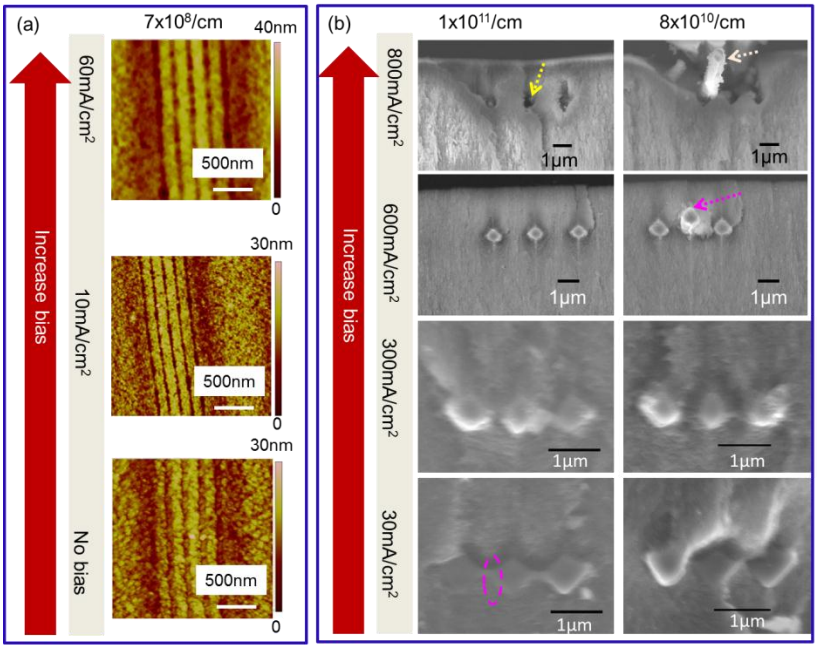

Figure 4.21 Influence of applied bias. Experimental results showing the effect of increasing the applied bias on both (a) low energy helium irradiation and (b) high energy proton cases.

By increasing the applied bias, the drift current component is enhanced. Figure 4.21 (a) shows that increasing the etch current density from zero bias to 60mA/cm^2 for 30 keV He^+ with same line fluence, the funnelling effect is stronger (better resolved grooves) due to a relatively weaker opposition by the built-in potential. The experiment procedure is the same as described in section 4.4. Similarly, for a higher energy lighter ion beam, a stronger funneling is observed for a higher applied bias. In Figure 4.21, direct nanobeam patterning using 250 keV protons produced buried silicon wires in p-Si. Figure 4.21(b) shows that by increasing the applied current density from 30 mA/cm^2 to 800 mA/cm^2, the opposition of the built-in potential by the end-of-range cores is also less, resulting in the cores from being connected

(marked by pink dashed circle) to being separate, then being smaller, and then becoming isolated and free-rotating due to an extremely highly p-Si (porosity close to 1 which is formed due to both a strong funneling as well as a higher applied etch current density) formed surrounding the core (marked by the yellow and white, and pink dashed arrow). The core marked by the pink arrow came out of the plane, due to high porosity in the surrounding p-Si region.

4.6.4 Etch depth, especially for low energy heavy ion

Etch time is important, since the defect and hole density distributions change with etch depth, especially for low energy heavy ions where the ion range is very short. Figure 4.22 used the same experiment procedure described in section 4.4. It shows the surface profile for fluences of $1x10^9$ and $5x10^9$/cm, as the etch time increases from 0.5 s to 4 s. Due to the funneling effect, the deep and central groove increases with etch time as well as a reduced opposition from the built-in potential at a larger etch depth.

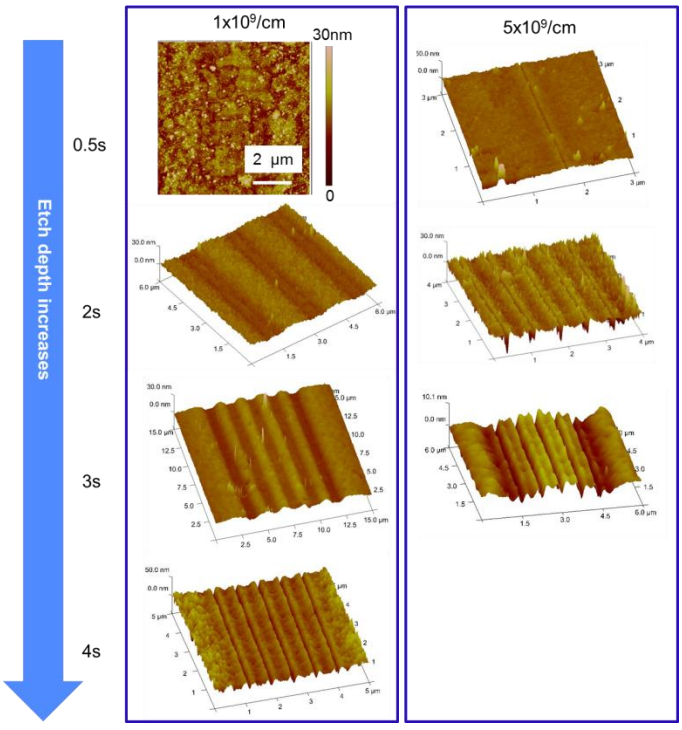

Figure 4.22 Influence of etch depth. Experimental results of helium irradiation with increasing the etch time (etch depth).

4.6.5 Wafer resistivity

Wafer resistivity also plays an important role in the funnelling effect. Highly-doped wafers have a higher hole density which enables a larger available hole concentration gradient ∇p, producing a stronger diffusion current which enhances the funnelling effect. Meanwhile, the built-in potential largely depends on the native wafer doping density. Higher-doped wafers have a smaller built-in potential, so a weaker opposition to the funnelling effect. Considered together, a highly-doped wafer has stronger diffusion current, and less opposition from the built-in potential, thus, a stronger funnelling effect. Figure 4.23 shows the simulation results of wafers with two different resistivity, which clearly show a difference in the scale of potential and the current which can flow between 0.9 µm spaced defect regions in low resistivity wafer but cannot in the high resistivity wafer.

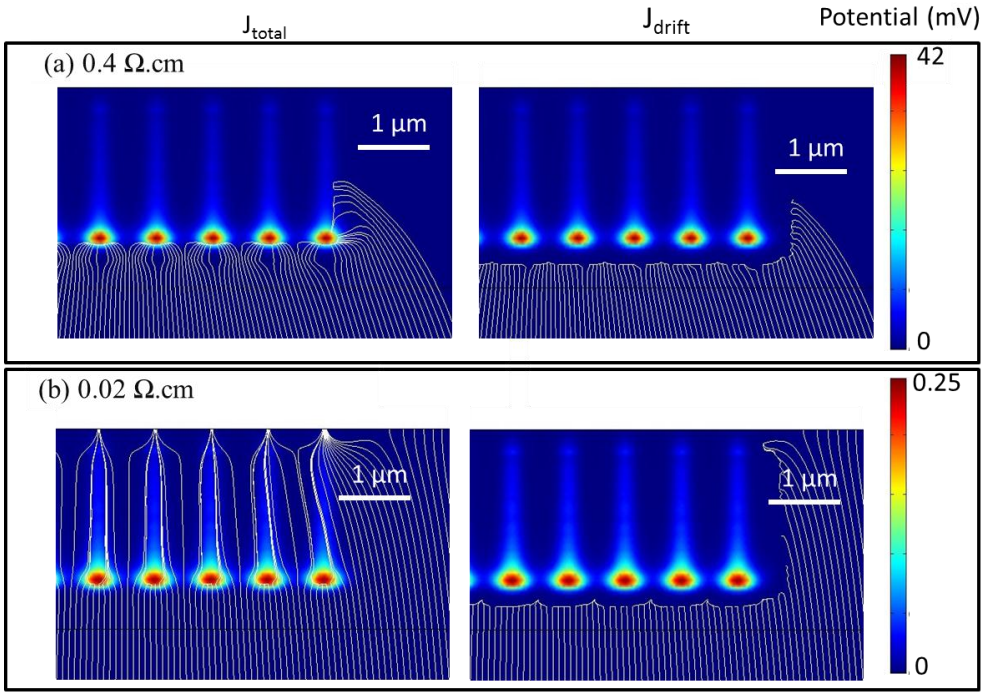

Figure 4.23 Potential map and current streamlines for 250 keV protons with line irradiation of 0.9 µm spacing and line fluence of 4.2×10^{10}/cm for left column: J_{total}, and right column: J_{drift} on (a) 0.4 Ω·cm wafer, (b) 0.02 Ω·cm wafer.

Due to the differing importance of the two current components in different resistivity wafers, the resultant structure after etching can be significantly

different. For example, the buried silicon wires have flat lower edge in 0.02 Ω.cm wafers, while a "tail" is visible at the bottom of buried cores in 0.4 Ω.cm wafers. The reason is a dominant role of diffusion current in 0.02 Ω.cm wafers while in 0.4 Ω.cm wafers due to dominant role of drift current, as in Figure 4.24. In Figure 4.24, direct nanobeam patterning using 250keV protons produced buried Si wires in p-Si. The mechanism of formation of different core shape in different resistivity wafers will be discussed in greater detail in section 5.3. [54]

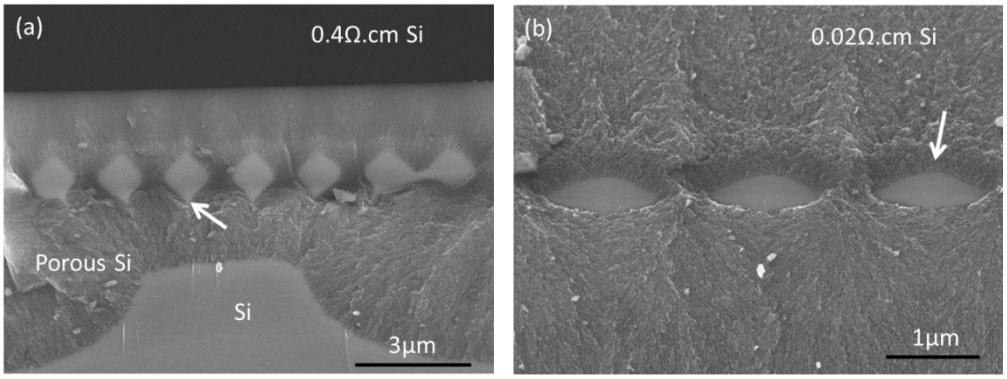

Figure 4.24 Different core shapes in different resistivity wafer. Cross-section SEMs of individual wires for line fluence of 250 keV protons of (a) 6×10^{10}/cm in 0.4 Ω.cm wafers, and (b) 1×10^{11}/cm in 0.02 Ω.cm wafers.

This section has discussed the factors that influence the funnelling effect. The good agreement in many aspects between simulation and experimental results proves the validity of our simple simulation model in predicting some aspects of the etching behavior under various irradiation conditions.

4.7 Mathematical treatment

The total current density is composed of drift and diffusion current density and the main resultant structures depend on the dominant component, however, the effects from these two components exist at the same time for any experimental conditions. In this section, equations are derived for factors that influence the current flow in order to further provide a capability to predict the likely behavior. These mathematical treatment were carried out by the author based on the basic equations in semiconductor physics, but incorporated the effect of ion irradiation.

4.7.1 Bragg peak is near the surface

In this case, the highest defect region is located in very narrow region near the surface of the wafer, therefore, the current directly diffuses into the highest defect region which itself has a built-in potential pointing outwards. To simplify the case the defect region is seen as a single point, meanwhile, only the vertical direction is considered, and the electric field is simplified as follows:

$$\mathrm{E_{vertical}} = \mathrm{E_{applied}} - \mathrm{c}(\vec{\mathrm{r}})\Phi \qquad 4\text{-}14$$

where $\mathrm{E_{vertical}}$ is the electric field in the depth direction, $\mathrm{E_{applied}}$ is the applied electric field, Φ is the fluence, and $\mathrm{c}(\vec{\mathrm{r}})$ is a proportional constant by assuming a linear relationship between built-in potential and the fluence, which is a function of position.

$\mathrm{p} \approx \mathrm{N_{eff}}$

According to Equation 4-4 and 4-11,

$$\overrightarrow{J_{diff}} = \mathrm{qD}\nabla\mathrm{p} = \mathrm{qD}\nabla(\mathrm{N_{a0}} - fv\Phi) = -\mathrm{qD}f\Phi\nabla v \qquad 4\text{-}15$$

v is the defect density, ∇v is the gradient of defect density, and q, D, f, Φ as defined in above text. Equation 4-15 shows that the amplitude of $\overrightarrow{J_{diff}}$ is

proportional to amplitude of the gradient of the defect density, and the ion fluence Φ. The direction of $\overrightarrow{J_{diff}}$ is along the direction of -∇v.

By replacing electric field in equation 4-8 using equation 4-14, replacing hole density using effective doping concentration in equation 4-4,

$$J_{\text{drift(vertical)}} = \text{qp}\mu_{\text{p}}\text{E} = \text{q}\mu_{\text{p}}(\text{N}_{\text{a0}} - fv\Phi)(\text{E}_{\text{applied}} - \text{c}(\vec{\text{r}})\Phi) = \text{q}\mu_{\text{p}}[\text{c}(\vec{\text{r}})fv(\vec{\text{r}})\Phi^2 - \left(\text{c}(\vec{\text{r}})N_{a0} + fv(\vec{\text{r}})\text{E}_{\text{applied}}\right)\Phi + N_{a0}\text{E}_{\text{applied}}] = k_2\Phi^2 - k_3\Phi + b \quad \text{4-16}$$

$k_2 = \text{q}\mu_{\text{p}}\text{c}(\vec{\text{r}})fv(\vec{\text{r}})$ >0, $k_3 = \text{q}\mu_{\text{p}}\left(\text{c}(\vec{\text{r}})N_{a0} + fv(\vec{\text{r}})\text{E}_{\text{applied}}\right)$ >0, $b = \text{q}\mu_{\text{p}}N_{a0}\text{E}_{\text{applied}}$>0, $\Phi \geq 0$

$J_{\text{drift(vertical)}}$ is the drift current density in the vertical direction, q is the charge of holes, μ_{p} is the mobility of holes, $v(\vec{\text{r}})$is the defect density, and all the others defined earlier. Hole mobility does not change a lot with respect to fluence, and can be seen as a constant. Equation 4-16 shows a quadratic dependence of drift current density on ion fluence, and the symmetric axis of $\text{J}_{\text{drift}} = k_2\Phi^2 - k_3\Phi + b$ is $\frac{k_3}{2k_2}$>0.

According to equation 4-15, the amplitude of diffusion current density is:

$$J_{diff} = \text{qD}f\Phi\,|\nabla v| = k_1\Phi \quad \text{4-17}$$

$k_1 = \text{qD}f\,|\nabla v|$>0, $\Phi \geq 0$, and all the others were defined earlier.

Figure 4.25 plots J_{drift} and J_{diff} with respect to Φ, and shows two intersecting points.

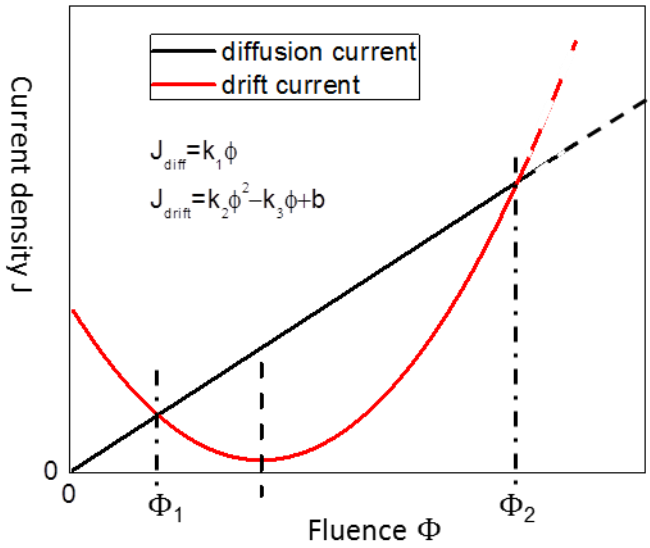

Figure 4.25 Three fluence regimes. Schematic plot of the diffusion current and drift current versus ion fluence (Φ) for low energy heavy ion beam irradiated silicon

The overall fluence is split into three regimes by these two intersecting points, as shown in Figure 4.25 and Equation 4-18:

$$\begin{cases} J_{drift} > J_{diff} & (0 < \Phi < \Phi_1) \\ J_{drift} < J_{diff} & (\Phi_1 < \Phi < \Phi_2) \\ J_{drift} > J_{diff} & (\Phi > \Phi_2) \end{cases} \quad \text{4-18}$$

Figure 4.25 is derived based on ignoring other effects, such as amorphization and sputtering. This figure shows that at low fluence, the diffusion current is weak; at moderate fluence, diffusion becomes dominant; at a higher fluence, drift current is dominant again. However, Figure 4.26, fabricated using the "surface patterning process" in section 4.4, shows the profile for different line fluences where at highest fluence $2x10^{10}$/cm, a dip is overlapped to the up ridge predicted above, though the first two regimes match with prediction from above discussion. The reason is that the amorphization becomes prominent at high fluence, shown by the deep line down in the center (marked by white arrow). This will be discussed in last section of chapter 7.

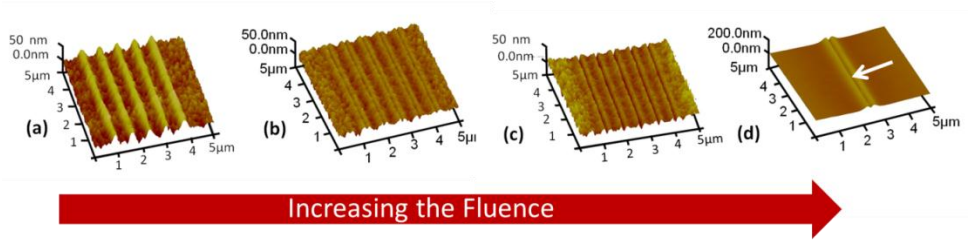

Figure 4.26 Comparison of three regimes with experiments. AFM surface profile images of 0.4 Ω.cm p-type type silicon irradiated with 30 keV He ions with a period of 700 nm with (a) 6×10^{7}/cm, (b) 3×10^{8}/cm, (c) 6×10^{8}/cm, (d) period of 5 µm for 2×10^{10}/cm. [67]

4.7.2 Bragg peak is beneath the surface

In this case the defect density is located beneath the surface and extends over a region due to straggling. The high defect region cannot be seen as a single point any more, instead, it is simplified as having a series of contours, each of which has a constant defect density. Figure 4.27(a) shows the onset of core formation (when etching comes to the upper side of high defect region).

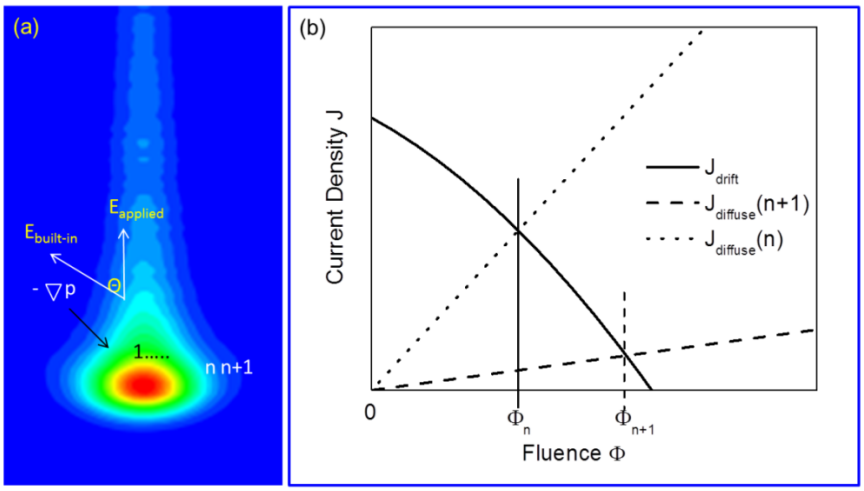

Figure 4.27 Core formation for high energy light ions. (a) Defect contours and the electric field; (b) The regimes of fluence for high energy case.

Only the normal (with respect to the tangent of contour) direction is considered, since the diffusion current is in this direction along the doping gradient, and shown in equation 4-19, where c is a parameter that is dependent on the distance from the defect points:

$$E = E_{applied}\cos\theta + E_{built-in} = E_{applied}\cos\theta + c(\vec{r})\Phi \quad 4\text{-}19$$

For contour with number **n**:

$$J_{diffuse}(n) = -qD\nabla p = -qD\nabla N_a^{eff}(n) = qDf\boldsymbol{\Phi}\nabla v(n) \quad \sim\mathbf{k_1\Phi} \quad 4\text{-}20$$

$$J_{drift} = q\mu pE = q\mu[-fv(n)c(n)\Phi^2 - (fv(n)\cos\theta E_{applied} + c(n)N_a^0)\Phi + \cos\theta E_{applied}N_a^0] = -k_2\Phi^2 - k_3\Phi + b \quad 4\text{-}21$$

μ is also dependent on Φ, however the change is ignored for simplification. k_2>0, k_3>0, b>0, $\Phi \geq 0$. The symmetric axis of $J_{drift} = -k_2\Phi^2 - k_3\Phi + b$ is $-\frac{k_3}{2k_2} < 0$.

Figure 4.27(b) plots J_{drift} and J_{diff} with respect to ψ, and they only have one intersecting point. This point splits the fluence into two regimes. At a lower fluence, J_{drift}>$J_{diffuse}$, where holes are drifted towards the etch front due to the residual electric field in spite of the diffusion of holes in the opposite direction, and defect region etched; at a higher fluence, $J_{drift} < J_{diffuse}$, where holes are diffused into the core region, and no holes are drifted towards the etch front, and defect region is not etched and forms a core. One can analyse the core size based on the relative amplitude of two current components of different contours, Figure 4.27(b). For contour n and n+1, $\nabla v(n) > \nabla v(n+1)$, $v(n)>v(n+1)$, $c(n)<c(n+1)$, so $J_{drift}(n)$ does not change a lot with n for same Φ, while $J_{diffuse}(n) > J_{diffuse}(n+1)$. Therefore, when $\Phi_{n+1} > \Phi > \Phi_n$, $J_{diffuse}(n+1) < J_{drift}(n+1)$, contour n+1 is etched away, contour n remains unetched; thus core size (Φ_n)= size(contour n); when fluence $\Phi_{n+2} > \Phi > \Phi_{n+1}$, $J_{diffuse}(n+1) > J_{drift}(n+1)$, contour n+1 remains unetched, contour n+2 is etched away, thus core size(Φ_{n+1})=size(contour n+1). Core size increases with fluence Φ. This matches with the experiment results and will be discussed in a more precise manner in chapter 5. The effect of applied electric field can also be studied in this context. J_{diff} is not related to $E_{applied}$.

$$J_{drift} = q\mu pE = q\mu(N_a^0 - f\Phi v(n))\cos\Theta\left(E_{applied} + c(n)\Phi/\cos\Theta\right) \quad 4\text{-}22$$

For contour n and n+1, $\nabla v(n) > \nabla v(n+1)$, $v(n) > v(n+1)$, $c(n) < c(n+1)$. The current for these two contours is shown in Figure 4.28. At a $E_{applied,}$ where $E_{applied1} < E_{applied} < E_{applied2}$, the outer contour n+1 is etched away, since $J_{diffuse}(n+1, E_{applied}) < J_{drift}(n+1, E_{applied})$; but for inner contour n, it is left as a core, since $J_{diffuse}(n, E_{applied}) > J_{drift}(n, E_{applied})$.

When $E_{applied}$ is increased, such that $E_{applied} > E_{applied2}$,

$J_{diffuse}(n, E_{applied}) < J_{drift}(n, E_{applied})$, inner contour n is also etched away, as in Figure 4.28. This explains why at a higher etching current density, a smaller core is obtained for the same irradiated samples. This is consistent with the study in chapter 5.

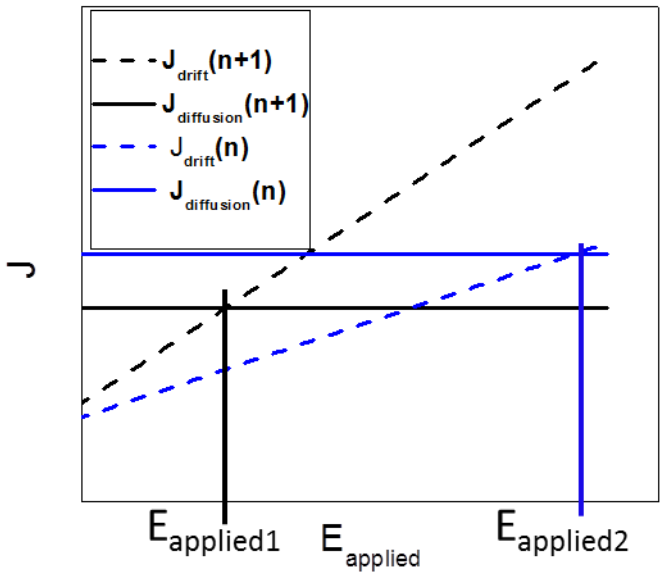

Figure 4.28 Drift and diffusion current for two applied bias

Conclusion

Following the proposed model and concept of effective doping concentration, two current components in ion irradiated wafers were explored; one is drift current, where the electrical potential is a superposition of applied potential and built-in potential in the defect regions. The other is diffusion current, which arises due to the nonuniformity of hole density. The funnelling effect was introduced which represents an enhancement of hole current density in the region with highest hole density gradient, since the diffusion current is usually pointing towards a small region resulting in a high current density even though the built-in potential usually deflects the holes away to a large spatial distance. This leads to fabrication of buried channels, free-rotating silicon wires surrounded by p-Si, buried p-Si with strong PL, hollow columns between p-Si. Different factors that influence the funnelling effect were discussed based on the comparison between experiment and simulation, as well as on mathematical derivation by simplification. This chapter is the first highlight of this thesis work where a reasonably complete picture of current flow for a variety of cases is drawn, and the proposed mechanism matches quite well with experimental results.

Chapter 5 . Etching front evolution: core formation

The time evolution is incorporated into study of core formation mechanism. This detailed study on the formation of cores lays a foundation for the next few chapters. To interpret the core formation mechanism, two concepts are defined in the first two sections. Section 5.1 defines selectivity; section 5.2 discusses the space charge region. Section 5.3 illustrates the respective dominance of these two concepts for two differently doped wafers and their core formation mechanism. Section 5.4 briefly discusses how to regularize and control the size of cores formed in these two wafers.

5.1 Selectivity

In this section, we first review the concept of selectivity with respect to doping density in previous literature, and then develop the definition of a selectivity coefficient in the context of ion irradiated p-type Si. When a Si wafer of different regions of doping concentration is anodized at a fixed current or potential, the dissolution current will be higher in regions of higher doping level and p-Si formation can only take place there. This can tell the doping impurity profile by converting potential values to dopant concentration based on $V_a = f(N_A^{0.5})$ discussed in section 3.1, and the electrolysis time to a depth scale. [72, 73]

The doping concentration influences voltage drop in the Helmholtz layer in lightly doped silicon. This voltage drop is of the order of a few millivolts, but it increases up to 150 mV for the highest doping concentration in the investigated range varying from 2.5×10^{15} cm^{-3} to 10^{19} cm^{-3}.[55]

In literatures, selectivity is used to describe the difference of etch rate caused by variable doping concentration. The definition of selectivity coefficient is $S = d_N/d_{N0}$, where d_N and d_{N0} are the porous silicon thicknesses, formed respectively in the variable and constant concentration regions.

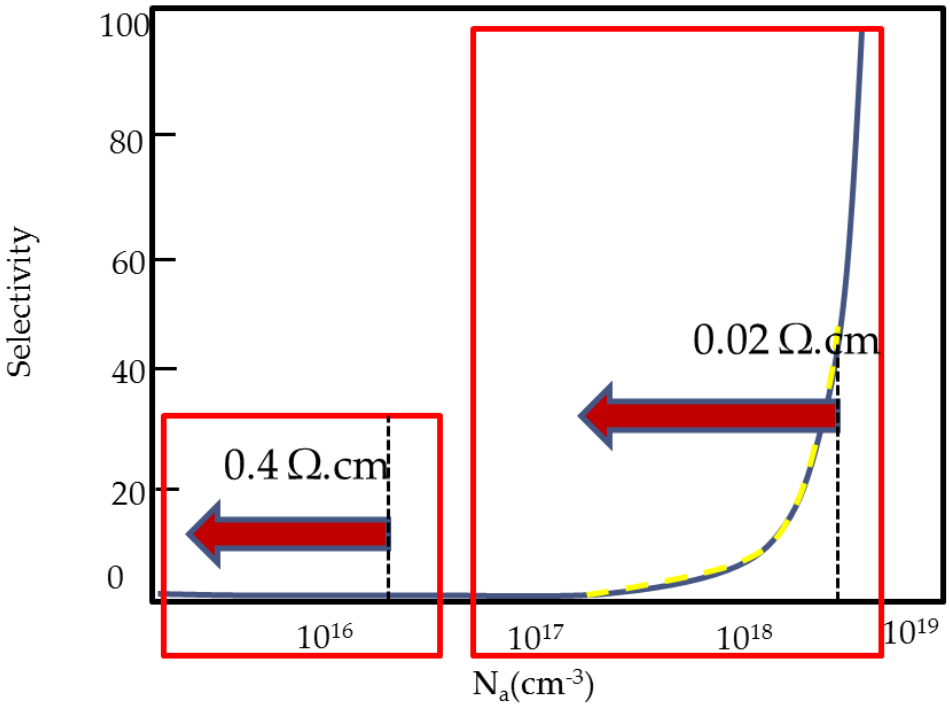

Figure 5.1 Selectivity coefficient versus doping concentration. Selectivity coefficient of the porous silicon formation reaction at constant current density(10mA/cm^2) as a function of silicon doping concentration (reference doping level 10^{15} cm^{-3}). (Reproduced from Ref. [73])

In Figure 5.1, an infinite selectivity coefficient is found for high doping levels (greater than 3x10^{18} cm^{-3}), but a sharp decrease with the dopant concentration is observed. When formation of p-Si is localized, it is important to consider the selectivity coefficient. If the highest dopant concentration is limited to l0^{18}cm^{-3}, a low selectivity is obtained. In this case, regions of different doping concentrations are simultaneously in contact with the electrolyte, the anodic reaction will also proceed in regions of lower doping concentrations. But if the regions to be converted to p-Si exhibit dopant concentrations of the order of 3xl0^{18} cm^{-3}, p-Si formation will be localized.[73] Though this study on selectivity in literature is matching with discussion in section 4.5 where the ideal initial doping concentration of the wafer for maximum increase of porosity is around 2x10^{18}~1x10^{19}/cm^3, it takes no account of the increase of current density arising from diffusion. A more complete understanding on the selectivity study should consider both doping concentration, and increase of current density.

In locally ion irradiated silicon wafers, the etching rate at irradiated regions is different from non-irradiated regions, either enhanced or slowed down. Similarly, here the selectivity coefficient can be defined as $S=d_U/d_I$, where d_U and d_I are the p-Si thicknesses, respectively, formed in the unirradiated and irradiated regions. This definition is consistent with the one in literatures, where unirradiated regions have constant doping concentration; while ion irradiated regions have variable doping concentration. The selectivity coefficient not only depends on initial doping concentration, but also the ion fluence, ion energy, etch depth, etch current density, etc. Here, three 0.4 Ω.cm p-Si wafers were irradiated with lines with 250 keV proton at different fluences of $1x10^{13}$/cm, $5x10^{12}$/cm, $1x10^{12}$/cm, $5x10^{11}$/cm, $1x10^{11}$/cm, $5x10^{10}$/cm, $1x10^{10}$/cm, $5x10^{9}$/cm, $1x10^{9}$/cm, and each sample was etched for different time, 3 s, 25 s, 40 s, 75 s, for which the etch depth at non-irradiated region is 120 nm, 1 μm, 1.6 μm, 3 μm, correspondingly. For 75s, the irradiated region is already undercut. The surface profile was studied after removal of all p-Si and smoothing by oxidation at 1000 ºC for 20 mins, and oxide removed. The profile of these surfaces is a big bump superposed with a narrow shallow groove in the middle. The step height and width increases with fluence. With a larger etch depth, the step height as well as step width increases. This is due to both a higher defect density and an accumulated effect along the etch path before coming to the etch front of certain etch time, shown in Figure 5.2(a).

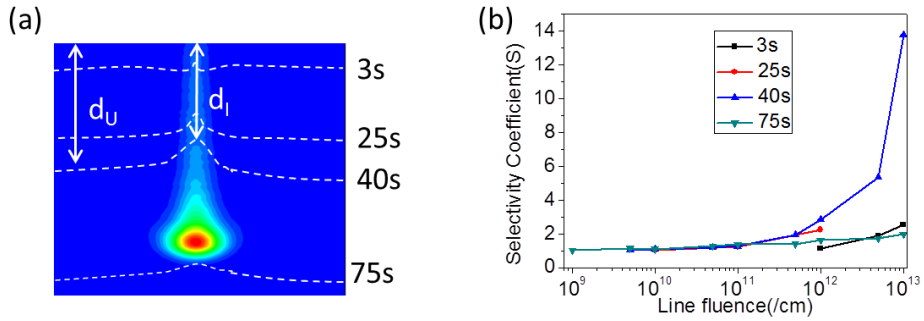

Figure 5.2 Defined selectivity coefficient of ion irradiated silicon. (a) Schematics showing accumulation effect with increasing etch time and depth at irradiated and non-irradiated regions; (b) Measured selectivity coefficient S with respect to ion fluence for different etch time.

Selectivity coefficient study in 0.02 Ω.cm wafers is under progress.

5.2 Space charge region

In section 3.1, it was shown that the potential is mostly dropped within the space-charge layer for p-type Si such as 0.4 Ω.cm wafers which are not heavily doped. A good example illustrating the space charge region (SCR) is macroporous silicon formation, for which the basic electrostatics of the porous electrode is sketched in Figure 5.3(a). A SCR is present in the semiconductor electrode close to the interface with the electrolyte. [74]

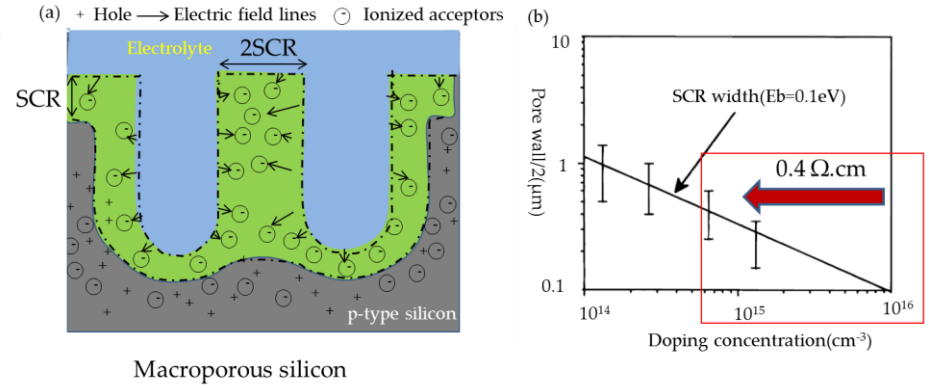

Figure 5.3 Space charge region in macroporous silicon formation. (a) sketch of the equilibrium charge distribution and the electric field around pores in a p type semiconductor electrode; (b) Values of pore wall thickness as a function of doping density together with the SCR width for a potential(V_{bi}+V-2kT/e) of 0.1 V (Reproduced from Ref. [74]).

The forward current in a p-type Si wafer which is anodized in HF is either dominated by diffusion, by thermionic emission, or by tunneling of holes. If the distance between two neighbouring pores becomes smaller than 2W, the pore wall becomes passivated due to the depletion of the holes in the SCR. [74] Figure 5.3(b) shows a square root dependence of space charge region width (W) on N_A. With an initial doping concentration of $3x10^{18}/cm^3$, W after irradiation is ~tens of nm, still very small compared to the size of the defect region; while with an initial doping concentration of $4.8x10^{16}/cm^3$, W after irradiation significantly increases which is ~hundreds of nm, several μm or even larger. [74] Therefore, in a 0.4 Ω.cm wafer, SCR plays a more significant role than in a 0.02 Ω.cm wafer.

When the defect density is high enough, the SCR at the interface of silicon and the electrolyte overlap and form a complete depletion region. In Figure 5.4,

the color represents defect density, and the schematics show interface region between silicon and electrolyte.

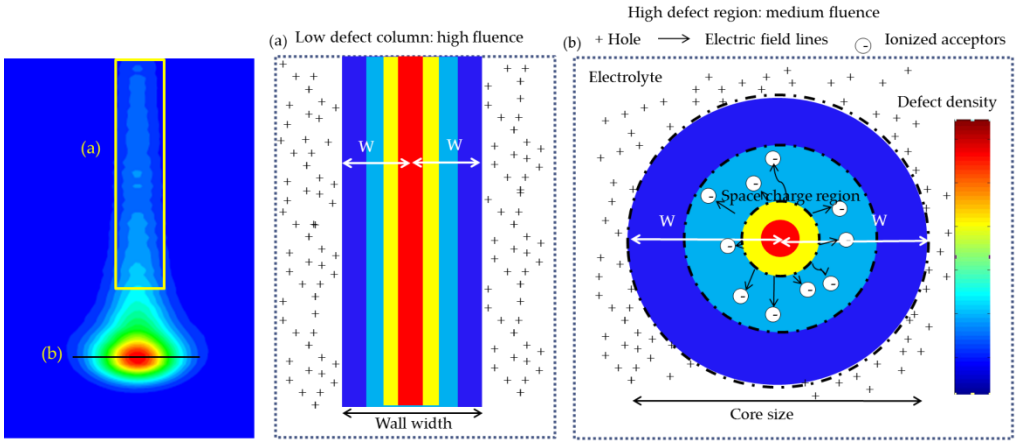

Figure 5.4 Overlapping space charge region in the low defect column or end of range region. (a) Low defect region along the ion track column and overlapped SCR at extremely high fluence; (b) High defect region at end-of-range, and overlapped SCR to form Si core at moderate fluence for 0.4 Ω.cm wafer.

This is the region that will remain unetched. Figure 5.4 (a) shows high fluence case, where the low defect column is completely depleted. Figure 5.4(b) shows moderate fluence case, where high defect end of range region is completely depleted.

5.3 Core formation

This section proposes the core formation mechanism in wafers with 0.02 Ω.cm and 0.4 Ω.cm resistivity. Based on this core formation mechanism, a variety of factors that influence the core size, minimum gap, and core shape are discussed in detail.

5.3.1 Core formation mechanism

As discussed in section 4.5, high energy light ions with moderate fluences produce buried silicon wires at the end-of-range regions. This is a combined result of selective etching at unirradiated regions, and formation of a depletion region in the irradiated regions, Figure 5.5.

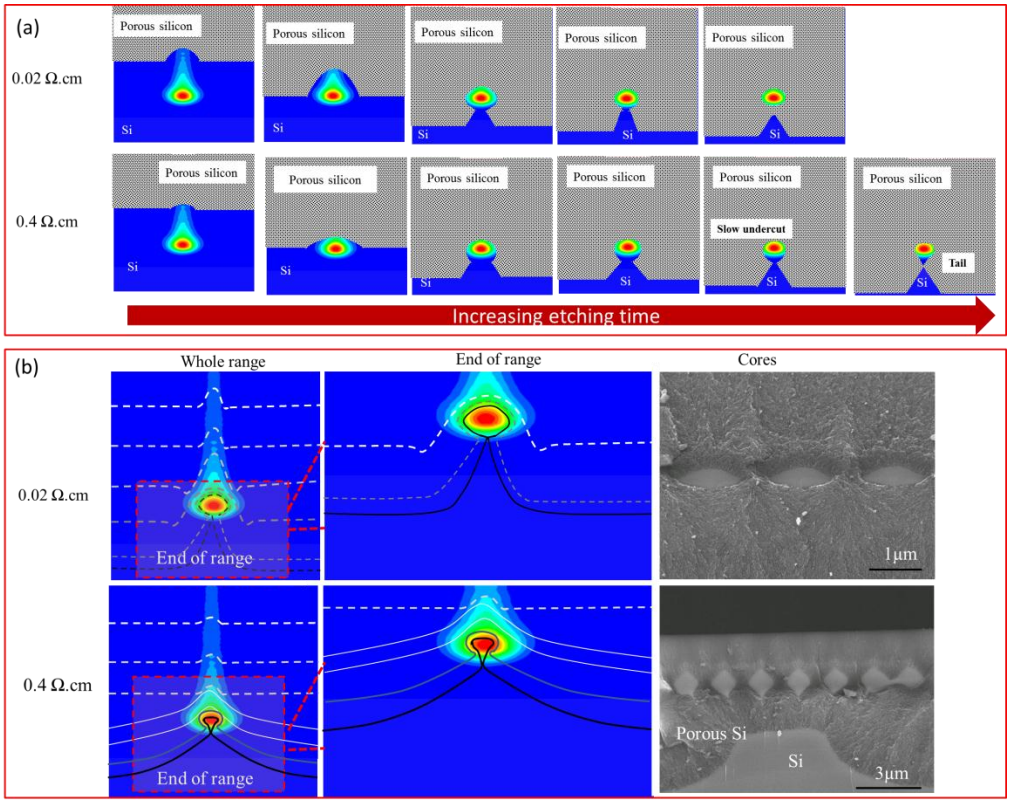

Figure 5.5 (a) Time evolution of etching front; (b) Core formation mechanism and comparison with experimental results: 0.02 Ω.cm wafer (1st row); 0.4 Ω.cm wafer (2nd row).

The selectivity for non-irradiated and irradiated regions in a 0.02 Ω.cm wafer is quite high, such that when the etch front comes to end-of-range region, the step height is so big that a silicon region is easily undercut and isolated, even though the SCR is small, see Figure 5.5. In contrast to 0.02 Ω.cm wafer, the

selectivity for a 0.4 Ω.cm wafer is very low, such that the etch front evolves at a similar rate in irradiated and unirradiated regions. However, SCR width is so large when it comes to the end-of-range region that they easily overlap, resulting in a complete depletion region which is slowly undercut, leaving a tail below the core due to a slowly reduced width of the depletion region see Figure 5.5. This is in contrast with a core with flat lower edge in 0.02 Ω.cm wafer, discussed in section 4.6.5 and shown in the most right column as comparison. Therefore, the width and height of end of range cores are determined not only by the straggling determined by ion energy and ion type, as mentioned in chapter 2, but also the wafer resistivity, ion fluence and etching conditions. Therefore, even though the lateral and longitudinal straggling is equivalent for certain ion type and ion energy, the width and height of the cores are not necessarily the same, as discussed below. Since the current flow is partly deflected from the irradiated regions, the etch front is moving slower than in irradiated regions than unirradiated regions. This gives rise to the silicon mount below in the right lower image.

Table 5.1 Importance of two factors in different wafers and different core shapes

Factors	**0.02 Ω.cm**	**0.4 Ω.cm**
Selectivity	Dominant	Trivial
Space charge region	Trivial	Dominant
Core shape	Flat lower edge	Tail at the lower edge
Number of ions	Total number of ions	Local defect density

The shape is also determined by the ion fluence, ion energy, and etching current density, etc. With increasing fluence, selective etching of non-irradiated regions becomes more obvious in a low resistivity wafer (0.02 Ω.cm), such that a trapezium-shaped core with a flat upper edge. When the ion energy increases, selective etch becomes more important, such that the difference in shape between the two wafers becomes more trivial. When the etch current density increases, the width of the space charge region decreases, such that the tail is shortened for 0.4 Ω.cm wafers, as in Table 5.2.

Table 5.2 Role of selectivity and SCR according to different experimental conditions

Factors	Ion fluence	Ion energy	Etch current density
Selectivity	Increased	Increased	None
SCR	Increased	None	Decreased

In a 0.4 Ω.cm wafer, the core width W_{core} depends on the defect density in the final silicon core. In comparison, in a 0.02 Ω.cm wafer, W_{core} depends on the size of defect contour at the time the core is undercut.

Table 5.3 Dependence of core width and core height on different effects for two different resistivity wafers

Core size	Width	Height
0.02Ω.cm	Defect contour size	Accumulated step from low defect column
0.4Ω.cm	Local space charge region width	Local space charge region width

The core in 0.02 Ω.cm wafer follows the contour shapes of ion distribution as calculated in the left of figure while it is not in 0.4 Ω.cm wafers, Figure 5.6.

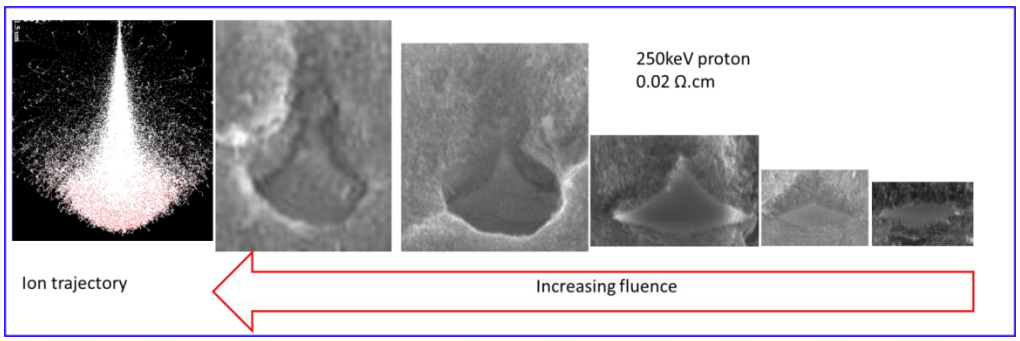

Figure 5.6 (Left) SRIM calculated ion distribution of 250keV proton in Si; (Right) Cross section SEM image of cores in 0.02 Ω.cm wafers versus fluence of 250 keV protons

Mathematical derivation based on their different core formation mechanism in wafers with two different resistivity can provide more information on the core shape. In the following text, core width is W_{core} and core height is H_{core}, Φ is the ion fluence, E the ion energy, J the etch current density.

In 0.02 Ω.cm wafer, assume that the core is undercut with contour n exposed, and t is the time when the etch front at a non-irradiated region is at the same depth with the lowest edge of the high defect region at irradiated regions, shown in Figure 5.7.

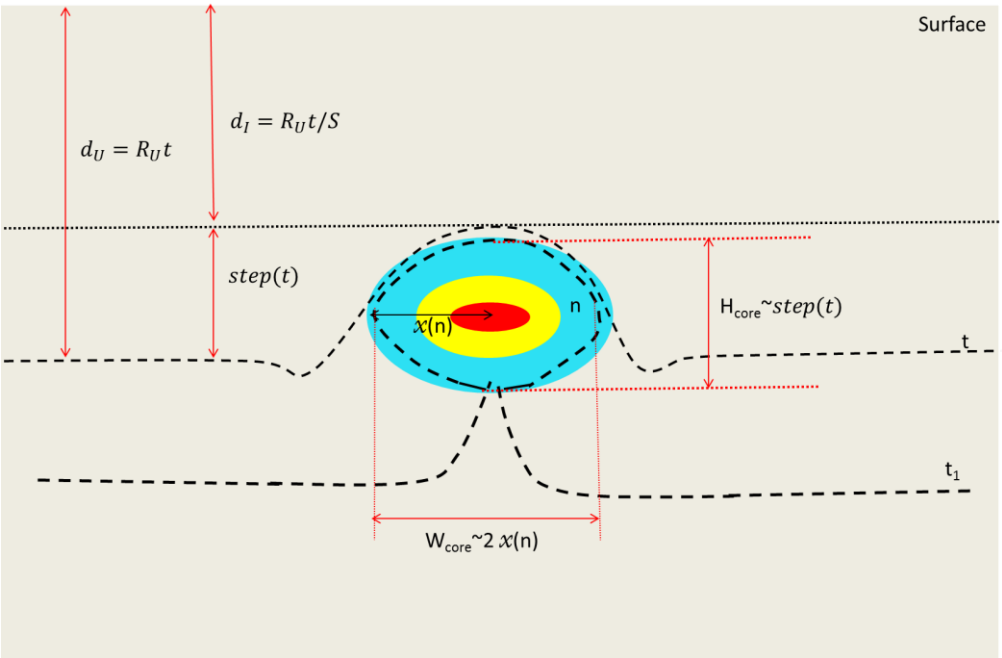

Figure 5.7 Schematics showing the derivation of core size in 0.02 Ω.cm silicon wafer

$$W_{core} = 2\,x(n) \qquad 5\text{-}1$$

x(n) is the size of contour n (shown by light blue color contour) in the high defect region.

$$H_{core} = step(t) - \int_t^{t_1} \frac{1}{S(t)} R(t)dt \approx step(t) \qquad 5\text{-}2$$

Since the selectivity coefficient S→ ∞ after t.

$$H_{core} = R_U[t - \int_0^t \frac{1}{S(t)} dt] \quad 5\text{-}3$$

It mainly depends on accumulated step from selective etch of non-irradiated region along low defect region.

In 0.4 Ω.cm wafer, t is the time when the space charge regions from both sides overlap at the interface of irradiated region, W(t) is the SCR width at t at the interface, θ is the angle between vertical line and the normal of etch front, shown in Figure 5.8.

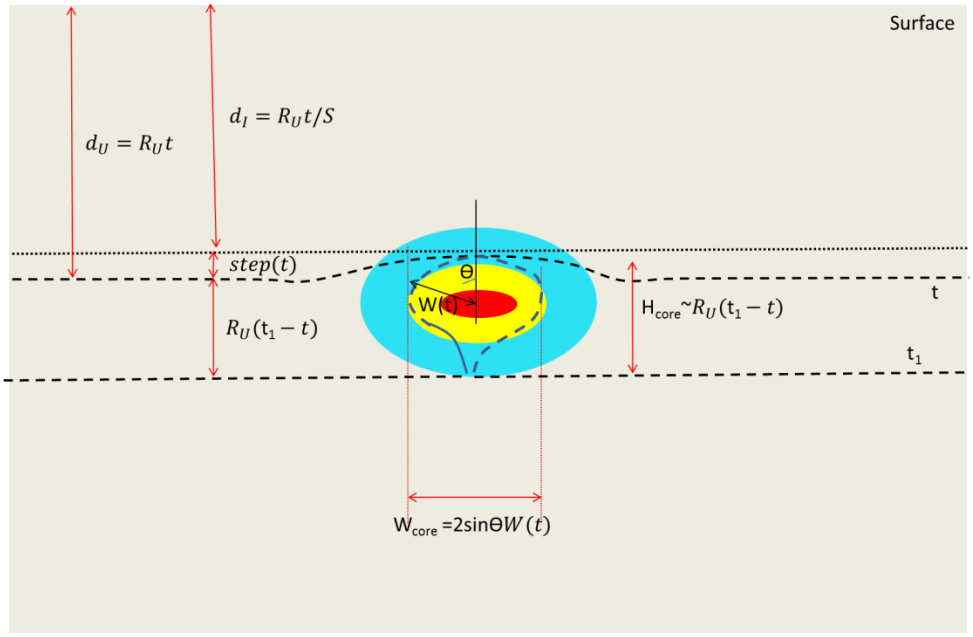

Figure 5.8 Schematics showing the derivation of core size in 0.4 Ω.cm silicon wafer

$$W_{core} = 2\sin\theta W(t) \quad 5\text{-}4$$

According to equation 5-4 and the equation of space charge region[75],

$$W_{core} = 2\sin\theta \sqrt{\frac{2\varepsilon V}{eN_{eff}(t)}} = 2\sin\theta \sqrt{\frac{2\varepsilon V}{e(N_{A0} - f * \Phi * \nu(t))}} \quad 5\text{-}5$$

It mainly depends on the defect density at the interface at time t. The etching front moves forward, and finally meet at t_1.

$$H_{core} = step(t) + \int_t^{t_1} R_U(t)dt \approx \int_t^{t_1} R_U(t)dt = R_U(t_1 - t \quad 5\text{-}6$$

In this equation, $step(t) \approx 0$ due to the small selectivity for 0.4 Ω.cm wafers. Since it is an isotropic etching, the etched layer thickness in vertical direction and horizontal direction is the same. That is, $R_U(t_1 - t) \approx W_{core}$, therefore, according to equation 5-6,

$$H_{core} \sim W_{core} \quad 5\text{-}7$$

The discussion above explained the clear difference in the shape of the cores, a high selectivity in 0.02 Ω.cm wafers produces a wide and short core, while a wide space charge region in 0.4 Ω.cm wafer produces a tail-like core with equivalent width and height. The effect of different factors will be discussed respectively in the following sections, in each of which only one factor is variable, while other factors are constant.

5.3.2 Influence of fluence on cores

The most important parameter governing core formation is the ion fluence Φ. Figure 5.9(a) shows the cross section of cores, where a direct nanobeam patterning using 1MeV protons produced buried Si wires in multilayer p-Si.

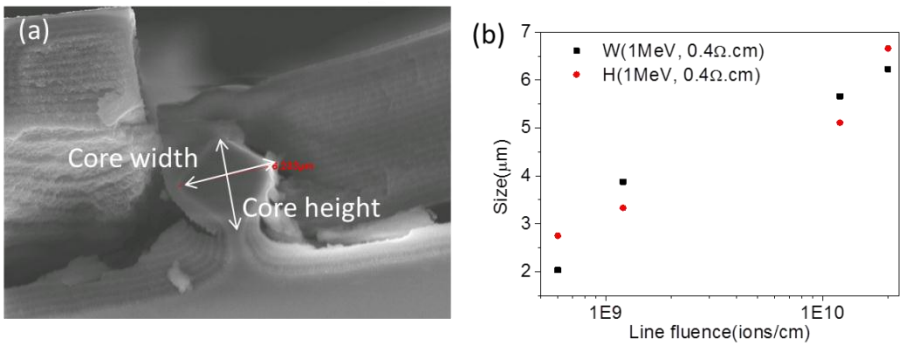

Figure 5.9 Influence of fluence on cores in 0.4 Ω.cm wafer. (a)Cross section SEM images of cores in 0.4 Ω.cm wafer from 1000 keV protons with fluence of $2x10^{10}$/cm; (b) Variation of core width and height with respect to line fluence.

The shapes of the cores resulting from 1 MeV proton irradiation in 0.4 Ω.cm wafer are all diamond-like. Varying the fluence does not significantly change

the shape, except for the aspect ratio. Figure 5.9(b) plots the variation of core size vs. Φ, showing the same order of width and height, matching with equation 5-7.

According to equations 5-4, 5-5,

$$W_{core}(\Phi) = 2\sin\theta\sqrt{\frac{2\varepsilon V}{e(N_{A0} - f*\Phi*v(t_2))}} = c_1\frac{1}{\sqrt{1-c_2\Phi}} \quad 5\text{-}8$$

c_1 and c_2 is constant when Φ is the only variable.

According to equations 5-7, 5-8,

$$H_{core}(\Phi) \sim W_{core}(\Phi) = c_1\frac{1}{\sqrt{1-c_2\Phi}} \quad 5\text{-}9$$

Figure 5.10 shows cross sectional images of Si cores buried in multilayer p-Si produced by using direct nanobeam patterning with 250 keV protons with decreasing ion fluence in 0.02 Ω.cm wafer. The shape of the cores strongly varies with fluence. At medium fluences as in (c)~(f), the cores are flat short, while increasing the fluence, it grows taller and narrower on the top edge, becoming as in (a), (b), while on decreasing the fluence, the top edge is flat, and lower edge is narrower, as in (g); while decreasing the fluence more, no core is formed, as in (h). It is evident in all the etched cross section a faint white line is visible below the core, which is formed during the undercut of the cores. When the core width is wider (for example, a larger beam size, a larger lateral straggling due to a higher ion energy) or etching selectivity is not so high (for example, a lower ion fluence), the undercutting process takes a longer time, and this white line is more visible. Figure 5.11 shows variation of H_{core} and W_{core} vs. Φ. The core is not a perfect square, so the core width and core height do not have particular values, and the data points plotted in the figure have certain errors depending on the core shape.

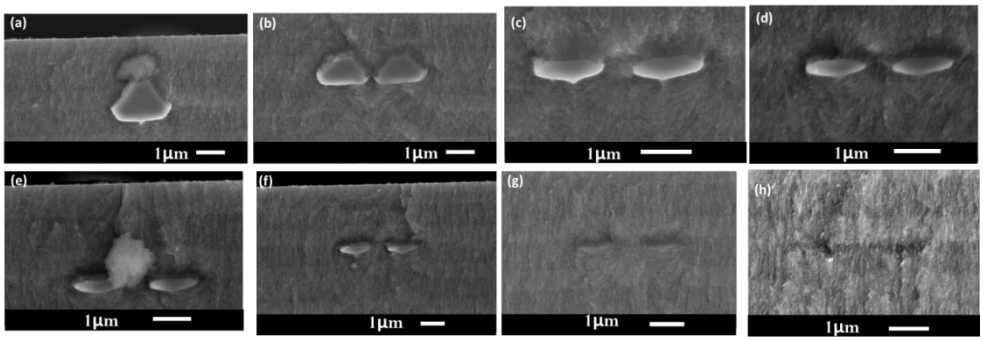

Figure 5.10 Influence of fluence on cores in 0.02 Ω.cm wafer. Cross sectional SEM images of cores in 0.02 Ω.cm wafer with 250 keV protons with fluence of (a)5x10^{11}/cm, (b)3x10^{11}/cm, (c)1x10^{11}/cm, (d)8x10^{10}/cm, (e)6x10^{10}/cm, (f)5x10^{10}/cm, (g)2x10^{10}/cm, (h)1x10^{10}/cm.

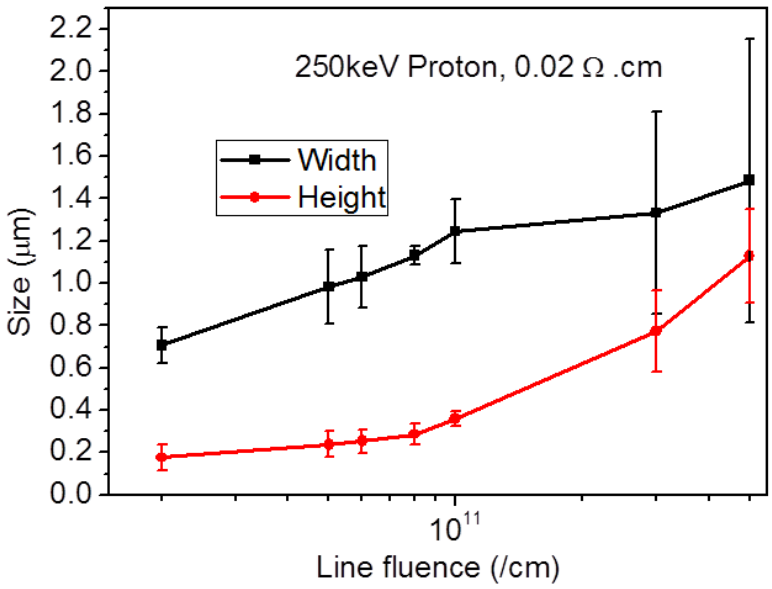

Figure 5.11 Core width and height with respect to the line fluence in Figure 5.10(0.02 Ω.cm wafer)

According to equation 5.3, $H_{core}(\Phi)=R_U[t-\int_0^t \frac{1}{S(t,\Phi)}dt]$, with increasing Φ, S increases significantly, and H increases sharply. According to equation 5.1, $W_{core}(\Phi) = 2x(n(\Phi))$, with increasing Φ, n increases, $W_{core}(\Phi)$ increases, however, the change is small since even within the adjacent contour defect

density changes a lot. Therefore, the core height has much more significant change with fluence compared to the width for a 0.02 Ω.cm wafer.

5.3.3 Influence of ion energy on cores

With increasing ion energy, the depth of the end-of-range region increases, and selective etching of non-irradiated regions becomes more important. Furthermore, ion scattering increases as discussed in section 2.3, such that the defect density within the high defect region for the same ion fluence is lower.

In 0.4Ω.cm wafers: according to equation 5-5,

$W_{core}(E) = 2\sin\theta\sqrt{\frac{2\varepsilon V}{e(N_{A0}-f*\Phi*\nu(t(E))}}$, where only t and ν is dependent on energy. With higher E, to have equal ν, the contour is more inside, $W_{core}(E)$ is smaller. The same is for height. Therefore, to have the same core size for a higher E, a much higher fluence is needed. Therefore, with the same ion fluence and other conditions, higher energy ions produce narrower and longer cores in 0.4 Ω.cm wafers.

In 0.02 Ω.cm wafers: according to equations 5-1, 5-3, $H_{core}(E) = R_U[t - \int_0^t \frac{1}{S(t)}dt]$

$t_2(E) = \frac{R_i(E)}{R_{UN}}$, where $R_i(E)$ is the ion range,

To simplify that S is a constant along the depth,

$$H_{core}(E) = R_U\frac{R_i(E)}{R_U}\left(1-\frac{1}{S}\right) = \left(1-\frac{1}{S}\right)R_i(E) \quad 5\text{-}10$$

Therefore, the height of core increases significantly with the ion energy in 0.02 Ω.cm wafers.

Besides, due to straggling at the end of range regions as mentioned in chapter 2, the minimum core size is determined not by the beam size at the irradiated sites, but by other factors, mainly ion energy. For example, 50keV protons were used to fabricate free-standing nanowires with diameters below 50nm,[53] while higher energy protons were used to fabricate much thicker wires.[24]

5.3.4 Influence of etch current density on cores

Figure 5.12 and 5.13 shows the influence of increasing etch current density on the cores in wafers with both resistivity. It used direct nanobeam writing with 250 keV protons.

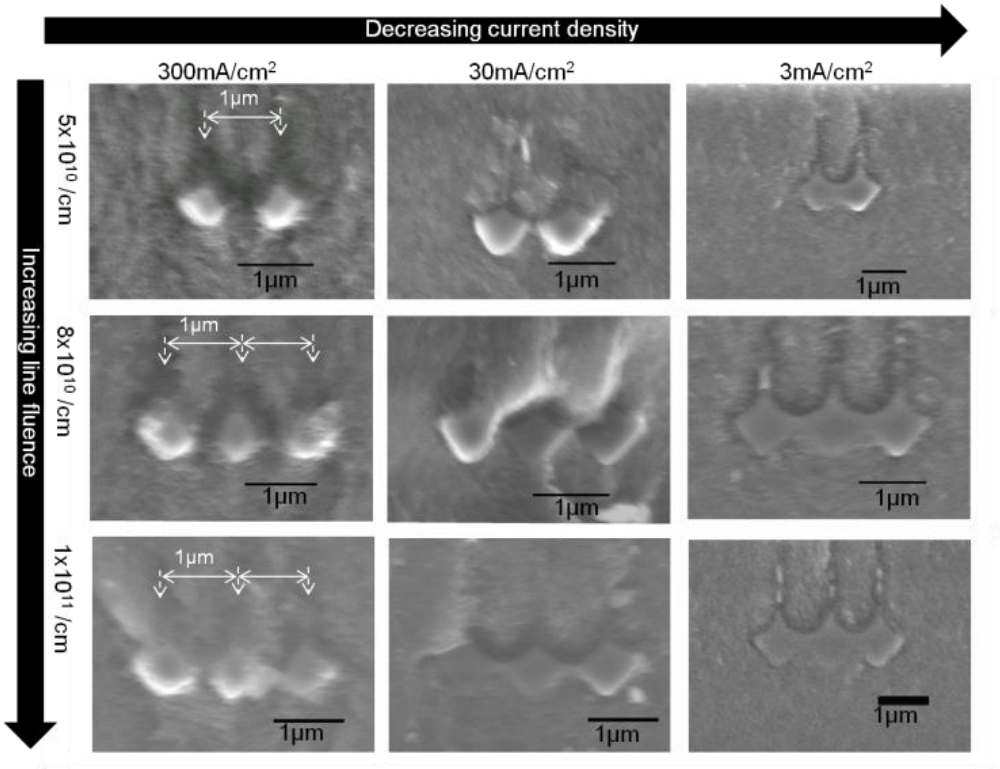

Figure 5.12 Influence of etch current density on cores in 0.02 Ω.cm wafer. Cross section SEM images of cores produced by 250 keV protons in 0.02 Ω.cm wafer for varying the line fluence and etch current density

A consistent observation with the studies in section 4.6.3, smaller cores as well as smaller minimum gap are achieved with a higher current density in both wafers. For example, for the same fluence $5x10^{10}$/cm, cores are connected at 3 mA/cm^2, while separate on increasing the current density to 30 and 300 mA/cm^2. [54]

An obvious change in 0.4 Ω.cm wafer is that the lower part of the core, the tail becomes shorter on increasing the etch current density, due to the reduced SCR width.

Extracting the values of core width from Figure 5.12, figure below plots this value vs. J.

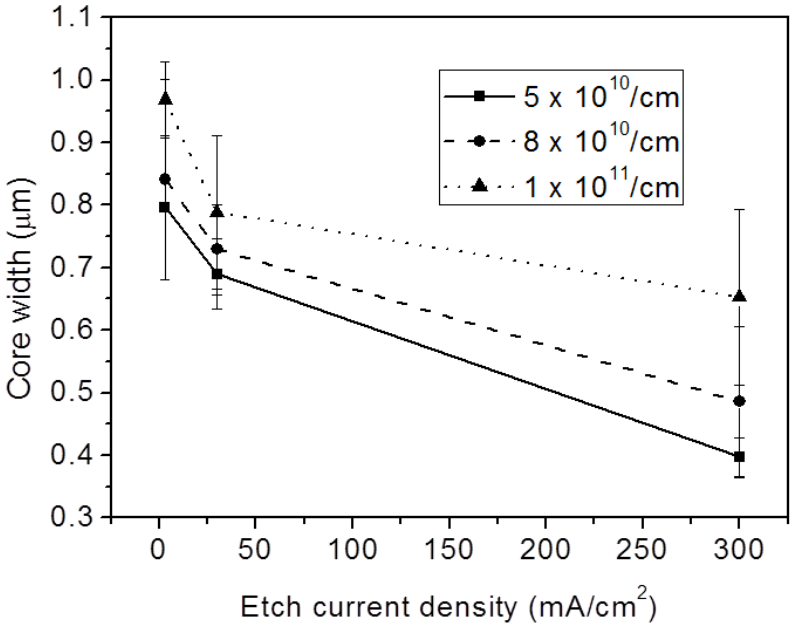

Figure 5.13 Variation of core width with respect to current density for different line fluences in Figure 5.12

In 0.02 Ω.cm wafers, H_{core} (J)$= R_U t - R_{UN} \int_0^t \frac{1}{S(t)} dt$, the first item is not related to J, while in the second item, R_U increases significantly with J. Thus H decreases with increasing J. The same for W_{core}. In 0.4 Ω.cm wafers, a higher J leads to lower V(J) and smaller W_{core}(J). The same is for the height. Besides, for 0.4 Ω.cm wafers, a lower J produces a lower undercutting of the tail, producing a longer tail.

5.3.5 Influence of etching mode (AC/DC) on cores

Apart from the variation with etch current density, the etching mode can also be changed between direct current and alternate current. The aim of using an AC current is to significantly reduce the effect from capacitor, which was earlier discussed in chapter 3.

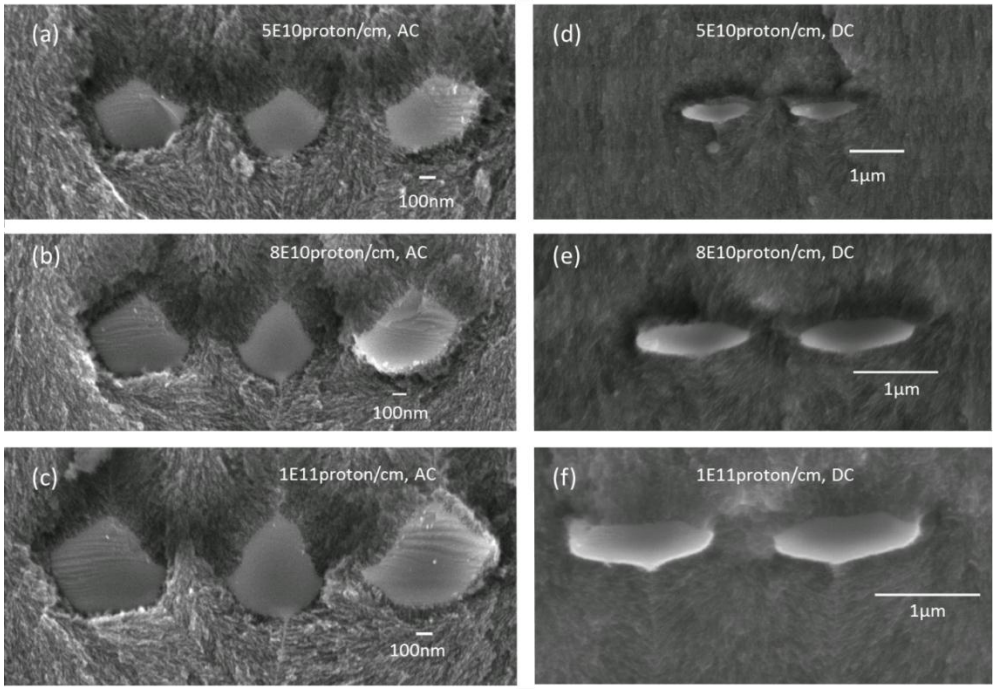

Figure 5.14 Comparison between AC and DC etched end of range cores in 0.02Ω.cm wafers for three ion fluences

Figure 5.14 shows cross sections of cores produced using direct nanobeam patterning method with 250 keV protons with the same ion fluence and energy, but different etching mode. Even though the etch current density is different, the significant difference in core shape mainly arise from the different etching modes. By using AC etching mode with frequency of 100 Hz, the central part of the cores in 0.02 Ω.cm become more circular instead of flat short cores, which indicates that selectivity becomes less important in AC etching mode.

5.3.6 Influence of "environment" on cores

All these factors mentioned above only consider single irradiated features (though many of the examples given show several adjacent features). However, the formation of cores also depends on its "environment". When the spacing between two irradiated points/lines becomes small, such that the

current flow between them is influenced by both regions, core size and shape also depends on the defect distribution of its neighbors.

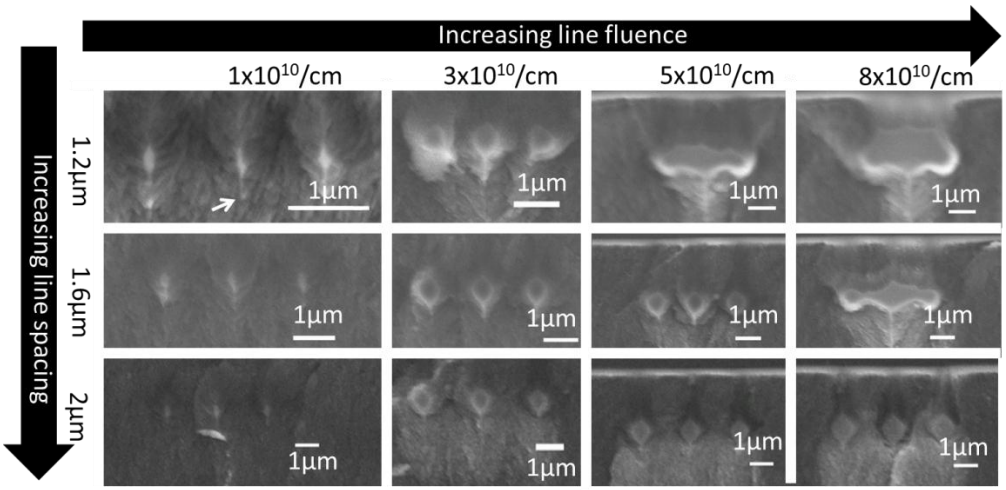

Figure 5.15 Influence of spacing on cores. Cross sectional SEM images of cores produced by 250keV protons while increasing ion fluence and line spacing, while keeping a constant etch current density

The direction of the tail is a very good indication of current flow in 0.4 Ω.cm wafers, such as the slanted tail of cores on either side for $3x10^{10}$/cm with 1.2 μm spacing in Figure 5.15 which indicates a deflection of current from the whole irradiated area. The influence of ion fluence on minimum spacing achievable will be discussed later. Here, direct nanobeam patterning using 250 keV protons produced wires with different spacing and ion fluences. By extracting the value of core widths, and plotting with respect to the spacing, it indicates that the core size decreases with a smaller spacing between adjacent lines when the cores are still resolvable. Figure 5.16 shows this effect, where the core size reduces with decreasing spacing, which is due to a stronger local J.

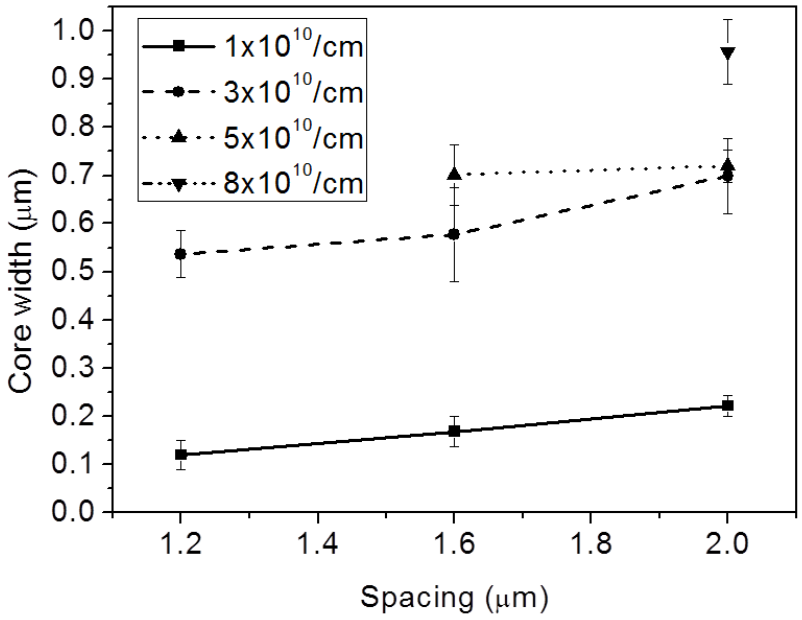

Figure 5.16. Variation of core size with respect to line spacing for results in Figure 5.15.

Another point worth noticing is that for a lower fluence the core size increases more rapidly with spacing. This can be explained by the importance of the built-in potential in this wafer, which is so large that the hole current is deflected away from the whole irradiated region such that the local J does not increase so much. Therefore, cores in the middle are smaller when they are not so close and the fluence is not so high. Also cores on the outer edge are smaller when they are close and the fluence is quite high, as observed in Figure 5.15.

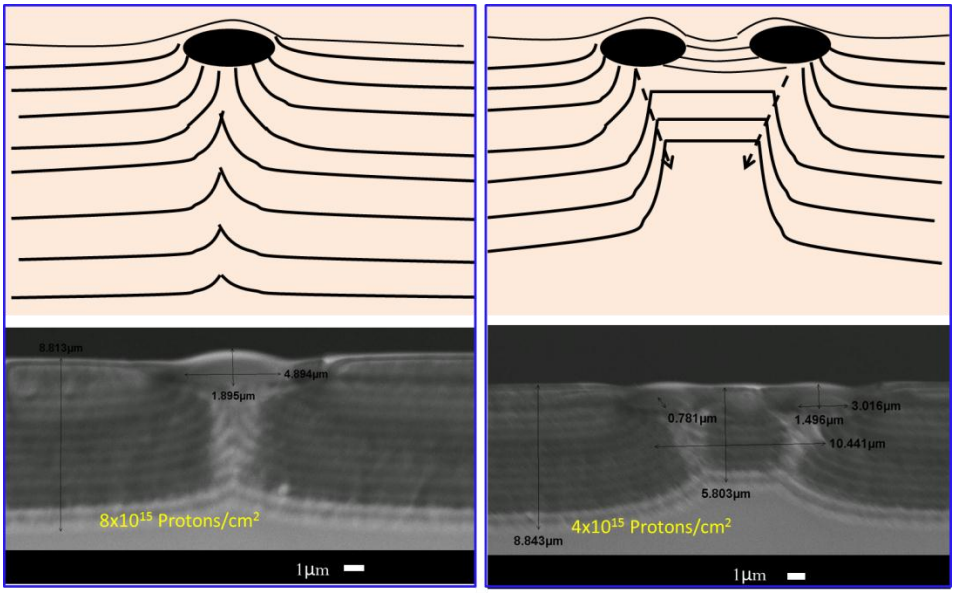

Figure 5.17 Etch front evolution of single and two closely spaced lines. 250 keV proton line irradiation in a 0.02 Ω.cm wafer, etched with periodic high/low current density to observe the evolution of the etch front: Left single line with fluence 8 x10^{15}/cm^2; Right: two lines with 10 µm spacing, with fluence 4x10^{15}/cm^2

When adjacent features interact together, the region between closely spaced regions also has a reduced etch rate as illustrated in the 1st row of Figure 5.17, even though this region is not irradiated and has no defects. Due to this, the etch front after undercutting the cores moves closer together, as shown by the arrow (right), instead of the straight etch front in single core case (left), or cores with a larger spacing. Therefore, the core on the outer edge is usually not symmetric when the spacing is small.

All the discussions in this section on the "environment" are limited to cores at the same depth; however, for cores of different depth it is even more complicated. It is necessary to analyze the overall and local "environment" of each wire and get the proper design for final current flow, to form structures for particular applications.

5.3.7 Minimum spacing between features

The above discussion focused on core size, while another specification is the minimum gap achievable, which is important in the application context of coupling different photonic components. Figure 5.15 shows that the minimum spacing between adjacent wires decreases with decreasing ion fluence, for

example, the minimum spacing for $8x10^{10}$/cm is 2 μm, for $5x10^{10}$/cm is 1.6 μm, and for $3x10^{10}$/cm is ≤ 1.2 μm, as plotted in Figure 5.18.

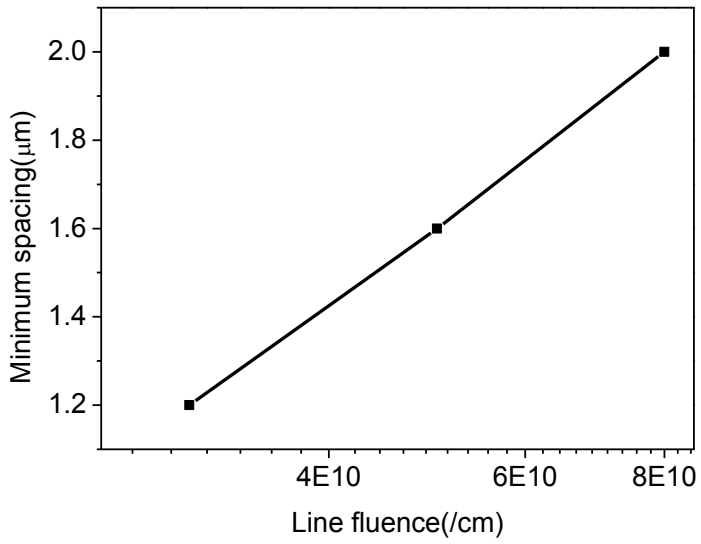

Figure 5.18 Minimum spacing for different ion fluences for 250keV proton in 0.4 Ω.cm wafers

The minimum spacing is firstly limited by the straggling of the ions at the end of range regions, as mentioned in chapter 2. Lower energy ions have less straggling, and should be chosen when a small spacing is necessary. However, the minimum spacing is not only limited by the straggling of ions, but also the current flow mechanism. As shown in Figure 5.18, the selectivity between two closely spaced features is not zero, and has a reduced etching rate. In the case of 0.02 Ω.cm, when this effect is so obvious that the lines cannot be separated even when the whole irradiation area is undercut completely, the wires merge together. In a 0.4 Ω.cm wafer, even though this effect is not so dominant, a large built in potential from the whole area is so high that current tends to bend around the whole irradiated area rather than passing between closely spaced adjacent features.

The minimum spacing is between the centers of adjacent features, however, another concept of a minimum gap between cores is the distance between cores, which does not necessarily happens at a minimum spacing case. Minimum gap = Spacing - Core width, in 0.02 Ω.cm wafer, the cores tend to

be flat and wide, such that a much smaller minimum gap is available than in a 0.4 Ω.cm wafer.

Therefore, to this extent, we can draw the conclusion that to fabricate extremely thin wires, a 0.4 Ω.cm wafer is favorable, while to obtain extremely small gaps, a 0.02 Ω.cm wafer is recommended.

5.4 Control the core shape

Therefore, according to a variety of factors that affect the core shape and size, it is possible to regularize the core shape, which is important in relevant applications, such as waveguides, photonic crystals, etc. Regularizing the core shape means to make core more regular in shape, like a circle or trapezium, rather than extended tail above or below the core.

There are several different points worth noting for regularization of core shape.

To vary the etch J at the proper etch time to change the etch front;

To design proper “neighbours”, to tune the current flow and core shape;

To choose the right resistivity and etch mode to get proper shape.

Conclusion

Time evolution is investigated in this chapter to understand the core formation process, which complements the study in chapter 4 on the current flow mechanism. Dominance of either selectivity or depletion region width leads to different core formation processes in two types of resistivity wafers. In the core formation regime of 0.02 Ω.cm wafers, due to extremely higher selectivity and relatively narrower depletion region width, selectivity plays a major role in forming a flat low-edge silicon core. Since the etching front of the unirradiated region is already at the same depth level as the lower edge of high defect region when the etching front reaches the high defect region, a silicon region is easily isolated in further etching. In core formation in 0.4 Ω.cm wafers, due to a large depletion region width and extremely low selectivity, the depletion region plays a major role in forming a tail-like silicon core, since in this case the etch front in irradiated and unirradiated regions move almost together. A core forms when the defect density at the etch front of the irradiated region is high enough to create a depletion region which remains unetched, and a silicon region is slowly completely undercut and isolated. A better understanding of such mechanisms enables an easier manipulation of shape, size, minimum gap in fabrication of silicon nanowires and photonic devices, and further applications which is discussed in chapter 6 and 7.

Chapter 6 . 3D structuring

The previous chapter discussed the mechanism of core formation and the factors that are important for obtaining the proper shape, width, height, spacing, and gap. Core formation is the central aspect to true 3D structuring of Si, and it is one of the advantages of our method compared to conventional approaches. This chapter presents experimental results on structuring of p-Si and glass, where glass structuring is realized based on oxidation of structured p-Si with a proper porosity. The first section discusses bulk micromachining of Si where a variety of types of structures and methods are introduced. The last two sections discuss new fabrication methods on structuring p-Si and glass based on the basic mechanism of chapter 4.

6.1 Si bulk micromachining method

There are two main steps in 3D Si micromachining using ion beam irradiation combined with our electrochemical etching process. Building up a localized defect distribution by ion beam irradiation in designed patterns is the first step. There are two ways to do this. The proton beam writing beam line in CIBA allows focusing of proton or helium beam with energies from 100 keV to 2 MeV, to beam sizes in both directions of 50~100 nm, with a beam current of tens to hundreds pAs. The focused beam is scanned over the Si surface with pre-designed patterns, Figure 6.1(a), referred as "direct nanobeam patterning" in the text in previous chapters. The other method is to fabricate patterns on polymer or metal using standard UV lithography or electron beam lithography, and electroplating techniques, referred as "projection through mask". Then a large area ion beam is irradiated passes through the pattern and a defect distribution is formed in p-type Si wafer, Figure 6.1(b). The advantage of second method is mass production and large area structuring, which is simply achieved by conventional lithography and large area ion beam irradiation in CIBA. Earliest work on masked exposure of protons in materials is [43]. It is much less time consuming and more efficient. However, the resolution is limited by the diffraction limit of UV lithography; whereas on the other hand, e-beam lithography cannot penetrate thick photoresist due to its low energy and large scattering. Therefore, the first method of proton beam writing has significant advantages for producing structures with high aspect ratio and high resolution at the same time.

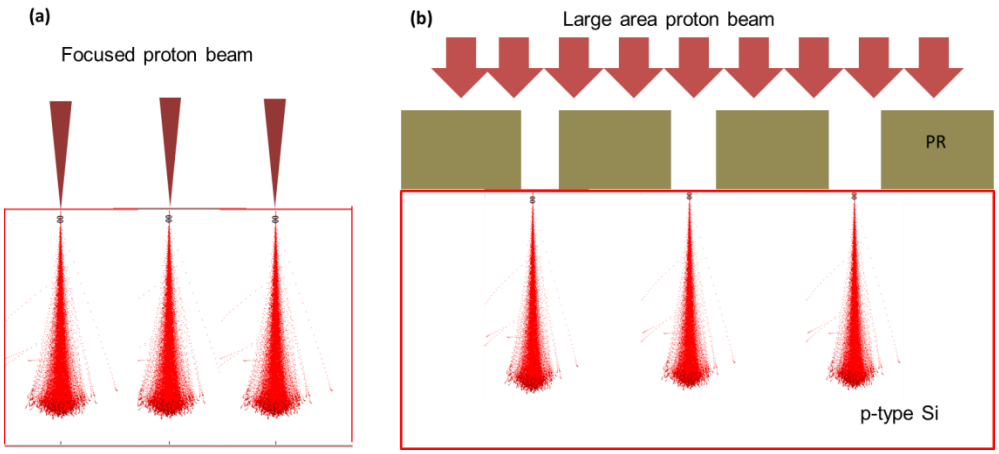

Figure 6.1 Two irradiation methods. Schematic of two methods: (a) Proton beam writing and defects from SRIM calculation by focused proton beam patterning in Si; (b) Large area irradiation through patterned mask and defects from SRIM calculation to build patterns in Si.

In these two ways, defects are generated, as in the first row of Figure 6.2. The second step is electrochemical etching, where due to modulation of the hole current by the introduced defects, porous silicon selectively forms, as illustrated in the second row of Figure 6.2. Si structures are buried within p-Si after the second step; a further step of removing the p-Si by a simple dip in diluted KOH solution is needed. The three columns in Figure 6.2 represent three most common structure types, where in the left column a single high energy ion beam with high fluence totally stops p-Si formation in irradiated regions and produces high aspect ratio pillars or walls. In the middle column, a high energy ion beam with a high fluence produces walls to serve as supports for free-standing wires which are fabricated at high defect regions of lower energy ion beam with moderate fluences, discussed in chapter 5. In the rightmost column, the formation of multiple level Si wires using two different low energy ions is shown.

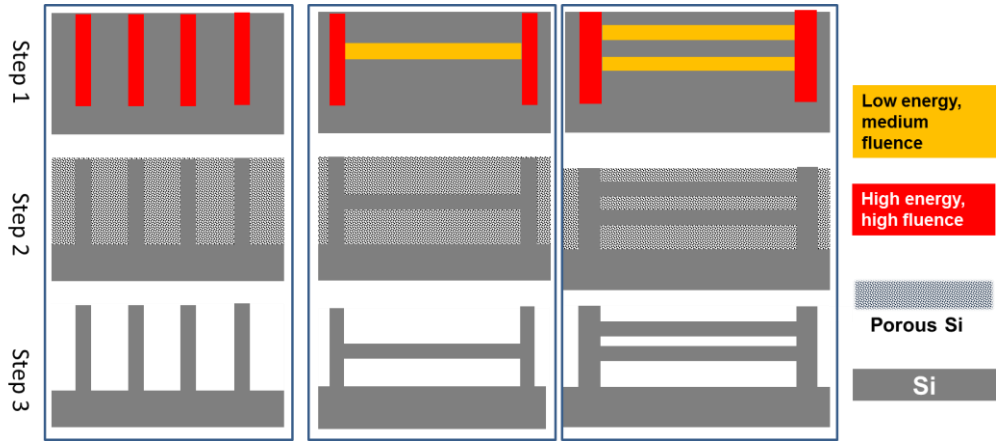

Figure 6.2 Procedure of 3D Si micromachining in cross sectional view. (1st row) Step 1: Ion beam irradiation and defect distribution; (2nd row) Step 2: Electrochemical etching and p-Si formation selectively; (3rd row) Step 3: Removal of p-Si and formation of three type of Si structures: (1st column) Walls or pillars; (2nd and 3rd column) Free standing single of multiple level wires.

Based on the procedures discussed above in figure 6.2, the following Si structures have been fabricated.

6.2 Si bulk micromachining results

6.2.1 Si walls and support structures

A high fluence produces Si walls where the etching in irradiated regions can be completely stopped. Figure 6.3 shows an example of fabricating Si walls with direct nanobeam patterning method, using 2 MeV H_2^+, with a fluence of $2x10^{13}$ protons/cm to irradiate a 0.02 Ω.cm wafer with lines of 2 µm width and 20 µm spacing. The structure area is 400 µm x 400 µm. Figure 6.3(a) shows the top view of the Si walls, and (b) shows a tilted view, while (c) shows a magnified image of (b). The top surfaces of these walls are not very smooth which indicates some etching of the irradiated regions after a long etch depth in spite of the high defect density at these regions.

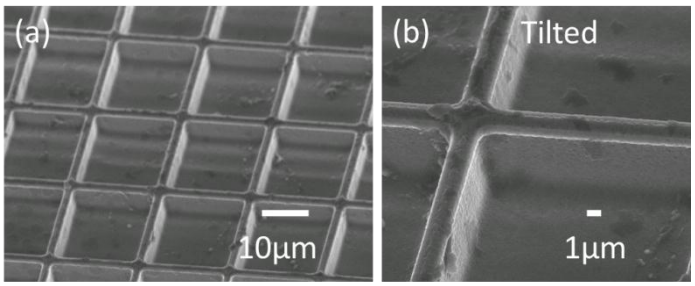

Figure 6.3 Si wall structures. Si walls with a spacing of 20 µm, width of 2 µm and area of 400 µm. (a) shows the tilted view, while (b) is magnified image of (a).

Such Si walls have been used as supports for free standing Si wires as in Figure 6.4(b). Focused 2 MeV H_2^+ is used to write wires with a line fluence of $1x10^9$ protons/cm, and focused 2 MeV protons with a fluence of $2x10^{13}$ protons/cm are used to write supports. The sample was etched at 40 mA/cm^2 in 24% HF for 21 mins and p-Si removed by KOH solution, oxidized at 1000 ^oC for 2 hours in ambient condition, and oxide was removed.

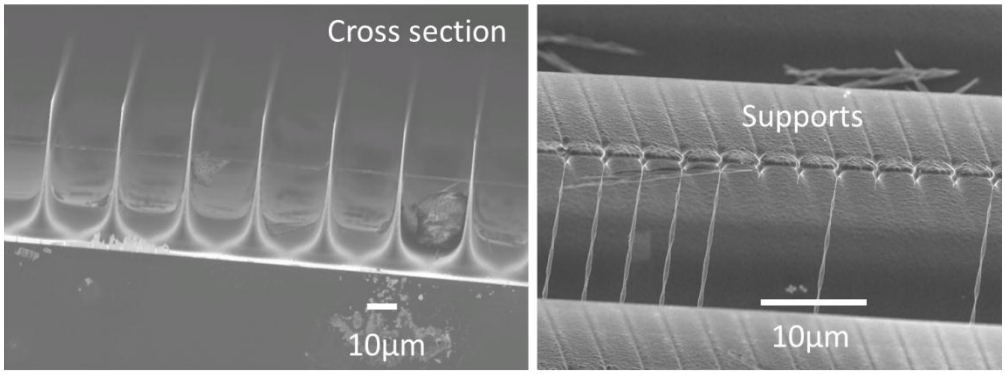

Figure 6.4 Support structures. (a) Cross section of silicon walls; (b) Wires that are supported by Si walls.

High-aspect ratio structures and dense structuring is necessary for many applications. However, to achieve both is difficult, for which the main reason is that a fluence which is high enough to stop the low defect column region from being etched produces a large high built-in potential which tends to deflect current away from irradiated regions. There are different ways to reduce this effect. The first way is to use dot patterns instead of line patterns, the other is to use a higher etch current density to overcome the built-in potential as discussed in the previous chapter. The schematics in Figure 6.5(a)-(c) show the procedure of fabricating high aspect ratio structures. In Figure 6.5(d) direct nanobeam patterning using 2 MeV H_2^+ irradiation in a 0.02 Ω.cm wafer generated defects in the Si wafer and the wafer was etched at 60 mA/cm^2 for 2 mins, and then 200 mA/cm^2, for 30 s, 80 mA/cm^2, for 70 s, and at 250 mA/cm^2, for 30s, finally at 60 mA/cm^2, for 30s. The reason for using this etch sequence is to get a thin wall while maintaining a reasonable height, as shown in the inset schematics of Figure 6.5(d). Compared to line irradiation, the built-in potential from point irradiation is smaller, so the anodization current can flow between the patterned points, enabling high aspect ratio pillars with small spacing as shown in Figure 6.5(e).

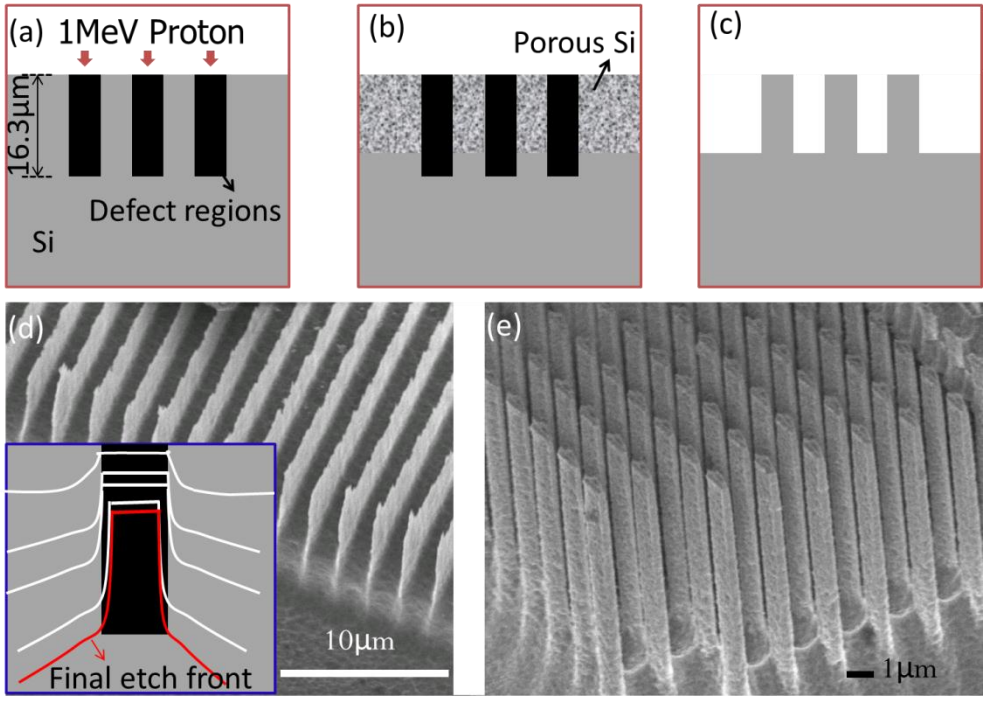

Figure 6.5 High aspect ratio structures. Schematics of fabricating high aspect ratio structures: (a) Irradiation with high fluence, and formation of high defect density columns; (b) selective formation of porous silicon in unirradiated regions; (c) removal of porous silicon and formation of silicon walls or pillars with thick silicon substrate; (d) thin silicon walls with small spacing formed on silicon substrate by applying high etch current density (inset is schematics of etch front movement with time); (e) high aspect ratio pillars with 2µm spacing on silicon substrate by applying point irradiations.

The fluences used in these high aspect ratio structures are in the high fluence regime discussed in chapter 4.

6.2.2 Free-standing wires with uniform diameter

With moderate fluences, Si cores form beneath the surface, as discussed in chapter 5.

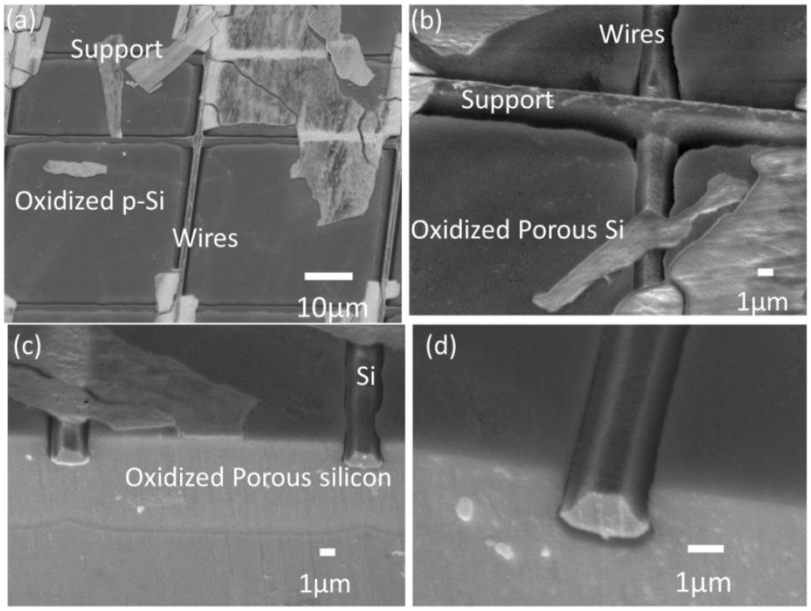

Figure 6.6 Free-standing wires with p-Si partly removed. Wires supported by thick walls and only the highly p-Si surrounding the wires removed and rest of p-Si left: (a) Overview; (b) Magnified image of intersecting parts; (c) Cross section of wire; (d) Magnified image of cross section of wire.

Figure 6.6 shows the Si wires fabricated using direct nanobeam patterning with 500 keV H_2^+ with a line fluence of $5x10^{10}$ protons/cm supported by thick walls fabricated with 2 MeV H_2^+, etched for 3 mins with 40 mA/cm^2. The p-Si surrounding the wires is easily removed by oxidation at 300˚C for 1h, at 1000 ˚C for 2h and removal of oxide in 2%HF for 30 mins, due to its higher porosity (section 4.5). The wire shape shown in (c, d) matches well with that discussed in chapter 4 and has been studied, particularly for applications as waveguides. [28] p-Si is further removed by oxidation and oxide removal, as in Figure 6.7, where the wires (waveguides) become completely free-standing and remaining defects removed. Meanwhile, surface roughness can be reduced, and wires could be made more uniform and smooth. This method was used to improve the properties of the waveguides and to reduce their loss, which will be discussed in section 8.3.

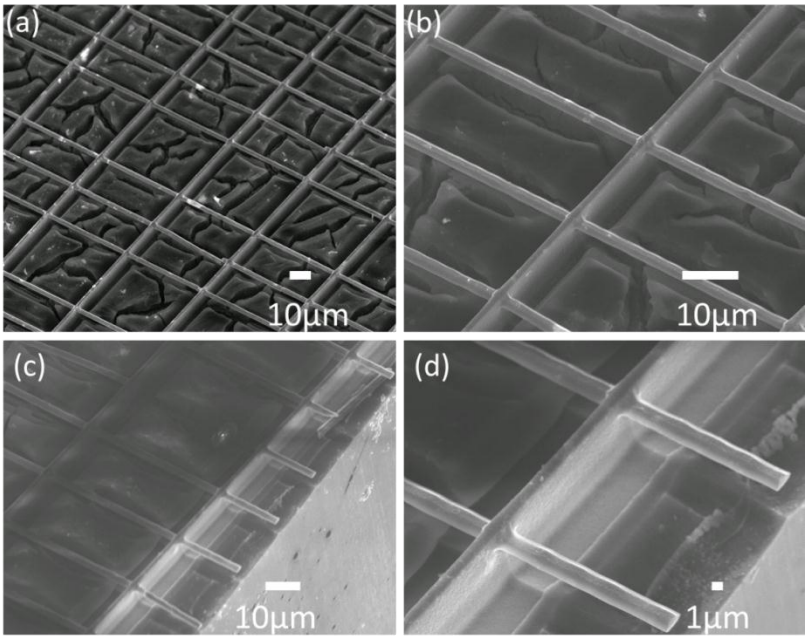

Figure 6.7 Free-standing wires with p-Si completely removed. A further oxidation step to increase the uniformity of structures and remove the defects, and completely make the structures free-standing.

One can reduce the spacing between wires, for example, Figure 6.8 shows free-standing silicon wires supported by thick walls fabricated by 250 keV and 218 keV protons with a spacing of 2, 3, and 4 µm.

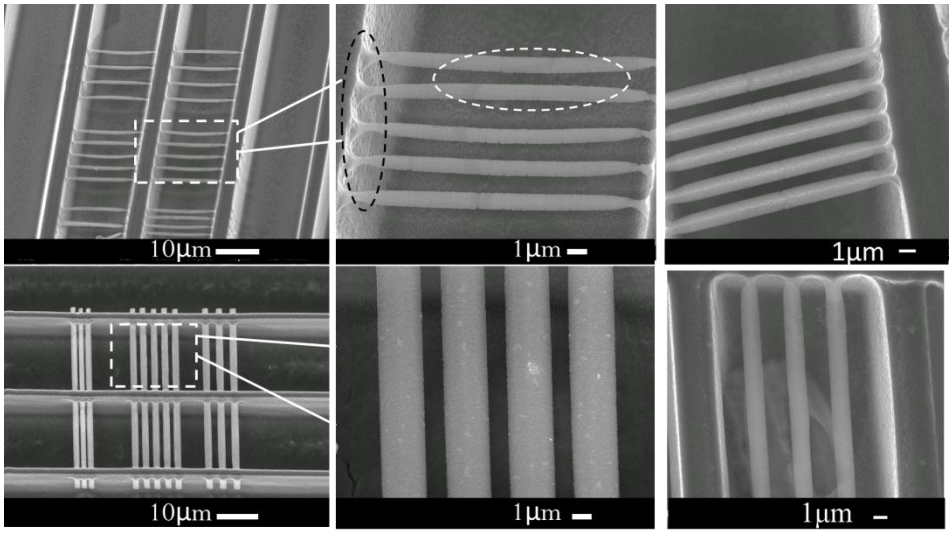

Figure 6.8 Free-standing Si wires. (1st row) 250keV, 1x10^{11}proton/cm; (2nd row) 218keV proton, 1x10^{11} proton/cm.

Interestingly, the connecting part of wires and supports is thinner, as marked by the black dashed ellipse. This is attributed to a higher current density flowing at these sites, since the hole current which is deflected around the solid wall flow through these regions. Such thin connections are likely to be broken by mechanical vibration, or by a thermal oxidation step, such as the broken wires in Figure 6.4(b), and should be avoided when producing well-supported structures. Another interesting point is the attraction between free-standing adjacent wires, marked by the white ellipse in the middle of 1st row of Figure 6.8. The wire in the 1st row Figure 6.8 on the edge is attracted by the wire on one side, consequently the distance between the second wire and the third wire is larger and the attraction of the third wire by the fourth wire is stronger therefore it is closer to the fourth wire. As a result the wires prefer to exist "in pairs", for example in Figure 6.9(a). The attracted parts are marked by a yellow dashed ellipse. The attraction between suspended wires (one side is not supported by the thick wall) is stronger than supported wires (both sides are supported by the thick wall). The attraction by thick wall is also strong, shown in left marked ellipse. This has also happened in polymer lithography. The reason to attraction may be because of remaining charge of the wires after etching, or cooperative effect due to the environment. The reason may also be

capillary force between adjacent wires, and the effect of capillary force on nanostructures has been studied before in Ref [76].

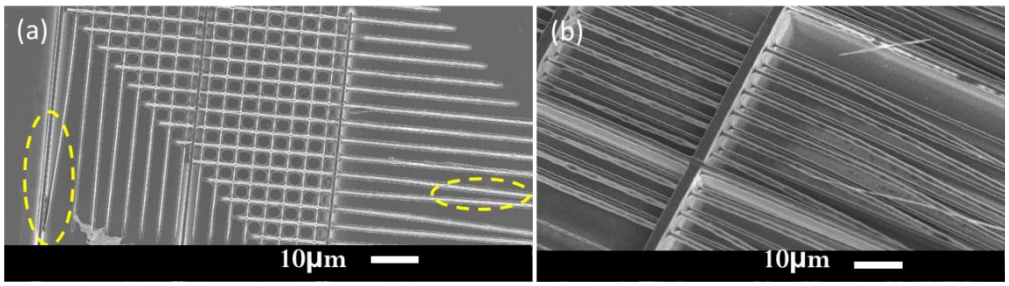

Figure 6.9 (a) Attracted wires to each other or to the walls; (b) Suspended bending silicon wires

Suspended wires demonstrate good elasticity, as shown in Figure 6.9(b), where they are nicely bent and not broken also observed in Ref.[77].

All these free standing wires have a uniform diameter in spite of the roughness induced in the fabrication process. However, a modulated diameter may be required for particular applications, such as Bragg waveguides, which is considered next.

6.2.3 Free-standing wires with modulated diameter & grids

To produce wires with a modulated diameter, there are two methods. The first is to design complex irradiated patterns, and can only be done by using the ion scan mode (refer to Appendix), which has a limited scan area. The other is to irradiate intersecting lines, using the 'line scan' mode (refer to Appendix) integrating stage motion with ion scan, which can achieve a larger pattern area, shown in Figure 6.10. Figure 6.10(a) uses the same energy ions to irradiate horizontal and vertical lines, where the horizontal lines have a lower fluence which is not enough to form a wire, however, at intersecting parts the effect of irradiation in the horizontal direction is to increase the defect density, as in the first image of (b), thus producing vertical lines with increased diameter at these intersecting points after anodization, shown in the second and third image of (b). The structure in Figure 6.10(c) is fabricated using this method. When intersecting lines are irradiated with different energies, the defect density of upper level lines increases such that the same effect is

observed in the upper level wires, see Figure 6.10(d). Only the upper level of wires are modulated while the lower level of wires are not in Figure 6.10(d) simply because the energy for the wires perpendicular is between these two energies, such that the lower level of wires are not affected. However, the structures shown here are some examples, the minimum feature size can go down to 50nm by choosing the ion energy, wafer resistivity and etching current density properly.

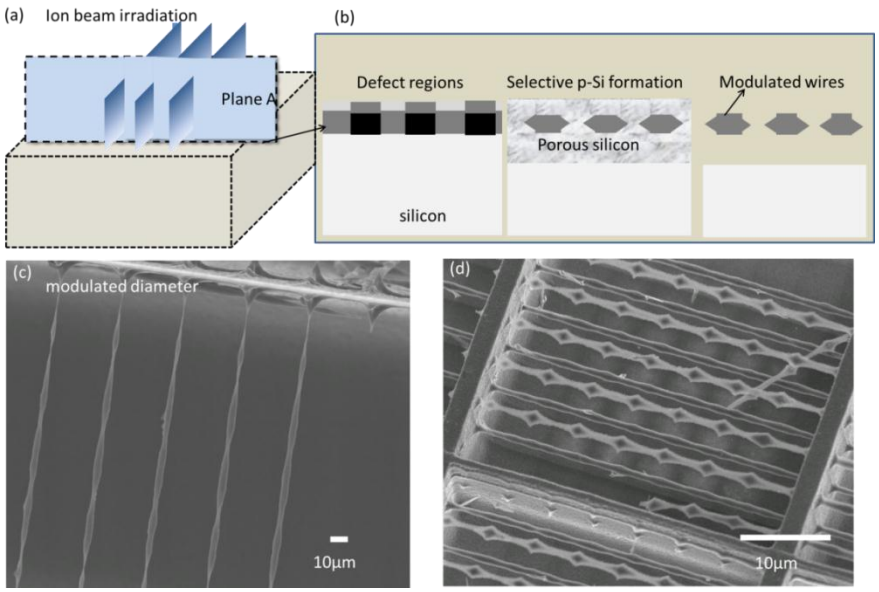

Figure 6.10 Free-standing wires with modulated diameter. (a) Intersecting line irradiation; (b) Cross sectional view along plane A in (a), showing formation of modulated diameter wires; (c, d) SEM images of free-standing wires with modulated diameter.

It is noteworthy that an additional effect is caused by the increased defect density at intersecting parts. Hole current is deflected away from intersecting points and non-intersecting parts have higher etch current density and form very thin wires. Such single level or multiple levels modulated free standing silicon wires can have extra applications, for example, as Bragg waveguides, such modulation provides a further confinement of the wavelength of light that is allowed due to the induced periodicity.

With sufficient fluence used for both directions of intersecting lines, a grid forms instead of wires with a modulated diameter, as shown in Figure 6.11(a, b).

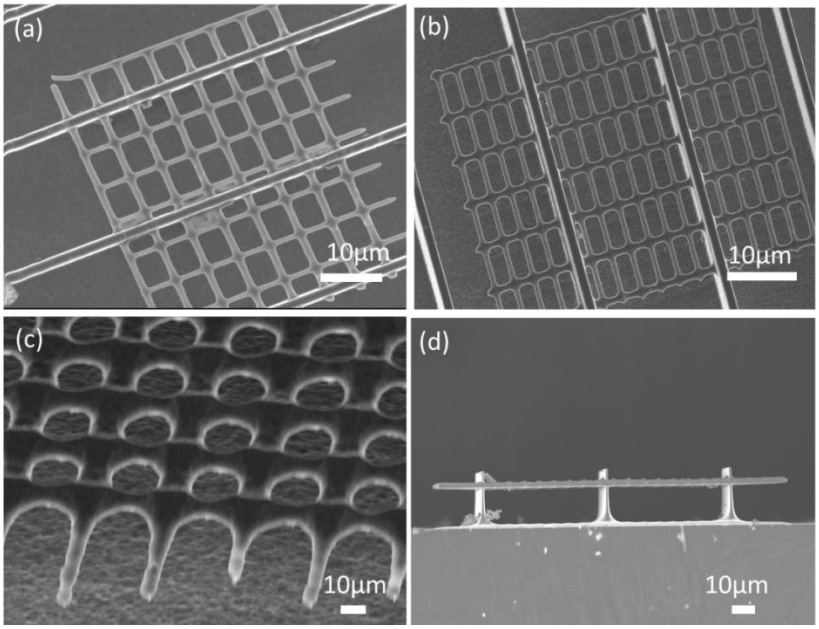

Figure 6.11 (a, b) Free-standing Si grids with squares and rectangles; (c, d) Non-uniform thickness of the grid fabricated by intersecting lines: tilted 55°(left), cross section view (right).

The thickness of these grids is not uniform, with a larger thickness at the intersecting points, as shown in Figure 6.11(c, d).

6.2.4 Free-standing tip arrays

Si tips have very wide applications in scanning probe microscopy. [78, 79] Fabrication of sharp tips and ridges using our method was reported earlier in Ref. [80], which uses a photoresist pattern with sloping sidewalls. The silicon structures follow the sloping photoresist sidewall profiles and form tips. Here another method of fabricating free-standing tips is introduced.

As has been shown at the site of the broken wire in Figure 6.10(c), at the connecting point of these wires with the supports, a large hole current passes through due to the deflection by the thick wall regions, such that the diameter of wires at these regions is even smaller, which was also discussed in Figure 6.8. With a low fluence, the wires break from this point, and a sharp tip is left, as shown in Figure 6.12.

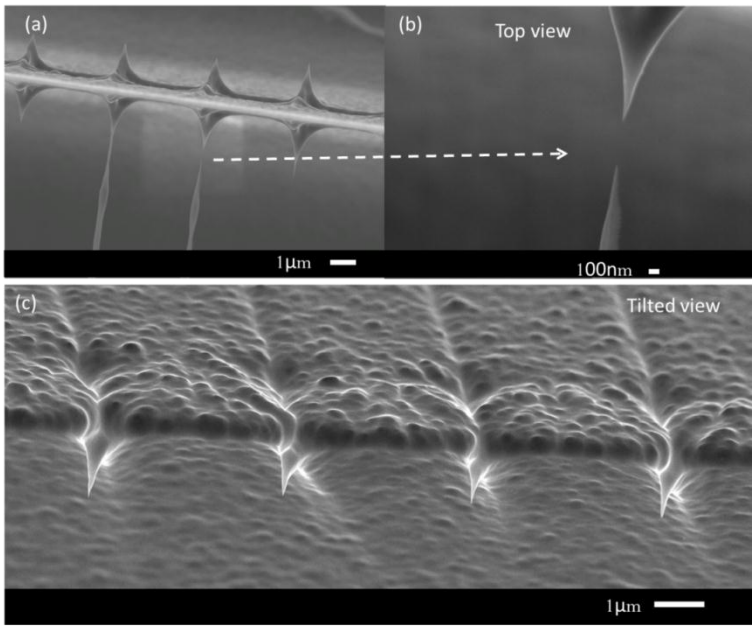

Figure 6.12 Free-standing tips. (a) Breaking of a wire at the connecting point with support walls due to increased current density; (b) magnified image showing sharp tips of (a); (c) an array of sharp supported tips.

Figure 6.12(b) shows two Si tips pointing towards each other at the broken site, by controlling the experimental position, this distance can be well controlled. A further oxidation process can sharpen the tip, as discussed in [79]. These tips differ from the conventionally fabricated tips which are usually supported by a thick substrate and directed upwards. Here the tips are oriented parallel to the substrate and supported by vertical walls.

6.2.5 Multiple level free-standing structures

By applying several different energy ions, multiple level free-standing wires and grids can be fabricated. Figure 6.13 shows cross section images of arrays of Si wires with a spacing of 5 μm buried in p-Si, fabricated by direct nanobeam patterning with 400 keV (range: 1.8 μm) and 500keV H_2^+ (range: 2.4 μm), etched with 60 mA/cm^2 for 4 mins. The upper level Si wire cross-section is fatter and shorter compared to the taller, narrower shape of the lower Si wires. In the middle row of Figure 6.13 (c) the contrast is different from surroundings simply because the cross section is not flat after cleaving, the middle row is lower in this particular image. Here the tails are clearly visible at the bottom of each core as discussed and explained in chapter 4 and chapter 5. Stage inaccuracy(~ 0.5 μm) and errors in alignment using channel electron

multiplier (CEM) (~0.5 μm) causes an obvious misalignment since the second level of structures were designed to be in the middle of the two cores on the first level. Relative locations of defect regions at different depths in the fabrication of multilevel structures influence the wire shape, size. The spacing in Figure 6.13 is 5 μm, and the fluences for four set of lines are $1x10^{10}$, $3x10^{10}$, $5x10^{10}$, $8x10^{10}$ proton/cm.

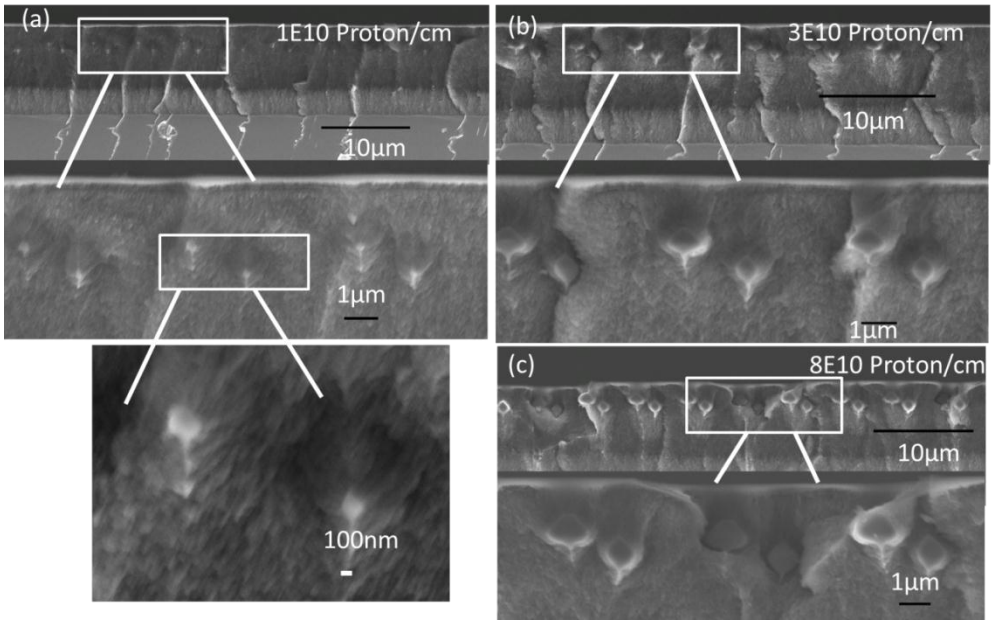

Figure 6.13 Buried cores in p-Si on two levels. Cross section of double level silicon wires buried in porous silicon using 500 keV and 400 keV H_2^+ with different ion fluences: (a)$1x10^{10}$/cm; (b)$3x10^{10}$/cm; (c)$8x10^{10}$/cm.

After removal of p-Si, free standing multilevel Si wires can be obtained. Figure 6.14 shows two levels of Si wires fabricated, respectively on 0.4 Ω.cm (a, b) and 0.02 Ω.cm wafers (c, d), where direct nanobeam patterning with 500 keV, and 400 keV H_2^+ generated defects in the wafers and the samples with resistivity of 0.4 Ω.cm (a, b) were etched with 60mA/cm^2 for 5 mins in 24% HF and the ones with 0.02 Ω.cm (c, d), were etched with 60 mA/cm^2 for 3.5 mins in 24% HF. The samples are oxidized for 1hour at 300 ºC, and 1.5 hours at 950 ºC and then the oxide was removed.

Due to different current flow mechanisms described in earlier chapters, the wires are connected in (a, b) since the tails of the upper wires connect with the lower wires, while in 0.02 Ω.cm wafer (c, d), the wires on different levels are

very close, yet still more separated compared to those in (a, b). This is a favorable consideration for choosing 0.02 Ω.cm wafers for fabrication of a 3D woodpile structure to realize photonic crystal as discussed in chapter 8.

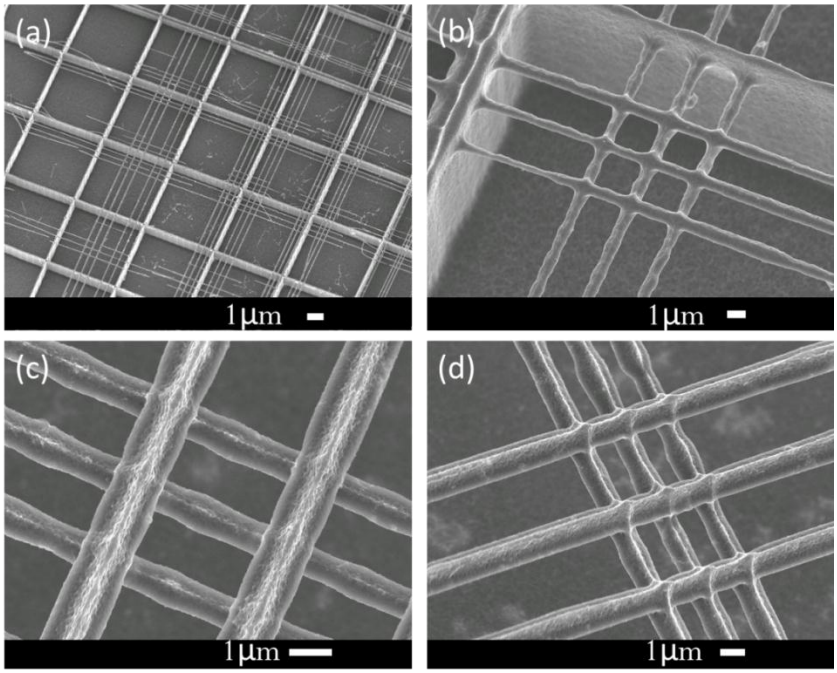

Figure 6.14 Two level intersecting wires. 500 keV and 400 keV H_2^+ ions to form two level intersecting wires: (a) 0.4 Ω.cm, overview of different line spacing and ion fluences; (b) 0.4 Ω.cm, magnified image of line spacing 3 µm and fluence of 3 x 10^{10}/cm for both levels; (c) 0.02 Ω.cm, vertical line spacing of 3 µm and fluence of 8 x 10^{10}/cm and horizontal line spacing of 2 µm and fluence of 5 x 10^{10}/cm ; (d) 0.02 Ω.cm, line spacing of 2 µm and fluence of 5 x 10^{10}/cm.

During wafer irradiation, to change the accelerator terminal voltage, to stabilize, focus and align the different beam energies is a time consuming job. Furthermore, it is also not reliable over long periods due to the beam drift, and the inaccuracy of alignment using CEM. Therefore, for efficient 3D fabrication using multiple energies, changing the energy of ions that penetrate into the silicon wafer without changing the terminal voltage of accelerator is necessary.

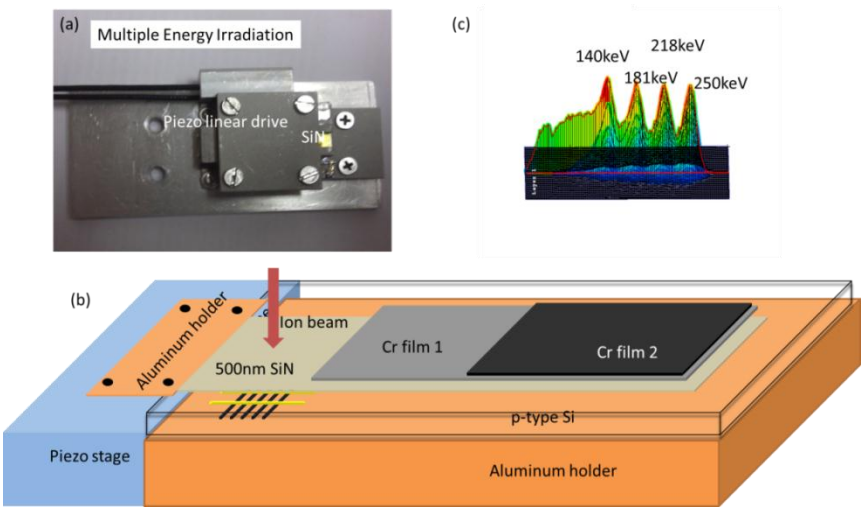

Figure 6.15 Designed stage for changing the ion energy easily by passing through thin films. (a) Optical image of piezo stage mounted with a thin SiN membrane; (b) schematics showing how it works; (c) proper design of film thickness from SRIM simulation results.

To implement a contrivance capable of changing the focused beam energy without any alteration to the accelerator or microprobe settings, a piezo stage (Figure 6.15(a)) was used. An aluminum holder was built to hold a membrane coated with films of different thicknesses on different regions across its surface, Figure 6.15(b). The material and thickness of each film was chosen such that the beam energy after passing through one film thickness was suitably varied to fabricate a different depth of structures. If 250keV proton beam is focused to 100nm on the plane of top surface of thin film, the beam size after passing through 500nm Si_3N_4 membrane is about 120nm according to SRIM calculation.

Figure 6.16 shows one example fabricated by this method. Figure 6.16(a) shows a schematic of the structure; and (b) shows a cross section of the double layer wires fabricated in 0.02 Ω.cm wafer with 250 keV protons with fluences $1.6x10^9$/cm and $4x10^8$/cm, with and without a membrane respectively. (c) shows two levels of free standing wires perpendicular to each other and (d) shows two levels of free standing wires parallel to each other, for (c) and (d) the wire fluence is $1x10^{11}$/cm.

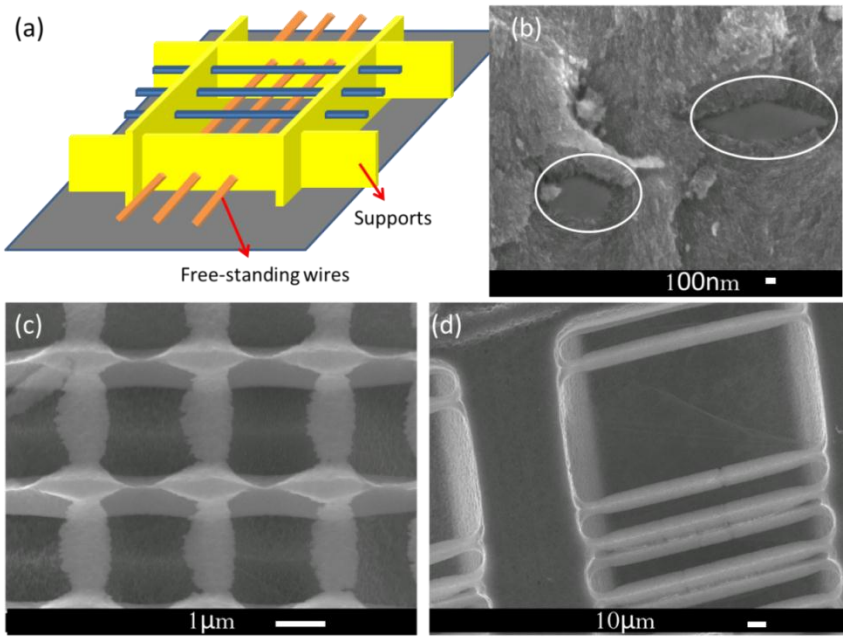

Figure 6.16 Two level free-standing wires from the designed stage. (a) schematic of the structure; (b) cross section of double layer wires; (c) plane view of two levels of intersecting wires; (d) plane view of two levels of parallel wires.

However, the main challenge for this method is to achieve as small a gap between Si wafer surface and the thin membrane as possible, such that the focused ion beam is not scattered much in the gap and so the fluence is not effectively reduced much. The method used to achieve a small gap is by tuning the amount of tightening of the four retaining screws and observing the fringes through the thin membrane. When the gap is small, more fringes are seen, and by tightening, the number of fringes increases. On further tightening a uniform gap removes the fringes. One point worth noting here is that the wafer surface and membrane should be very clean since a dust particle of several μm may easily break the membrane. The thin, brittle upper level of wires in Figure 6.16(c) shows the reduced ion fluence due to a large gap. Meanwhile, other challenges that should be born in mind are misalignments caused by stage inaccuracy, changing beam size in different positions due to a slanted thin membrane plane, moving of the sample due to friction force while moving the thin membrane, etc. The accuracy of alignment in fabricating multiple level structures achievable in case of stable ion beam is ~0.5 μm.

6.2.6 Completely free-standing structures

High aspect ratio structures, comprising a single level or multiple level free-standing wires and grids in previous sections are held in place on the thick Si substrate. But a substrate is not always necessary and sometimes one may wish to fabricate completely free-standing structures.

The fabrication methods are described in top view and cross sectional view in Figure 6.17(a, b), respectively. Firstly SU8 with a thickness enough to stop the ions with energy used in irradiation is patterned with UV lithography. The wafer coated with this SU8 pattern is irradiated with large area ion beam with high fluence. This is shown in the first column of (a, b). After irradiation, the photoresist pattern is removed and the silicon wafer is etched, in which p-Si selectively forms. With adequate amount of etching time, the end-of-range regions of 1 MeV Helium ions are undercut, shown in the second column of (a, b). p-Si is removed and the structure is lifted off by being dipped into dilute KOH solution, as in the third column of (a, b). Figure 6.17(b) is shows the cross section in square shape, however, the realistic case is that undercutting is gradual process and the cross section of these features is round and irregular instead of the square and regular shape shown in schematics.

Using the methods shown in (a, b), a Si grid is fabricated, shown in Figure 6.17(c), with an area of 5 mm x 5mm (left figure in (c)), period of 30 μm(optical image in the right figure in (c)), and thickness of 3.5 μm.

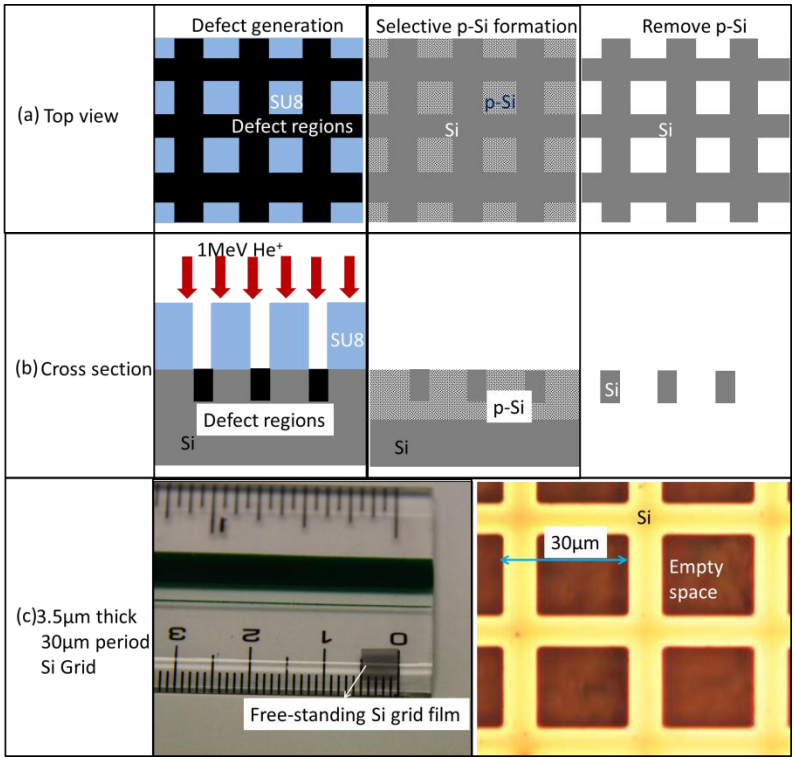

Figure 6.17 Free-standing Si grid fabricated by 1 MeV Helium ions, with a fluence of $1x10^{15}/cm^2$. (a) Schematics in top view; (b) Schematics in cross section view; (c) Photograph and microscope graph showing transparent Si grids with area of 5mm x 5mm, thickness of 3.5 µm with period of 30 µm.

By using the above structure as a thick support, and combining the method of fabricating thin wires described in section 6.2.2, completely free-standing wires supported by thick walls can also fabricated, for which the three possible methods are shown in Figure 6.18(a, b, c), and one example is shown in Figure 6.18(d). There are three methods to fabricate completely free-standing structures devoid of the substrate, shown in Figure 6.18. In the method shown in (a), the defect regions are first undercut (the first figure of (a)), then the porous layer is lifted off from the substrate by an electropolishing step (the second figure of (a)). The free-standing porous layer containing the silicon grid is then dipped into dilute KOH to remove the p-Si, leaving a free-standing grids devoid of substrate (the third figure of (a)).

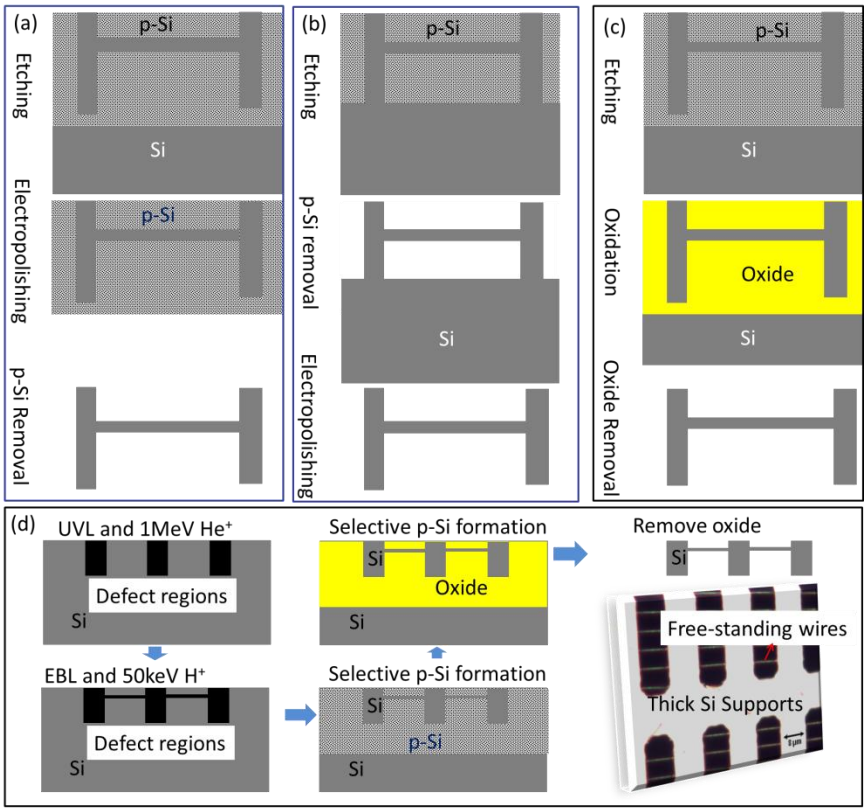

Figure 6.18 Three methods of fabricating completely free-standing structures: (a) Undercut the support and electropolish to lift the porous layer; (b) Electropolish to lift the free-standing silicon structures; (c) Oxidation and removal of oxide to lift the structure. (d) Schematics and microscope graph of one example structure of using UV lithography to make supports, and e-beam lithography to make free standing wires, and method (c) to lift the structures.

However a large amount of bubbles generated by removing the thick p-Si layer may break the free-standing wires. Thus, in the process of (b), free-standing structures are fabricated first and then electropolishing is used to release the structure. Another method to remove p-Si is by oxidation of a p-Si layer and removing the oxide to lift and fabricate free-standing structures at the same time. This method is shown in (c), which avoids the bubbles and the chance of breaking. However, in this method we should carefully choose the oxidation conditions to avoid curving of the substrate, and breakage of the oxidized porous silicon.

Figure 6.18(d) shows one example of such structures fabricated by method (c). In (d), a thick support fabricated by above process in Figure 6.17 is fabricated,

along with thin wires fabricated by large area irradiation using 50 keV protons through e-beam patterns.

6.3 p-Si structuring

p-Si has many advantages in variety of applications as described in chapter 1. The simplest structuring method of p-Si is to use a laser to turn p-Si into oxide and then remove the oxide with HF, as in Figure 6.19(a), as in Figure 6.19(b). [81] Another method of p-Si structuring is to use a mask and heavy ions to directly pattern it, which was previously used to make p-Si based photonic crystals, as in Figure 6.19(c). [82]

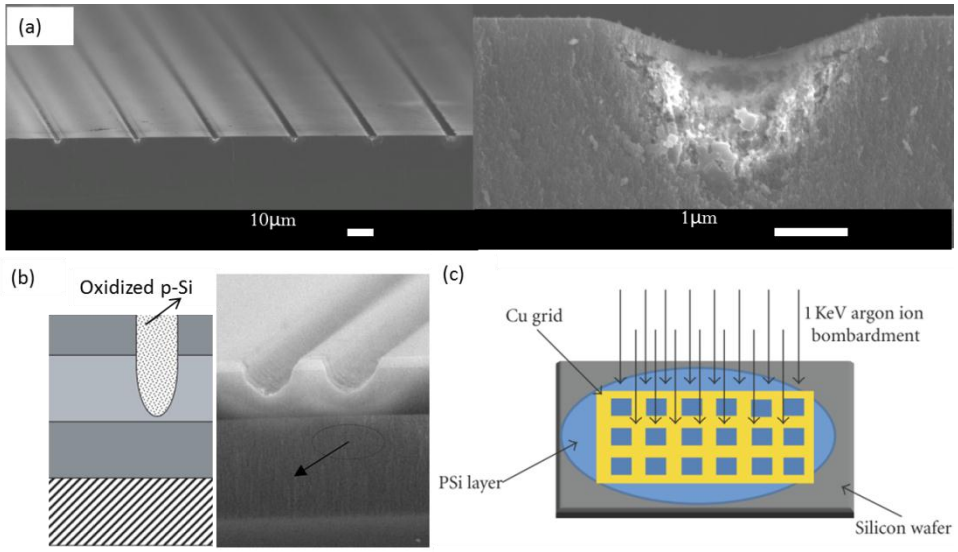

Figure 6.19 Review of methods to structure p-Si. (a) SEM images of laser oxidized porous silicon and after removal by HF solution; (b) Scheme of waveguide geometry using laser oxidation, and its SEM image[81]; (c) Schematic representation of the photonic crystal structure fabrication process[82].

p-Si based Bragg reflectors have been widely studied, as in Ref. [5], which shows that photoluminescence spectrum of p-Si can be considerably narrowed using optical microcavities. Ion irradiation was used to modify p-Si formation, and generate full color display, as in [27, 83].

Structures made entirely of p-Si are tempting in many applications. In the previous study on the anodization mechanisms at low ion fluences in chapter 4, we discussed how highly porous regions surrounded by regions with lower porosity were formed. By a further oxidation step in ambient environment, the highly porous regions can be turned into oxide while the other p-Si still remains, as in Figure 6.20(a). However, the porosity of p-Si should be

considered for a proper oxidation time. For example, a p-Si layer formed in 0.02 Ω.cm wafer by an etching current density of 300 mA/cm^2 can be oxidized completely and removed by a dilute HF solution after several months, but a two week ambient oxidation is only able to oxidize the highly porous regions and leave the other p-Si still porous and remaining.

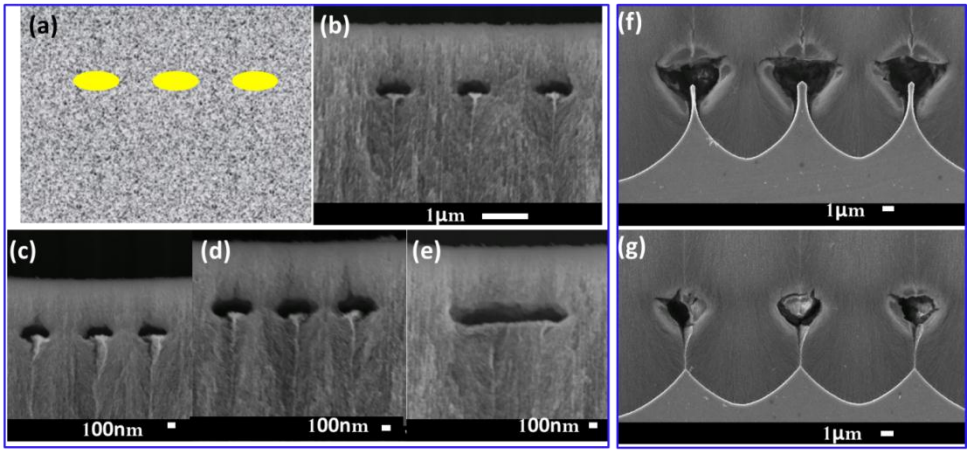

Figure 6.20 Buried channel formation in p-Si. (a) Schematic of oxidation of highly p-Si; (b-e)100 keV proton: (b) Cross section image of hollow channels in p-Si after removal of oxidized p-Si by HF; the lower three images have the same conditions as (b) except different line spacing, (c) 0.85 µm, (d) 0.75 µm, (e) 0.35 µm; (f-g)2 MeV proton: (f) 4 x 10^{11}/cm, (g) 2 x 10^{11}/cm.

A further step of dipping in dilute HF solution removes the oxidized porous silicon and produces structures made of p-Si and air, as in Figure 6.20(b), where an etch current of 300 mA/cm^2 is used for etching and the etched sample was left in air for two weeks to oxidize the highly p-Si regions. Figure 6.20 (c), (d), and (e) shows results of structures with different spacing. When the spacing is too small as in (e) three lines merge together and form a single channel. Figure 6.20 (f), (g) shows the channels fabricated by 2 MeV protons. However, porous silicon is not transparent, and it is difficult for imaging in microfluidics study. However, these structures can be turned into glass by oxidation, as discussed in the next section.

Using a slightly higher fluence, Si wires with only the lowest surface in contact with the p-Si channel wall can be fabricated, Figure 6.21(a), and with an even higher fluence, grooves or columns within p-Si can be fabricated, as

in Figure 6.21(b), which have also been demonstrated in chapter 4 earlier. Figure 6.21 (c), (d) shows the high aspect ratio channels fabricated by 2 MeV protons.

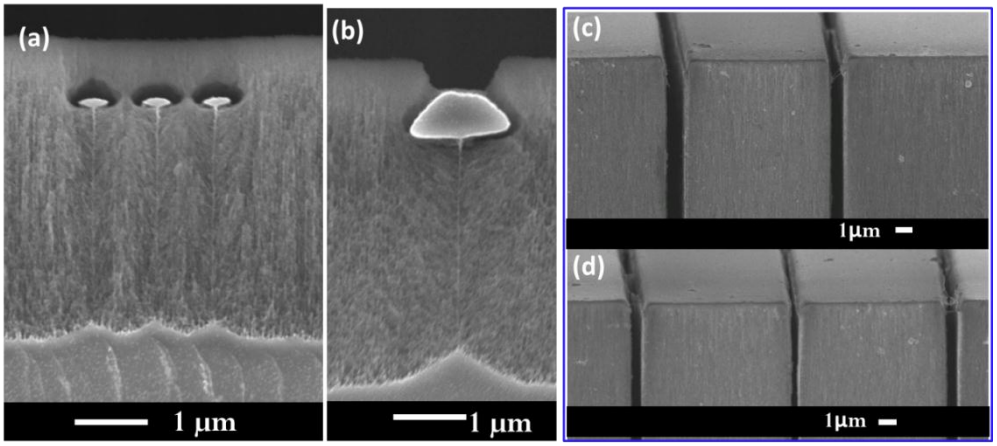

Figure 6.21 (a-c) 100 keV proton: (a) Three Si wires with only the low edge connected with the channel wall within three separate p-Si channels, with 100 keV protons of fluence of $3x10^9$/cm, and spacing of 0.85μm; (b) columns within p-Si, with 100keV proton of effective fluence of $2x10^{10}$/cm, and 3 lines of spacing of 0.25 μm merged together. (c-d) 2 MeV proton: (c) 4×10^{12}/cm, (d) 2×10^{12}/cm.

Compared to other methods of p-Si structuring, this method has many advantages. Table 6.1 shows the comparison of our method with other previous reported methods.

Table 6.1 Comparison of our method with other previous reported methods of structuring p-Si

Method	Laser annealing	Heavy ion etching	Our method
Buried channels	Possible	Not possible	Possible
Efficiency	Slow	Fast, through mask	Slow
Beam used	fs laser, need high power	Heavy ions, such as Ar^+	High energy light ions, such as 100keV~2MeV proton

6.4 Glass structuring

For structuring p-Si, with the optimum value of porosity, it is easy to oxidize whole porous structures into silicon dioxide. This method provides a way for glass patterning, which is very useful in many fields. Here we first give a general review on glass patterning methods and its applications.

6.4.1 Glass structuring review

There are different ways to pattern glass surfaces, such as fs laser irradiation of self-assembled silica particle mask,[84] imprinted patterns on glass substrate,[85] etc. To form buried channels in glass one may pattern a top template layer by UV lithography and reactive ion etching (RIE), and then use plasma enhanced chemical vapor deposition (PECVD) of Borophosphosilicate glass (BPSG). This is a type of silicate glass that includes additives of both boron and phosphorus, which is commonly used in semiconductor device fabrication for inter-metal layers, i.e., insulating layers deposited between metal or conducting layers and high temperature anneal to form channels, Figure 6.22(a).[86] One may also use femtosecond laser-assisted etching of three-dimensional inverted-woodpile structures in fused silica,[87] Figure 6.22(b).

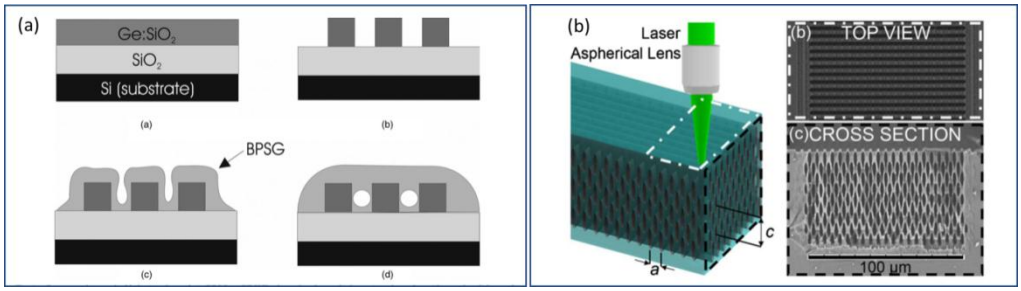

Figure 6.22 Review of fabrication of buried channels in glass. (a) Schematics of formation of buried channels in BPSG; [86] (b) Laser assisted etching of structures in fused silica.[87]

Fabrication of a half-circle channel based on standard lithography and etching procedure and aligned direct bonding[88] has also been done. These glass patterning structures were used in photonics, microfluidics, and sensing, etc.

6.4.2 Structuring in oxidized porous silicon

In this section, we first describe the important factors to turn p-Si into oxide, and then discuss the influence of different factors, mainly ion fluence, on the glass patterns.

Oxidation of p-Si to form an oxide layer has two processes, oxidation of silicon in the porous layer and densification of silica.[8] The porous texture in silicon for both p^+ and p^- is very sensitive to heat treatment, even at 400 ºC a coarsening of the texture is observed which reduces the surface area and reactivity of porous silicon to oxidation. This problem can be solved by first oxidation at 300 ºC where no distinct coarsening is observed. A complete oxidation can only be achieved if the initial porosity of the layer is high enough. Below a critical porosity value the porous layer cannot be fully oxidized. An oxidized fraction of 100% can be reached on a scale of hours only if the initial porosity is greater than about 56% and if the oxidation temperature is above 750 ºC. The thermal expansion coefficients of silicon and silica are very different. When the temperature changes, strain emerges inside the bodies of silica and silicon substrate. The strain cracks the SiO_2 layer from silicon substrates. Pores inside the SiO_2 layer release the strain, so SiO_2 layer with micro-pores in it can avoid cracking. Therefore, appropriate temperature variation during oxidation is desirable for forming a non-cracked glass layer from porous silicon. Besides, the thickness of oxidized layers at 750~800 ºC is always greater than the starting porous layer thickness, and the oxide in this temperature range is still porous. The dissolution of the oxide formed in this range is very fast. The porosity of oxide is calculated from P_{oxide}=1-2.27(1-porosity)($t_{initial}/t_{oxide}$), where t is the thickness. When the temperature is above 1000 ºC, oxide densification occurs, which is sensitive to the texture of the layer. The densification time increases sharply when the pore size in the initial porous layer is larger. After densification, the oxide obtained from p-Si exhibits properties and electric behavior which are similar to a standard thermally grown oxide. [8]Therefore, to form glass, an initial porosity over 56% and a high temperature over 1000 ºC is needed.

The first step to pattern glass is to structure p-Si, as shown in Figure 6.20 and 6.21. Fluence, wafer resistivity, etch current density, ion energy play important roles in this process. A strong diffusion current component is

desirable for formation of highly porous silicon, where the doping concentration gradient is maximized. Therefore highly doped wafers, such as 0.02 Ω.cm wafers, with a doping concentration of $3x10^{18}/cm^3$, are used in the following studies. Besides, as discussed, a stronger applied bias enhances the funneling phenomena, meanwhile, it produces higher porosity p-Si and therefore, 300 mA/cm^2 is used in the following studies, instead of 40 mA/cm^2 which was used in previous studies for silicon micromachining processes. Besides, an ion energy of 200 keV H_2^+ was used, to avoid the necessity of forming thick p-Si layer, which is more difficult to properly form an oxide with good quality.

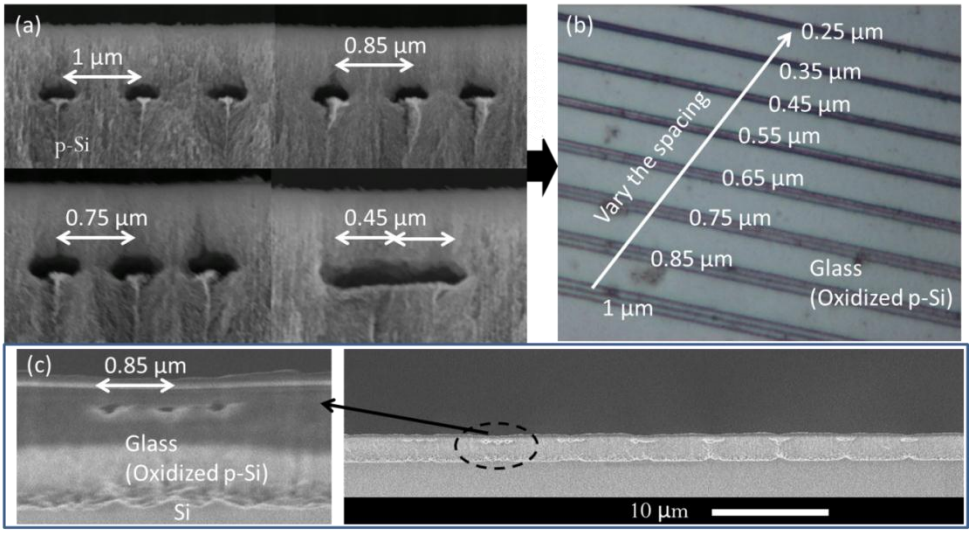

Figure 6.23 Overall picture of p-Si structuring and glass structuring using 100keV proton with 1 x 10^9/cm. (a)Cross section SEM images of channels in p-Si with spacing of 1, 0.85, 0.75, 0.45 µm; (b) OM image of buried channels in glass(oxidized p-Si) with spacing from 0.25-1 µm; (c) Cross section SEM images of channels in glass: (Right) spacing from 1 µm to 0.25 µm from left to right; (Left) magnified image of spacing 0.85 µm.

Figure 6.23 shows the results for glass patterning. In (a) the buried channels with spacing of 1, 0.85, 0.75 µm are formed in p-Si. A wide channel forms when the spacing is 0.45 µm and too small to be resolved. After oxidation of the p-Si sample in (a), p-Si turns into oxide, and (b) shows the top view OM image. The cross sectional SEM images after oxidizing p-Si thermally is shown in Figure (c).

Buried channels at large depth can also be fabricated by using high energy ions. Figure 6.24(a) shows top view optical image of buried channels in oxidized p-Si obtained by oxidation at 300ºC for 2h, and 1000ºC for 3h. The cross section of two of the sets of channels are shown in (b), for which the etch current density is 100 mA/cm^2, and corresponding porosity is ~0.7, such that the oxidized p-Si still has small pores inside. In order to study the quality of oxidized p-Si formed by different etch current density, Figure 6.25 (a) shows the SEM images of top view of oxidized p-Si by increasing the etch current density. The etched depth is around 10 µm, and firstly the stablization of porous silicon was realized by oxidation at 300 degree for 3 hours in ambient; then the fully oxidation of porous silicon was realized at 750 degree for 4 hours in ambient. The SEM images show the grain size increases with etch current density. Lower current density produces oxide with better quality. By reducing the etch current density to 40 mA/cm^2, corresponding porosity is ~0.58, and the oxidized p-Si (Figure 6.25(b, c)), has better quality than 100 mA/cm^2 (Figure 6.24). The morphology in cross section after removing the oxidized p-Si in air shows the streamlines of the current flow, verifying the diffusion current towards the region above end of range.

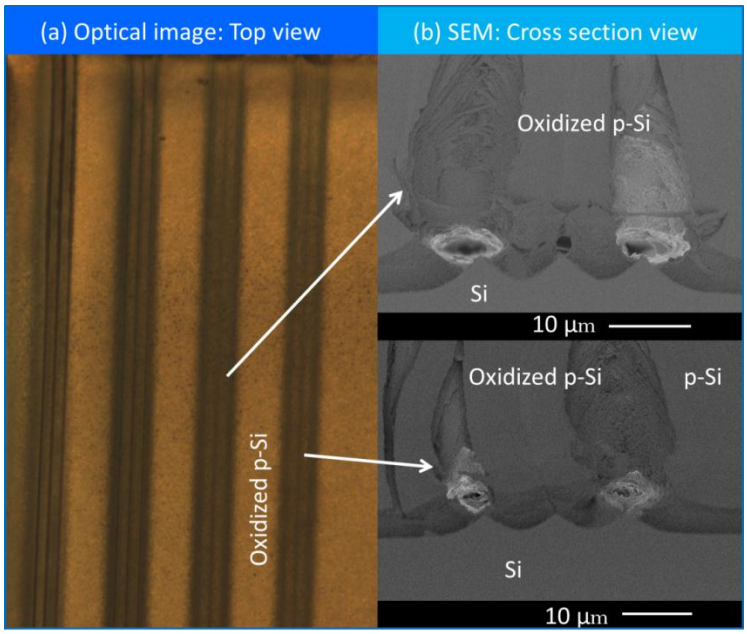

Figure 6.24 (a) Top view optical image of buried channels in oxidized p-Si(glass); (b) Cross section SEM image of two set of buried channels at a depth of about 48 µm in oxidized p-Si, fabricated by 2MeV proton with

line fluence of 2 x10^{11}/cm(upper), 1x10^{11}/cm(bottom) in 0.02 Ω.cm wafer and etching current of 100mA/cm^2

Comparison between cross section view before and after oxidation in Figure 6.25, it shows thermal expansion occurs, and the small trench above the end of range region closes. Therefore etch current density and the thermal annealing conditions should be chosen properly to get structure size required, as well as glass of good quality.

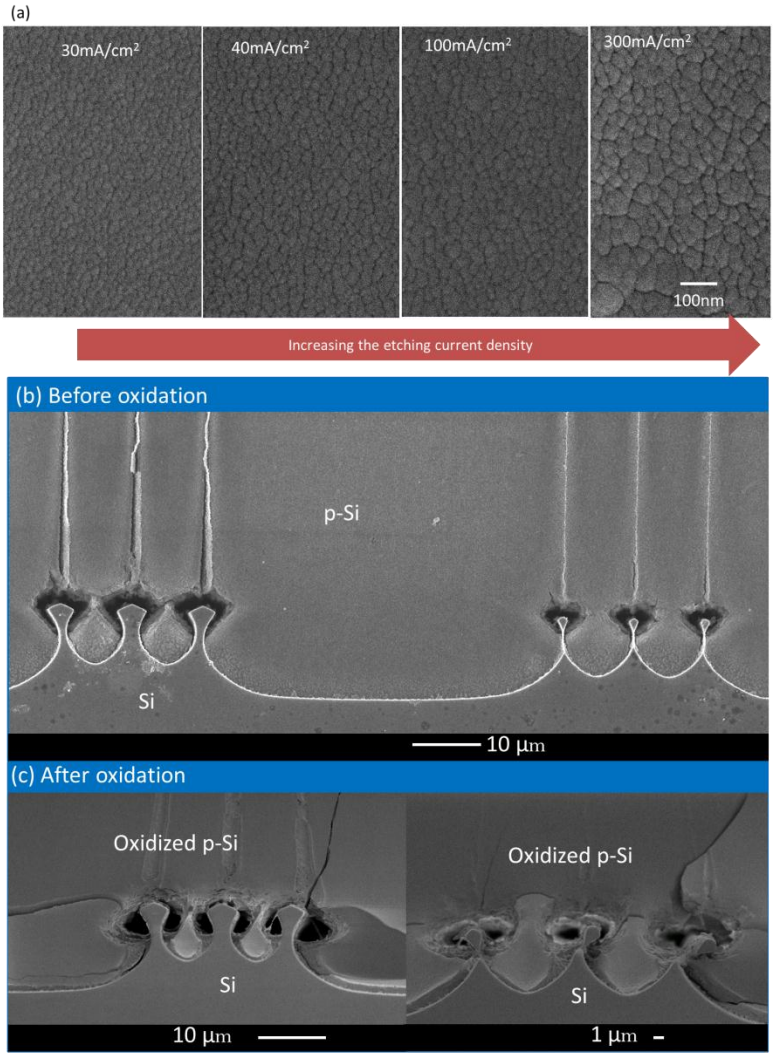

Figure 6.25 (a) Top view SEM images of oxidized porous silicon formed at different etch current density; (b, c) Cross section SEM of buried channels fabricated by 2 MeV proton in 0.02 Ω.cm wafer and etching current of 40 mA/cm^2 with line fluence of 8 x10^{11}/cm(left) 4x10^{11}/cm(right) in (b) p-Si and (c) oxidized p-Si(glass).

Similarly, multi-level channels in glass can be fabricated using this method by multiple energy irradiations with proper fluences. This capability will provide the means to significant developments in fields such as nanofluidics, lab/systems-on-a-chip technologies and sensing and the sample are currently tested for DNA studies.[89]

Conclusion

Following the basic anodization mechanism, this chapter demonstrates use of the hindering of the current flow in ion irradiated regions in Si bulk structuring. The methods mainly include direct writing and pattern transfer by lithography followed by large area irradiation. Using the defect regions and their influence on current flow, p-Si selectively forms depending on the ion fluence, etch current density, and other factors discussed in previous chapters. Based on this, a variety of Si structures are fabricated including Si walls supported free-standing Si wires, tips, grids either in single level or multiple levels. Multiple energy irradiation and core formation enables multiple level free-standing Si wires. Completely free-standing structures devoid of substrate have also been demonstrated.

Besides, this chapter demonstrates use of the enhancement of the current flow in ion irradiated regions in p-Si structuring by forming highly p-Si regions and subsequent removal of highly p-Si regions. In this method, buried channels, high aspect ratio trenches in p-Si or p-Si walls can be fabricated. A further oxidation step with proper p-Si parameters and oxidation conditions turns p-Si into glass, which demonstrates the capability of fabricating buried channels, high aspect ratio trenches or walls in glass.

This chapter not only shows how to use the basic etching mechanisms that have been discussed in previous chapters to fabricate structures, but also lays a foundation for their further application in fabricating photonic crystals, discussed at length in chapter 8.

Chapter 7 Silicon surface patterning

The previous chapter discussed the method of bulk micromachining of Si, structuring of p-Si and glass, while here surface pattering of Si is mainly discussed. Firstly, the methods of nanoscale patterning of Si used previously are reviewed, after which CIBA process is discussed. Different types of ions, facilities and methods are discussed in detail. Comparison with other methods demonstrates several advantages of surface patterning of Si using this method.

7.1 Brief review of nanoscale patterning of Si

From a review of the literature, there are a variety of methods used for nanoscale patterning of Si. Five well-known methods are reviewed as follows.

(1) Scanning probe lithography: Nanoscale patterning of Si surface can be achieved by atomic force microscope (AFM) [90] or scanning tunneling microscope (STM) and chemical modification. [91]

(2) Chemical etching: Stencil mask on Si membrane can be achieved by KOH etching and patterning of SOI wafer. [92] Anodic aluminum oxide (AAO) membranes with pore sizes were transferred to silicon surface by reactive ion etching, then a thin layer of silver or gold was deposited onto the patterned Si (100) substrate and the rate of chemical etching by the silver film was faster than that of silver particles, finally vertically oriented sub-10nm Si nanowires with high crystalline quality on Si (100) substrates are obtained; [93]

(3) Ion Beam etching: Arrays of ion-focusing microlenses, such as small round holes through a metal/insulator structure) on a Si wafer is fabricated and then a broad-area collimated beam of ions is directed at the substrate. By applying an electric potential to the lens the ions are focused at the bottom of the holes and etch the Si wafer. [94]

(4) Indentation and chemical etching: By combining indentation which induces transformation to the high pressure phases, which are highly resistant to subsequent and anisotropic wet chemical etching, nanoscale maskless patterning in Si can be done. [95]

(5) Ion implantation and reactive ion etching, or wet etching: Gallium ion implanted Si behaves as a mask for reactive ion etching to fabricate high aspect ratio nanostructures in Si [18] or by combining with wet etching, free standing structures can be fabricated. [19]

7.2 Surface patterning of Si using ion beam irradiation combined with electrochemical etching

Surface patterning of Si simply uses the etch front of the ion irradiated surface. The ions that have been used include protons from 50 keV to 2 MeV at CIBA, 30 keV He^+ ions from a HIM, 15 keV Cs^+ ions from a SIMS machine, and 30 keV Ga^+ ions from a FIB system, as introduced in chapter 1. A microprobe to focus high energy proton beams produces a beam with size of 50 nm, and it has relatively larger scattering size at the end of range. A HIM focuses a beam down to 0.5 nm and a FIB system provides a beam with 6 nm size. For Cs^+ ions, in our case a broad beam is used with a minimum size of 25μm in the current system, so a photolithography process is needed before ion beam irradiation to realize surface patterning. Table 7.1 shows the comparison between these 4 types of ions for Si nanoscale surface patterning.

Table 7.1 Comparison of different type of ions from different systems

Ions & System	**Protons, CIBA accelerator**	**He^+, Helium Ion Microscope**	**Cs^+, SIMS**
Energy & range in Si	50 keV~2 MeV, 1 μm~48 μm	30 keV, ~800 nm	15 keV, ~15 nm
Resolution of Beam	Down to 50 nm	~0.5 nm	25 μm
Resolution achieved in our structures	~80 nm, Depends on energy, and aspect ratio	Minimum spacing~60 nm	not known yet
Advantages	Either maskless or masks for mass production	Maskless, highly focused	Very heavy ions, high defect production

Usually the etch front is terminated above the end of range region. Using the surface patterning process described in section 4.4, silicon surface patterning studies are carried out in this chapter. The etch depth is usually quite shallow for surface patterning, where the etch time is accurately controlled by computer software to accuracy of milliseconds. The oxidation and oxide removal steps have two effects from a patterning point of view, one is to remove the remaining p-Si, and the other is to make the pattern smooth. Figure

7.1 shows line grooves and dot structures formed on a silicon surface using 30 keV He^+ and etching on 0.4 Ω.cm wafers.

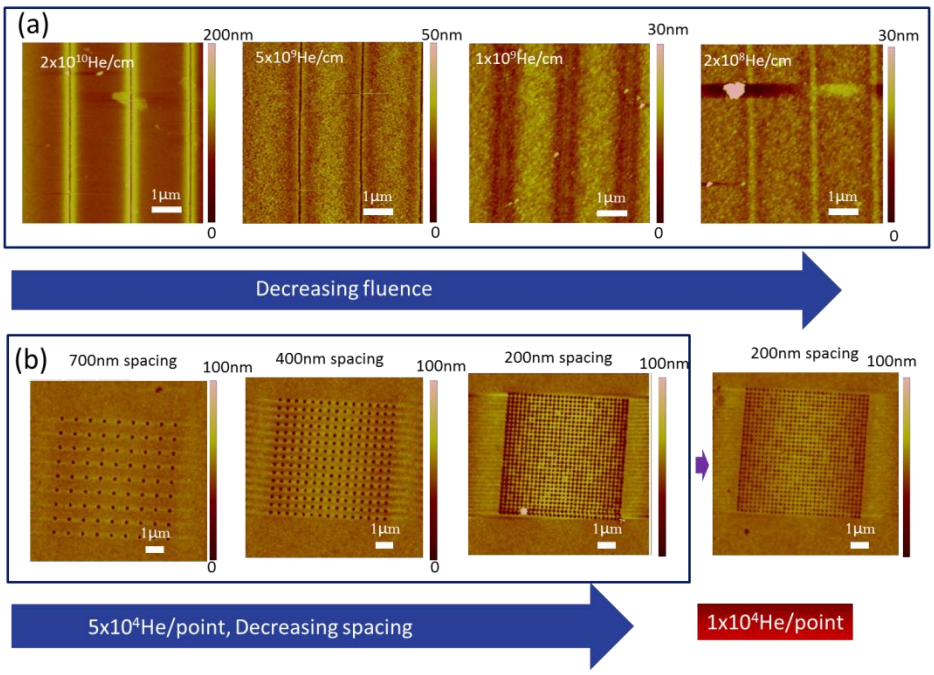

Figure 7.1 AFM images of surface patterns. (a) AFM images show lines with 2 µm spacing either as grooves or bumps, or grooves with wings, for different ion fluences using 30 keV He+; (b) AFM images of dot pattern with fluence of 5x104Helium/point, of different spacing from 700 nm to 200 nm, the last one with fluence of 1x104Helium/point, and spacing of 200 nm.

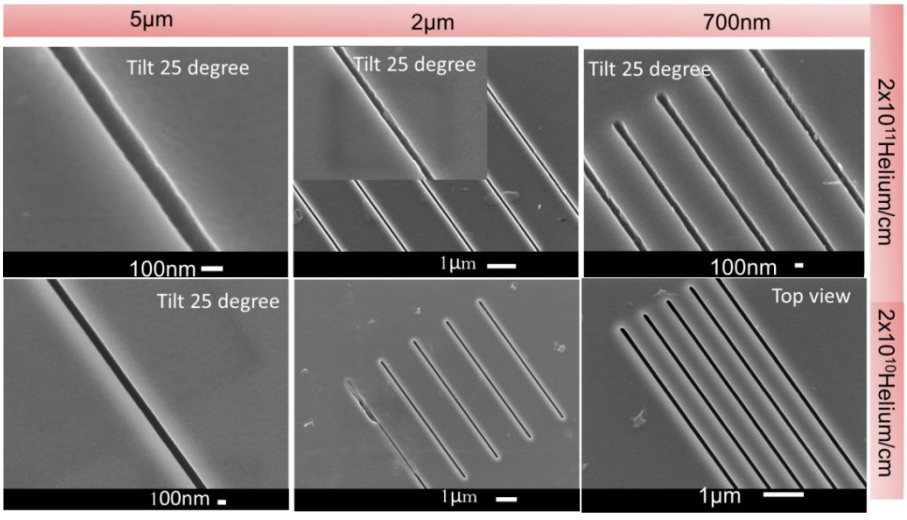

Figure 7.2 SEM images of surface patterns. SEM images of grooves formed at fluence of $2x10^{11}$Helium/cm and $2x10^{10}$Helium/cm with spacing of 700 nm, 2 µm, and 5 µm formed by 30 keV He^{+}.

Figure 7.1(a) shows grooves or bumps fabricated by the experiment procedure described in section 4.4, with line irradiation with different line fluences, while (b) shows pits with spacing from 1 μm to 200 nm fabricated by point irradiation. The smaller the spacing is, the more difficult to resolve the features, such as the dots with a 200 nm spacing. A good combination of factors, such as spacing and fluence, is needed to pattern the surface of silicon with high resolution and good feature quality.

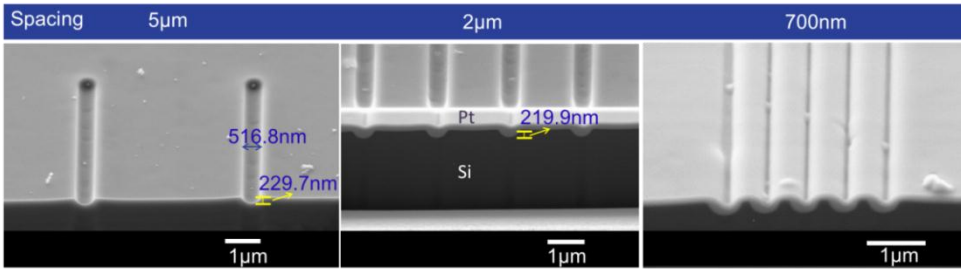

Figure 7.3 FIB cutting and cross section SEM of grooves of $2x10^{18}/cm^2$ for spacing of 5 μm, 2 μm and 700 nm formed by 30 keV He^+.

To observe more clearly the surface patterns, SEM images are taken as in Figure 7.2. FIB cutting enables a better view of cross section SEMs of these small grooves, as in Figure 7.3. Cross section image shows a half circle profile of the groove.

Such surface patterns can be transferred to other material by imprinting technology, as shown in Figure 7.4. Such Si surface patterns can be used as mold and to make patterns on polymer or metal for different applications, such as metamaterials and plasmonics.

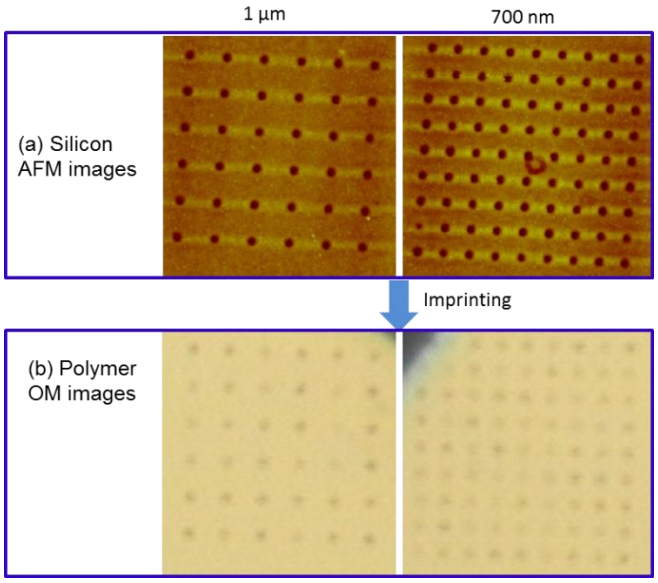

Figure 7.4 (a) AFM images of dot pattern on silicon using 30 keV He^+; with fluence of $1x10^5$ Helium/point with spacing of 1 µm, and 700nm; (b) Optical micrograph of inverted patterns on polymer after imprinting the dips in (a).

All the above methods for surface patterning are based on shallow etching where the etching depth is less than the range of ions used. Another method for surface patterning is to use deep etching, where the etch depth is beyond ion range, as shown in schematics in Figure 7.5, where lines with 2 µm width and 4 µm spacing were irradiated on 0.02 Ω.cm wafer with 1 MeV H_2^+ of (a) $3x10^{16}/cm^2$; (b)$1x10^{16}/cm^2$; (c)$5x10^{15}/cm^2$; (d) $3x10^{15}/cm^2$, and then etched in 12% HF at 10 mA/cm^2 for 111 s (1 µm) and at 83mA/cm^2 for 27 s (1 µm), and repeated 5 times, and then the p-Si removed using KOH. After undercutting, the curvature will become smaller and smaller and tend to be flat finally. These silicon surface patterns can be used as mold to replicate structures into other materials.

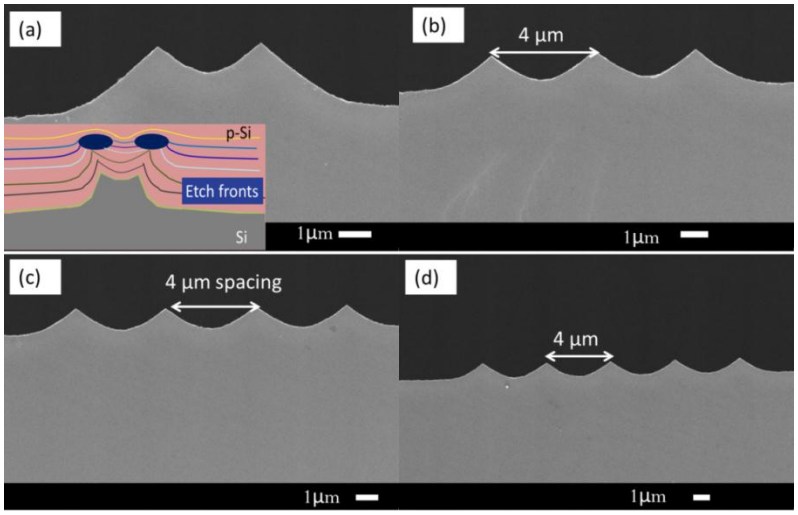

Figure 7.5 Surface patterning by etching beyond the end of range regions, lines with 2 µm width and 4 µm spacing were irradiated on 0.02 Ω.cm wafer with 1 MeV H_2^+: (a) $3x10^{16}/cm^2$; (b)$1x10^{16}/cm^2$; (c)$5x10^{15}/cm^2$; (d) $3x10^{15}/cm^2$, (inset) schematics of etching front evolution for two closely-spaced defect regions.

7.3 Amorphization, sputtering effect, reduction of work function

In surface patterning using heavy ions with high fluences, effects from amorphization, sputtering effect, and reduction of work function, becomes important, which was ignored in the previous study in chapter 4. Bombardment enhanced etching due to amorphization was reported earlier. In Ref.[96], the reported effect of irradiation with 30 keV Helium ions was to convert the surface layer to a quasi-stable amorphous form, and this amorphous layer is soluble in aqueous hydrofluoric acid by soaking in 49% aqueous hydrofluoric acid for 30 minutes after irradiation. It was found that removal of the bombarded material proceeded rapidly during the first ten minutes in hydrofluoric acid, but then the rate of removal decreased rapidly. The thickness of material removed was approximately one-tenth of the incident ion range for a fluence of ~10^{14}/cm^2, and approximately proportional to the logarithm of the fluence for fluences greater than this. In Ref.[97], it was reported that by properly selecting the ion, the beam energy, the fluence and a suitable etchant, it was possible to remove layers of any desired thickness between approximately 100 Å and 10^4 Å. It was observed that the steps in Dash etch (1 ml Hydrofluoric Acid, 1 ml Nitric Acid,10 ml Glacial Acetic Acid) reached their full depth after an etch of less than 10sec and do not change any more within the measuring accuracy for etches up to 1 min in duration. The damaged layers can be removed by soaking the samples in HF, though the etch rate is *very low* and highly variable. For instance, one sample irradiated with 5 x 10^{15} Ne at 50keV energy required 3 h in HF to develop a step of approximately 1800 Å.

Here the second micromachining method using project through mask is used, since the SIMS facility is not equipped with direct nanobeam writing function. A 0.4 Ω.cm p-type silicon wafer was coated with photoresist and patterned by UV lithography. A 15 keV Cs^+ beam with a beam current of 0.01~0.1 nA, and beam size of 25 μm instead of a broad beam was scanned with an angle of 20°. After bombardment, the photoresist was removed. The sample was dipped in 2% HF for 8mins and 24% HF for 2mins. An electrochemical etching of the

irradiated silicon was done using a 60 mA/cm^2 current density in 24% HF for 100 ms, which causes porous silicon formation at the top several nms. After electrochemical etching, the porous silicon was removed by oxidation and removal of oxide.

Here instead of direct writing using proton, helium, or gallium beams, a lithographically fabricated resist pattern was defined, which is much less time consuming. This is needed for Cs beam irradiation where the minimum beam size is 25 μm.

Sputtering is important and has been widely studied and used. [22, 98] The sputtering yield data from SRIM for normal incidence 15 keV Cs^+ shows the sputtering yield is around 2.47 Atoms/Ion. Since the sputtering is only in top several nanometers, which is equivalent to the thickness of native oxide, so the native oxide cannot be ignored here. According to [99], the native oxide is around 1.6 nm. By taking the incidence angle and native oxide layer into account, it shows the sputtering yield for 20° incident 15 keV Cs^+ in 1.6 nm native oxide coated silicon is only 0.04 Atoms/Ion. Defect distribution shows a penetration depth of ~20 nm, and highest defect density peaks at ~10nm depth.

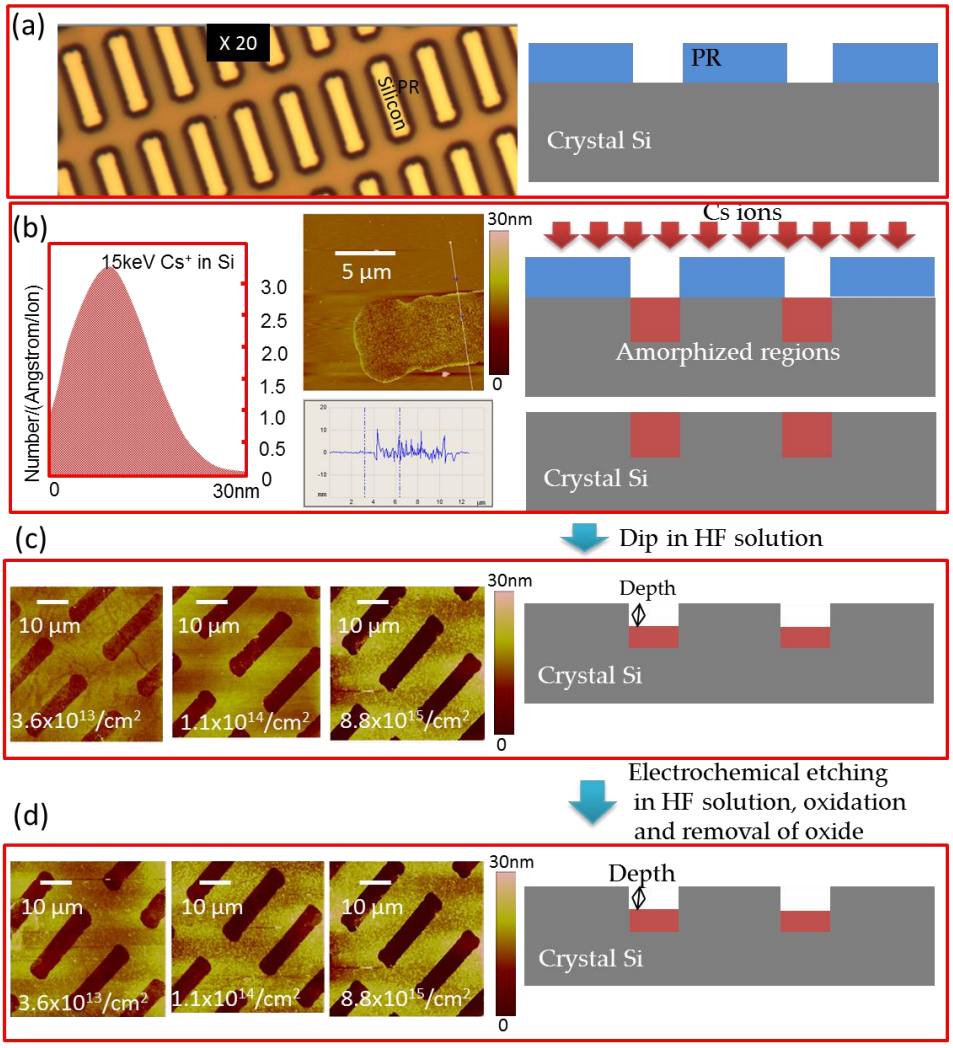

Figure 7.6 Schematics of experiment steps (right) and the experiment results after each step (left): (a) UV lithography to pattern photoresist, (left) top view optical image of patterned photoresist; (b)Ion bombardment and removal of the photoresist, (left) SRIM calculated defect density distribution and the AFM image of roughened surface; (c) Chemical removal of amorphized layer; (d) Electrochemical etching and removal of p-Si.

By reading step values from AFM images after removing photoresist (Figure 7.6(b)), Figure 7.7(a) shows the increase of roughness of bombarded area by increasing the ion fluence. The possible mechanism may be due to a sputtering effect. The step between bombarded and non-bombarded region is less than 2 nm. This step height is in the range of the native oxide thickness, thus most of the sputtering in this experiment only occurs in the native oxide layer since the sample was bombarded without removing the native oxide formed in the normal storage conditions in ambient atmosphere, indicating that trivial

sputtering occurs in silicon beneath, and sputtering has little effect on the etching process of silicon later.

By reading step values from AFM images after chemical etching and electrochemical etching step (Figure 7.6 (c, d)), Figure 7.7(b) shows at higher fluences chemical etching partially or completely removes the defect regions. Step height is equal to bombarded area-non-bombarded area. For lower fluence, bombarded area are not influenced by chemical etching, while electrochemical etching still induces an enhanced etching, and results in formation of dips. To study the mechanism, amorphization induced chemical etching, electrochemical etching effect, and reduction of work function of Si should be taken into account.

In the case of Cs^+ ion implantation, a reduction of the work function due to formation of a Si-Cs surface dipole was observed on n-type [100] crystal Si. [21, 26] This decrease of the work function in spite of low sputtering may play a role, as discussed later.

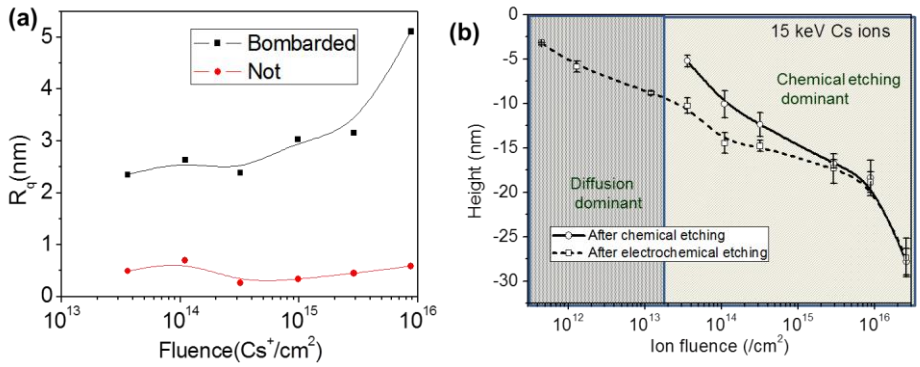

Figure 7.7 (a) Roughness of bombarded area by increasing the ion fluence; (b) Step height after etching and electrochemical etching (step height=bombarded area-non-bombarded area).

At the lowest fluence of 10^{11}/cm^2 ~10^{13}/cm^2, there is an obviously enhanced etch rate caused by electrochemical etching. This is due to diffusion current caused by lower hole densities in the bombarded area, as well as the reduction of work function. At fluences higher than $4x10^{13}$/cm^2, faster etching occurs at irradiated regions mainly due to amorphization induced chemical etching. At the fluence between these two regimes, amorphization occurs partially and

only top layer is removed by chemical etching, which subsequently reduces the potential barriers built by the defects, and induces diffusion current and an enhanced etching. As illustrated in Figure 7.8, there are three regimes for the ion fluences. Diffusion current is dominant at low fluences. While increasing the fluence, the potential barrier built by defects also increases, however, amorphization occurs and the top layer is removed by chemical etching. This removes the maximum defect density regions and the diffusion current is again dominant. By further increasing the ion fluence, the whole damaged region is completely amorphized and removed chemically. Thus, a full picture of the precluded behavior across all fluence regimes for low energy heavy ions is shown.

For 30keV He+ case at high fluences amorphization also takes place. Figure 7.9 (b) shows the SRIM calculation results of projection of defect density distribution onto the Si surface. It indicates that the defect regions overlap when the spacing between adjacent irradiation point is less than ~400 nm. Therefore when the spacing is from 10 nm to 100nm, it is equivalent to a broad beam irradiation. Figure 7.9 (a) shows the AFM images of different ion fluence for different point spacing, where 0.4 Ω.cm Si wafer was irradiated with points with spacing from 10nm to 100nm, and then electrochemical etching was carried out for short time. Porous silicon was oxidized and removed. Figure 7.9 (c) plots the step height measured from AFM images vs. effective areal fluence. It shows at low fluence diffusion current is dominant and etching is enhanced in irradiated area. While increasing the ion fluence, the potential barrier deflects the current away, and etching is hindered. By further increasing the ion fluence, chemical etching starts to remove part of amorphized layer and the holes are able to cross the reduced potential barrier and this subsequently induces enhanced etching. This explains the small dip in the middle of the bumps at high fluence for 30keV He ions in previous discussions in chapter 4.

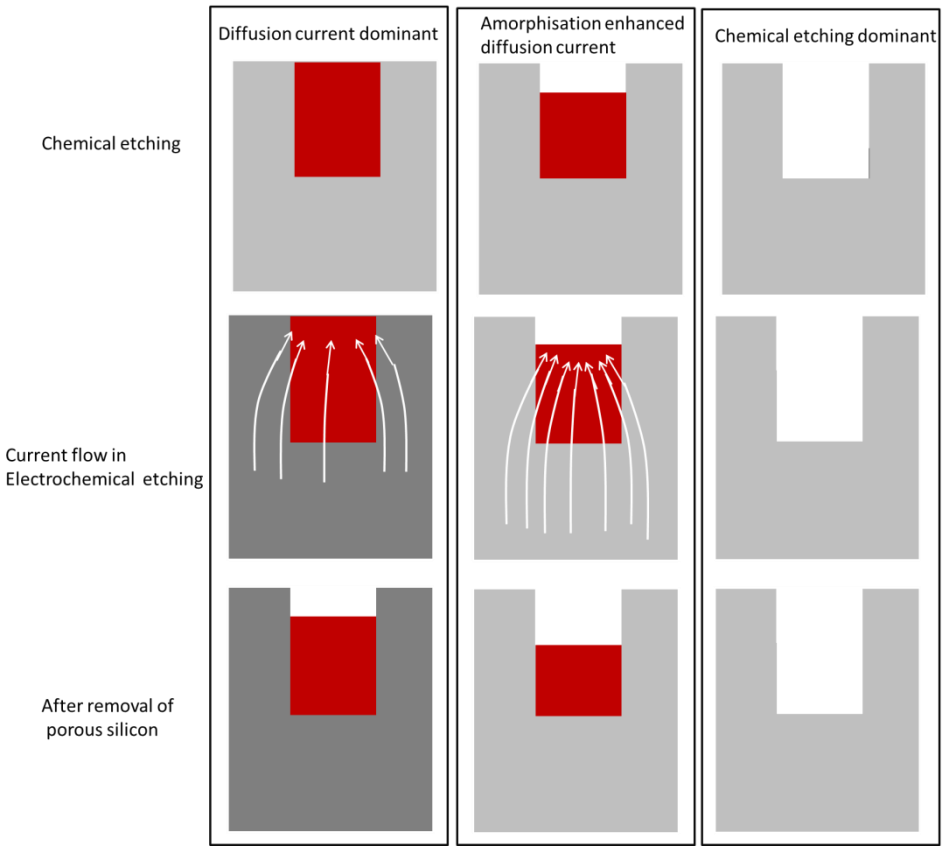

Figure 7.8 Three regimes of the fluence for 15 keV Cs ion irradiation case. (Left)Regime 1: Diffusion current is dominant; (Middle)Regime 2: Amorphization induces removal of high defect density layer, and induces diffusion current; (Right)Regime 3: Amorphization induced chemical etching removes the damaged regions.

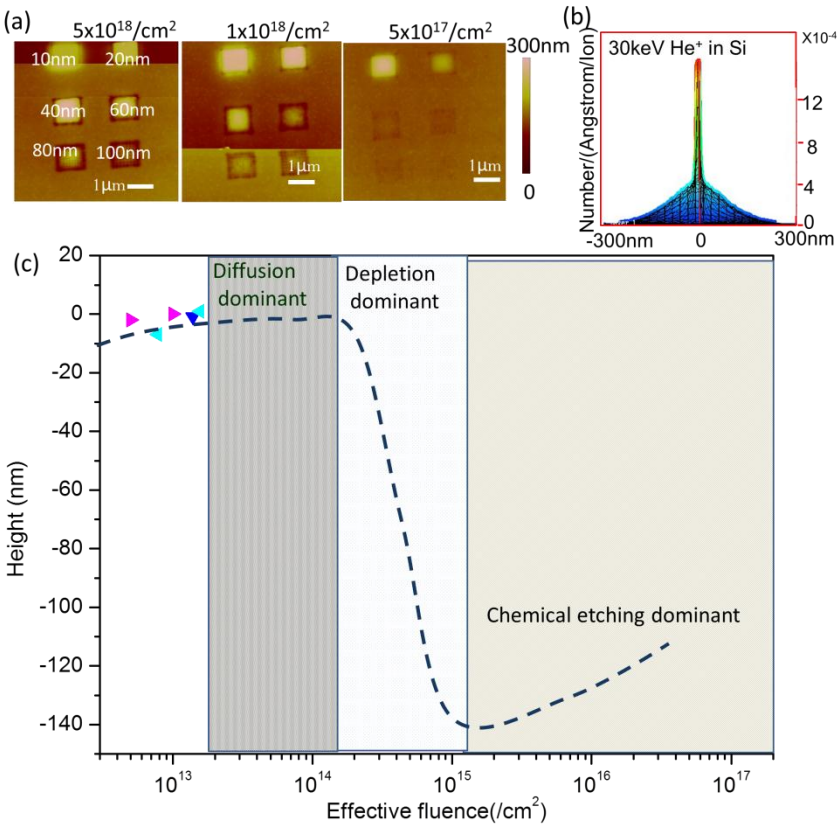

Figure 7.9 (a) AFM images after removing porous silicon formed by electrochemically etching the 30keV He ions closely spaced point irradiated silicon; (b) Projection of defect density on the surface of Si; (c) Step height vs. effective ion fluence.

Conclusion

This chapter demonstrates Si surface patterning using the etch front of ion irradiated Si, either by shallow etching less than the ion range, or beyond the ion range. Nanoscale patterning is achievable using strong funneling effect induced by highly focused low energy ion irradiation. Mass production is achievable using photolithography and large area ion irradiation. The surface patterns can be transferred to other materials, such as polymer. Besides, in the context of Si surface patterning using low energy heavy ions, sputtering effects, amorphization becomes important for high fluences, and reduction of the work function occurs for Cs ion irradiation. All these factors are taken into account to give a more complete picture for current flow during electrochemical etching of ion irradiated p-type Si, which have been ignored in the simulation model of chapter 4.

Chapter 8 . Mid-infrared Si and p-Si based photonic crystals and devices

---

The structures that have been fabricated in previous chapters have applications in photonics, microfluidics and sensing. This chapter mainly focuses on realising MIR photonic crystals and their possible applications. Section 8.1 serves as an introduction to photonic crystals. The basic concepts and the fabrication methodologies of Mid Infrared (MIR) PhCs are briefly reviewed. Section 8.2 discusses the characterization methods for MIR PhCs. Section 8.3 discusses importance of wafer resistivity and thermal annealing in fabricating structures for photonics applications. Section 8.4 discusses the manufacture of simple 2D PhCs using this method. Section 8.5 discusses the fabrication of air or p-Si hole slabs (or perforated Si slabs) in Si matrix. Section 8.6 discusses the modification of multilayer p-Si to fabricate 2D PhCs. Section 8.7 discusses the efforts made and the challenges faced towards the fabrication of 3D PhCs and section 8.8 discusses a simple demonstration of the potential in achieving integrated photonic circuits.

Chapter 8. Mid-infrared Si and p-Si based photonic crystals and devices

8.1 Photonic Crystals

In this section, firstly the basic concepts of photonic crystals are introduced, then fabrication of PhCs in the MIR and their applications are reviewed, finally the advantages of Si and p-Si based MIR PhCs are discussed.

8.1.1 Basic concepts of photonic crystals

A photonic crystal is material with a periodic dielectric constant. Photonic crystals respond to light with a wavelength of the same order of the periodicity. A line grating could be considered as 1 dimensional photonic crystal. Butterflies (Figure 8.1(a)) and insects display structural color [100] due to the presence of periodic layers structures on their colourful wings. Photonic crystal is an optical analogue of electronic crystals, but they are different in many aspects, as listed in Table 8.1. The photonic crystals don't allow the propagation of light of certain Eigen frequencies whereas electrons with energies in the bandgap region of semiconductor don't exist. The fields involved in the PhC are optical vector fields, whereas scalar fields are involved in case of electronic crystals. Since the photonic crystals are governed by Maxwell's equations, the solution is exact. On the other hand, the electronic crystals are governed by Schrodinger equation where electrons interact strongly and hence only an approximate solution exists.

Engineering the periodicity of refractive index is the key to manipulation of light. Under certain conditions, the photonic crystals exhibit a band gap, and the electromagnetic wave propagation inside a photonic crystal may be manipulated by engineering its photonic bands. By introducing line and point defects, photonic crystals can be employed for confinement of light in one (waveguides) and two (cavities) dimensions respectively.

Table 8.1 Comparison between photonic crystal and electronic crystal

	Photonic Crystal	**Electronic Crystal**
Dimension	~wavelength of light, ranging from 10^{-8}m(Ultraviolet)~10^{3}m(radio)	~de Broglie wavelength of electrons in material $\lambda=h/p=h/(mv)$ ~size of atoms(Angstrom)
Elemental particle	Photons	Electrons
Field	Vector: Electric field	Scalar: Wave function
Fundamental equation	Maxwell's EM equations	Schrodinger function
Periodic function	Dielectric constant $\varepsilon(r+a)=\varepsilon(r)$	Potential $U(r+a)=U(r)$
Bandgap	Structure Dependent	Natural/Material Dependent
Application	Manipulation of light: Photonic Devices	Microelectronics, etc.
Defect mode	Used for waveguide, cavity…	Used for doping

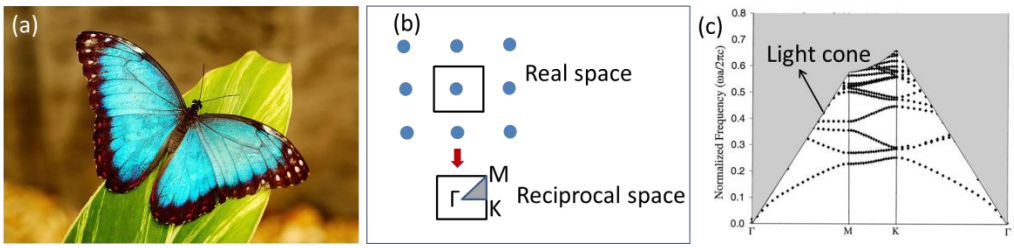

Figure 8.1 (a) Structural color on butterfly's wings; (b) 1st Brillouin zone for a 2D square lattice; (c) Photonic band structure, and the light cone.

1st Brillouin zone (one example is shown in Figure 8.1(b)) is a primitive cell in reciprocal space, and the Bloch wave in a periodic system can be characterized by the behaviour in a single Brillouin zone. In Brillouin zone, there are several critical points which are of high symmetry and widely used in photonic band structures. Polarization describes the orientation of the oscillation of transverse waves (light). Even parity mode is where the electric field is invariant under mirror reflection and it is called TE-like modes; Odd parity mode is where the

mirror reflection turns a z-directed polarization vector to –z and it is called a TM-like mode. A normalized unit is used to incorporate the scale invariance, therefore, the units of the following are:

Frequency, $\nu=c/a$

Angular frequency, $\omega= 2\pi c/a$

Wave vector, $k = 2\pi/a$

Wavelength, $\lambda= a$

Bandgap refers to the band of light frequencies that cannot propagate in photonic crystal. The origin of the band gap occurs when the wavelength of incident light satisfies the Bragg condition. Defect modes are the characteristic electromagnetic field distributions excited locally near a defect or the region with a disorder. A point (0D) defect can be used to create an optical cavity or a very narrow band-pass filter. A line defect, on the other hand, could be used as a waveguide. Apart from these basic concepts, a light cone is used for 2D slabs to overlap on a 2D infinite lattice to get the band structure (Figure 8.1(c)).

Photonic crystals can be designed to operate as different optical components such as polarizers, waveguides, cavities, modulators, etc. for manipulation of light. Using such basic building blocks, one can envisage of a photonic integrated circuit akin to electronic circuits designed for a particular application. The photonic circuits complexly manage the light pathways like discrete optical experiments, except that they are conducted on a single chip. It is a multidisciplinary field, which can be combined with several main fields in physics, biology and medicine, as shown in Figure 8.2. In microfluidics[101], three-dimensional photonic crystals were used for refractive index sensing in a microfluidic channel where a change in the refractive index of the fluid in the microchannel results in a shift in the band gap or band gap defect position of the photonic crystal. It was also used for biological sensing applications. [4, 101] It can be integrated with electronics.[102] Ref. [102] demonstrates light-beam steering that is extremely wavelength dependent by using photonic crystals fabricated on Si. Besides these applications, photonic crystals have also been used in the field of energy conversion,[103] where a design that significantly increases the absorption of a thin layer of absorbing material such

as amorphous silicon was achieved by patterning a one-dimensional photonic crystal in this layer.

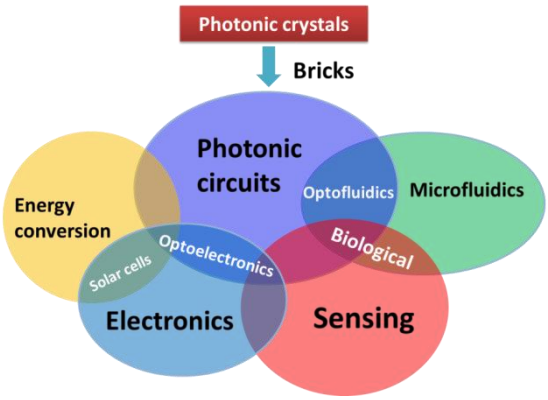

Figure 8.2 Schematics showing application of photonic crystals

8.1.2 Photonic Crystals in Mid-Infrared range

Most of the photonic crystals that have been fabricated and used are in near infrared(NIR) range, which are typically based on fabrication approaches involving electron beam lithography and reactive ion etching.[104] For visible PhCs, the optics used to ascertain the photonic crystal properties are readily available. However, the research in the field of the photonic crystals in the mid-infrared range is less mature due to the lack of characterization optics, even though the fabrication procedure is much easier. Generally, infrared light covers a wide spectral range which can be categorized into different regions, each of which has different applications, as listed in Table 8.2.

Table 8.2 Categorization of infrared light into different regimes and respective applications

Name	Wavelength	Applications
Near-Infrared(NIR)	0.75~1.4μm	Fiber optic telecommunication
Short wavelength Infrared	1.4~3μm	Long-distance telecommunications: 1530~1560nm
Mid-Infrared(MIR)	3~8 μm	3~5 μm portion: atmospheric window
Long wavelength Infrared	8~15 μm	Atmospheric window, “thermal imaging” region
Far-Infrared (FIR)	15~1000 μm	

8.1.3 Si, p-Si, and glass based photonic crystals and brief review of fabrication methods in these two materials in MIR range

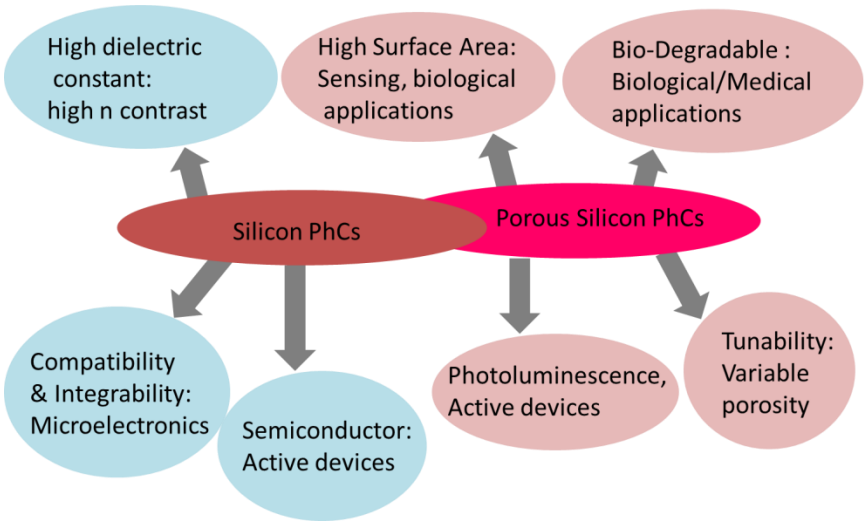

Figure 8.3 Advantages of Si and p-Si in the applications of PhCs

Silicon has a high dielectric constant, and good compatibility and integrability with microelectronics. p-Si has high surface to volume ratio, bio-degradability, variable porosity, and photoluminescence property. Therefore, Si and p-Si PhCs have unique advantages in their respective application areas, as shown in Figure 8.3. Due to its high dielectric constant, Si based PhCs enables a complete bandgap, and due to its wide use in microelectronics, Si based PhCs have good compatibility and integrability with electronic devices. Besides, due to its semiconductor nature, Si based PhCs can be used for active devices incorporating modulation due to bias etc. Due to its high surface-to-volume ratio, p-Si based PhCs are suitable for sensing and biological applications, and since p-Si is bio-degradable, it can be used for medical applications such as drug delivery. Due to a tunable refractive index originating from the variability of porosity and flexibility of infiltration of other media, p-Si based PhCs have a tunable photonic band gap. In addition to this, p-Si based PhCs could be potentially used for active devices due to the photoluminescence property of p-Si. There are different ways of fabricating Si based PhCs in MIR range, as in Figure 8.4, and 8.5. Figure 8.4(a) shows a fabrication process of a Si woodpile structure by transferring the polymer template produced by direct laser writing to silicon by Chemical Vapour Deposition (CVD) and

subsequent removal of the polymer. The agreement between calculation and measurement results on the right shows the good quality of the structure. Figure 8.4(b) shows the fabrication of a 2D photonic crystal by macroporous silicon formation following the prepatterning of surface by KOH etching.

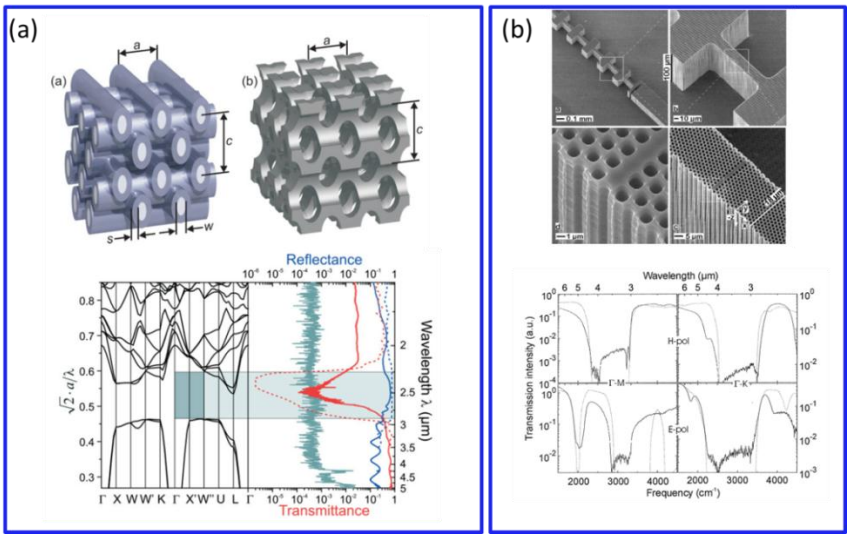

Figure 8.4 Review of fabrication of MIR PhCs. (a) Fabrication of 3D Si PhCs with Photonic Band Gap (PBG) at around 2.5 μm by using a polymer template;[105] (b)Fabrication of 2D Si PhCs with PBG around 3.5 μm by macroporous silicon formation.[106]

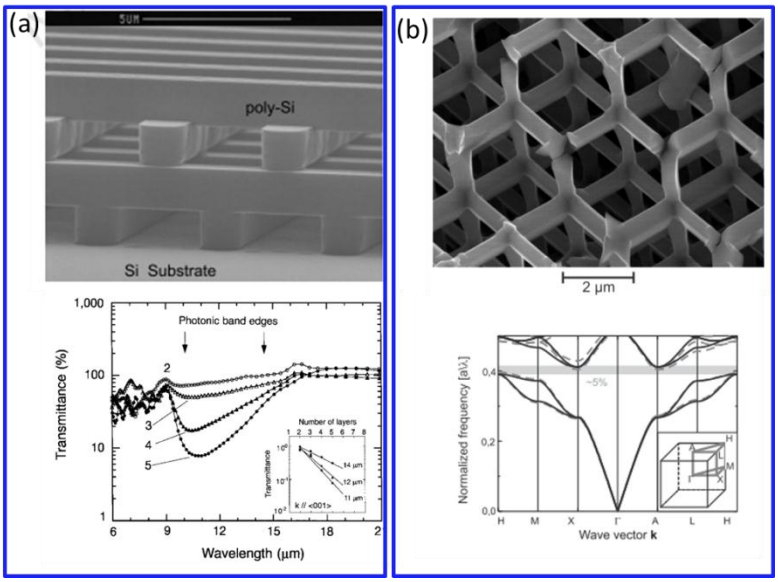

Figure 8.5 Review of fabrication of MIR PhCs. (a) Fabrication of Si woodpile structures with PBG at around 11μm by layer by layer

approach;[107] (b)Fabrication of 3D photonic crystal with simple cubic by anisotropic erosion. [108]

Figure 8.5(a) shows the layer-by layer approach used to fabricate a woodpile structure which exhibits a photonic band gap around 11 μm. Figure 8.5(b) shows a simple cubic 3D photonic crystal fabricated by anisotropic erosion and the simulation results predict a complete band gap.

Table 8.3 Comparison of different methods for fabricating Si and p-Si based MIR PhCs

Method	Flexibility	Mass production	Cost	Integration, Compatibility with IC	Tunability of PBG
Polymer template from direct laser writing	Flexible due to direct laser writing	No	high	Yes	No
Macroporous silicon formation	Lattice type is limited	Yes	Low	Yes	No
Anisotropic errosion	Limited	Yes	Low	Yes	No
Layer by layer approach	Limited	Yes	High	No	No
Our approach	Highly flexible due to proton beam writing	No (PBW line); Yes (Large area Irradiation)	High	Yes	Tunable due to porous silicon

Table 8.3 compares different approaches towards making Si and p-Si PhCs with our approach. Flexibility means that variety of experimental parameters can be changed easily to tune the photonic properties over a large range. Compatibility means how the fabrication process of photonic structures can be compatible with the electronic circuits' industry procedures. Tunability means how the photonic band gap can be tuned by applying external fields or infiltrating other medium. Our approach is highly flexible since proton beam writing enables easy change of the fluence, line spacing, and scanning pattern, while electrochemical etching enables easy change of etching current density. This will be discussed in section 8.5 in detail. Besides, our approach is compatible with electronics since it is based on ion irradiation and conventional etching. Our approach is highly tunable since the porous silicon can be infiltrated with other medium to change the effective refractive index. When it is infiltrated with liquid crystals, external electric field or temperature

change can tune the PBG. However, our approach has relatively high cost in fabrication of Si and p-Si based MIR PhCs.

8.2 Mid-infrared PhCs Characterization: FTIR and Ellipsometer

Fourier transform infrared spectroscopy (FTIR) is a standard technique to measure the transmission and reflection of light from a sample in the infrared region. The time domain data yields a frequency spectrum upon Fourier transformation of the interferogram obtained from a scanning Michelson interferometer with a laser beam as a reference. Characterization of photonic crystals is done the same way as normal bulk materials ensuring the beam goes through the desired sample area. In order to access the bandgap of the photonic crystal, the propagation vector of light should be in the plane of periodicity. In this respect, 1D and 3D Photonic crystals in the MIR range are relatively easier to characterize because of their huge sample area. For instance, Lin et al [107]reported the fabrication of a 3D photonic crystal operating in MIR fabricated by repetitive deposition and etching of multiple dielectric films. The back of the Si substrate was polished to a smoothness of better than 0.3 μm to avoid significant light scattering.

However, a 2D photonic crystal in MIR presents more challenges in their characterization. The reason is due to the inadequate height of the structure in the third dimension. Ideally 2D photonic crystals have infinite z-dimension. Practically it is difficult to fabricate such high aspect-ratio periodic structures. A. Birner et al reported characterization of samples with different filling factors to verify the gap map of electric and magnetic modes using FTIR Spectroscopy, in which the complete band gap could be tuned from 3.3 to 4.3 μm wavelength.[106] They cut out approximately 10×1 mm^2 out of the wafer and mount it between two blade-like holders, the upper one of which was placed on the top of the thin porous bar to block leakage light. The cleaved facets were screened with silver paint. A tunable MIR laser source could be employed to directly characterize 2D photonic crystals due to good coupling and high source brightness. For example, an optical parametric oscillator (OPO) was used to investigate integrated waveguide-like structures.[109] In this reference, they demonstrated guided modes in the wavelength regime between 2.9 and 3.9 μm in mid-infrared photonic crystal waveguides on a

silicon-on-insulator platform. Characterization was performed with a proprietary intra-cavity Optical Parametric Oscillator in a free space optical setup and with a fiber coupled setup, using a commercial Quantum Cascade Laser.

An indirect method to study the photonic band structure is to use angle-dependent reflectance to map the photonic band. This technique relies on the observation of resonant features in the reflectance spectra at different incidence angles. The resonant features occur when the incident light wave vector component parallel to the photonic crystal surface matches the wave vector of a propagating mode inside the photonic crystal. It is related to as $k_{\parallel} = (\omega /c) \sin \theta$, where c is the speed of light, θ is the angle of incidence on the photonic crystal surface and ω is the incident light frequency. By recognizing the resonant features in the reflectivity spectra, the photonic bands can be mapped out. Kral et al [110] reported angular-dependent reflectivity measured in the mid-IR region(4000-400 cm^{-1}) using a FTIR spectrometer (Bruker, model Vertex 70) equipped with a special reflectivity attachment(VeeMAX2), and the light source was a broadband halogen-tungsten lamp. The angle of incidence was varied from 12º to 66º in steps of 2 and the plane of the incidence was perpendicular to the sample surface. The reflectivity spectra were recorded with a liquid-nitrogen-cooled MCT detector.

All the previous studies focus on the photonic band structure of 2D photonic structures in 2D plane. However, there are a lot of interesting phenomena in the direction that is perpendicular to the photonic crystal plane which may have very important applications. For example, Prodan et al [111] observed Fano and Fabry–Perot-type transmission resonances and found that Fano resonances originate from the photonic hole structure.

We characterized our MIR PhCs using two available facilities at SSLS. The FTIR spectrometer (IFS 66v/S) at SSLS has a spectral range spanning from 30 to 7000 cm^{-1}. There are two main sources for transmission and reflection studies, namely, globar source and the synchrotron source. Globar source is used commonly for thermal spectroscopy as a light source comparable to

traditional blackbody sources. However, globar source doesn't require preheating and operates at 1400 K emitting wavelengths of the range 4-15 μm. An extra attachment for characterizing small area samples with focused light beams is the beam condenser (MIRacle) comprising two elliptic mirrors reducing the beam size to 1/4. (See more details in Appendix) Thus for a 2 mm aperture, a beam spot size of 500 μm is obtained. A microscope attached to the spectrometer can be used for near IR (0.9 to 2 μm) and MIR (2-12 μm) spectral ranges for characterizing small samples in transmission and reflection modes.

Ellipsometry is an optical technique used for the investigation of the dielectric properties (complex refractive index or dielectric function) of thin films. Ellipsometry measures the change of polarization upon reflection or transmission. Figure 8.6 depicts a common ellipsometric measurement setup. By measuring the amplitude and phase change of reflected light, information on photonic band gaps of photonic crystal structures is obtained. One common problem faced with FTIR setup is that 2D PhC samples manufactured have very small thickness in the z-direction. In order to couple light into the PhC, one has to align the sample very precisely and also the focusing is inadequate to achieve the maximum coupling. Ellipsometry helps in avoiding this issue as it characterises the sample at an angle and gives the information about the band structure indirectly.

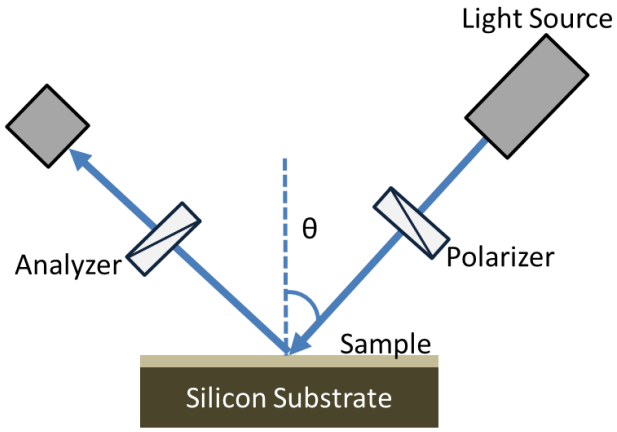

Figure 8.6 Schematics of spectral ellipsometric measurement of photonic crystal

8.3 HF etching of ion irradiated Si in photonics applications

The previous studies on irradiation and the anodization mechanism only considered structural parameters. But it is necessary to consider the optimum choices of resistivity and a further annealing process to use these structures for photonic applications.

8.3.1 Choice of appropriate wafer resistivity and thickness

Depending on the type of silicon used, the characterization of the sample differs. Some silicon samples are good for transmission, but some are bad, depending on whether silicon wafers are single-side polished, double-side polished or unpolished and their resistivity. Double-side polished substrates have a higher transmittance, but most of the experiments were performed in MIR range in transmission mode on one-side polished wafers. However, in future, new structures will be fabricated, and characterized in FIR range.

A highly doped wafer has more impurities leading to high optical scattering losses. Figure 8.7(a) shows the measurement results on the transmission spectra of MIR beam through wafer of three different silicon wafer resistivity.

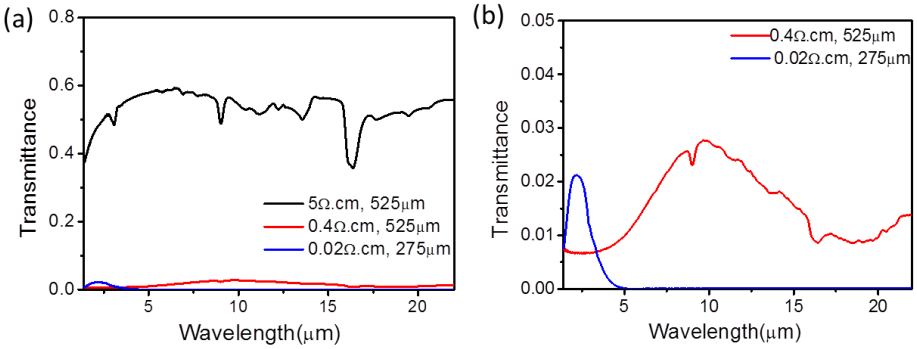

Figure 8.7 Transmission spectra in MIR range for p-type Si substrate of three different resistivity, with respective thicknesses. The figure on the right is for highlighting the transmittances of highly doped silicon wafers.

Therefore, the transmission range of highest resistivity (5 Ω.cm) wafer is from 1-25 μm. Compared to highest resistivity, the two lower resistivity wafers have very low transmittances in the measured range. Figure 8.7(b) shows the zoomed-in spectra of two lower resistivity wafers. For medium resistivity (0.4

Ω.cm) relatively transparent window is from 5-25 μm; for low resistivity (0.02 Ω.cm) wafer, it is from 1.4 μm~5 μm. Above 5 μm, the beam is completely blocked by 0.02 Ω.cm wafers. A high and medium resistivity wafer is better choice for MIR PhCs, since a low resistivity wafer has poor transmission. However, due to brittleness of p-Si formed in high resistivity wafers and presence of high built-in potential after ion irradiation which renders etching difficult, high resistivity wafers are not used here. Overall, medium resistivity (0.4 Ω.cm) wafers produces good transmission (20%), and are suitable for structuring using CIBA process.

However, the choice of wafer resistivity should take multiple factors into consideration. For multilayer structures, a large range of porosity is needed. Highly microporous silicon is brittle,. Therefore, it is desirable to produce mesoporous silicon. In this case, a low resistivity (0.02Ω.cm) wafer is used where mesoporous silicon is preferentially formed.

8.3.2 Thermal annealing considerations

Optical transmission becomes weaker due to the presence of additional energy levels in the band gap introduced by defects. The large number of defects generated in the ion beam irradiation step of micromachining process need to be removed to reduce the scattering loss of light for optical applications.[112, 113] Usually, thermal annealing of samples at an appropriate temperature can remove these defects.[114, 115] Ref [116] shows that cell's photovoltaic parameters are restored to nearly to their pristine state by thermal annealing to about 500°C after irradiation with 4.6 MeV protons of fluence $1x10^{12}$proton/cm^2. Due to removal of vacancies and ion induced dislocations, the residual stress is relaxed. A thermal annealing processing of Si structures under ambient conditions can reduce the roughness, which has been discussed previously in [117, 118] in detail. Thermal oxidation and removal of the oxide is another way of adjusting the size of the structures.[118]

8.4 2D high aspect-ratio Si pillars on a Si substrate

Chapter 6 discussed the fabrication of high aspect-ratio pillars. The resistivity of the wafer used plays an important role in the minimum spacing, the shape of pillars and the aspect ratio of the pillars. Figure 8.8(a) shows pillars obtained in high resistivity (5 Ω.cm) wafer where direct nanobeam patterning with 2 MeV H_2^+ is used. Due to the huge built-in potential from the entire irradiated area, the etch current tends to get deflected away from the irradiated area, such that the central region is only slightly etched, giving a small pillar height (left part of Figure 8.8(a)), while the pillars have a greater height towards the edges. To reduce this effect, a low resistivity wafer should be used. Figure 8.8(c) shows pillars fabricated in medium resistivity (0.4 Ω.cm) wafer, in which the period was set to be 4.2 μm, and the fluence was set to be 1.25×10^8/point. Medium resistivity wafers provide a significant improvement in the shape and aspect ratio of pillars. To investigate the effect of a further decrease of resistivity of the wafer, the pillars in Figure 8.8(d) are fabricated in 0.02 Ω.cm wafer, for which a higher fluence of about 2.5×10^8/point is needed. The result shows a much more uniform distribution of pillar diameters along the depth compared to both 5 Ω.cm and 0.4 Ω.cm. Therefore, a 0.02 Ω.cm wafer is a better choice in order to achieve high aspect-ratio pillars with a uniform diameter, at the cost of higher ion fluence which translates to longer irradiation time. However, a 0.02 Ω.cm wafer has a high doping concentration of $3 \times 10^{18}/cm^3$ which causes a huge loss of the MIR beam due to scattering from the impurities, as discussed in the last section. Therefore, the wafer resistivity should be chosen carefully to achieve good structural features and low optical losses. The abrupt increase in the diameter of the pillars marked by yellow arrow in Figure 8.8(d) indicates that the etch depth reaches the end of range, and confirms that the more uniform part of the pillars is formed from the low defect region, and that the etch depth should be well below the range of ions, to produce strong, upright pillars.

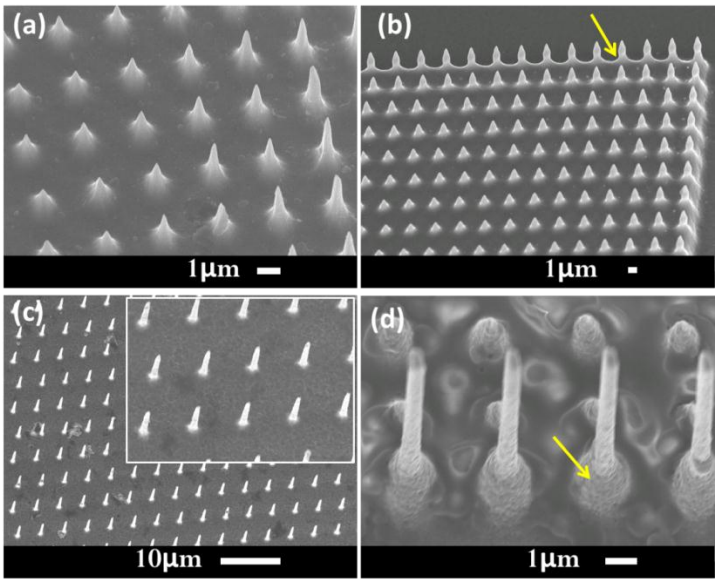

Figure 8.8 Pillars on different resistivity substrates. (a) 5 Ω.cm p-type Si, the edge of pillar area is shown; (b) 5 Ω.cm p-type Si, the edge of pillar area is shown; (c) 0.4 Ω.cm p-type Si, with period 4.2 μm, inset is the magnified figure; (d) 0.02 Ω.cm p-type Si, 3.5 μm several left pillars at the edge of a broken sample are shown. (1MeVproton with 16 μm range in Si, $1.25x10^8$/point for (a, b, c), $2.5x10^8$/point for (d))

Table 8.4 Comparison of three resistivity wafers in producing the pillar structures to form photonic crystals

Resistivity	Doping concentration	Ion fluence required	Scattering loss(quantify)	Uniformity of pillars	Formation of thick p-Si
5Ω.cm	$2x10^{15}/cm^3$	~ $10^{15}/cm^2$	Relatively low	Sharp top, thick bottom	Difficult, easy to crack
0.4Ω.cm	$4x10^{16}/cm^3$	~$10^{16}/cm^2$	High	Less uniform	Easy to crack, Need multiple etch and removal
0.02Ω.cm	$3x10^{18}/cm^3$	~$10^{17}/cm^2$	Extremely high	Uniform	Thick, Strong

Apart from the wafer resistivity, the etch current density also plays an important role. The pillars for 5 Ω.cm and 0.4 Ω.cm wafers with a single etching current density have a narrower diameter at the top and increased

diameter with depth due to the increased scattering width along the ion track. A higher current density overcomes the built-in potential and produces smaller dimension structures. Thus, in Figure 8.8(b), a varying current density is used. 100 mA/cm^2 produces much thinner pillars since the high applied electric field drifts more electrical holes towards the interface for the same defect density as compared to 10 mA/cm^2. Therefore, the pillars with a thin waist (marked by the yellow arrow) and a thick body can be formed with a varying current density, as shown in Figure 8.8 (b). However, this is most obvious at the edge of pillar area, due to a large deflection of current from the entire area in this resistivity wafer.

In conclusion, the comparison of three resistivity wafers in fabricating pillar structure is shown in Table 8.4. Proper choice in the resistivity of wafer, ion fluence, and etching conditions should be combined to produce photonic crystals for particular applications.

In addition to a uniform diameter and high aspect ratio, uniform periodicity and proper lattice type are equally important to produce photonic crystals. The 10^o proton beam writing line in CIBA suffers from bad orthogonality of the scanned areas, which was improved in next generation proton beam writing line.[34] The comparison of two square lattices of pillars written using these two beamlines is shown in Figure 8.9.

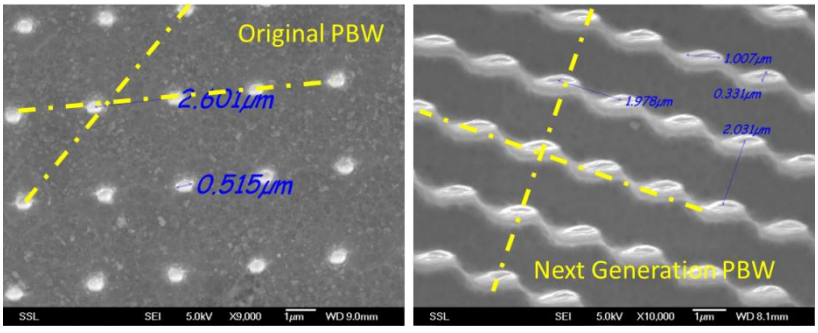

Figure 8.9 Comparison of orthogonality using two PBW beamlines.

As shown above, the next generation PBW line gives nearly perfect orthogonality and shall be used for producing photonic crystals using designs

implemented by our indigenously developed ion-scanning software IonScan.[42] (Appendix)

The maximum height of the pillars depends on the period required. For small periods, the pillars are so close to each other that they collectively deflect current away from the entire irradiation area. As a result, the etching at the outer edge of the pillar area is faster than the central regions. Meanwhile, a small spacing between the irradiated points causes an unwanted simultaneous etching of the tops of the pillars. Therefore, a smaller period typically results in a lower maximum height. However, a large pillar height is necessary for measurements using the FTIR microscope described further. When the size of the object is equivalent to the wavelength of the light, the diffraction of light is most obvious preventing the coupling of light into the structure. Diffraction is the effect of a wave spreading as it passes through an opening or goes around an object of the dimension comparable to the wavelength. When a wave encounters an obstacle, diffraction occurs, and this can be avoided in the case of a large pillar height. The pillar array is characterized from sideways in a cross-sectional view, as depicted in Figure 8.10(c). Therefore, the requirement of the pillar lattice is that the period of the lattice a ~ wavelength, height h >> wavelength. For getting such pillars, the low resistivity (0.02 Ω.cm) wafer is recommended.

Figure 8.10(a) shows the FTIR microscope in SSLS, with a spectra range of 400~ 7000 cm^{-1}. The microscope provides an easy way of characterizing the samples by locating them visually and focusing the light down to very small beam spot-sizes objectives. The microscope also offers ability to measure the transmission and reflection spectrum of the sample. The relevant photonic properties of the pillar structures can be characterized laterally on the FTIR microscope, as shown in Figure 8.10(b).

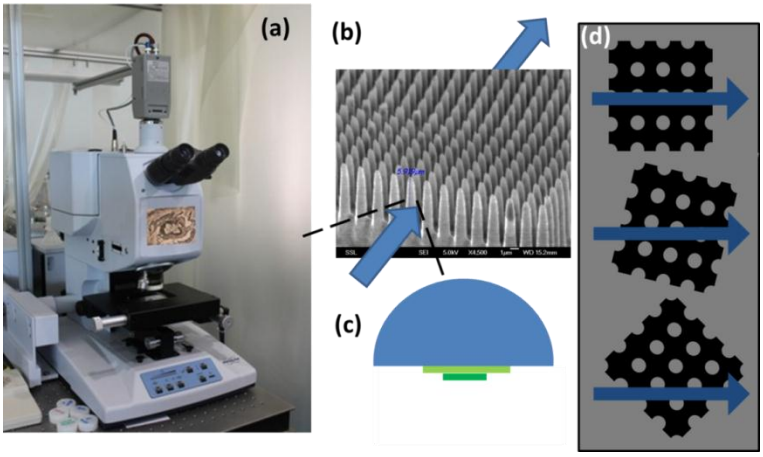

Figure 8.10 Measurements using the FTIR setup. (a) FTIR microscope; (b) Measurement of 2D photonic crystal in the periodic plane; (c) Schematics showing the way of mounting the sample (plane view); (d) Fabrication of equivalent structures with different orientation, to change the incident angle of the characterization with respect to structure .

One of the main problems in characterization of the photonic crystals is to change the angle of incident light accurately and automatically. One way is to rotate the sample, and the other is to fabricate an equivalent structure on the same sample with different orientations, as in Figure 8.10(d). In this way, angular bandgap dependence of the sample can be obtained from multiple measurements with samples fabricated at different angular positions.

The MIT photonic band package has been used to study the photonic band structure (PBS) for these photonic crystal structures. [119]The software is based on conjugate-gradient minimization of the Rayleigh quotient in a plane-wave basis.[120]

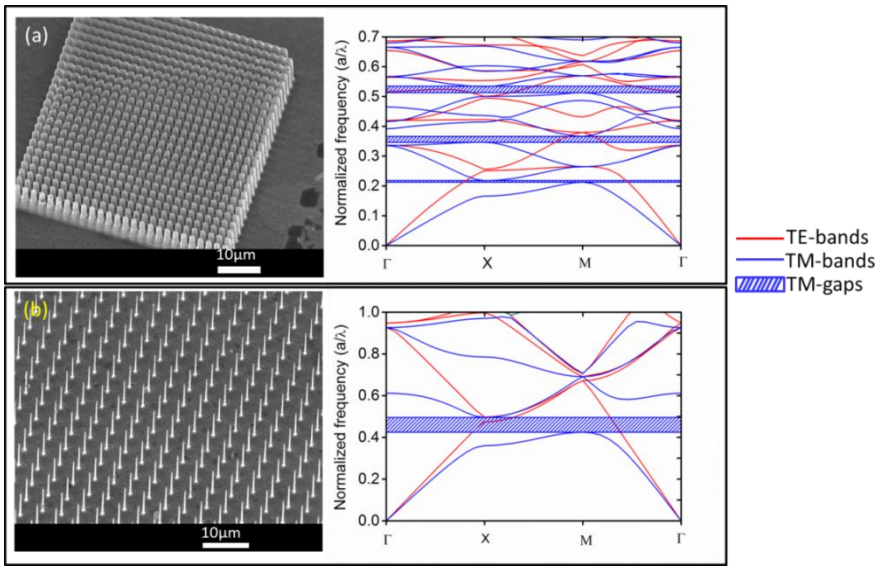

Figure 8.11 Photonic band structures of a square lattice of Si-pillars: (a) 2D-PBS of structure shown on the left, period of 2 μm with a large pillar radius *r*/lattice period *a*; (b) 2D-PBS of structure on the left, period of 4 μm with small *r/a*.

In the 2D calculations, we assume that the pillar height is many times longer than the wavelength range used for characterization. Therefore, the scattering due to finite z-dimensions has been neglected. Figures 8.11 shows the computed 2D-PBS for the experimental structures on the left respectively. In both figures, a TM photonic gap opens between the first and second band. However, the gap size is much higher in Figure 8.11(b). This is due to the different concentration factor in both structures. In Figure 8.11(b), the radius of the Si pillars is r =0.1a, where a is the lattice period, and the gap opens from 0.422 to 0.495 of the normalized frequency. While the radius of the Si pillar in the structure of Figure 8.11(a) is r=0.415a, and the gap opens from 0.210 to 0.218 of the normalized frequency. As the first photonic band concentrates its energy in the high dielectric constant region i.e. in the Si-pillar, the second band concentrates its energy in the low dielectric constant region, in order to be orthogonal to the first band.[121] When the ratio r/a is smaller, the different concentration factors between both bands increase, and the gap size is higher. If the radius of the Si-pillar is too small, the first band cannot concentrate its energy in them, and the gap disappears.

On the other hand, in Figure 8.11(a) other gaps open at higher frequencies. Between the third and fourth bands, a gap opens from 0.345 to 0.365 of the normalized frequency and between the sixth and seventh bands from 0.513 to 535. However, no TE gap opens in either structure. The flexibility of the fabrication process allows us to vary the radius of the Si pillar and the lattice period, to tune the band gaps for a specific application. However, due to the difficulties in characterization using FTIR, the experimental results have not been obtained and are still under progress.

To further decrease the period of the structures to move towards near IR, a 0.02 Ω.cm wafer and lower irradiation energy needs to be used. However, the structural height is very small and the incident light also suffers from high scattering losses. As observed from Figure 8.12(a), (b), the height of the pillars is less than the etch depth because of simultaneous etching at both irradiated and non-irradiated regions. Thus, an optimization of ion fluence, ion energy, etching current density and etching time is needed for achieving a designed pillar height for these small period structures. However, using direct nanobeam writing method, it is not applicable to fabricate such structures. To achieve period as small as hundreds of nms, proton energy has to be low enough to have small scattering. But such low energy is difficult to focus due to its low beam current in our accelerator designed to operate at energy as high as 2MeV. Therefore, electron beam lithography is used to produce photoresist patterns on silicon surface and then the patterns are transferred to silicon after ion irradiation and removing photoresist pattern. This work is still under progress.

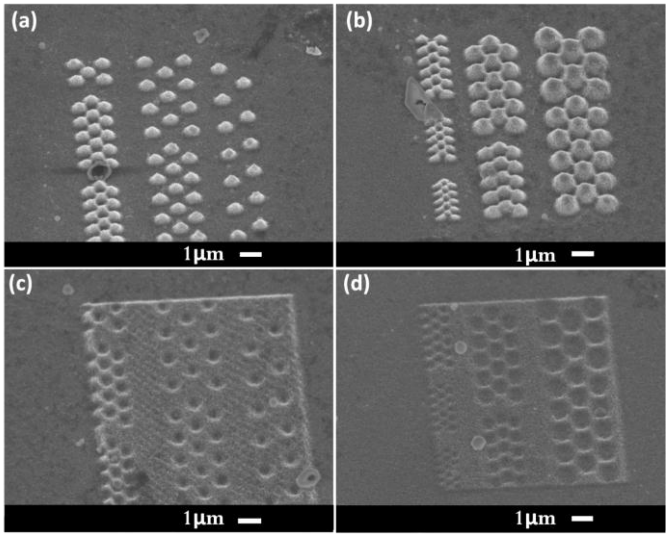

Figure 8.12 Pillars or air holes, with hexagonal lattice, irradiated with a 500 keV H_2^+, ion fluence $3x10^{15}/cm^2$, and etched to a depth of 1.7 µm on 0.02 Ω.cm wafer, porous silicon removed: (a) uniform diameter 500nm, but different period; (b) same period, but different diameter. Air hole with hexagonal lattice, irradiated with 500 keV H_2^+, etched with depth 1.77 µm on 0.02 Ω.cm wafer, porous silicon removed: (c) uniform diameter, different period, ion fluence $1x10^{15}/cm^2$; (d) same period, different diameter, ion fluence $3x10^{15}/cm^2$.

8.5 2D Si, p-Si, and glass Photonic slabs

Instead of making pillars, we can also design inverse patterns to form air/p-Si holes in a silicon matrix, Figure 8.12(c), (d). However, due to low ion fluence, the depth of the hole is so small that it does not make a good 2D photonic crystal. To increase the depth of the hole, higher ion fluences were used, for which a higher etch current density needs to be applied, Figure 8.13, where 300 mA/cm^2 was used instead of commonly used 40mA/cm^2. For the same period, for a larger hole diameter, with same fluence, lesser defects occur in the irradiated regions. Thus, the etch rate is faster, as shown in Figure 8.13(a).

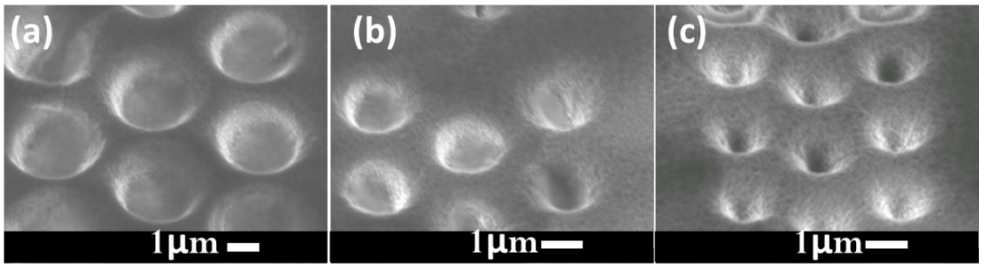

Figure 8.13 Air holes in silicon matrix with a hexagonal lattice, fluence 1x10^{17}/cm^2, on 0.02 Ω.cm wafer, etched at 300mA/cm^2 for 18.5 s, with different hole diameters.

To move towards photonic crystals in near infrared (NIR) operating wavelength regime, a lower ion energy and smaller beam spot size is needed, as in Figure 8.14. A 30 keV Helium beam with 0.5 nm spot size was used to write the square lattice of air hole patterns on 0.4 Ω.cm wafer, which was then etched in 24%HF at 60 mA/cm^2 for 3 s, and the porous silicon was removed by KOH solution. To get smoother features, the sample was oxidized at 1000 C^o for 20 mins, and the oxide was removed in dilute HF. Figure 8.14 shows the 3D AFM profile of square lattice air holes, with a fluence of 5x10^4/point and a period of 1 µm.

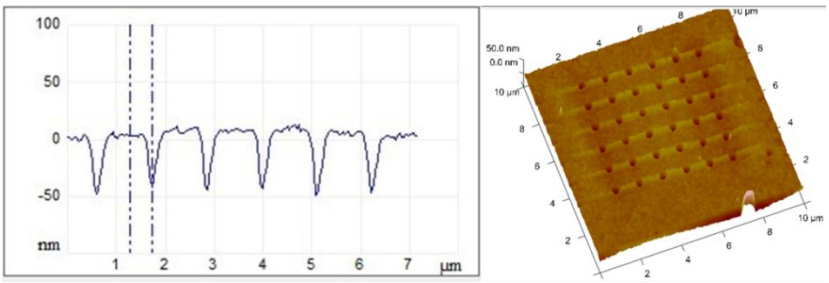

Figure 8.14 NIR air hole PhCs fabricated by Helium Ion Microscope irradiation and etching.

The above structures are all 2D, which only confines photons in the plane, requiring z dimension to be large, ideally infinite. 2D photonic crystals with finite height, called photonic crystal slabs, have been widely fabricated and studied. These structures confine the light in the third direction based on total internal reflection instead of a photonic band gap. [122] Figure 8.15(a) shows a structure obtained accidentally in one experiment which was aimed at fabricating wires at different depths. Direct nanobeam patterning was used. Due to a failure in achieving different energies, lines in horizontal and vertical directions were written on the same level, such that the defect density of intersecting points was higher than the other irradiated parts. The resultant circular and elliptical air gaps in the silicon matrix show an extra method of fabrication air/porous silicon hole slabs, Figure 8.15(b), where horizontal and vertical lines were irradiated at the same area with 500 keV H_2^+ ions in 0.4 Ω.cm wafer, and the p-Si was removed subsequently.

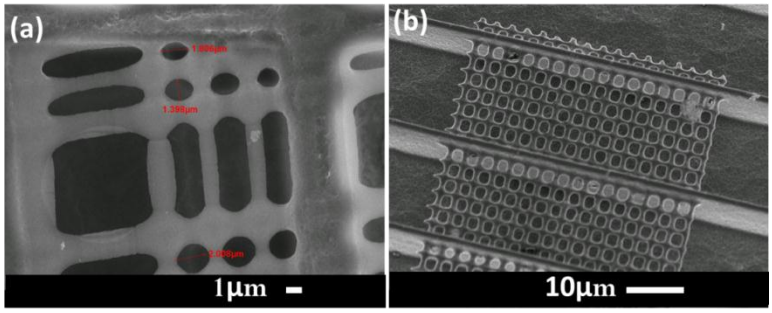

Figure 8.15 Air holes from intersecting wires. (a) Formation of circular or elliptical region from intersecting irradiated lines; (b) Free-standing air hole slab based on intersecting irradiation lines, with period of 3 µm.

An obvious advantage of using this method is that it can produce large area photonic crystal slabs, since the 'line scan' mode in the proton beam writing line can be used instead of 'point scan' mode used for all the previous pillars and holes. In line scan mode, the focused beam is scanned along a line while the stage is moved at a fixed speed, where the size of the scanned area can be as long as the distance the sample stage can move, ~20 mm in this case. In comparison, in point scan mode the maximum scanned area is 500 µm x 500 µm. This method is highly flexible due to variability of variety of factors, such as ion fluence, line spacing, ion energy, wafer resistivity, etching current density, etc. Figure 8.16 shows 2D photonic crystal slabs fabricated with different line periods and hole diameters by varying line spacing and ion fluence.

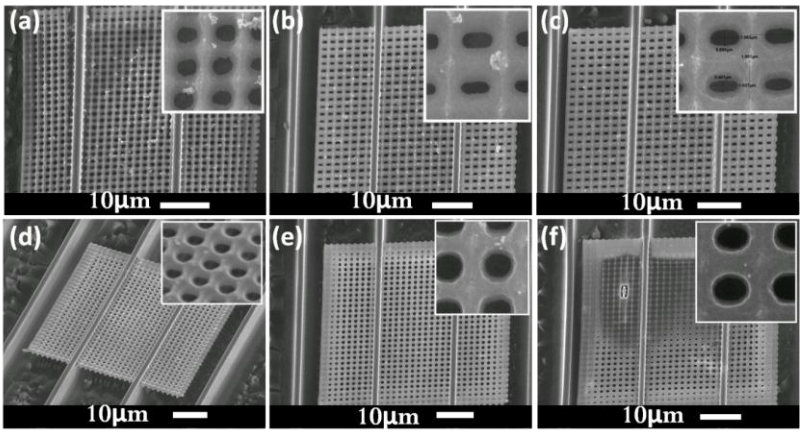

Figure 8.16 2D photonic crystal slabs with different line period and hole diameter in on 0.02Ω.cm wafer, with the p-Si removed: (a) line period 2µm, fluence $5x10^{15}/cm^2$; (b) line period 2µm, fluence $8x10^{15}/cm^2$; (c) line period 2µm, fluence $1x10^{16}/cm^2$; (d) line period 1.5µm, fluence $5x10^{15}/cm^2$; (e) line period 1.5µm, fluence $8x10^{15}/cm^2$; (e) line period 1.5µm, fluence $1x10^{16}/cm^2$.

Figure 8.16(a), (b), (c) show planar views of slabs with periods of 2 µm, and different hole diameters produced by direct nanobeam patterning using various ion fluence while keeping the etch current density constant. Figure 8.16(d), (e) and (f) are produced with the same ion fluence as the figure directly above, but with a smaller period of 1.5 µm. It is observed that smaller periods are more difficult to resolve, for the same fluence, especially for a high fluence. Interestingly, opposite to what was observed in fabricating arrays of pillars, the edges of the air hole slabs are not etched. The reason is that for pillar structures, the electrical holes drifting from the back wafer surface are deflected away from the entire region by the very high defect density (ten times higher than the air hole slab) in the high defect region, such that the central region does not have enough available holes. However, for the air hole slab structures, the low defect regions are etched away, and the holes are diffused into the surrounding of high defect regions, which is stronger inside the slab area. For a low fluence, as the line period increases the influence of doubled fluence in intersecting parts is not big enough to form circular region, and the holes have round corners as in Figure 8.17 (a) and (b).

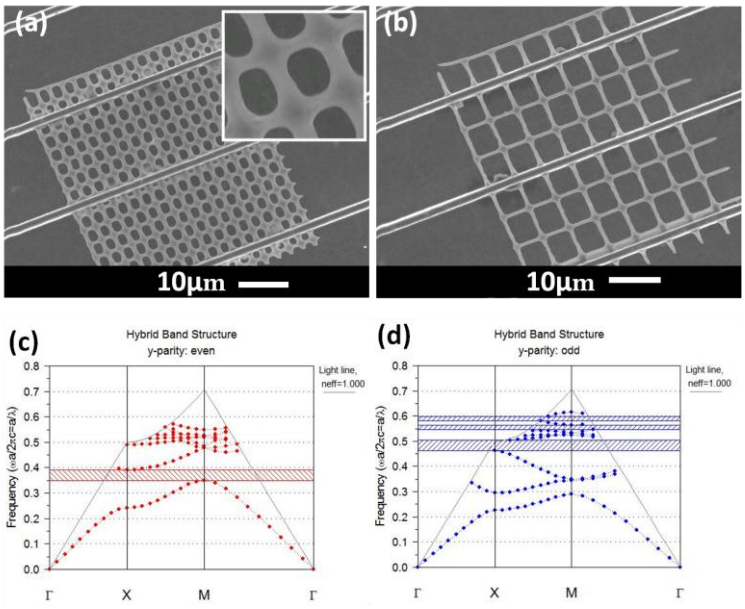

Figure 8.17 SEM images and photonic band structure of square lattice of holes. (a) Square lattice of circular air holes, with a period of 3 µm; (b) square lattice of square air holes, with period of 6 µm; (c) photonic band structure with odd-parity even for structure in (b); (d) photonic band structure with odd-parity odd for structure in (b).

Figure 8.17(c), (d) show the simulated photonic band structure from RSoft of the structure in figure 8.17(b). The shapes of the air hole could be changed from circular to elliptical by varying the line fluence of horizontal and vertical lines; the shapes of square hole can also be changed from square to rectangles by varying the fluence.

MPB (MIT Photonic Bands) is used to compute PBS of this quasi-3D PhC. The eigenstates of the slab are calculated first using preconditioned conjugate-gradient minimization of the Rayleigh quotient in a plane-wave basis. Then, the light cone is overlapped. A z-supercell approach assuming a periodic sequence of slabs separated by enough background region is used. [123]

Figure 8.18 shows PBS for a square lattice of cylindrical air holes in a silicon, where the ratios r/a and h/a where a line fluence of $5x10^{10}$ proton/cm and a current density of 300 mA/cm^2 experiment data are used.

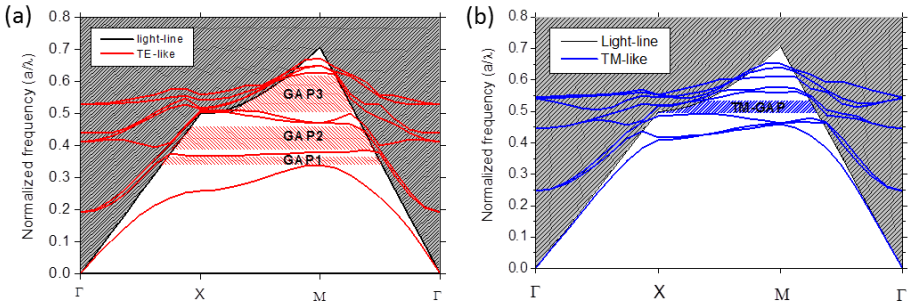

Figure 8.18 Photonic bands structure of a square mesh of cylindrical air holes in a Si matrix. Ratios r/a=0.38 and h/a = 0.4, ε=11.56. (a) shows slab bands with even symmetry with respect to the z-plane (TE-like). (b) presents slab bands with odd symmetry with respect to the z-plane.

In Figure 8.18(a), several gaps can be observed below the light cone for the bands with even symmetry (TE-like) with respect to reflections through the z-plane (z direction being the slab height direction). The largest gap opens from the 4th to 5th bands, between 0.503 and 0.617 of the normalized frequency. In this structure, a gap also appears for the bands with odd symmetry with respect to the z-plane (TM-like) below the light cone. This gap shares a range of frequencies with the third gap for the TE-like bands. Hence this structure has a complete photonic gap between 0.503 and 0.535 of normalized frequency. However, due to the difficulties of characterization of these thin slab structures, experimental results have not been obtained. This work is still under progress.

The frequency ranges where the gaps open depend on the lattice parameter of the structure, hence, by controlling the period, the frequency range where these structures operate, can be tuned. The fabrication process allows control of the period by changing line spacing of the proton beam when the structure is being irradiated. Figure 8.19 presents different frequency ranges of the gaps for several different periods of the photonic slab.

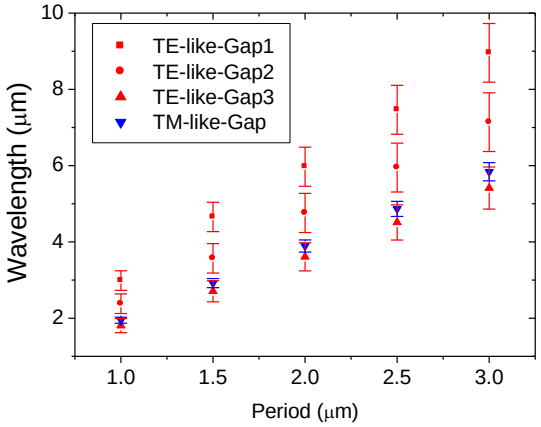

Figure 8.19 Frequency ranges of the gaps for different periods, for a square mesh of cylindrical air holes in a Si matrix, where ratio r/a and h/a were set as 0.38 and 0.4 respectively. Dielectric constant of Si was set as ε=11.56.

The frequency range can be tuned over the NIR-MIR range by changing the period of the structure from 1 μm to 3 μm. Once the frequency ranges where the structures operate is determined by fixing the period, a minor tuning of these frequency ranges can be carried out by changing the thickness of the slab and radius of the cylindrical air holes. These two parameters can be tuned by changing two main factors in the fabrication process, line fluence of the ion beam during the irradiation process, and applied current density in the electrochemical anodization. To study the effect of proton fluence and applied current density on the ratios r/a and h/a, lines lengths of a few millimeters were irradiated on Si with different proton fluences. The irradiated zones were electrochemically anodized by applying different current densities. For a square lattice of an air hole slab, the relationship between the radius of the air holes and core-width is given by $r = [a - \text{core width}]/2$, whereas the slab thickness is equal to the core height h.

As the proton fluence is increased, the core width and core height are larger, thus, the ratio r/a decreases, whereas h/a increases for all of current densities. Besides for a fixed proton fluence, the higher the applied current density is, the smaller the core size is and the higher the ratio r/a, the smaller the ratio h/a becomes. The effect of varying the proton fluence and the current density on

the optical properties of these structures was studied. Figure 8.20 shows the frequency ranges of the photonic gaps for the different line fluences and current density, when the period was fixed as 1.5 μm. Gap size is defined as $Gap(\%) = \frac{\Delta\omega}{\omega c}$ ·x 100, where ω is the normalized frequency, $\Delta\omega=\omega_{band\text{-}n} - \omega_{band\text{-}n\text{-}1}$ and ω_c= central frequency of the gap.

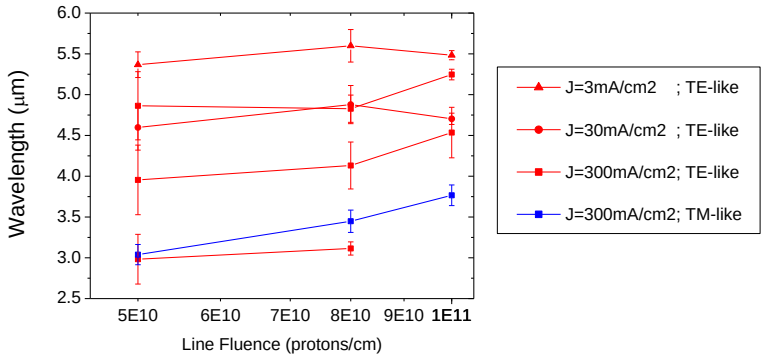

Figure 8.20 Computed frequency ranges of the photonic gaps for different line fluences and current densities, when the period was fixed to 1.5 μm.

When the etch current density is increased to 300mA/cm^2, new gaps open for both symmetries. For the first TE-like gap, between 1st and 2nd band, the gap size is more than 17% for a low fluence (5x10^{10} protons/cm). The second TE-like gap, between the 2nd and the 3rd band, shows its maximum size for a low fluence (22%). A complete gap for all the symmetries only appears for the lowest line fluence (5x10^{10} protons/cm). The fabrication process allows tuning of the frequency at which the gaps open, by simply changing two main factors, the ion fluence during irradiation, and the etch current density. Fixing the lattice parameter to 1.5 μm, TE-like gaps can be tuned over a large frequency range over the NR-mid infrared, from 2.4 to 6 μm. Moreover, the gap size can be modified too, allowing setting the frequency range where the gap opens for its proper applications. This process can be extended to a range of visible and near-IR wavelengths by decreasing the period, and using suitable proton fluence and etch current density. Nevertheless, a TM-like gap is not so flexible since it only appears for a high current density of 300mA/cm^2. However, it can also be modified by changing the ion fluence. Also, a complete gap only

appears in special cases, but due to the flexibility of the method, the experimental parameters can be chosen to obtain these special cases.

For measurements in the FTIR microscope, the above height is too small. For example, the maximum height of 500 keV H_2^+ is only 2.5 μm. To achieve a greater height,1 MeV H_2^+ ions, instead of 500 keV H_2^+ were used with a high fluence, following Figure 8.21, where on 0.02 Ω.cm wafer 1MeV H_2^+ ions were used to write the wires and 2 MeV protons with a fluence of $1x10^{14}$protons/cm were used to write the supports. The sample was etched at 40mA/cm^2 in 24%HF for 8mins. Then the sample was polished and p-Si was removed by KOH solution on and the sample was oxidized at 1000C^o for 1 hour, and then the oxide was removed by immersing the sample in 24% HF for 1 hour. Comparison of parameters of these four structures is listed in Table 8.5.

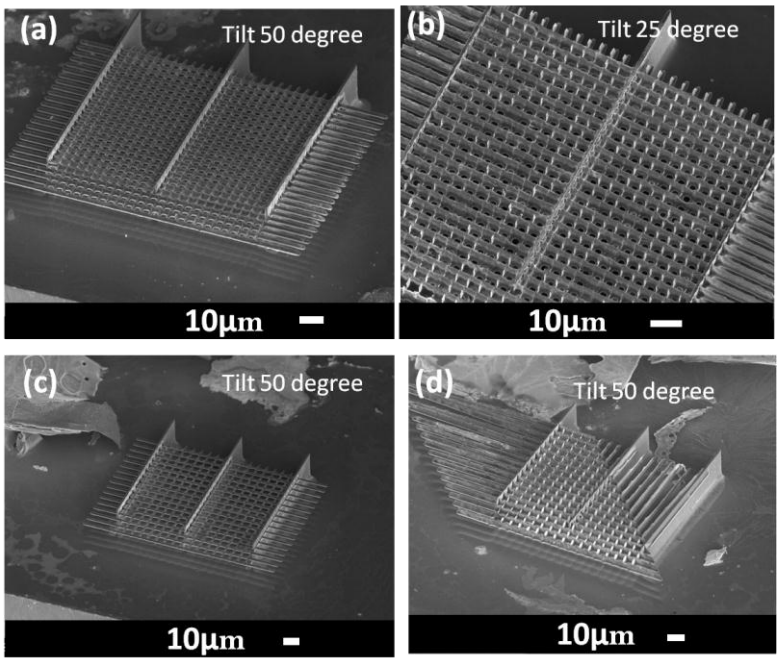

Figure 8.21 Tilted SEM images of four structures for which the parameters are shown in following table.

Table 8.5 Structural parameters of photonic crystal slabs in Figure 8.21

Sample No	Period(µm)	Height(µm)	Ion fluence(/cm^2)	r/a	h/a
(a) 1	4	2.34	4.9/4.7x10^{16}	0.307	0.584
(b) 2	6	4.6	2.4/2.3x10^{17}	0.21	1
(c) 3	6	2	4.9/6x10^{16}	0.35	0.33
(d) 4	4	4.01	2.4/3x10^{17}	0.305	0.76

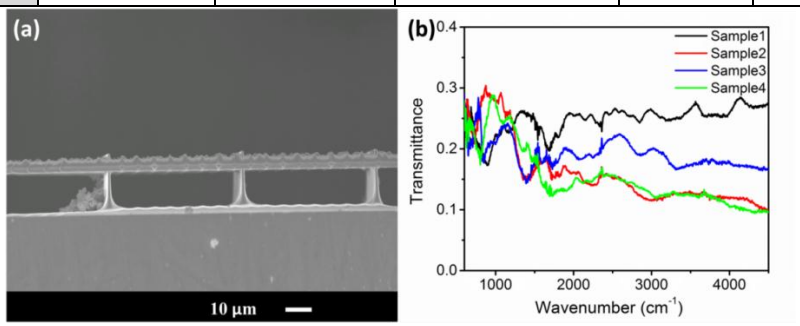

Figure 8.22 Preliminary measurement spectra of air hole slabs. (a) Cross section view of Figure 8.20(b), in which way the samples are mounted in

FTIR microscope; (b) Transmission spectra from four samples in Figure 8.20.

FTIR results in Figure 8.22 for these four slabs show that sample 1 transmission differs a lot from the rest of samples. To study the photonic band gap properties and find complete gaps, more measurements based on various incident angles and further optimizations are needed and this work is still in progress. Characterization of such structures using the FTIR microscope is obviously very difficult due to limited slab height. Instead, due to its large area, measurements using an ellipsometer may be a good choice, which is still under progress. A simple comparison between the air hole slabs and pillar structures is shown in Table 8.6.

Table 8.6 Comparison of air hole slabs and silicon pillar structures

Structure	Defect region	Measurement	Lattice type	Area of structures	Confinement of photons
Slab	High defect region	Ellipsometer	Square lattice	Large, can be ~cm2	2D Photonic band gap
Pillars	Low defect region	Ellipsometer, FTIR microscope	Arbitrary	Small, ~(50-500μm) 2	2D photonic band gap+ internal reflection

p-Si can be infiltrated with different media such as water, IPA, or liquid crystals, to tune the photonic band gap. Besides, it can have variable porosity, with variable refractive index. Figure 8.23 shows the gap-map of porosity for a photonic slab of square lattice of porous silicon hole in silicon matrix, with r/a=0.3125, and h/a=0.75, where r is radius of the porous silicon hole, h is thickness of slab, and a is period of lattice.

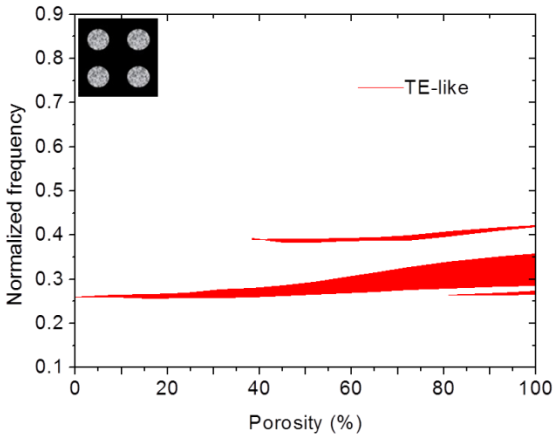

Figure 8.23 Gap-map of photonic slab of square lattice of porous silicon holes in a silicon matrix, with r/a=0.3125, and h/a=0.75.

The above structures are all made of silicon and another dielectric, either porous silicon or air. Here a fabrication method for making photonic crystals based purely on porous silicon is proposed and the initial results are shown.

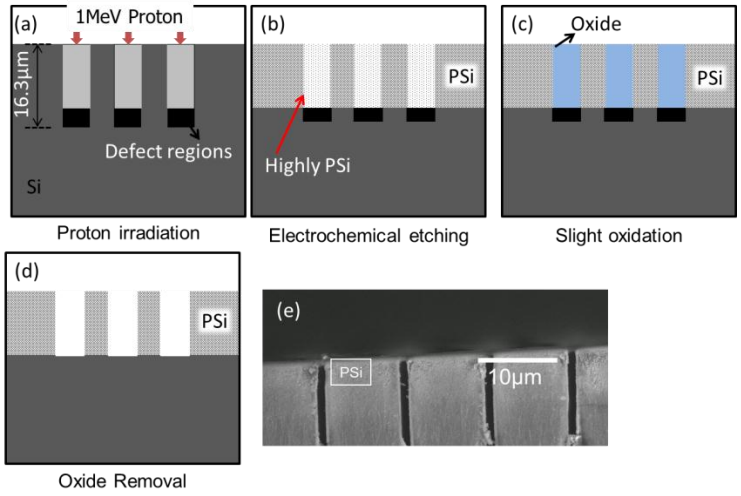

Figure 8.24 Trenches formation in p-Si under moderate fluence irradiation: (a) Proton beam writing and induced defect regions; (b) formation of porous silicon during electrochemical etching process; (c) oxidation of highly porous silicon regions in air; (d) removing the oxidized regions to produce air trenches in porous silicon matrix; (e) Cross sectional SEM image of trenches in porous silicon.

In Figure 8.24, direct nanobeam patterning with 1 MeV protons with a moderate fluence was used. The low defect density column forms high porosity silicon, while the high defect density region deflects the current away, so these regions remain as silicon. In the etching process, p-Si with higher porosity forms in the low defect density region surrounded by lower porosity silicon. The higher porosity silicon is easily oxidized in air, removing which, leaves behind trenches or holes in a porous silicon matrix. Figure 8.24(e) shows a cross section SEM image fabricated with 1 MeV protons with 1 μm line width on the surface, and a line fluence of $4x10^{11}$/cm, with a spacing of 10 μm, in 0.02 Ω.cm wafers.

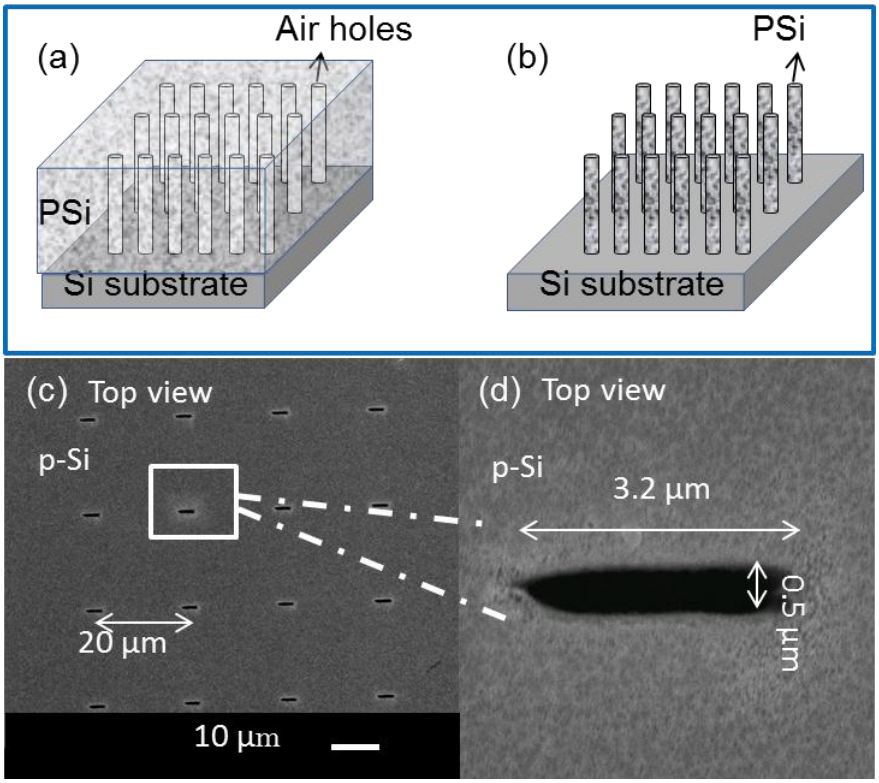

Figure 8.25 p-Si PhCs fabrication methods. (a) Air holes in porous silicon matrix on silicon substrate; (b) Porous silicon pillars on silicon substrate.

2D porous silicon based photonic crystals with air holes in a porous silicon matrix in the MIR range can be obtained by point irradiation and shrinking the spacing between the holes down to the size needed for the mid-infrared range, as shown in Figure 8.25(a). Such air hole structures in a porous silicon matrix have a greater height than air hole slabs in a silicon matrix which has a limited slab thickness, thus, solving the problem faced in characterization using FTIR. Similarly, by irradiation of intersecting lines as in the fabrication of air hole slabs in a silicon matrix, circular-shaped porous silicon regions form at moderate fluences, as shown in Figure 8.25(b). Figure 8.25(c) shows top view of a square lattice of air hole in p-Si matrix with a period of 20 µm, and estimated depth of ~40 µm. The magnified image of one of the air holes is shown in Figure 8.25(d), which shows the air hole is a rectangle with sides of 3.2 µm and 0.5 µm.

The p-Si photonic crystals could be turned into glass photonic crystals by a thermal annealing step where porosity, annealing conditions are carefully chosen.

8.6 Modified porous silicon multilayer

Ref. [124] discusses 2D photonic crystal fabricated by multilayers stacked by an appropriate combination of sputter deposition and sputter etching, in Figure 8.26(a). Measured results in (b) and simulation results in (c) show photonic band gaps in the visible range. Multilayers of porous silicon with alternate porosity can be modified to fabricate 2D porous silicon based photonic crystals. Porous silicon based Bragg reflectors have been widely studied, including the effect of ion irradiation to reduce the etching rate and cause a blue shift of the response. Here direct nanobeam patterning with 1 MeV protons, focused to 100nm, are used to modify the Bragg reflector profile, with the aim of fabricating a 2D photonic crystal based on a modified Bragg reflector by inducing a periodicity in the direction parallel to the surface. Fourier transform infrared spectroscopy (FTIR) was used to measure the transmission spectra. Figure 8.26(d) shows a cross section SEM image of a porous silicon multilayer where a 0.02 Ω.cm p-type silicon wafer was etched at an alternating current density of 50 mA/cm^2 for 15 s and 85 mA/cm^2 for 15 s in 12% HF (48%HF:ethanol: DI water =1:2:1). Figure 8.26(e) shows a cross section SEM image of a modulated porous silicon multilayer where the wafer was irradiated with a 100 nm wide 1 MeV proton beam to a line fluence of 1×10^{11}/cm, with a lateral period of 1 μm, with etching conditions the same as in Figure 8.26(d).

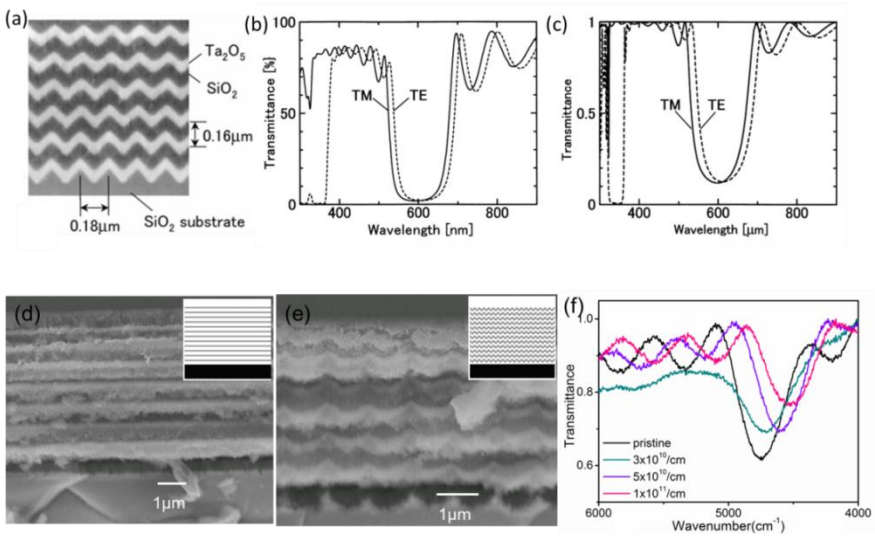

Figure 8.26 (a~c)2D photonic crystals based on multilayers stack (Reproduced from Ref. [124]): (a) Cross section SEM photograph; (b) Measured transmission spectra; (c) Simulated transmission spectra. (d~f) Modulated multilayer p-Si: (d) Cross section SEM of a porous silicon multilayer (inset shows the dielectric constant variation); (e) Cross section SEM of modulated porous silicon multilayer (inset shows the dielectric constant variation); (f) Transmission spectra of structures in (a) and modulated multilayer by three different line fluences.

By varying the line fluence, the curvature of the modulated profile is changed. The higher the line fluence is, the larger is the curvature, and hence a greater modulation of the transmission spectrum. However, a proper design of the irradiation period, the layer thickness and porosity is needed to achieve the 2D photonic crystal of choice. Figure 8.26(c) shows the transmission spectra of the modulated porous silicon multilayers with three different line fluences, compared to the pristine multilayer, measured using FTIR at an incident angle of 0˚. The right shift of the dip is attributed to a reduction in etching rate. The dip becomes shallower as the line fluence increases. The analysis and comparison with simulation, as well as further optimization of the structure are still under progress.

8.7 3D photonic crystals

The first type of structure is a simple cubic lattice with air blocks distributed periodically in 3 directions. Horizontal wires and vertical wires arranged in different depth levels touching with each other produce such structures. True 3D silicon micromachining is achieved by changing the ion energy, to tune the depth of end of range regions. However, accurate alignment is difficult for different level structures due to ion beam drift and stage positioning inaccuracy. To solve the alignment problem, an aluminum membrane was translated across the silicon wafer surface to reduce the ion beam energy without changing the terminal voltage of the accelerator (section 6.2.5). In Figure 8.27(a) a bi-layer array of silicon wires fabricated using 1000 keV and 800 keV H_2^+ is shown. Their range in silicon is 6.1 μm and 4.5 μm respectively. In Figure 8.27 (b) two layers were fabricated by 1000 keV H_2^+ with and without 3 μm aluminum foil, respectively. In Figure 8.27 (c) three layers were fabricated by 1000 keV H_2^+ with and without 3 μm aluminum foil, and 800 keV H_2^+.

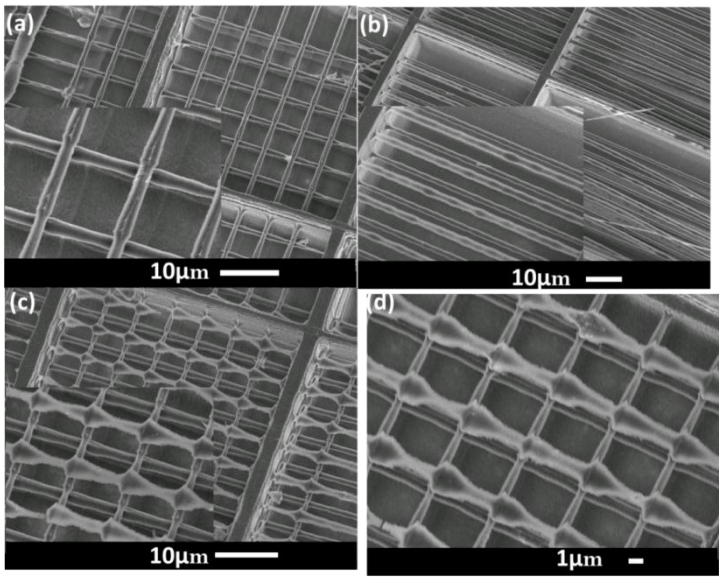

Figure 8.27 Three layer wires. (a)1000keV H_2^+:3x10^{10}/cm; 800keV H_2^+: 8x10^{10}/cm; (b) 1000keV H_2^+ without foil: 3x10^{10}/cm, with foil: 3x10^{10}/cm; (c) 1000keV H_2^+ without foil : 5x10^{10}/cm, 1000keV H_2^+ with foil: 5x10^{10}/cm,

800keV H_2^+ without foil: 5x10^{10}/cm, tilt view, inset is its magnified image ; (d) top view of structure in (c).

Figure 8.27(d) shows the top view, from which it shows that the wires on the first and third level are well aligned. By tuning the ion fluence, the wire width could be optimized.

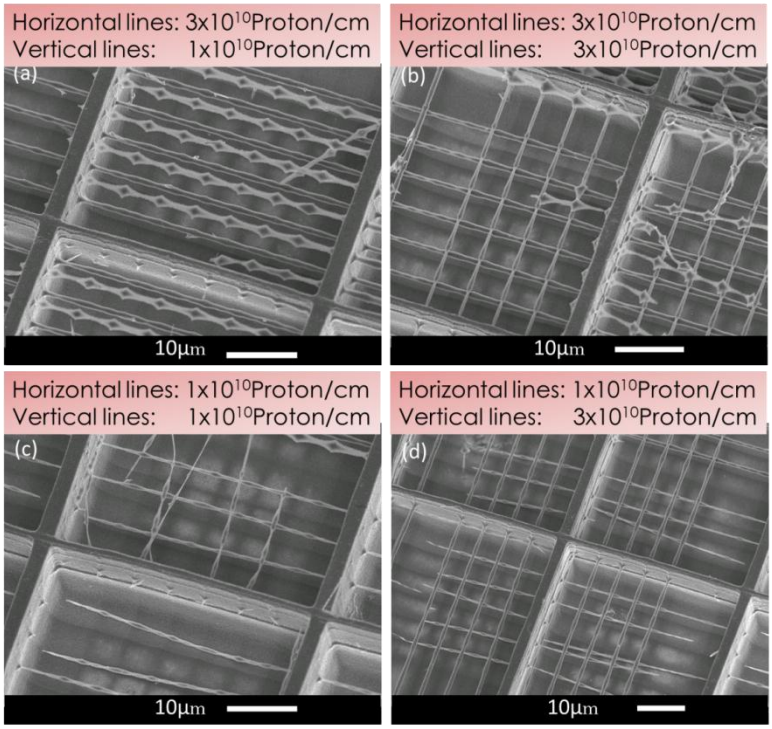

Figure 8.28 Fluence optimization of three layer wires. (a) 1000keV H_2^+ without foil and with foil: 3x10^{10}/cm, 800keV H_2^+: 1x10^{10}/cm; (b) 1000keV H_2^+ without foil and with foil: 3x10^{10}/cm, 800keV H_2^+: 3x10^{10}/cm; (c) 1000keV H_2^+ without foil and with foil: 1x10^{10}/cm, 800keV H_2^+: 1x10^{10}/cm; (d) 1000keV H_2^+ without foil and with foil: 1x10^{10}/cm, 800keV H_2^+: 3x10^{10}/cm.

Figure 8.28(a) shows that for very low fluences the wires are so thin that they break. It was used as an example of modulated wires in chapter 6. In (c), the fluence for each of the three layers is 1x10^{10}/cm, for which only the layer using 1000 keV H_2^+ without a foil survived. This indicates that the layer with 1000keV H_2^+ with foil needs higher fluence than the layer without foil, 800 keV H_2^+ needs higher fluence than the layer below it due to both focusing effect of current and gap between wafer surface and the foil. By increasing the

fluence of the 800 keV H_2^+ layer to $3x10^{10}$/cm, as in (d), this layer is robust enough to remain intact. By increasing the fluence of 1000 keV H_2^+ without foil and with foil to $3x10^{10}$/cm, these two layers survived, while the 800keV H_2^+ layer is completely dissolved away. Increasing the fluence of three layers to $3x10^{10}$/cm did not produce three layers of wire, instead, the layer with foil was dissolved away due to focusing of current from the 800 keV H_2^+ layer. Therefore, for fabrication of 3D photonic crystals using multiple energies, the fluence should be optimized since all the layers are dependent on each other.

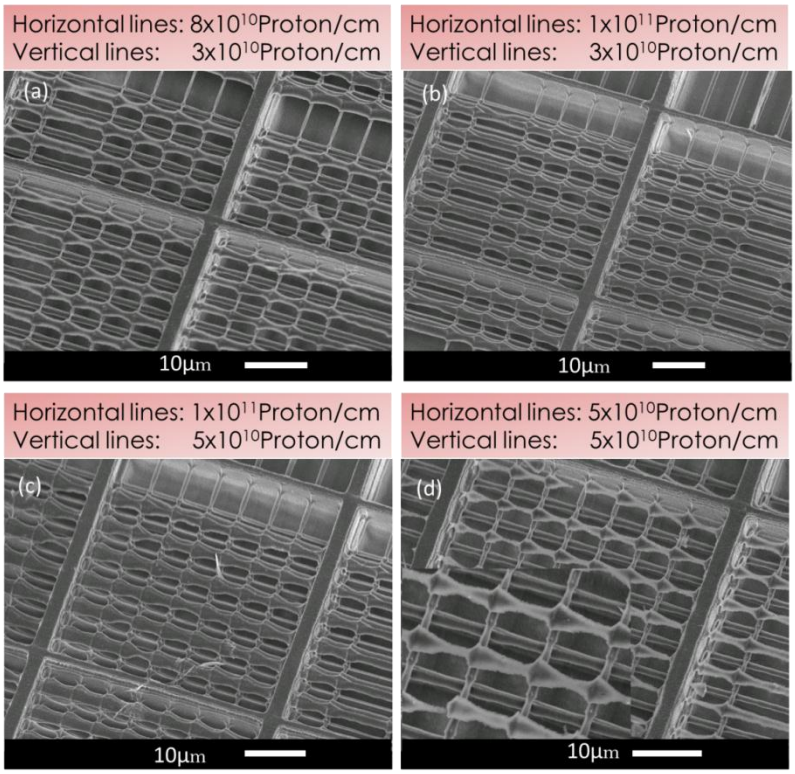

Figure 8.29 Fluence optimization of three layer wires. (a)1000keV H_2^+ without foil and with foil: $1x10^{10}$/cm, 800keV H_2^+: $3x10^{10}$/cm; (b) 1000keV H_2^+ without foil and with foil: $8x10^{10}$/cm, 800keV H_2^+: $3x10^{10}$/cm; (c) 1000keV H_2^+ without foil and with foil: $1x10^{11}$/cm, 800keV H_2^+: $3x10^{10}$/cm; (d) 1000keV H_2^+ without foil and with foil: $1x10^{11}$/cm, 800keV H_2^+: $5x10^{10}$/cm; (h) 1000keV H_2^+ without foil : $5x10^{10}$/cm, 1000keV H_2^+ with foil: $5x10^{10}$/cm, 800keV H_2^+ without foil: $5x10^{10}$/cm.

The fluence of the 800 keV H_2^+ layer was kept at $3x10^{10}$/cm, and the fluence of the two other layers was increased to $8x10^{10}$/cm, as in Figure 8.29 (a), and $1x10^{11}$/cm, as in (b), where all the three layers survived, but the second level

structure was very thin, and top layer too thick. Based on (b), the fluence for 800 keV H_2^+ was increased to $5x10^{10}$/cm, as in (c), and fluence for 1000 keV H_2^+ without foil and with foil decreased to $5x10^{10}$/cm, as in (d). Therefore, the fluence in (d) is relatively good after the optimization process. In conclusion, in fabrication of 3d photonic crystal using multiple energies, the following factors are important and need optimization. Table 8.7 lists the influence of variety of factors of fabrication on properties of 3D photonic crystals.

Table 8.7 Variety of factors that influence structure parameters and 3D photonic crystal properties

Factors	Stage accuracy, Beam stability	Choice of Energies	Ion fluence
Structure parameters	Good alignment between different levels, and affect the fluence needed.	Proper periodicity in the vertical direction	Size, shape of the wires
Photonic Crystal property	Periodicity in 2D plane	Periodicity in the 3rd direction	Size of band gap

Characterization of such 3D photonic crystal is relatively easy using a FTIR microscope, an ellipsometer, and an IFS 66v/S (high performance research grade FTIR spectrometer). Therefore, for characterization of 3D photonic crystals using FTIR, the size should be designed with photonic band gap in the range where IR beam can pass through the thick substrate without significant loss.

Another type of 3D photonic crystal is a woodpile structure, where the third level of wires are moved half of period away from the first level, and the fourth level of wires are moved half of period away from the second level. However, the fluence of each layer will be affected due to variation in relative locations, which shall be optimized accordingly, as in above discussions.

Modulation of pore size of macroporous silicon to fabricate 3D photonic crystal was reported. Figure 8.30 (a) shows the cross-sectional image.[125] In this reported work, the illumination intensity and time in the anodization process of n-type Si was modulated to achieve a periodic change in diameter along the depth. By adjusting the modulation period, the dispersion relation

along the pore axis can be controlled nearly independently from the dispersion relation in the plane perpendicular to it. The transmission along Γ-A was measured using a Fourier transform infrared spectrometer equipped with a globar source, a KBr beamsplitter and a mercury cadmium telluride detector. The measured spectrum is shown in Figure 8.30 (b). Indeed around a wave number of 1500 cm^{-1} a distinct drop of the transmission can be observed. This agrees well with the theoretically predicted band gap in this region indicated by the gray shaded bar on the right.

We propose fabrication of 3D photonic crystal by modulation of the pillar diameter by either changing the current density, or an overlapped irradiation to create regions with increased defect density but using a constant etching current density, as in Figure 8.30 (c), (d).

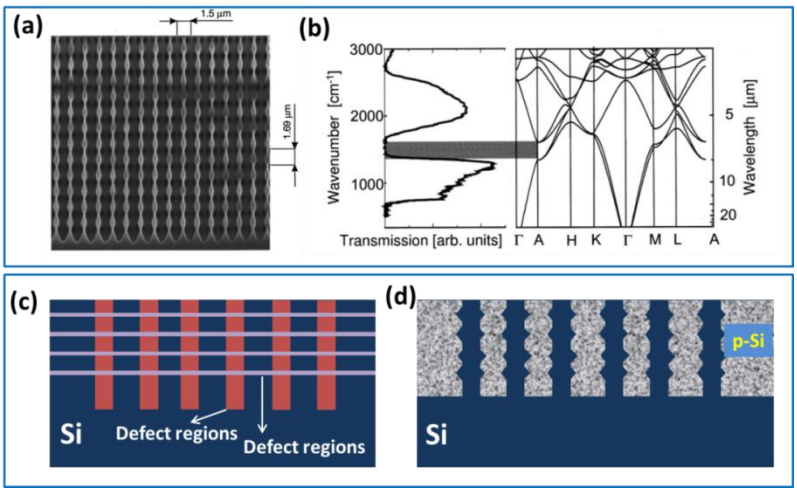

Figure 8.30 Modulation of pillar diameter in depth direction. (a, b)3D photonic crystal fabrication on the basis of macroporous silicon by modulation of the pore diameter. (Reproduced from Ref. [125]): (a)Cross section SEM; (b)Transmission along Γ -A; (c)Calculated 3D band structure. (c, d) Proposed fabrication method of 3D photonic crystal by modulation of the pillar diameter by multiple energy irradiation: (c) Defect distribution after point direction using high energy ion beam, and large area irradiation using multiple lower energy ion beam; (d) Porous silicon formation in subsequent electrochemical etching with constant current density, and formation of pillars with modulated diameter.

8.8 Building 3D integrated photonic circuit

One of the main advantages of using proton beam writing combined with electrochemical etching method for photonic crystals is the ability to allow separate structuring at different depths, favorable for moving towards a compact photonic circuit. Figure 8.31(b) shows two 2D photonic crystals at a depth of 7.0 μm and 2.4 μm, which was fabricated by using proton beam with 550 keV, and 250 keV, respectively, in a 0.02 Ω.cm wafer of which Figure 8.31 (a) shows wires at 7.0 μm depth in one direction.

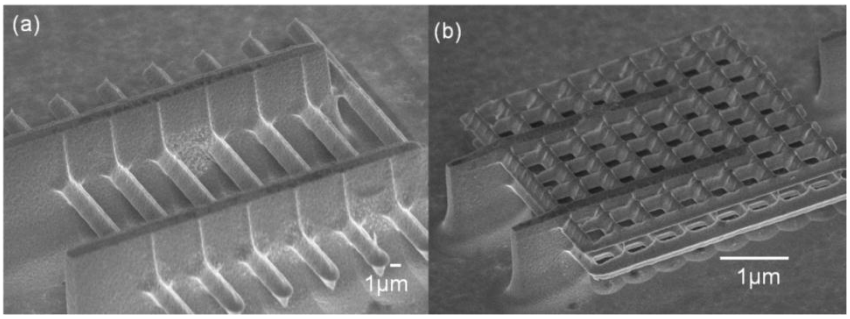

Figure 8.31 PhCs on two different depths. (a) Free-standing silicon wires at 7 μm depth; (b) Two level of photonic crystals slabs at 7.0 μm and 2.4 μm depths.

Conclusion

PhCs are artificially engineered components for making periodic structures for manipulation and confinement of light. Silicon being a widely available material and the platform for IC technology holds tremendous potential in realizing high index gradient photonic crystals. These photonic crystal devices could further be utilized as bricks of complex photonic circuits having vast applications. Si, p-Si and glass based PhCs have unique advantages due to their respective nature. The techniques described in this chapter allow us to design our photonic crystals with regions comprising of silicon, porous silicon or glass. Most of the previous work done in Si PhCs is in visible/NIR operating regime, while this chapter showcases the application of the fabrication approach introduced and discussed in previous chapters. The fabrication technique and an annealing step could be utilized to produce many types of PhCs in MIR range and take us closer towards the possibility of achieving integrated circuits. The fabricated PhCs include 2D PhCs, such as, 2D high aspect ratio Si pillars, 2D air hole in p-Si or glass matrix, and modified p-Si multilayer structures; 2.5D PhCs, such as air hole slabs in Si matrix. A proposal and initial results on 3D PhCs, such as woodpile structures are also shown. The simulation results using structural parameters of fabricated structures show the flexibility of this method in fabricating PhCs in a large MIR range. Characterization methods were briefly reviewed and the challenges of measurement based on FTIR and ellipsometry were discussed and the experiments are still under progress. Photonic circuits could be potentially realized due to the unique advantage of true 3D capability of this method of using ion irradiation combined with electrochemical etching of Si.

Chapter 9 . Conclusions and outlook

This chapter draws the conclusion from previous discussions in chapter 1-8; and discusses the outlook, which involves interesting future work based on and related to previous work in chapter 1-8.

9.1 Conclusions

Silicon, porous silicon and glass have respective unique properties. This thesis uses ion irradiation to modify the electrical properties of p-type silicon. This leads to two current components in the subsequent electrochemical anodization. The total current density tends to focus into small region and contributes to formation of highly porous regions with enhanced PL. It is this new observation leading to structuring method of p-Si, and further to structuring of glass. A better understanding of core formation mechanism is obtained by taking account of the time evolution of the etch front. The core formation mechanism helps us understand the core size and core shape is determined by straggling, ion energy, ion fluence, anodization current density as well as wafer resistivity. This work gives us better guide in designing the structures based on current flow. However, the significance of this understanding is not limited to the context of a micromachining process, since charged particle irradiated semiconductors is a topic of interest in diverse fields. It is relevant to other fields where any residual defect density may result in similar effects, which may adversely affect performance, such as in wafer gettering, [126, 127] since metal impurities can dramatically degrade device properties in Si even when they are present at quite small concentrations below 10^{12} cm^{-3}. The creation of favourable impurity precipitation or trapping sites, so-called gettering sites, by the introduction of appropriate near-surface flaws or defects, has been routinely used to avoid such effects. Various ion implanted species have been investigated as suitable gettering sources by the introduction of defects or defect-impurity complexes.[128, 129] A similar effect could be observed in satellite-based microelectronics,[130, 131] proton isolation of device areas[132, 133] and ion irradiation of wide band gap semiconductors. [134]

Apart from the basic understandings, this work explored the capability of 3D micromachining, and the use of resultant structures in photonic crystals. The basic understandings help in choosing suitable materials, ion energies, ion types, ion fluences, and designing better patterns and using suitable anodization conditions, to achieve desirable structures.

9.2 Outlooks

This basic study enables better control over the silicon micromachining process. Meanwhile, it gives insight on structuring of two other related materials, p-Si and glass (oxidized p-Si). These new fabrication processes have promising applications in other areas such as microfluidics etc., which should be explored further to a working device.

Future work mainly includes the application of these Si, p-Si, glass structuring in following areas.

9.2.1 Microfluidics: Application of buried channels in p-Si, glass

Porous silicon is a widely used material in biotechnology, micro- and nanofabrication, photonics, micro-reactors and micro-fluidics where the ability to machine surface microchannels is crucial. Such surface channels can subsequently be covered to provide shallow, buried channels using additional processing steps. Uses of porous silicon based channels include micro-reactor fabrication and as a gas pre-concentrator.[135] In nanotechnology, patterned porous silicon substrates are used to generate interconnected networks of niobium nanowires,[136] and thin films of nanostructured porous silicon filled by capillary forces.[137]

Microfluidics relies on the ability to fabricate small grooves and hollow channels as the basic building blocks of structures and devices, acting as connections between valves and pumps, sensors,[138] as separation columns for chromatography[139] or as heat exchangers.[140] Micromachined channels in electrically insulating and optically transparent materials such as glass and quartz, are very important.[141, 142] Integrating complex three dimensional micro/nanostructures, including channel networks, valves, sensors and actuators, in a single device is an important development for lab-on-a-chip systems; integrating various molecular biology operations relies on using biocompatible materials, which include porous silicon and glass. Glass substrates are robust and transparent but fabricating complex geometries comprising deeply buried channels, and/or nanoscale channels, chambers and other geometries using existing methods are challenging. The capability of fabricating buried channels, high aspect ratio trenches in glass using our

method overcomes this difficulty, and enables a potential application in microfluidics, the study of which is under progress.

9.2.2 Si nanodots and nanowires fabrication

The surface patterning of Si which was introduced in chapter 7 has a potential application in fabricating quantum wires and quantum dots, as schematically shown in Figure 9.1, where the surface patterning can be realized on the thin device layer of Silicon on insulator wafer. Si quantum wires can be used in single-electron transistor, etc. [143] These semiconductor nanowires are useful in investigating light generation, propagation, detection, amplification and modulation. And they can be used to fabrication nanowire photonic devices including photodetectors, chemical and gas sensors, waveguides, LEDs, microcavity lasers, solar cells and nonlinear optical converters. A fully integrated photonic platform using nanowire building blocks promises advanced functionalities at dimensions compatible with on-chip technologies. [144]

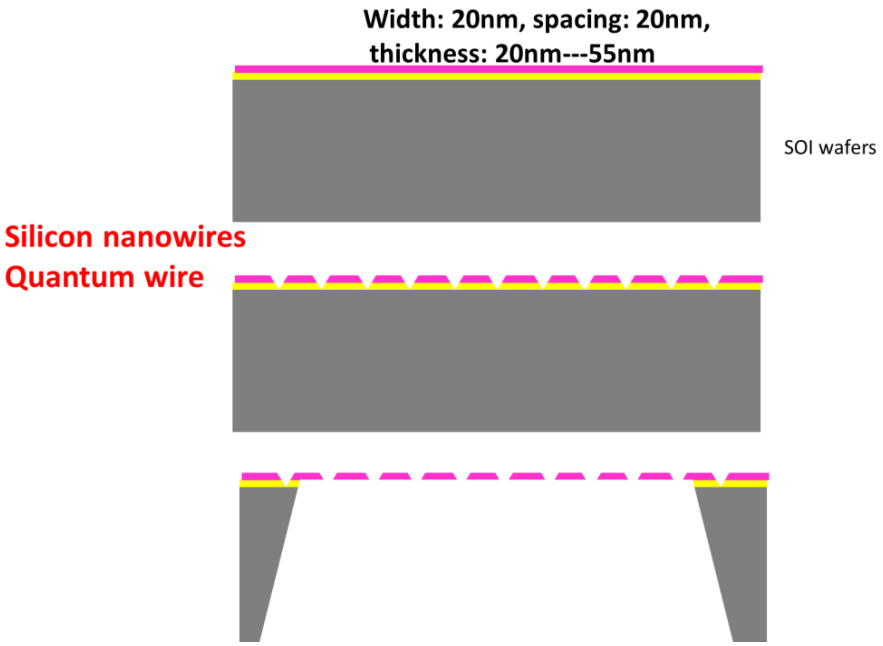

Figure 9.1 Fabrication of silicon quantum wires, quantum dots by patterning of SOI wafers with thin device layer

9.2.3 Photonics: Further characterization on photonic crystal

This thesis has explored fabrication of photonic crystals in MIR into a great detail. However, further characterization, and optimization is necessary to

display its significance, and potential use in practice, which have been discussed in chapter 8 earlier. Its application in photonics also includes fabrication of active devices by using the unique properties of Si and p-Si. For example, in Ref. [145], it shows that structures consisting of a metal hole array (MHA) lying on top of a 2D photonic crystal (PhC) exhibit the extraordinary transmission effect. In contrast to single MHAs, the extraordinary transmission in such hybrid structures is due to the coupling of an incident wave to eigenmodes of the PhC. Thus, the spectral positions of the transmission peaks are defined by the spectral positions of the corresponding PhC eigenmodes which provide a novel powerful tool to manipulate light on a sub-wavelength scale. Figure 9.2 illustrates an approach to make silicon based hole array wherein instead of using metal, highly-doped Si could be used as a metal. Additionally, the photocarrier generation could be triggered by blue light excitation. An important advantage of p-Si is that the porous structure could be infiltrated with a medium, which changes the refractive index and can be used to tune the band gap. For example, Ref. [146] uses the temperature dependent refractive index of a liquid crystal which was infiltrated into the air pores of a macroporous silicon photonic crystal with a triangular lattice pitch of 1.58 μm and a band gap wavelength range of 3.3–5.7 μm to tune the band gap.

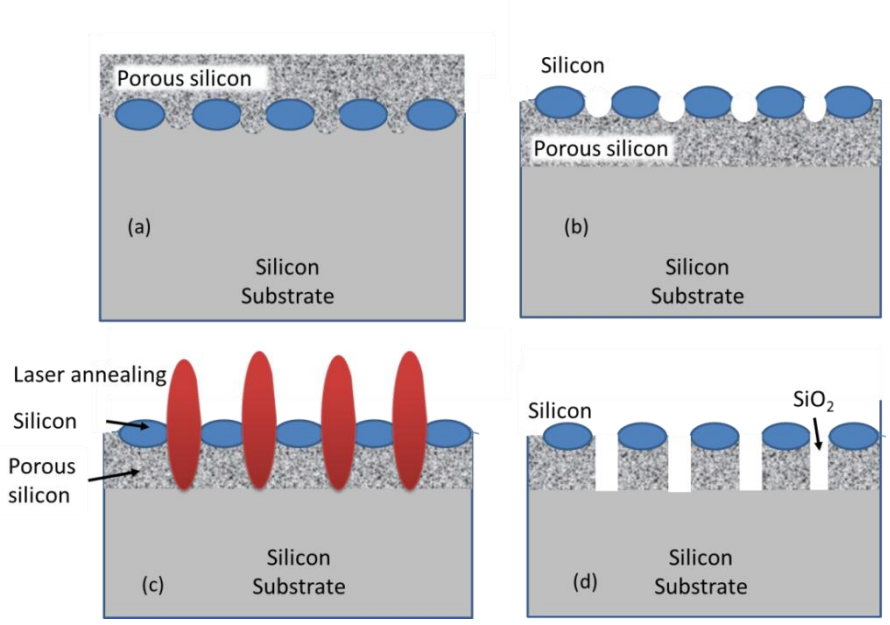

Figure 9.2 Fabrication of silicon hole array photonic crystal hybrid structures, which can be used for extraordinary transmission study by using the fact that silicon is an active material.

9.2.4 Phononics

The fabricated structures can also be used in phononics or the science of confinement of vibrations. Ref. [147] show the existence of large complete phononic band gaps in two-dimensional phononic crystals (PCs) formed by embedding cylindrical air holes in a solid plate (slab). Besides, the nanowires can be used for thermal conductivity study, as in Ref. [148], where the thermal conductivities of individual single crystalline intrinsic Si nanowires with diameters of 22, 37, 56, and 115 nm were more than two orders of magnitude lower than the bulk value. The strong diameter dependence of thermal conductivity in nanowires was ascribed to the increased phonon-boundary scattering and possible phonon spectrum modification.

9.2.5 Metamaterials

The Si structuring methods can also be used in realization of silicon metamaterials by making subwavelength structures. For example, Ref. [149] shows rendering objects invisible using a cloak composed of nanometre-size silicon structures with spatially varying densities (such that they are not detectable by an external observer) operating in the near infrared at a

wavelength of 1550 nm. The cloak conceals a deformation on a flat reflecting surface, under which an object can be hidden. The density variation is defined using transformation optics to define the effective index distribution of the cloak.

Appendix

Measurement method of beam size and two scanning modes: The ion beam was cut to be less than 1 pA, and used to scan a Ni standard grid[150], as in Figure 2.16(a), where 2MeV proton was used to scan over a 22 µm x 22µm area. The enhanced secondary electrons from the sharp edges are used to measure the beam size, as in following figure, Figure 2.16(b).[151] A developed software "Ionscan"[42] scans the focused ion beam in a vector style pattern with controlled blanking and timing while the stage is fixed at certain location. Multiple exposures are included in the Ionscan software, which scans all the exposures that are required for a run with designed dose at certain location of the stage. The area is limited to 500 µm x 500 µm. This is referred as "ion scan", which is a point scan mode. For the ease of fabricating long waveguide,[152] a stage scan mode is also developed where the ion beam is scanned in one direction, and stage is moved at a designed speed constantly to certain position. This is referred as "line scan", and enables long wires up to ten mm in length.

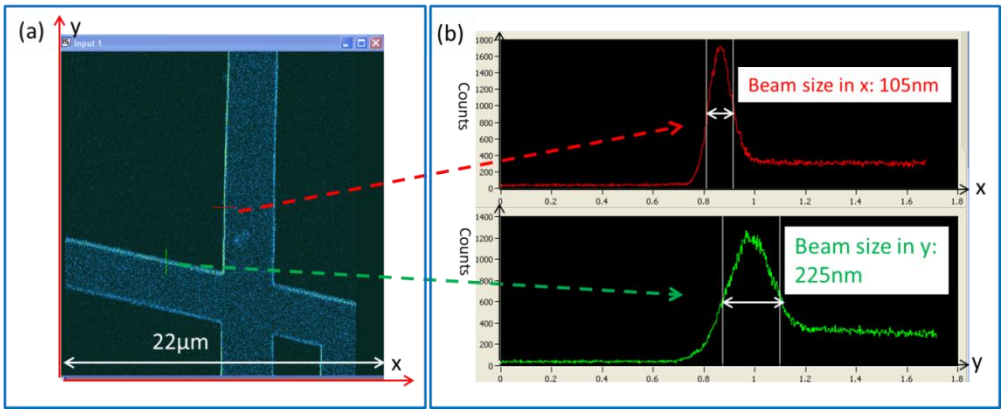

Figure. Focusing and measurement of beam size. (a) Image of secondary electrons of a Ni standard grid detected by Channel electron multiplier(CEM) detector with a 2 MeV proton beam of scan size of 22 µm; (b)Measurement of the beam size by drawing two lines across the sharp edges and measuring full width at half maximum(FHWM)

Specifications of FTIR: The source can either be synchrotron source or globar source. IFS 66v/S is a high performance research grade FTIR spectrometer, through the use of interchangeable optical components, this

spectrometer is capable of acquiring data over the near-IR (10000-4000 cm^{-1}), mid-IR (4000-400 cm^{-1}), and far-IR (680-10 cm^{-1}) regions. There are two Measurement types: Transmission and Grazing incidence reflection. The beam condenser can shrink the beam spot size ¼, which has 4 times beam de-magnification, meaning that for aperture set to 8 mm- spot size on the sample will be 2 mm (6mm aperture-1.5 mm spot size). It offers only sample rotation and two polarizers can be used for characterization.

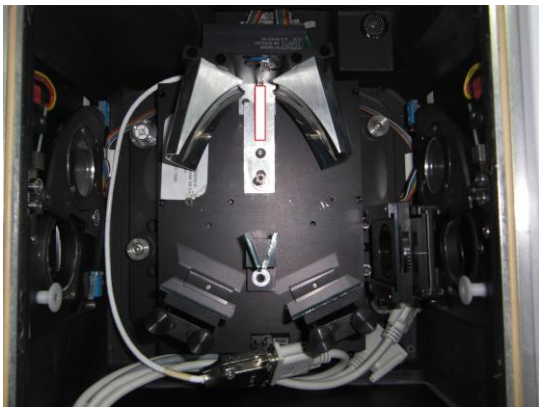

Figure. Photograph of the beam condenser inside the sample chamber

References

1. Petersen, K.E., *Silicon as a mechanical material.* Proceedings of the IEEE, 1982. **70**(5): p. 420-457.
2. Lehmann, V., *Electrochemistry of Silicon: Instrumentation, Science, Materials and Applications*2002: Wiley-VCH.
3. Lotsch, B.V. and G.A. Ozin, *Photonic Clays: A New Family of Functional 1D Photonic Crystals.* ACS Nano, 2008. **2**(10): p. 2065-2074.
4. De Stefano, L., et al., *Porous silicon microcavities for optical hydrocarbons detection.* Sensors and Actuators A: Physical, 2003. **104**(2): p. 179-182.
5. Torres-Costa, V., et al., *Porous silicon optical devices for sensing applications.* Optical Materials, 2005. **27**(5): p. 1084-1087.
6. Cullis, A.G., L.T. Canham, and P.D.J. Calcott, *The structural and luminescence properties of porous silicon.* Journal of Applied Physics, 1997. **82**(3): p. 909-965.
7. Araki, M., H. Koyama, and N. Koshida, *Precisely tuned emission from porous silicon vertical optical cavity in the visible region.* Journal of Applied Physics, 1996. **80**(9): p. 4841-4844.
8. Yon, J.J., et al., *The kinetics and mechanism of oxide layer formation from porous silicon formed on Si substrates.* Journal of Applied Physics, 1987. **62**(3): p. 1042-1048.
9. Weigold, J.W. and S.W. Pang, *Fabrication of thick Si resonators with a frontside-release etch-diffusion process.* Microelectromechanical Systems, Journal of, 1998. **7**(2): p. 201-206.
10. Jerwei, H. and F. Weileun, *A boron etch-stop assisted lateral silicon etching process for improved high-aspect-ratio silicon micromachining and its applications.* Journal of Micromechanics and Microengineering, 2002. **12**(5): p. 574.
11. Dang, Z.Y., et al., *Fabrication of large-area ultra-thin single crystal silicon membranes.* Applied Physics Letters, 2011. **99**(22).
12. Tanaka, M., *An industrial and applied review of new MEMS devices features.* Microelectronic Engineering, 2007. **84**(5–8): p. 1341-1344.
13. Yano, T., et al., *Wavelength Modulation Over 500 kHz of Micromechanically Tunable InP-Based VCSELs With Si-MEMS Technology.* Selected Topics in Quantum Electronics, IEEE Journal of, 2009. **15**(3): p. 528-534.
14. Bühler, J., F.P. Steiner, and H. Baltes, *Silicon dioxide sacrificial layer etching in surface micromachining.* Journal of Micromechanics and Microengineering, 1997. **7**(1): p. R1.
15. Chang, S.-W., et al., *Densely Packed Arrays of Ultra-High-Aspect-Ratio Silicon Nanowires Fabricated using Block-Copolymer Lithography and Metal-Assisted Etching.* Advanced Functional Materials, 2009. **19**(15): p. 2495-2500.
16. Bischoff, T., et al., *Frontside micromachining using purous-silicon sacrificial-layer technologies.* Sensors and Actuators A: Physical, 1997. **60**(1–3): p. 228-234.
17. Crawford, T.H.R., A. Borowiec, and H.K. Haugen, *Femtosecond laser micromachining of grooves in silicon with 800 nm pulses.* Applied Physics A, 2005. **80**(8): p. 1717-1724.
18. Chekurov, N., et al., *The fabrication of silicon nanostructures by local gallium implantation and cryogenic deep reactive ion etching.* Nanotechnology, 2009. **20**(6).

19. Sievila, P., N. Chekurov, and I. Tittonen, *The fabrication of silicon nanostructures by focused-ion-beam implantation and TMAH wet etching.* Nanotechnology, 2010. **21**(14).
20. Venkataraman, S., et al., *Fabrication of three-dimensional photonic crystals using silicon micromachining.* Applied Physics Letters, 2004. **85**(11): p. 2125-2127.
21. Watt, F., et al., *Proton beam writing.* Materials Today, 2007. **10**(6): p. 20-29.
22. Ziegler, J.F., M.D. Ziegler, and J.P. Biersack, *SRIM – The stopping and range of ions in matter (2010).* Nuclear Instruments and Methods in Physics Research Section B: Beam Interactions with Materials and Atoms, 2010. **268**(11–12): p. 1818-1823.
23. Breese, M.B.H., et al., *Hole transport through proton-irradiated p-type silicon wafers during electrochemical anodization.* Physical Review B, 2006. **73**(3): p. 035428.
24. Azimi, S., et al., *Fabrication of complex curved three-dimensional silicon microstructures using ion irradiation.* Journal of Micromechanics and Microengineering, 2012. **22**(1).
25. Teo, E.J., et al., *Three-dimensional micromachining of silicon using a nuclear microprobe.* Nuclear Instruments and Methods in Physics Research Section B: Beam Interactions with Materials and Atoms, 2004. **222**(3–4): p. 513-517.
26. Teo, E.J., et al., *Controlled intensity emission from patterned porous silicon using focused proton beam irradiation.* Applied Physics Letters, 2004. **85**(19): p. 4370-4372.
27. Mangaiyarkarasi, D., et al., *Controlled blueshift of the resonant wavelength in porous silicon microcavities using ion irradiation.* Applied Physics Letters, 2006. **89**(2): p. 021910-3.
28. Teo, E.J., et al., *Three-dimensional control of optical waveguide fabrication in silicon.* Opt. Express, 2008. **16**(2): p. 573-578.
29. Ow, Y.S., M.B.H. Breese, and A.A. Bettiol, *Proton beam writing for producing holographic images.* Nuclear Instruments and Methods in Physics Research Section B: Beam Interactions with Materials and Atoms, 2009. **267**(12–13): p. 2289-2291.
30. Watt, F., et al., *ION BEAM LITHOGRAPHY AND NANOFABRICATION: A REVIEW.* International Journal of Nanoscience, 2005. **04**(03): p. 269-286.
31. Liu, F., et al., *Fabrication of nickel molds using proton beam writing for micro/nano fluidic devices.* Microelectronic Engineering, 2013. **102**(0): p. 36-39.
32. Sum, T.C., et al., *Proton beam writing of low-loss polymer optical waveguides.* Applied Physics Letters, 2003. **83**(9): p. 1707-1709.
33. Zhang, C., et al., *Macromolecular crowding induced elongation and compaction of single DNA molecules confined in a nanochannel.* Proceedings of The National Academy of Sciences, 2009. **106**(40).
34. Van Kan, J.A., P. Malar, and A. Baysic de Vera, *The second generation Singapore high resolution proton beam writing facility.* Review of Scientific Instruments, 2012. **83**(2): p. 02B902-02B902-3.
35. Watt, F., et al., *The Singapore high resolution single cell imaging facility.* Nuclear Instruments and Methods in Physics Research Section B: Beam Interactions with Materials and Atoms, 2011. **269**(20): p. 2168-2174.
36. Brillson, L.J., *Rutherford Backscattering Spectrometry*, in *Surfaces and Interfaces of Electronic Materials*2010, Wiley-VCH Verlag GmbH & Co. KGaA. p. 183-196.

37. Folkmann, F., et al., *Proton induced X-ray emission as a tool for trace element analysis.* Nuclear Instruments and Methods, 1974. **116**(3): p. 487-499.
38. Breese, M.B.H., et al., *Applications of scanning transmission ion microscopy.* Nuclear Instruments and Methods in Physics Research Section B: Beam Interactions with Materials and Atoms, 1992. **64**(1–4): p. 505-511.
39. Chan, T.K., et al., *Interface strain study of thin Lu2O3/Si using HRBS.* Nuclear Instruments and Methods in Physics Research Section B: Beam Interactions with Materials and Atoms, 2008. **266**(8): p. 1486-1489.
40. Watt, F., *The nuclear microprobe: a unique instrument.* Nuclear Instruments and Methods in Physics Research Section B: Beam Interactions with Materials and Atoms, 1997. **130**(1–4): p. 1-8.
41. van Kan, J.A., A.A. Bettiol, and F. Watt, *Proton Beam Writing of Three-Dimensional Nanostructures in Hydrogen Silsesquioxane.* Nano Letters, 2006. **6**(3): p. 579-582.
42. Bettiol, A.A., et al., *Ionscan: scanning and control software for proton beam writing.* Nuclear Instruments and Methods in Physics Research Section B: Beam Interactions with Materials and Atoms, 2005. **231**(1–4): p. 400-406.
43. Stengl, G., et al., *Ion projection system for IC production.* Journal of Vacuum Science & Technology, 1979. **16**(6): p. 1883-1885.
44. Economou, N.P., J.A. Notte, and W.B. Thompson, *The history and development of the helium ion microscope.* Scanning, 2012. **34**(2): p. 83-89.
45. Benninghoven, A., F.G. Rudenauer, and H.W. Werner, *Secondary ion mass spectrometry: basic concepts, instrumental aspects, applications and trends*. Other Information: From review by Kenneth L. Busch, Indiana Univ., in J. Am. Chem. Soc., Vol. 109, No. 20 (1987)1987. Medium: X; Size: Pages: 1262.
46. Breese, M.B.H., et al., *Electrochemical Anodization of Silicon-on-Insulator Wafers Using an AC.* Electrochemical and Solid-State Letters, 2010. **13**(8): p. H271-H273.
47. Palmetshofer, L., *Rutherford Backscattering Spectroscopy (RBS)*, in *Surface and Thin Film Analysis*2011, Wiley-VCH Verlag GmbH & Co. KGaA. p. 191-202.
48. McMullan, D., *Scanning electron microscopy 1928–1965.* Scanning, 1995. **17**(3): p. 175-185.
49. Giessibl, F.J., *Advances in atomic force microscopy.* Reviews of Modern Physics, 2003. **75**(3): p. 949-983.
50. Langford, R.M. and A.K. Petford-Long, *Preparation of transmission electron microscopy cross-section specimens using focused ion beam milling.* Journal of Vacuum Science & Technology A: Vacuum, Surfaces, and Films, 2001. **19**(5): p. 2186-2193.
51. M. B. H. Breese, D.N.J., and King, P. J. C., *Materials Analysis using a Nuclear Microprobe* 1996.
52. *Defects in Solids*, in *Solid State Physics*2007, Springer Berlin Heidelberg. p. 587-608.
53. J. Song, Z.Y.D., S. Azimi, M. B. H. Breese, J. Forneris and E. Vittone, *On the Formation of 50 nm Diameter Free-Standing Silicon Wires Produced by Ion Irradiation.* ECS J. Solid State Sci. Technol. , 2012. **1**(2): p. p66-p69.
54. Dang, Z.Y., et al., *On the formation of silicon wires produced by high-energy ion irradiation.* Nuclear Instruments and Methods in Physics Research Section B: Beam Interactions with Materials and Atoms, 2013. **296**(0): p. 32-40.

55. Gaspard, F., et al., *CHARGE-EXCHANGE MECHANISM RESPONSIBLE FOR P-TYPE SILICON DISSOLUTION DURING POROUS SILICON FORMATION.* Journal of the Electrochemical Society, 1989. **136**(10): p. 3043-3046.
56. Zhang, X.G., *Morphology and formation mechanisms of porous silicon.* Journal of the Electrochemical Society, 2004. **151**(1): p. C69-C80.
57. Wijesinghe, T., S.Q. Li, and D.J. Blackwood, *Influence of doping density on the current-voltage characteristics of p-type silicon in dilute hydrofluoric acid.* Journal of Physical Chemistry C, 2008. **112**(1): p. 303-307.
58. Allongue, P., V. Kieling, and H. Gerischer, *Etching mechanism and atomic structure of H ・ Si(111) surfaces prepared in NH4F.* Electrochimica Acta, 1995. **40**(10): p. 1353-1360.
59. Astrova, E.V. and A.A. Nechitaĭlov, *Boundary effect in electrochemical etching of silicon.* Semiconductors, 2008. **42**(4): p. 470-474.
60. Pham, M.T. and J. Hueller, *Ion implanted silicon-electrolyte interface.* Journal of Applied Electrochemistry, 1977. **7**(6): p. 531-537.
61. Pokotilo, Y.M., A.N. Petukh, and V.V. Litvinov, *Donor center formation in silicon implanted with hydrogen ions.* Technical Physics Letters, 2004. **30**(11): p. 962-963.
62. Yamaguchi, M. and K. Ando, *Mechanism for radiation resistance of InP solar cells.* Journal of Applied Physics, 1988. **63**(11): p. 5555-5562.
63. Yamaguchi, M., et al., *High energy and high fluence proton irradiation effects in silicon solar cells.* Journal of Applied Physics, 1996. **80**(9): p. 4916-4920.
64. Imai, K., *A new dielectric isolation method using porous silicon.* Solid-State Electronics, 1981. **24**(2): p. 159-164.
65. Petris, M. *Radiation induced change of the effective doping concentration in silicon detectors*. in *Semiconductor Conference, 1999. CAS '99 Proceedings. 1999 International*. 1999.
66. Hallen, A., et al., *Lifetime in proton irradiated silicon.* Journal of Applied Physics, 1996. **79**(8): p. 3906-3914.
67. Azimi, S., et al., *Defect enhanced funneling of diffusion current in silicon.* Applied Physics Letters, 2013. **102**(4): p. 042102-042102-5.
68. Scharfetter, D.L. and H.K. Gummel, *Large-signal analysis of a silicon Read diode oscillator.* Electron Devices, IEEE Transactions on, 1969. **16**(1): p. 64-77.
69. Yuan, J.S. and J.J. Liou, *Semiconductor Device Physics and Simulation*1998: Springer.
70. Teo, E.J., et al., *Multicolor photoluminescence from porous silicon using focused, high-energy helium ions.* Advanced Materials, 2006. **18**(1): p. 51-55.
71. Azimi, S., et al., *A thousand-fold enhancement of photoluminescence in porous silicon using ion irradiation.* Journal of Applied Physics, 2013. **114**(5): p. -.
72. Gharbi, A., et al., *Investigation of current-voltage characteristics of p-type silicon during electrochemical anodization and application to doping profiling*, in *Physica Status Solidi C: Current Topics in Solid State Physics, Vol 8, No 3*2011, Wiley-V C H Verlag Gmbh: Weinheim.
73. Ligeon, M., et al., *APPLICATION OF POROUS SILICON FORMATION SELECTIVITY TO IMPURITY PROFILING IN P-TYPE SILICON SUBSTRATES.* Journal of Applied Physics, 1989. **66**(8): p. 3814-3819.
74. Lehmann, V. and S. Ronnebeck, *The physics of macropore formation in low-doped p-type silicon.* Journal of the Electrochemical Society, 1999. **146**(8): p. 2968-2975.

75. Arutyunyan, V.M., *Physical properties of the semiconductor-electrolyte interface.* Soviet Physics Uspekhi, 1989. **32**(6): p. 521.
76. Duan, H., J.K.W. Yang, and K.K. Berggren, *Controlled Collapse of High-Aspect-Ratio Nanostructures.* Small, 2011. **7**(18): p. 2661-2668.
77. Liang, H.D., et al., *Ion beam irradiation induced fabrication of vertical coupling waveguides.* Applied Physics Letters, 2013. **102**(13): p. 131112-4.
78. Brugger, J., R.A. Buser, and N.F. de Rooij, *Silicon cantilevers and tips for scanning force microscopy.* Sensors and Actuators A: Physical, 1992. **34**(3): p. 193-200.
79. Folch, A., M.S. Wrighton, and M.A. Schmidt, *Microfabrication of oxidation-sharpened silicon tips on silicon nitride cantilevers for atomic force microscopy.* Microelectromechanical Systems, Journal of, 1997. **6**(4): p. 303-306.
80. Ow, Y.S., et al., *Modification of Porous Silicon Formation by Varying the End of Range of Ion Irradiation.* Electrochemical and Solid-State Letters, 2011. **14**(5): p. D45-D47.
81. Rossi, A.M., et al., *Lateral structuring of porous silicon: application to waveguides.* physica status solidi (a), 2003. **197**(1): p. 284-287.
82. *Nanostructured Porous Silicon Photonic Crystal for Applications in the Infrared.* Journal of Nanotechnology, 2012. **2012**: p. 6.
83. Mangaiyarkarasi, D., et al., *Fabrication of large-area patterned porous silicon distributed Bragg reflectors.* Opt. Express, 2008. **16**(17): p. 12757-12763.
84. Zhou, Y., et al., *Direct femtosecond laser nanopatterning of glass substrate by particle-assisted near-field enhancement.* Applied Physics Letters, 2006. **88**(2): p. 023110-3.
85. Hung, Y.M., Y.J. Lu, and C.K. Sung, *Microstructure patterning on glass substrate by imprinting process.* Microelectronic Engineering, 2009. **86**(4–6): p. 577-582.
86. Dumais, P., et al., *Monolithic integration of microfluidic channels, liquid-core waveguides, and silica waveguides on silicon.* Applied Optics, 2006. **45**(36): p. 9182-9190.
87. Ho, S., et al. *Femtosecond laser-assisted etching of three dimensional woodpile micro-channel arrays in fused silica*. in *Lasers and Electro-Optics (CLEO), 2011 Conference on*. 2011.
88. Axel, G., G. Matthias, and F. Henning, *Deep wet etching of fused silica glass for hollow capillary optical leaky waveguides in microfluidic devices.* Journal of Micromechanics and Microengineering, 2001. **11**(3): p. 257.
89. Guo, L.J., X. Cheng, and C.-F. Chou, *Fabrication of Size-Controllable Nanofluidic Channels by Nanoimprinting and Its Application for DNA Stretching.* Nano Letters, 2003. **4**(1): p. 69-73.
90. Klehn, B. and U. Kunze, *SiO2 and Si nanoscale patterning with an atomic force microscope.* Superlattices and Microstructures, 1998. **23**(2): p. 441-444.
91. Abeln, G.C., et al., *NANOSCALE STM-PATTERNING AND CHEMICAL MODIFICATION OF THE SI(100) SURFACE.* Microelectronic Engineering, 1995. **27**(1-4): p. 23-26.
92. Couderc, S., V. Blech, and B. Kim, *New Surface Treatment and Microscale/Nanoscale Surface Patterning Using Electrostatically Clamped Stencil Mask.* Japanese Journal of Applied Physics, 2009. **48**(9).
93. Huang, Z.P., et al., *Extended arrays of vertically aligned sub-10 nm diameter 100 Si nanowires by metal-assisted chemical etching.* Nano Letters, 2008. **8**(9): p. 3046-3051.

94. Xu, L., et al., *Nanopantography: A new method for massively parallel nanopatterning over large areas.* Nano Letters, 2005. **5**(12): p. 2563-2568.
95. Rao, R., J.E. Bradby, and J.S. Williams, *Patterning of silicon by indentation and chemical etching.* Applied Physics Letters, 2007. **91**(12).
96. Gianola, U.F., *Damage to Silicon Produced by Bombardment with Helium Ions.* Journal of Applied Physics, 1957. **28**(8): p. 868-873.
97. Gibbons, J.F., E.O. Hechtl, and T. Tsurushima, *ION-BOMBARDMENT-ENHANCED ETCHING OF SILICON.* Applied Physics Letters, 1969. **15**(4): p. 117-119.
98. Gnaser, H., *Incidence-angle dependent Cs incorporation in Si during low-energy bombardment: A dynamic computer simulation study.* Nuclear Instruments and Methods in Physics Research Section B: Beam Interactions with Materials and Atoms, 2009. **267**(16): p. 2608-2611.
99. Demenev, E., et al., *Calibration correction of ultra low energy SIMS profiles based on MEIS analyses for arsenic shallow implants in silicon.* Nuclear Instruments and Methods in Physics Research Section B: Beam Interactions with Materials and Atoms, 2012. **273**(0): p. 192-194.
100. Ghiradella, H., *Light and color on the wing: structural colors in butterflies and moths.* Appl. Opt., 1991. **30**(24): p. 3492-3500.
101. Wu, J., D. Day, and M. Gu, *A microfluidic refractive index sensor based on an integrated three-dimensional photonic crystal.* Applied Physics Letters, 2008. **92**(7): p. 071108-071108-3.
102. Kosaka, H., et al., *Photonic crystals for micro lightwave circuits using wavelength-dependent angular beam steering.* Applied Physics Letters, 1999. **74**(10): p. 1370-1372.
103. Park, Y., et al., *Absorption enhancement using photonic crystals for silicon thin film solar cells.* Opt. Express, 2009. **17**(16): p. 14312-14321.
104. Xing, A., et al., *Fabrication of InP-based two-dimensional photonic crystal membrane.* Journal of Vacuum Science & Technology B: Microelectronics and Nanometer Structures, 2004. **22**(1): p. 70-73.
105. Hermatschweiler, M., et al., *Fabrication of Silicon Inverse Woodpile Photonic Crystals.* Advanced Functional Materials, 2007. **17**(14): p. 2273-2277.
106. Birner, A., et al., *Transmission of a microcavity structure in a two-dimensional photonic crystal based on macroporous silicon.* Materials Science in Semiconductor Processing, 2000. **3**(5–6): p. 487-491.
107. Lin, S.Y., et al., *A three-dimensional photonic crystal operating at infrared wavelengths.* Nature, 1998. **394**(6690): p. 251-253.
108. Matthias, S., F. Muller, and U. Gosele, *Simple cubic three-dimensional photonic crystals based on macroporous silicon and anisotropic posttreatment.* Journal of Applied Physics, 2005. **98**(2): p. 023524-023524-4.
109. Reimer, C., et al., *Mid-infrared photonic crystal waveguides in silicon.* Opt. Express, 2012. **20**(28): p. 29361-29368.
110. Král, Z., et al., *Characterization of 2D macroporous silicon photonic crystals: Improving the photonic band identification in angular-dependent reflection spectroscopy in the mid-IR.* Materials Science and Engineering: B, 2008. **147**(2–3): p. 179-182.
111. Prodan, L., et al., *Mid-IR transmission of a large-area 2D silicon photonic crystal slab.* Journal of Physics D: Applied Physics, 2008. **41**(13): p. 135105.
112. Knights, A.P. and G.F. Hopper *Effect of ion implantation induced defects on optical attenuation in silicon waveguides*. Electronics Letters, 2003. **39**, 1648-1649.

113. Foster, P.J., et al., *Optical attenuation in defect-engineered silicon rib waveguides.* Journal of Applied Physics, 2006. **99**(7): p. 073101-073101-7.
114. Tamura, M., *Damage formation and annealing of ion implantation in Si.* Materials Science Reports, 1991. **6**(4–5): p. 141-214.
115. Narayan, J. and O.W. Holland, *Rapid thermal annealing of ion-implanted semiconductors.* Journal of Applied Physics, 1984. **56**(10): p. 2913-2921.
116. Faraday, B.J., R.L. Statler, and R.V. Tauke, *Thermal annealing of proton-irradiated silicon solar cells.* Proceedings of the IEEE, 1968. **56**(1): p. 31-37.
117. Azimi, S., Y.S. Ow, and M.B.H. Breese, *On the Dependence of the Surface Roughness of Electrochemically Anodized Silicon on Ion Irradiation Fluence.* Electrochemical and Solid State Letters, 2010. **13**(11): p. H382-H384.
118. Teo, E.J., et al., *Fabrication of low-loss silicon-on-oxidized-porous-silicon strip waveguide using focused proton-beam irradiation.* Opt. Lett., 2009. **34**(5): p. 659-661.
119. Johnson, S. and J. Joannopoulos, *Block-iterative frequency-domain methods for Maxwell's equations in a planewave basis.* Opt. Express, 2001. **8**(3): p. 173-190.
120. Sailor, W.C., F.M. Mueller, and P.R. Villeneuve, *Augmented-plane-wave method for photonic band-gap materials.* Physical Review B, 1998. **57**(15): p. 8819-8822.
121. Joannopoulos, J.D., *Photonic Crystals: Molding the Flow of Light*, 2008, Princeton Univ Pr.
122. Chow, E., et al., *Three-dimensional control of light in a two-dimensional photonic crystal slab.* Nature, 2000. **407**(6807): p. 983-986.
123. Johnson, S., et al., *Guided modes in photonic crystal slabs.* Physical Review B, 1999. **60**(8): p. 5751-5758.
124. Sato, T., et al., *Photonic crystals for the visible range fabricated by autocloning technique and their application.* Optical and Quantum Electronics, 2002. **34**(1-3): p. 63-70.
125. Schilling, J., et al., *Three-dimensional photonic crystals based on macroporous silicon with modulated pore diameter.* Applied Physics Letters, 2001. **78**(9): p. 1180-1182.
126. Myers, S.M., G.A. Petersen, and C.H. Seager, *Binding of cobalt and iron to cavities in silicon.* Journal of Applied Physics, 1996. **80**(7): p. 3717-3726.
127. Wong, et al., *Gettering of copper to hydrogen-induced cavities in silicon.* Applied Physics Letters, 1995. **66**(10): p. 1231-1233.
128. Wong, H., et al., *Proximity gettering with mega-electron-volt carbon and oxygen implantations.* Applied Physics Letters, 1988. **52**(12): p. 1023-1025.
129. Lecrosnier, D., et al., *Gold gettering in silicon by phosphorous diffusion and argon implantation: Mechanisms and limitations.* Journal of Applied Physics, 1981. **52**(8): p. 5090-5097.
130. Oldham, T.R., *Analysis of Damage in MOS Devices for Several Radiation Environments.* Nuclear Science, IEEE Transactions on, 1984. **31**(6): p. 1236-1241.
131. Oldham, T.R. and F.B. McLean, *Total ionizing dose effects in MOS oxides and devices.* Nuclear Science, IEEE Transactions on, 2003. **50**(3): p. 483-499.
132. Foyt, A.G., et al., *Isolation of junction devices in GaAs using proton bombardment.* Solid-State Electronics, 1969. **12**(4): p. 209-214.
133. Lurng Shehng, L., et al., *Isolation on Si wafers by MeV proton bombardment for RF integrated circuits.* Electron Devices, IEEE Transactions on, 2001. **48**(5): p. 928-934.

134. Colombo, E., et al., *IBIC analysis of CdTe/CdS solar cells.* Nuclear Instruments and Methods in Physics Research Section B: Beam Interactions with Materials and Atoms, 2009. **267**(12–13): p. 2181-2184.
135. Camara, E.H.M., et al., *A micro gas preconcentrator with improved performance for pollution monitoring and explosives detection.* Analytica Chimica Acta, 2011. **688**(2): p. 175-182.
136. Cirillo, C., et al., *Quantum phase slips in superconducting Nb nanowire networks deposited on self-assembled Si templates.* Applied Physics Letters, 2012. **101**(17): p. 172601-5.
137. Acquaroli, L.N., et al., *Capillary Filling in Nanostructured Porous Silicon.* Langmuir, 2011. **27**(5): p. 2067-2072.
138. Elwenspoek, M., et al., *Towards integrated microliquid handling systems.* Journal of Micromechanics and Microengineering, 1994. **4**(4): p. 227.
139. Terry, S.C., J.H. Jerman, and J.B. Angell, *A gas chromatographic air analyzer fabricated on a silicon wafer.* Electron Devices, IEEE Transactions on, 1979. **26**(12): p. 1880-1886.
140. Reston, R.R. and E.S. Kolesar, *Silicon-micromachined gas chromatography system used to separate and detect ammonia and nitrogen dioxide. I. Design, fabrication, and integration of the gas chromatography system.* Microelectromechanical Systems, Journal of, 1994. **3**(4): p. 134-146.
141. Harrison, D.J., et al., *Micromachining a Miniaturized Capillary Electrophoresis-Based Chemical Analysis System on a Chip.* Science, 1993. **261**(5123): p. 895-897.
142. Jacobson, S.C., et al., *PRECOLUMN REACTIONS WITH ELECTROPHORETIC ANALYSIS INTEGRATED ON A MICROCHIP.* Analytical Chemistry, 1994. **66**(23): p. 4127-4132.
143. Kim, D.H., et al., *Single-electron transistor based on a silicon-on-insulator quantum wire fabricated by a side-wall patterning method.* Applied Physics Letters, 2001. **79**(23): p. 3812-3814.
144. Yan, R., D. Gargas, and P. Yang, *Nanowire photonics.* Nat Photon, 2009. **3**(10): p. 569-576.
145. Glushko, O., et al., *Extraordinary transmission in metal hole array-photonic crystal hybrid structures.* Opt. Express, 2012. **20**(15): p. 17174-17182.
146. Leonard, S.W., et al., *Tunable two-dimensional photonic crystals using liquid crystal infiltration.* Physical Review B, 2000. **61**(4): p. R2389-R2392.
147. Mohammadi, S., et al., *Evidence of large high frequency complete phononic band gaps in silicon phononic crystal plates.* Applied Physics Letters, 2008. **92**(22): p. 221905-221905-3.
148. Li, D., et al., *Thermal conductivity of individual silicon nanowires.* Applied Physics Letters, 2003. **83**(14): p. 2934-2936.
149. Gabrielli, L.H., et al., *Silicon nanostructure cloak operating at optical frequencies.* Nat Photon, 2009. **3**(8): p. 461-463.
150. Zhang, F., et al., *Fabrication of free standing resolution standards using proton beam writing.* Nuclear Instruments and Methods in Physics Research Section B: Beam Interactions with Materials and Atoms, 2007. **260**(1): p. 474-478.
151. Udalagama, C.N.B., et al., *An automatic beam focusing system for MeV protons.* Nuclear Instruments and Methods in Physics Research Section B: Beam Interactions with Materials and Atoms, 2005. **231**(1–4): p. 389-393.
152. Udalagama, C., et al., *Proton beam writing of long, arbitrary structures for micro/nano photonics and fluidics applications.* Nuclear Instruments and

Methods in Physics Research Section B: Beam Interactions with Materials and Atoms, 2011. **269**(20): p. 2417-2421.